

**Decarboxylative Cross-coupling: Bimetallic Nanoparticles as  
Catalysts and Low-Temperature Optimisation**

Joseph Kyle Sheppard

Submitted in accordance with the requirements for the degree of Doctor of  
Philosophy

University of Leeds

School of Chemistry

September 2020

The candidate confirms the work submitted is his own and that appropriate credit has been given where reference has been made to the work of others.

## Acknowledgements

First and foremost, I would like to thank my supervisors Dr. Bao N. Nguyen and Prof. Patrick McGowan for providing me with the opportunity to undertake this PhD. Bao, you deserve a medal for putting up with me for four whole years! Thank you dearly for everything you have taught me. Patrick, though our meetings were few and far between, I always left them brimming with new ideas and knowledge.

I must also thank the wonderful Dr. Alexander Kulak; chiefly for all of your assistance with AAS and SEM analysis but also for being a friendly face that never failed to brighten my days. I'll deeply miss the hours we spent, shouting over the noise of the spectrometer and trying to work out why it would develop an entirely new issue every time we used it. I would also like to thank Dr. Rebecca Stones for all of her hard work running my TEM samples and teaching me how to analyse the micrographs. Special thanks must also go to Dr. Mary Bayana for her patience in teaching me how to use all of the arcane and intricate analytical machines of the iPRD and to Martin Huscroft for helping me refine my HPLC method.

To the members of the BNN research group, past and present, thank you for the copious assistance navigating the enigmatic world of academia and generally being a joy to work with. Thank you, Grant and Rachel, for putting up with all of my questions at the start of my PhD. Grant, your tastes in music were... definitely something! To Rosie, your quick wit and questionable reddit adventures will always be remembered; thank you so much for your diligent proof-reading. Thank you Sam, python wizard and saxophone maestro, for stimulating computational chemistry discussions and for providing the group with all of the juicy opera society gossip. To Tom, what can I say? You put the bantz into BNN and the fear of God into me when you were behind the wheel. James, mild of manners but ruthless when it came to curve fever; thank you for your assistance with many a disastrous column. Finally, I must thank Sannia; our sprawling office chats were very dear to me and I wish you all the best in your postdoc.

Without question, my largest thanks go to my family. To my dear old mum, thank you for keeping me stocked with motivational kit-kats and being there for me every step of the way. To my beloved fiancée Sophie, words are not enough to describe

everything you have done to get me to where I am now. You make me a better person and none of this would have been possible without you. Lastly, I would like to thank my grandad for always believing in me; I told you I'd do it! This thesis is dedicated to you.

## Abstract

Decarboxylative cross-coupling chemistry is an emerging field of research that promises the synthesis of a variety of biaryl products without the need for expensive and challenging to handle organometallic reagents. *Via* interaction with a transition metal catalyst, organometallic species are generated *in situ* from carboxylic acid functionality, eliminating carbon dioxide in the process. However, inducing the decarboxylation of even highly activated carboxylic acids often requires forcing conditions: high reaction temperatures; long reaction times; and in some cases, stoichiometric quantities of transition metal mediator. Such conditions bring with them issues regarding functional group tolerance and side reaction prevalence, which limit the broader applicability of the method.

The work detailed herein explores the applicability of both monometallic and bimetallic nanoparticles as potential solutions to these problems. A wide library of bimetallic catalysts have been synthesised containing group 10 (nickel or palladium) and group 11 (copper, silver or gold) transition metals, characterised *via* atomic absorption spectroscopy, transition electron microscopy and energy-dispersive x-ray spectroscopy and subsequently screened against a typical decarboxylative cross-coupling protocol utilising fluorinated potassium benzoate salts. Palladium/copper bimetallic nanoparticles were found to be excellent catalysts under both the literature conditions of 130 °C and the lower temperature of 100 °C. Palladium rich alloys performed best, and a synergistic effect was observed – the bimetallic nanoparticles displaying greatly enhanced reactivities over their monometallic analogues. Capping agent choice was also found to have a pronounced effect on catalyst activity, with the ethylene glycol-capped palladium/copper 1:1 bimetallic nanoparticle catalyst reaching reaction completion in 1 hour at 100 °C, outperforming competing homogeneous catalyst systems.

Substrate scope was also explored under these conditions, utilising small scale DFT calculations to make informed substrate choices. The result of this work was the elucidation of an interesting phenomenon, wherein certain substrate pairings performed considerably better than others. Through follow up experiments evidence is presented that suggests this phenomenon is kinetic in nature, with substrate choice

affecting the rates of the group 10 and group 11 catalytic cycles – parameters that are key to a reliable decarboxylative cross-coupling reaction.

Finally, scope for the replacement of toxic and harmful solvents typically used in DCC protocols was also investigated. Success was found utilising poly(ethylene glycol) both as a direct analogue for problem solvents such as diglyme and in smaller quantities as an additive in desirable but underperforming solvent systems to boost reactivity.

## Table of Contents

	<b>Page</b>
<b>Acknowledgements</b>	II
<b>Abstract</b>	IV
<b>Table of Contents</b>	VI
<b>List of Figures</b>	X
<b>List of Schemes</b>	XIII
<b>List of Tables</b>	XV
<b>List of Abbreviations</b>	XVII
<b>Chapter 1:</b>	
<i>Introduction</i>	
<b>1.1</b> Overview	1
<b>1.2</b> Decarboxylative Cross-coupling	1
<b>1.2.1</b> Background	1
<b>1.2.2</b> Bimetallic Catalyst Systems	5
<b>1.2.3</b> Monometallic Catalyst Systems	11
<b>1.2.4</b> Protodecarboxylation	16
<b>1.2.5</b> The <i>Ortho</i> - Effect	21
<b>1.3</b> Metallic Nanoparticles	26
<b>1.3.1</b> Routes to Synthesis	28
<b>1.3.2</b> Monometallic Nanoparticles in Catalysis	33
<b>1.3.3</b> Bimetallic Nanoparticles in Catalysis	36
<b>1.4</b> Project Aims	39
<b>Chapter 2:</b>	
<i>Investigations in Copper-catalysed Decarboxylative Cross-coupling</i>	
<b>2.1</b> Introduction	40
<b>2.2</b> Synthesis and Characterisation of Copper-containing Heterogeneous Catalysts	41
<b>2.3</b> Copper-catalysed Decarboxylative Cross-coupling	49
<b>2.3.1</b> Reaction Optimisation	55
	VI

2.3.2	Solvent Scope and the Role of Diglyme	58
2.3.3	Exploring the Effect of Varying Substrate Counter-ion	64
2.4	Induction Heating as a Novel Approach to Decarboxylative Cross-coupling	68
2.4.1	Reactor Design	72
2.4.2	Initial Investigations and Discussion	74
2.5	Conclusions and Future Work	77

### **Chapter 3:**

#### *Bimetallic Nanoparticles as Catalysts for Decarboxylative Cross-coupling*

3.1	Introduction	82
3.2	Catalyst Synthesis and Characterisation	83
3.2.1	PVP-capped Palladium/Copper Catalyst Series	85
3.2.2	PVP-capped Palladium/Silver and Palladium/Gold Catalyst Series	90
3.2.3	EG-capped Nickel/Copper and Palladium/Copper Catalyst Series	95
3.3	PVP-capped Nanoparticles in Decarboxylative Cross-coupling Reactions	101
3.3.1	Palladium/Copper Decarboxylative Cross-coupling	101
3.3.2	The Potential for Nanoparticle Leaching	104
3.3.3	Palladium/Silver and Palladium/Gold Catalysed Decarboxylative Cross-coupling	107
3.4	EG-capped Nanoparticles in Decarboxylative Cross-coupling Reactions	110
3.4.1	Palladium/Copper Catalysed Decarboxylative Cross-coupling	110
3.4.2	Nickel/Copper Catalysed Decarboxylative Cross-coupling	111
3.5	Conclusions and Future Work	112

### **Chapter 4:**

#### *Exploration of the Scope of Decarboxylative Cross-coupling under Low Temperature Conditions*

4.1	Introduction	116
4.2	Bimetallic Catalysis and Choice of Substrate	117
4.3	Screening Substrates & Catalysts in Decarboxylative Cross-coupling Reactions	124

4.4	Conclusions and Future Work	131
-----	-----------------------------	-----

## **Chapter 5:**

### *Poly(ethylene glycol) as an Additive to Promote Reactivity in Decarboxylative Cross-coupling*

5.1	Introduction	134
5.2	Applying Solvent Mapping to a Typical DCC Protocol	135
5.2.1	Using Glycols to Improve Reactivity	140
5.3	Exploring the Role of Poly(ethylene glycol) in DCC Reactivity	142
5.3.1	As an Additive	146
5.3.2	As a Solvent	147
5.4	Reaction Optimisation for Substrate with Lower Degrees of Fluorination	149
5.4.1	Design of Experiments	152
5.5	Conclusions and Future Work	161

## **Chapter 6:**

### *Experimental*

6.1	Methods and Instrumentation	165
6.2	Experimental Details	165
6.2.1	Synthesis of Nanoparticles and Catalytic Material	165
6.2.2	Synthesis of Functionalised Potassium Benzoates	173
6.2.3	Synthesis of Functionalised Caesium Benzoates	177
6.2.4	Synthesis and Purification of Biphenyl Products	177
6.2.5	General Experimental Procedures	182
6.3	Nuclear Magnetic Resonance Spectroscopy of Purified Compounds	187
6.4	Fourier-transform Infra-red Spectroscopy of Purified Compounds	200
6.5	High Resolution Mass Spectrometry of Purified Compounds	203
6.6	High Pressure Liquid Chromatography Yield Derivation Methodology	207
6.7	Nuclear Magnetic Resonance Yield Derivation Methodology	211
6.8	Calibration Data for Benzoate/Aryl Halide Coupling Reactions	214
6.9	Magnetochemical Analysis	220
6.10	Atomic Absorption Spectroscopy Data	222

<b>6.11</b>	Transition Electron Microscopy Data	228
<b>6.12</b>	Energy-dispersive X-ray Spectroscopy Data	241
<b>6.13</b>	Computational Chemistry Data	246
<b>References</b>		260

## List of Figures

	<b>Page</b>
<b>Chapter 1:</b>	
<b>Figure 1.1</b>	Hypothetical mechanism for Cu/Pd co-catalysed DCC 7
<b>Figure 1.2</b>	Shang and Liu's potential Cu DCC reaction pathways 12
<b>Figure 1.3</b>	Forgione's proposed Pd DCC mechanism 14
<b>Figure 1.4</b>	Dupuy and Nolan's proposed Au-catalysed protodecarboxylation mechanism 20
<b>Figure 1.5</b>	Calculated reaction pathway for Pd-catalysed decarboxylation 23
<b>Figure 1.6</b>	Calculated reaction pathway for Ag-catalysed decarboxylation 24
<b>Figure 1.7</b>	Biphasic synthesis of Au nanoparticles 29
<b>Figure 1.8</b>	Core/shell nanoparticle synthesis <i>via</i> alcohol reduction 31
<b>Figure 1.9</b>	Metal nanoparticle synthesis <i>via</i> electrochemical redox 32
<b>Chapter 2:</b>	
<b>Figure 2.1</b>	Structural analysis of catalyst <b>Cu(mono)</b> 45
<b>Figure 2.2</b>	Structural analysis of catalyst <b>FeCu<sub>2</sub></b> 45
<b>Figure 2.3</b>	Structural analysis of catalyst <b>Fe<sub>2</sub>Cu</b> 46
<b>Figure 2.4</b>	Structural analysis of catalyst <b>Fe<sub>4</sub>Cu</b> 46
<b>Figure 2.5</b>	EDX mapping analysis of catalyst <b>FeCu<sub>2</sub></b> 48
<b>Figure 2.6</b>	EDX mapping analysis of catalyst <b>Fe<sub>2</sub>Cu</b> 48
<b>Figure 2.7</b>	Comparison of various catalysts in the DCC reaction of <b>1a</b> and <b>2a</b> at 130 °C 50
<b>Figure 2.8</b>	Kinetic profile of DCC reaction between <b>1a</b> and <b>2a</b> ( <b>FeCu<sub>2</sub></b> ) 52
<b>Figure 2.9</b>	<sup>1</sup> H NMR spectrum of DCC reaction between <b>1a</b> and <b>2a</b> ( <b>FeCu<sub>2</sub></b> ) 53
<b>Figure 2.10</b>	Effect of temperature on yield of a typical DCC reaction 56
<b>Figure 2.11</b>	Effect of catalyst loading on yield of a typical DCC reaction 56
<b>Figure 2.12</b>	Hypothetical mechanism for the copper catalysed reaction of <b>1a</b> and <b>2a</b> 61
<b>Figure 2.13</b>	Photograph of a diglyme-solvated DCC reaction 64

<b>Figure 2.14</b>	DCC reaction of <b>6a</b> and <b>2a</b> at 130 °C, different catalyst loadings ( <b>Cu(mono)</b> )	65
<b>Figure 2.15</b>	Kinetic profile of DCC reaction of <b>6a</b> and <b>2a</b> ( <b>Cu(mono)</b> )	66
<b>Figure 2.16</b>	DCC reaction of <b>6a</b> and <b>2a</b> at 100 °C, different catalyst loadings ( <b>Cu(mono)</b> )	67
<b>Figure 2.17</b>	Hysteresis loops of various magnetic materials	70
<b>Figure 2.18</b>	Induction heating reactor designs	73
<b>Figure 2.19</b>	Comparison between conventional and induction heating	77
 <b>Chapter 3:</b>		
<b>Figure 3.1</b>	TEM/EDX spectra for Pd/Cu-PVP catalyst series	88
<b>Figure 3.2</b>	TEM/EDX spectra for Pd/Ag-PVP and Pd/Au-PVP catalyst series	92
<b>Figure 3.3</b>	TEM/EDX spectra for Ni/Cu-EG catalyst series	98
<b>Figure 3.4</b>	TEM/EDX spectra for Pd/Cu-EG catalyst series	99
<b>Figure 3.5</b>	Comparison of various catalysts in the DCC reaction of <b>1a</b> and <b>2a</b> at 130 °C	102
<b>Figure 3.6</b>	Comparison of Pd/Cu-PVP as catalysts for DCC	103
<b>Figure 3.7</b>	Mercury spiking test for nanoparticle leaching	105
<b>Figure 3.8</b>	Comparison of various catalysts in the DCC reaction of <b>1a</b> and <b>2a</b> at 100 °C	106
<b>Figure 3.9</b>	Plot emphasizing the linear relationship between DCC product <b>3aa</b> and time for two catalyst systems at the reaction outset	107
<b>Figure 3.10</b>	Comparison of Pd/Ag-PVP and Pd/Au-PVP as catalysts for DCC	108
<b>Figure 3.11</b>	Photograph depicting PdAu-PVP solubility issues	109
<b>Figure 3.12</b>	Effect of solvent on reactivity of PdAu-PVP in DCC	109
<b>Figure 3.13</b>	Comparison of Pd/Cu-EG as catalysts for DCC	110
<b>Figure 3.14</b>	Comparison of Ni/Cu-EG as catalysts for DCC	112
 <b>Chapter 4:</b>		
<b>Figure 4.1</b>	Comparison of aryl-carboxylate C-C bond lengths	122
<b>Figure 4.2</b>	Molecular structures of carboxylate salt candidates	123

<b>Figure 4.3</b>	Molecular structures of aryl halide candidates	123
<b>Chapter 5:</b>		
<b>Figure 5.1</b>	Molecular structures of solvent replacement candidates	138
<b>Figure 5.2</b>	<sup>1</sup> H NMR spectra of solvent screening experiments	139
<b>Figure 5.3</b>	<sup>19</sup> F NMR spectra of solvent screening experiments	139
<b>Figure 5.4</b>	Comparison of the molecular structure of diglyme, PEG and DM-PEG	140
<b>Figure 5.5</b>	<sup>1</sup> H NMR spectrum showing evidence of protodecarboxylation	144
<b>Figure 5.6</b>	<sup>19</sup> F NMR spectrum showing evidence of protodecarboxylation	145
<b>Figure 5.7</b>	Effect of temperature and PEG loading on product <b>3bb</b> yield	151
<b>Figure 5.8</b>	Effect of temperature and PEG loading on <b>4b</b> yield	152
<b>Figure 5.9</b>	DoE model summary	156
<b>Figure 5.10</b>	4D Contour plot for DoE response factor <b>3bb</b>	157
<b>Figure 5.11</b>	4D Contour plot for DoE response factor <b>4b</b>	158
<b>Figure 5.12</b>	Coefficient plot for DoE response factor <b>3bb</b>	159
<b>Figure 5.13</b>	Coefficient plot for DoE response factor <b>4b</b>	160
<b>Chapter 6:</b>		
<b>Figure 6.1</b>	Summary of HPLC method	208
<b>Figure 6.2</b>	Chromatogram of an example DCC reaction	208
<b>Figure 6.3</b>	<sup>1</sup> H NMR spectra of an example DCC reaction	212
<b>Figure 6.4</b>	Comparison of Figure 6.3 to pure compounds	212
<b>Figure 6.5</b>	Integration of Figure 6.3 for analysis	213

## List of Schemes

	<b>Page</b>
<b>Chapter 1:</b>	
<b>Scheme 1.1</b> Ullmann's copper mediated biaryl synthesis	2
<b>Scheme 1.2</b> Nilsson's initial trapping experiments	3
<b>Scheme 1.3</b> Nilsson's hypothetical DCC mechanism	4
<b>Scheme 1.4</b> Goossen's optimised DCC biaryl synthesis	6
<b>Scheme 1.5</b> Effects of halide ions on the decarboxylation step	7
<b>Scheme 1.6</b> Ag mediated, Pd catalysed DCC examples	9
<b>Scheme 1.7</b> Ag/Pd co-catalysed DCC	10
<b>Scheme 1.8</b> Cu catalysed DCC of polyfluorinated potassium benzoates	11
<b>Scheme 1.9</b> One-pot denitrogenative/ dehydrogenative/ decarboxylative cascade	13
<b>Scheme 1.10</b> Pd catalysed DCC of heterocyclic carboxylic acids	13
<b>Scheme 1.11</b> Pd catalysed DCC of polyfluorinated potassium benzoates	15
<b>Scheme 1.12</b> Cu catalysed protodecarboxylation	17
<b>Scheme 1.13</b> Ag catalysed protodecarboxylation	17
<b>Scheme 1.14</b> Au promoted decarboxylation	19
<b>Scheme 1.15</b> Goossen and Manjolinho's microwave assisted DCC method	22
<b>Scheme 1.16</b> Colloidal Pd catalysed Heck reaction	34
<b>Scheme 1.17</b> CuFe <sub>2</sub> O <sub>4</sub> catalysed coupling of thiols and aryl halides	37
<b>Chapter 2:</b>	
<b>Scheme 2.1</b> Synthesis of iron/copper catalytic material	42
<b>Scheme 2.2</b> Reduction of aqueous Cu <sup>2+</sup> and Fe <sup>2+</sup> salts by NaBH <sub>4</sub>	43
<b>Scheme 2.3</b> Shang <i>et al.</i> 's copper-catalysed DCC of <b>1a</b> and aryl halides	49
<b>Scheme 2.4</b> Model DCC reaction using potassium carboxylates	50
<b>Scheme 2.5</b> FeCu <sub>2</sub> catalysed DCC reaction between <b>1a</b> and <b>2a</b>	52
<b>Scheme 2.6</b> Wu's copper catalysed Ullmann homocoupling of <b>2a</b> in the presence of potassium base	53
<b>Scheme 2.7</b> Model DCC reaction utilising caesium carboxylates	65

<b>Chapter 3:</b>		
<b>Scheme 3.1</b>	Lo et al.'s citrate-aided PdCu bimetallic nanoparticle synthesis	85
<b>Scheme 3.2</b>	Reduction of aqueous Cu <sup>2+</sup> and Pd <sup>2+</sup> ions by formaldehyde under basic conditions	85
<b>Scheme 3.3</b>	Reduction of aqueous Ag <sup>+</sup> , Au <sup>3+</sup> and Pd <sup>2+</sup> ions by formaldehyde under basic conditions	90
<b>Scheme 3.4</b>	Reduction of aqueous Au <sup>3+</sup> ions by trisodium citrate	94
<b>Scheme 3.5</b>	Wu and Chen's synthesis of nickel nanoparticles	95
<b>Scheme 3.6</b>	Reduction of EG-solvated Cu <sup>2+</sup> and Ni <sup>2+</sup> ions by hydrazine hydrate under basic conditions	95
<b>Scheme 3.7</b>	Hypothesised reduction pathway for aqueous ethylene glycol	96
<b>Scheme 3.8</b>	Initial reaction conditions for Pd/Cu catalyst investigations	101
<b>Scheme 3.9</b>	Rai et al.'s Ni/Pd bimetallic nanoparticle catalysed Suzuki coupling	104
<b>Chapter 4:</b>		
<b>Scheme 4.1</b>	Bimetallic Pd/Cu DCC catalyst cycle	117
<b>Scheme 4.2</b>	Expanded Pd/Cu DCC cycle, with competing reactions	119
<b>Scheme 4.3</b>	The decarboxylation step	120
<b>Chapter 5:</b>		
<b>Scheme 5.1</b>	Examples of successful PCA solvent substitutions	136
<b>Scheme 5.2</b>	Model DCC reaction for solvent screening	138
<b>Scheme 5.3</b>	Modified DCC protocol incorporating PEG additives	141
<b>Scheme 5.4</b>	Illustration stressing the promotion of both DCC and Ullmann coupling under DMSO-solvated conditions	143
<b>Scheme 5.5</b>	DCC reaction of <b>1b</b> and <b>2bI</b> , with potential side product <b>4b</b>	150
<b>Scheme 5.6</b>	Summary of the conventional optimisation of <b>1b</b> + <b>2bI</b>	153
<b>Chapter 6:</b>		
<b>Scheme 6.1</b>	Example DCC reaction for HPLC analysis	207
<b>Scheme 6.2</b>	Example DCC reaction for <sup>1</sup> H NMR analysis	211

## List of Tables

	<b>Page</b>
<b>Chapter 2:</b>	
<b>Table 2.1</b>	AAS characterisation of Fe/Cu catalyst series 44
<b>Table 2.2</b>	Comparing expected Fe:Cu ratio to observed using EDX 47
<b>Table 2.3</b>	First order multiplet analysis of side product <b>5a</b> 54
<b>Table 2.4</b>	Karl Fischer analysis showcasing effectiveness of diglyme drying protocol 55
<b>Table 2.5</b>	Comparison of high and low temperature DCC methods 57
<b>Table 2.6</b>	Exploring solvent scope 59
<b>Table 2.7</b>	Probing the role diglyme plays in DCC reactivity 62
<b>Table 2.8</b>	Chelating additives promoting DCC reactivity 63
<b>Table 2.9</b>	Determining solubility of <b>1a</b> in various solvents 63
<b>Table 2.10</b>	Exploring solvent scope with caesium benzoates 68
<b>Table 2.11</b>	Comparing Fe/Cu bimetallic materials as catalysts under induction heating conditions 75
<b>Table 2.12</b>	Magnetic susceptibility measurements 76
<b>Chapter 3:</b>	
<b>Table 3.1</b>	AAS characterisation of Pd/Cu-PVP catalyst series 86
<b>Table 3.2</b>	TEM characterisation of Pd/Cu-PVP catalyst series 89
<b>Table 3.3</b>	AAS characterisation of Pd/Ag-PVP catalyst series 91
<b>Table 3.4</b>	AAS characterisation of Pd/Au-PVP catalyst series 91
<b>Table 3.5</b>	TEM characterisation of Pd/Ag-PVP and Pd/Au-PVP catalyst series 91
<b>Table 3.6</b>	AAS characterisation of Ni/Cu-EG catalyst series 97
<b>Table 3.7</b>	TEM characterisation of Ni/Cu-EG catalyst series 97
<b>Table 3.8</b>	AAS characterisation of Pd/Cu-EG catalyst series 98
<b>Table 3.9</b>	TEM characterisation of Pd/Cu-EG catalyst series 99
<b>Chapter 4:</b>	
<b>Table 4.1</b>	Screening carboxylate salts under 100 °C DCC conditions 125

<b>Table 4.2</b>	Screening aryl halides under 100 °C DCC conditions	127
<b>Table 4.3</b>	Screening bimetallic catalysts in the DCC reaction of <b>1b</b> and <b>2a</b> at various temperatures	128
<b>Table 4.4</b>	Screening bimetallic catalysts in the DCC reaction of <b>1b</b> and <b>2bI</b> at various temperatures	128
<b>Table 4.5</b>	The effect varying the halogen atom of aryl halide substrate has on DCC reactivity	130
<b>Chapter 5:</b>		
<b>Table 5.1</b>	Nearest-neighbour analysis of Murray PCA solvent database	137
<b>Table 5.2</b>	PEG additives improving reactivity in poor solvents	142
<b>Table 5.3</b>	Mathematical exercise justifying fixing the loading of DM-PEG additives by weight	144
<b>Table 5.4</b>	Karl Fischer analysis showcasing effectiveness of DM-PEG drying protocol	146
<b>Table 5.5</b>	Examining the effect of PEG additives on DCC reactivity in various solvents	146
<b>Table 5.6</b>	DM-PEG used directly as solvent	148
<b>Table 5.7</b>	<b>3bb:4b</b> yield ratios at various temperatures	152
<b>Table 5.8</b>	The selected levels for each input factor in the DoE study	154
<b>Table 5.9</b>	DoE experimental design	155
<b>Table 5.10</b>	Predicted reaction conditions for optimised <b>3bb</b> yield	158
<b>Table 5.11</b>	Observed <b>3bb</b> and <b>4b</b> yield using predicted optimal conditions	159
<b>Chapter 6:</b>		
<b>Table 6.1</b>	Derived data from integration of example chromatogram	208
<b>Table 6.2</b>	Information extracted from relevant HPLC calibration curves	209
<b>Table 6.3</b>	Determining concentration of <b>2bI</b> and <b>3ab</b> in example DCC reaction using HPLC	209
<b>Table 6.4</b>	Processing integration data of example <sup>1</sup> H NMR spectrum	213
<b>Table 6.5</b>	Deriving magnetochemical balance calibration constant, C <sub>bal</sub>	221
<b>Table 6.6</b>	Deriving magnetic susceptibility from experimental results	221

## List of Abbreviations

18-crown-6	1,4,7,10,13,16-hexaoxacyclooctadecane
Å	Angstrom ( $1 \times 10^{-10}$ metres)
$\delta$	Chemical shift
$\Delta$	heat
$\mu$ W	Microwave
$\mu$ m	Micrometre ( $1 \times 10^{-6}$ metres)
$\chi_g$	Mass susceptibility
A	Amplitude
AAS	Atomic absorption spectroscopy
aq	Aqueous
ATR	Attenuated total reflection
BINAP	2,2'-Bis(diphenylphosphino)-1,1'-binaphthyl
$^{\circ}$ C	Degrees Celcius
d	Doublet (NMR)
dd	Doublet of doublets (NMR)
dddd	Doublet of doublets of doublets of doublets (NMR)
DBU	Diazabicycloundecene
DCC	Decarboxylative cross-coupling
DEPT	Distortionless enhancement by polarization transfer
DFT	Density functional theory
diglyme	Diethylene glycol dimethyl ether
DMA	Dimethylacetamide
DMF	Dimethylformamide
DM-PEG	Dimethylated poly(ethylene glycol)
DMSO	Dimethyl sulfoxide
DoE	Design of experiments
dt	Doublet of triplets (NMR)
dt	Doublet of triplets of triplets (NMR)
$e^-$	Electron
EDX	Energy-dispersive X-ray spectroscopy
<i>e.g.</i>	<i>Exempli gratia</i> (for the sake of example)

EG	Ethylene glycol
equ	Equivalents
ESI	Electron spray ionisation
<i>et al.</i>	<i>Et alia</i> (and others)
EXAFS	Extended x-ray absorption fine structure
FTIR	Fourier transform infrared spectroscopy
GHz	Gigahertz ( $1 \times 10^9$ hertz)
h	Hour/hours
H <sup>+</sup>	Proton
h <sub>c</sub>	Coercivity
HPLC	High pressure liquid chromatography
HRMS	High resolution mass spectroscopy
<i>i.e.</i>	<i>Id est</i> (that is)
<i>J</i>	Coupling constant (NMR)
keV	Kilo electronvolt ( $1 \times 10^3$ electronvolts)
nm	Nanometres ( $1 \times 10^{-9}$ metres)
NMP	<i>N</i> -Methyl-2-Pyrrolidone
NMR	Nuclear magnetic resonance spectroscopy
MHz	Megahertz ( $1 \times 10^6$ hertz)
m	Multiplet (NMR)
min	Minute/minutes
MPa	Megapascal ( $1 \times 10^6$ pascals)
m <sub>rs</sub>	Remnant magnetisation saturation
m <sub>s</sub>	Magnetisation saturation
m/z	Mass to charge ratio
<i>o-</i>	<i>Ortho-</i>
PC	Principle component
PCA	Principle component analysis
PEG	Poly(ethylene glycol)
phen	1,10-Phenanthroline
ppm	Parts-per-million
PVP	Poly(vinylpyrrolidone)
RAM	Random access memory

RHF	Restricted Hartree-Fock
rpm	Revolutions per minute
r.t.	Room temperature
s	Singlet (NMR)
SEM	Scanning electron microscopy
SIMIT	Size-induced metal to insulator transition
t	Triplet (NMR)
TBAB	Tetra- <i>n</i> -butylammonium bromide
td	Triplet of doublets (NMR)
TEM	Transition electron microscopy
Temp.	temperature
TEMPO	(2,2,6,6-Tetramethylpiperidin-1-yl)oxyl
TFA	Trifluoroacetic acid
tt	Triplet of triplets (NMR)
ttd	Triplet of triplets of doublets (NMR)
V	Voltage
W	Watt

# 1. Introduction

## 1.1. Overview

This thesis describes a thorough investigation into a transition metal catalysed carbon-carbon bond forming reaction known as Decarboxylative Cross-coupling (DCC). This reaction provides an advantageous route to carbon-carbon bond formation over competing reactions as it utilises carboxylic acids as a starting material – a substrate class that can be found in nature and that is also highly commercially available. *Via* interaction with transition metal catalyst, typically copper or silver, carbon dioxide is extruded from these substrates, generating organometallic intermediates *in situ*, which can then be utilised for a variety of transformations. This chapter serves as an introduction to the field of DCC, providing a brief synopsis of the origins of the field through highlighting seminal pieces of research, as well as outlining core issues with this chemistry that persist even into the modern literature.

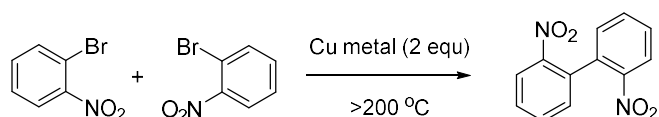
Much of this thesis details work performed with the aim of alleviating these issues, a key approach being the exploration of bimetallic nanoparticles as tuneable catalysts for challenging reactions such as DCC. Understanding the properties and synthesis of these materials is non-trivial, as such this chapter also aims to equip the reader with relevant theory and outlines of various modern approaches to the synthesis of bimetallic nanoparticles, as well as examples of their application as catalysts.

## 1.2. Decarboxylative Cross-coupling

### 1.2.1. Background

Aryl-aryl bond forming reactions are one of the most important tools available to the modern chemist. Such reactions are commonly employed to synthesise a whole host of products, from fine chemicals to agrochemicals to medicinal compounds. Amongst this class of reactions, transition metal catalysed carbon-carbon bond forming reactions are of particular importance. Early work in this field was pioneered by Ullmann and Bielecki, who in 1901 reported the successful homocoupling of 1-bromo-2-nitrobenzene mediated by stoichiometric amounts of finely divided copper metal or copper(I) salts at reaction temperatures in excess of 200 °C (see Scheme 1.1) <sup>1</sup>. Ullmann went on to refine this copper catalysed

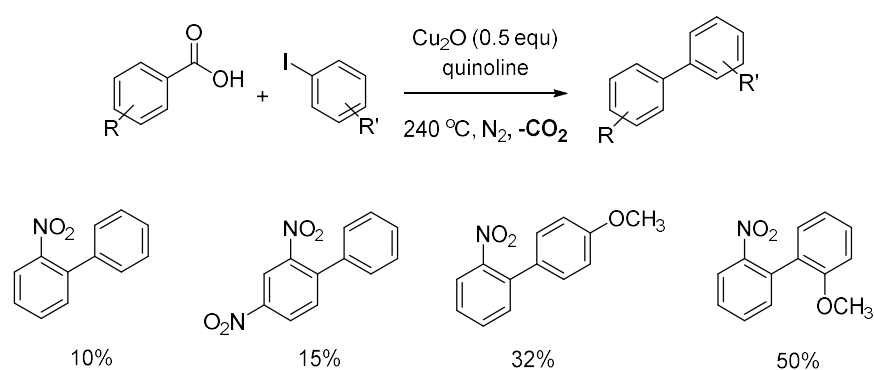
chemistry further, finding that it was possible to couple aryl halides with amines<sup>2</sup>. Later work built up upon this framework, bringing copper loadings down to sub-stoichiometric levels<sup>3</sup>, as well as broadening the scope for both carbon-carbon and carbon-heteroatom bond forming<sup>4,5</sup>. ‘Ullmann couplings’ however typically utilise very high reaction temperatures and catalytic loadings<sup>5</sup>. Other traditional biaryl forming solutions include the Scholl reaction<sup>6</sup> and the Gomberg-Bachmann reaction<sup>7</sup>, however like Ullmann coupling, these reactions require harsh, forcing conditions and can suffer from unsatisfactory yields for asymmetric biaryl products<sup>8</sup>.



*Scheme 1.1: Ullmann's copper mediated biaryl synthesis<sup>1</sup>*

The modern approach to aryl-aryl bond formation is the field of cross-coupling chemistry. Typically, this involves the coupling an organometallic reagent and a coupling partner such as an aryl halide, mediated by a palladium catalyst<sup>9</sup>. Cross-coupling has been extensively studied, with a whole host of reactions for different substrates. These include the Heck reaction for the coupling of vinyl arenes and aryl halides<sup>10</sup>; the Suzuki-Miyaura reaction for the coupling of organoboron reagents with aryl halides<sup>11</sup>; and the Negishi reaction for coupling organozinc reagents with aryl halides<sup>12</sup>. The profound applicability and robustness of these reactions is well reported; however, they are not without fault. This chemistry can be an expensive endeavour, not only because it is based around the use of palladium, but also in some cases the use of elaborate, bespoke ligands. The starting materials can also be costly, particularly in the case of Suzuki couplings which require stoichiometric quantities of organoboron reagent<sup>13</sup>. These materials can be derived either from the transmetalation of organolithium or Grignard reagents with boron containing compounds such as trimethyl borate, a route that typically requires cryogenic reaction temperatures to control and subsequent hydrolysis to yield the desired functionalised boronic acid product<sup>14</sup>, or *via* the palladium-catalysed borylation of aryl halide substrates *via* bis(pinacolato)diboron, a route that whilst achievable under milder conditions generates a pinacol boronate product that necessitates lengthy work up steps to generate boronic acid<sup>15</sup>. With such involved syntheses,

commercial boronic acid products are priced accordingly. Using commercially available boronic acids, particularly in the case of substrates with atypical functionality, can therefore incur significant costs<sup>13</sup>. It may also be that the particular coupling partner required is not commercially available, necessitating the lengthy synthesis and purification of bespoke boronic acid reagents.

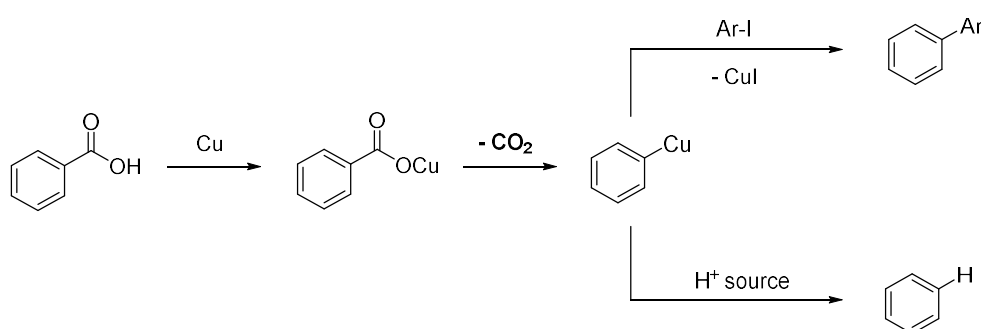


*Scheme 1.2: Nilsson's initial trapping experiments*<sup>16</sup>

In recent years, however, a new route to carbon-carbon bond formation has emerged: decarboxylative coupling. As the name may suggest, decarboxylative coupling chemistry involves the use of carboxylic acids, which *via* interaction with a transition metal catalyst are able to extrude carbon dioxide, forming an organometallic reagent that can then go on to join typical coupling mechanisms<sup>17</sup>. Despite the recent interest in the chemistry, the foundational work in this field was performed by Nilsson in 1966. He recognised a link between Ullmann biaryl synthesis and the copper-mediated decarboxylation of aryl carboxylic acids, hypothesising that they proceeded *via* a common intermediate species<sup>16</sup>. Nilsson went on to test this hypothesis by attempting to trap the intermediate *via* reaction with an electrophile, finding that stoichiometric amounts of copper(I) oxide could promote the coupling of functionalised benzoic acids with a small variety of aryl iodide coupling partners at reaction temperatures of 240 °C in quinoline, with yields ranging from 10-50 % (see Scheme 1.2)<sup>16</sup>. The reaction was presented as an alternative to Ullmann biaryl synthesis, however the yields reported by Nilsson were not as impressive as comparable Ullmann reactions, with Lindley reporting that yields of between 70-80 % were common in the copper-promoted substitution of aryl halides at the time<sup>18</sup>. A notable difference between Nilsson's reaction and

conventional Ullmann reactions however was that typical side reactions were not as prevalent - deactivation of the benzoic acid starting material being the major loss of material rather than the formation of unwanted and difficult to separate homocoupled side products<sup>16</sup>.

Nilsson then went on to explore the mechanism of this reaction, noticing that the rate of CO<sub>2</sub> evolution from the carboxylic acid starting material during the reaction was independent from the concentration of iodoarene coupling partners<sup>16</sup>. Drawing on the link between Ullmann biaryl synthesis and his own work through the hypothesised organocopper intermediate, he proposed a stepwise mechanism (see Scheme 1.3) whereby the carboxylic acid coordinates to the copper centre, followed by elimination of CO<sub>2</sub> that results in organic residue being directly bound to the copper itself. It is this intermediate that then goes on to react with aryl iodide, yielding the biaryl product. Nilsson also suggests that this intermediate can also abstract protons from its environment, yielding protodecarboxylated starting material<sup>19</sup>.



*Scheme 1.3: Nilsson's hypothetical decarboxylative cross-coupling mechanism<sup>19</sup>.*

Sheppard *et al.* demonstrated the isolation of a pentafluorophenyl-copper-quinoline complex, derived from the decarboxylation of copper(I) pentafluorobenzoate in quinoline at 60 °C<sup>20</sup>. This success owed to the relative stability of the pentafluorophenyl-copper complex compared to the organocopper intermediates expected from the work of Nilsson, and serves a direct demonstration of the organocopper intermediate, validating Nilsson's hypothesis. Mechanistic studies by Cohen further strengthened this notion. He confirmed that the evolution of CO<sub>2</sub> during the reaction was first order with respect to the copper(I) or copper(II)

carboxylate salt<sup>21</sup>, and also showed that the rate of decarboxylation when using copper(I) or copper(II) salts was near identical, due to the rapid reduction of copper(II) by quinoline under the reaction conditions, implying that copper(I) is the active catalyst<sup>22</sup>. Cohen also aimed to build up upon Nilsson's mechanism, by attempting to elucidate the nature of the decarboxylation step itself. Exploring substrate scope, Cohen's group found that carboxylic acids with saturated backbones, such as dodecanoic acid and adamantane-1-carboxylic acid do not decarboxylate under Nilsson's conditions<sup>21</sup>. From this they suggest that the copper centre first coordinates to the carboxylate before forming a  $\pi$ -bond with the unsaturated backbone. This then allows it to inductively stabilise the negative charge that would build up in the subsequent transition state<sup>22</sup>. This also helps to explain why rates are typically increased when coordinating solvents or ligands are utilised, which would help to stabilise the  $\pi$ -complex and potentially increase the copper(I) ion's electron-withdrawing potential.

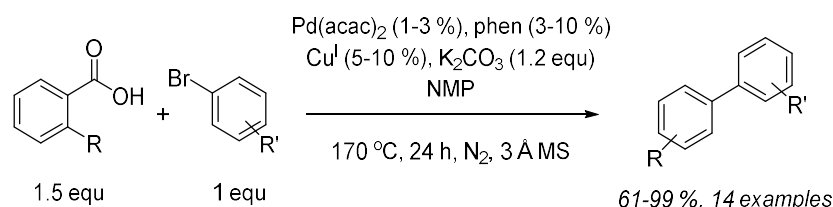
Cohen also demonstrated that copper-mediated decarboxylation does not proceed *via* a radical mechanism<sup>21,22</sup>, results which were later confirmed by Goossen *et al.* as the incorporation of TEMPO as a radical scavenger to their copper/palladium promoted decarboxylative cross-coupling reaction had no effect upon yields<sup>17</sup>.

### 1.2.2. Bimetallic Catalyst Systems

Despite the novelty of the cross-coupling reaction developed by Nilsson, its relatively poor performance compared to similar biaryl synthesis solutions such as Ullmann cross-coupling, and later palladium-catalysed solutions, meant that it saw relatively little attention<sup>23</sup>. This was exacerbated by the fact that the copper/quinolone decarboxylative cross-coupling reaction explored by Nilsson, Cohen and Sheppard required harsh, forcing conditions and high loadings of copper.

It was not until 2006 that interest in decarboxylative coupling was revitalized by the seminal works of Goossen *et al.*, who drew from the work of Nilsson but sought to improve on the unfavourable reaction conditions required. Their approach was to use a bimetallic catalytic system containing both copper salts and a typical palladium phosphine coupling catalyst. Initially, they utilised stoichiometric amounts of copper carbonate, which in conjunction with a mixture of Pd(acac)<sub>2</sub>, P(*i*-

Pr)Ph<sub>2</sub>, potassium fluoride and powdered molecular sieves in *N*-methylpyrrolidine was able to drive the coupling of 2-nitrobenzoic acid with 4-bromochlorobenzene at 120 °C, yielding 97 % coupled product<sup>13</sup>. The sieves serve to remove water generated *in situ* from deprotonation of the starting material by the carbonate base, protecting the reaction from protodecarboxylation.



*Scheme 1.4: Goossen's optimised biaryl synthesis via decarboxylation of ortho-substituted benzoic acids<sup>17</sup>.*

This approach was able to substantially reduce the reaction temperature required, but still required unacceptably high loadings of copper. Attempts to reduce the amount of copper carbonate yielded poor reactivity, as Cu(II) was reduced to Cu(I), becoming unreactive at these temperatures<sup>13</sup>. However, Cohen had shown that it was possible to promote this chemistry with copper(I) salts<sup>22</sup>. Therefore, a compromise was possible: catalyst loadings could be brought down if the reaction temperature was increased. An optimised protocol, catalytic in both copper and palladium, was developed, applicable to a wide variety of *ortho*-substituted carboxylic acids – this time utilising copper(I) salts such as copper(I) bromide and a reaction temperature of 170 °C (see Scheme 1.4)<sup>17</sup>.

Building on the works of Nilsson and Cohen *et al.*, Goossen suggested a possible mechanistic route that agreed with the stepwise nature of the decarboxylation process but elaborated upon it (see Figure 1.1)<sup>8,13</sup>. His proposition was that the carboxylic acid starting material would coordinate to the copper catalyst, before a decarboxylation step which eliminates CO<sub>2</sub> and results in the starting material being directly bound to the catalyst in the form of an organocopper compound, in keeping with Nilsson's trapping experiments<sup>16,19</sup>. This compound then enters a more traditional palladium catalytic cross-coupling cycle as an organometallic reagent, transferring the decarboxylated starting material onto the palladium catalyst, where

reductive elimination can occur with an organic residue bound to the centre in a prior oxidative addition step, yielding product. Both catalytic sites can then return to their starting conditions for another cycle.

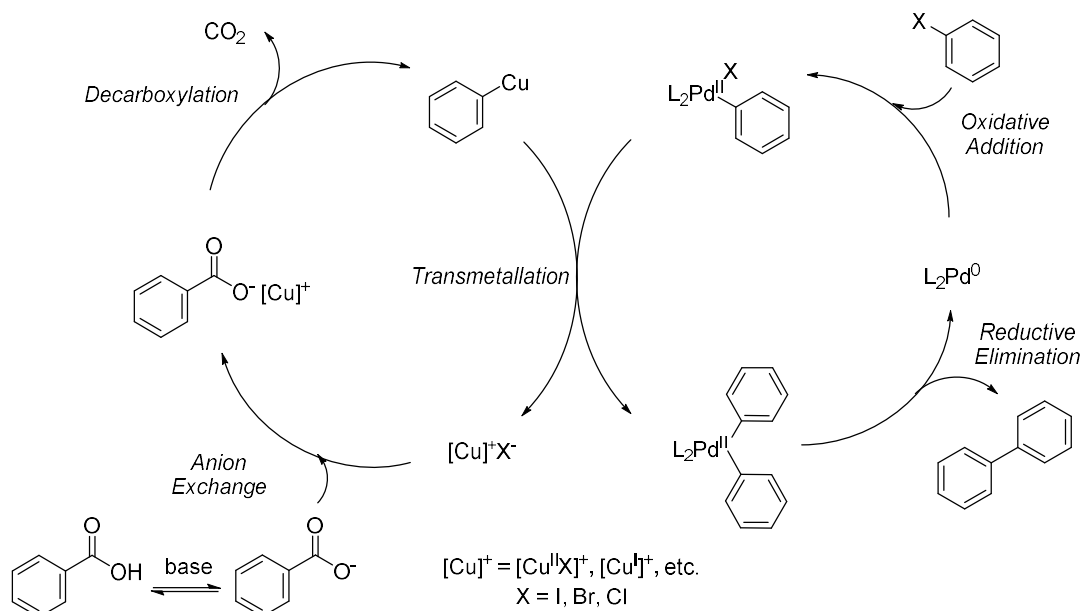
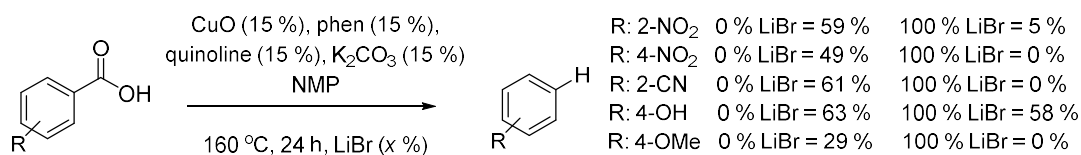


Figure 1.1: Hypothetical mechanism for copper/palladium co-catalysed decarboxylative cross-couplings<sup>13,17</sup>

Although hypothetical, this mechanism has been generally accepted in the literature. It is the *in situ* formation of organometallic species, derived from cheap and easy to handle carboxylic acid starting materials that makes decarboxylative cross-coupling an attractive solution when compared to more conventional palladium catalysed chemistry, and with Goossen's dual catalyst system the need for high catalyst loadings seen in the works of Nilsson<sup>16,19</sup>, Cohen<sup>22</sup> and Sheppard<sup>20</sup> is alleviated, the addition of a two electron transition metal catalyst dramatically promoting the cross-coupling.



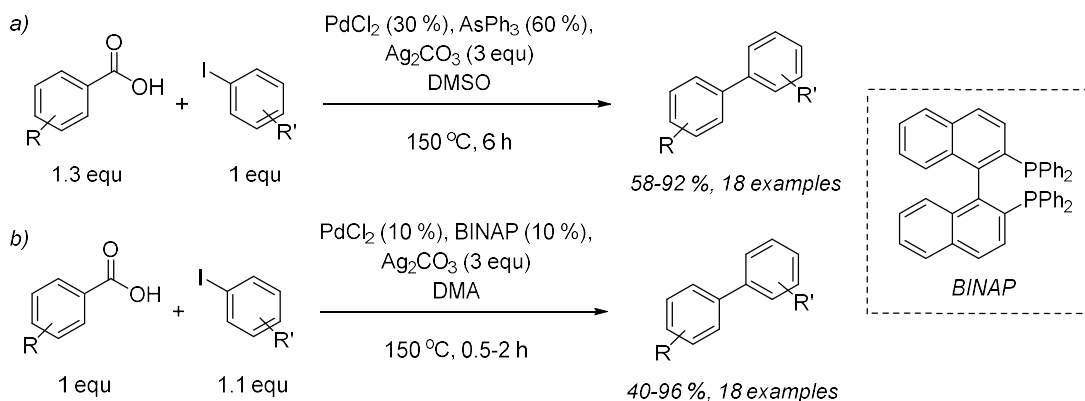
Scheme 1.5: Investigations into the effects of halide ions on the decarboxylation step

Concerning the scope of the copper/palladium bimetallic approach, a clear pattern of high reactivity towards *ortho*-substituted benzoic acids is present. Further investigations by Goossen *et al.*, replacing the aryl halide coupling partner with the equivalent aryl triflate provided insight into this substitution requirement<sup>24</sup>. It has been reported that the addition of halide ions inhibits the copper-catalysed decarboxylation of benzoic acid substrates (see Scheme 1.5). From this it can be inferred that the halide ions released during the course of the copper/palladium catalysed coupling with aryl halides have the potential to poison the copper catalyst – inhibiting further benzoic acid starting material from associating with the copper complex unless it possesses coordinating groups in the *ortho*-position to the carboxylic acid functional group. Switching to aryl sulfonate or even aryl tosylate<sup>25</sup> coupling partners dramatically widens the scope for benzoic acid substrate substitution – particularly in the case of *meta*- and *para*-substituted acids. Such results imply that, whilst the electronics of the *ortho*-substituents is significant in promoting or inhibiting the decarboxylation step, as shown both in Goossen’s exploration of substrate scope<sup>8,13</sup> and in the Density Functional Theory (DFT) calculations of both Nolan, in his exploration on the use of gold to promote decarboxylation<sup>26</sup> and Goossen<sup>27</sup>, the coordinating ability of the substituents is of greater importance in systems containing halide ions, allowing for the substrate to more easily enter the coordination sphere of the copper catalyst.

Given that silver(I) catalysts have been shown to promote protodecarboxylation at milder reaction temperatures, incorporating palladium as a co-catalyst can allow for the higher efficiency for decarboxylation that silver displays to be harnessed for decarboxylative cross-coupling reactions. Becht *et al.* were the first to publish such a system, reporting a 90 % yield in the decarboxylative cross-coupling of 2,6-dimethoxybenzoic acid and 1-iodo-4-methoxybenzene, in the presence of 30 mol% PdCl<sub>2</sub>, 60 mol% AsPh<sub>3</sub> and 3 equivalents of Ag<sub>2</sub>CO<sub>3</sub> in DMSO at 150 °C<sup>28</sup>.

Substrate scope was explored, with excellent to moderate yields depending on substituent choice and placement (see Scheme 1.6a) – a noteworthy observation is that their reaction system was able to produce sterically hindered 2,2',6-substituted biaryl products with yields of 50-78 %. However, any deviation from their optimised conditions caused yields to dramatically fall, be it changing the palladium catalyst,

ligand (even to other arsine compounds such as 1,2-bis(diphenyl-arsino)ethane), palladium loadings, silver loadings, reaction temperature, choice of aryl halide and even solvent<sup>28</sup>.



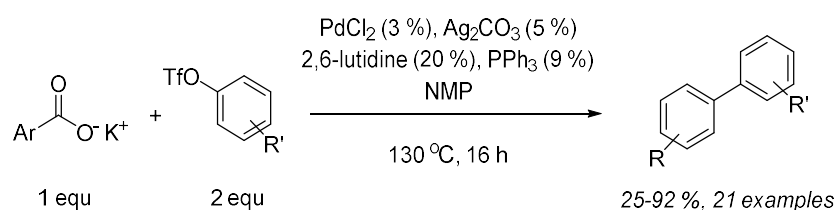
*Scheme 1.6: Silver-mediated/palladium-catalysed decarboxylative cross-couplings*<sup>28,29</sup>

Wu *et al.* expanded upon this work, finding that 2,2'-bis(diphenylphosphino)-1,1'-binaphthyl (BINAP) served as a much more effective ligand (see Scheme 1.6b)<sup>29</sup>. With 10 mol%  $\text{PdCl}_2$ , 10 mol% BINAP and 3 equivalents of  $\text{Ag}_2\text{CO}_3$ , they were able to promote the coupling of 2-nitrobenzoic acid with 1-iodo-4-methoxybenzene in dimethylacetamide (DMA), yielding 83 % product<sup>29</sup>, a marked improvement over Becht's reaction which could only give a yield of 61 %<sup>28</sup>.

Wu's group have also reported an interesting application of their silver/palladium methodology, being able to couple cinnamic acid derivatives with various aryl iodides utilising 10 mol%  $\text{PdCl}_2$ , 3 equivalents of  $\text{Ag}_2\text{CO}_3$  and 20 mol% of CyJohnPhos as a ligand, with yields ranging from 55-86 %, depending upon substrate choice<sup>30</sup>. Electron-withdrawing groups on the cinnamic acid enhanced yields, with 4-nitrocinnamic acid giving 86 % product when coupled with 4-iodoanisole under Wu's conditions<sup>30</sup>. Their reaction is of note as, unlike all previously discussed systems, their work moves away from biaryl synthesis and instead bears remarkable resemblance to what might be expected from a Heck reaction. Indeed, there is disagreement in the literature as to whether this is a true silver/palladium mediated decarboxylative coupling, or simply a silver-promoted protodecarboxylation of the cinnamic acid substrate – yielding the corresponding

phenyl alkene which could then go on to react with the aryl iodide in a traditional Heck mechanism<sup>17</sup>. Wu *et al.* do not address this deficiency.

Although successful at promoting decarboxylative cross-coupling, both Becht's and Wu's protocols show some substantial deficiencies when compared to Goossen's copper/palladium bimetallic system. Chief amongst which is the requirement for 3 equivalents of the group 11 co-mediator. Liu and Shang hypothesise that this is likely due to the formation of silver halide salts during the course of the reaction<sup>31</sup>. Such salts are insoluble under the reaction conditions, and therefore do not allow for the catalytically active silver species to be regenerated. This sentiment is echoed in the surrounding literature<sup>17</sup>.



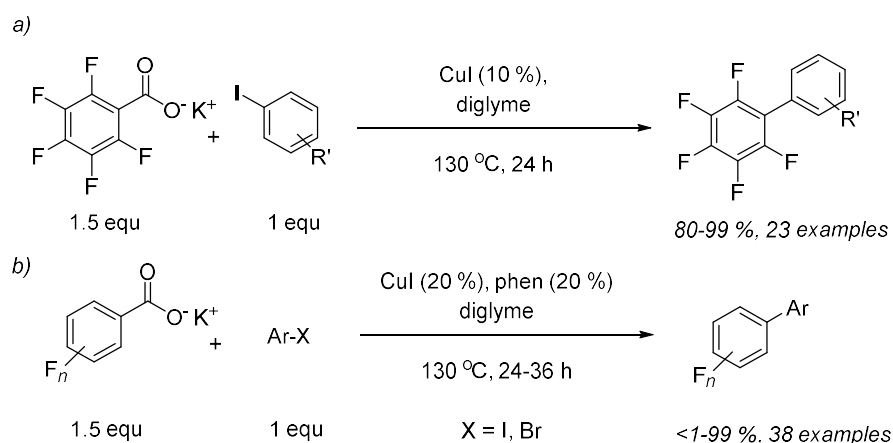
*Scheme 1.7: Silver/palladium co-catalyzed decarboxylative cross-coupling between aryl triflates and both aromatic and heteroaromatic carboxylic acids<sup>32</sup>.*

Goossen, having reported success in overcoming similar halogen-poisoning issues with his copper/palladium system<sup>24,25</sup>, showed that the use of aryl triflates could allow for the loading of silver(I) to be brought down to 10 mol%, in conjunction with 3 mol% PdCl<sub>2</sub>, as well as 9 mol% PPh<sub>3</sub> and 20mol% 2,6-lutidine which serve as ligands (see Scheme 1.7). Such conditions allowed for the successful coupling of a variety of *ortho*-substituted benzoic acids and heterocyclic carboxylic acids to aryl triflates at 130 °C, with yields ranging from 25-92 %<sup>32</sup> - a marked improvement on similar copper/palladium bimetallic catalyst systems, which generally require reaction temperatures of 160-170 °C. Notably, Goossen's silver/palladium protocol was also able to promote the smooth coupling of 2,6-dichlorobenzoic acid with 4-chlorophenyl trifluoromethanesulfonate, yielding the corresponding polychlorinated biaryl product with a yield of 76 %<sup>32</sup>. The triflate group does place some constraints on substrate scope however, with ester-, acyl- and nitro-groups on the 4-position on the aryl triflate increasing the acidity of the triflate to the extent that trans-

esterification between the aryl triflate and benzoic acid competes with DCC reactivity<sup>32</sup>.

### 1.2.3. Monometallic Catalyst Systems

As previously discussed, the main limitation of the pioneering works of Nilsson, Cohen and Sheppard was the need for stoichiometric quantities of copper reagents. Goossen's implementation of bi-metallic catalyst systems revolutionised the field, and opened the door to truly catalytic systems, however it brought with it the incorporation of palladium and associated ligands, whose toxicity and cost may prove prohibitive in applications such as pharmacological synthesis. Monometallic catalyst systems have also been studied alongside bimetallic systems and remains an active field of research.



*Scheme 1.8: Copper-catalysed decarboxylative cross-couplings of polyfluorinated potassium benzoates and aromatic/heteroaromatic halides<sup>33</sup>.*

The first report of a decarboxylative cross-coupling system catalytic with respect to copper was by Shang, Liu *et al.* in 2009, coupling potassium polyfluorobenzoates with a variety of aryl iodides in the presence of 10 mol% copper(I) iodide at 130 °C (see Scheme 1.8a)<sup>33</sup>. They found that the reaction proceeded well with diglyme as a solvent, giving yields between 99-80 % for a wide range of products. More challenging couplings using benzoates with a lower degree of fluorination, heteroaromatic halides and aryl bromides were accomplished using 20 mol% CuI and phenanthroline as an accompanying ligand (see Scheme 1.8b)<sup>33</sup>. Moving away from this solvent system caused yields to fall dramatically, however they do report

that dimethyl acetamide (DMA) performs well as a solvent when lower order polyfluorobenzoates are used. Through DFT calculations on the most simplistic reaction screened by the group, Shang and Liu identify two potential reaction paths (see Figure 1.2)<sup>33</sup>. The copper catalyst could first associate with the potassium pentafluorobenzoate substrate *via* salt metathesis and proceed to decarboxylate to yield the copper-aryl bond. The aryl halide coupling partner then associates with the complex *via* oxidative addition. This is identified as the rate-limiting step in this pathway, with predicted activation energy of 30 kcalmol<sup>-1</sup>. Finally, a subsequent reductive elimination step extrudes the product, and brings the copper catalyst back down to the +1 oxidation state. The second pathway sees oxidative addition occur before the salt metathesis and decarboxylation of the carboxylate substrate. This does substantially reduce the predicted energy barrier of oxidative addition to 18.9 kcal.mol<sup>-1</sup>, however requires that the system decarboxylate *via* a 6-coordinate transition state. This is clearly unfavourable as its predicted activation energy is 35 kcalmol<sup>-1</sup>, making decarboxylation rate limiting in this pathway. Due to the smaller rate-limiting energy barrier, it is likely decarboxylation occurs before oxidative addition. Such a finding is in agreement with the mechanisms predicted by Nilsson<sup>16,19</sup>, Cohen<sup>21,22</sup> and Sheppard<sup>20</sup>.

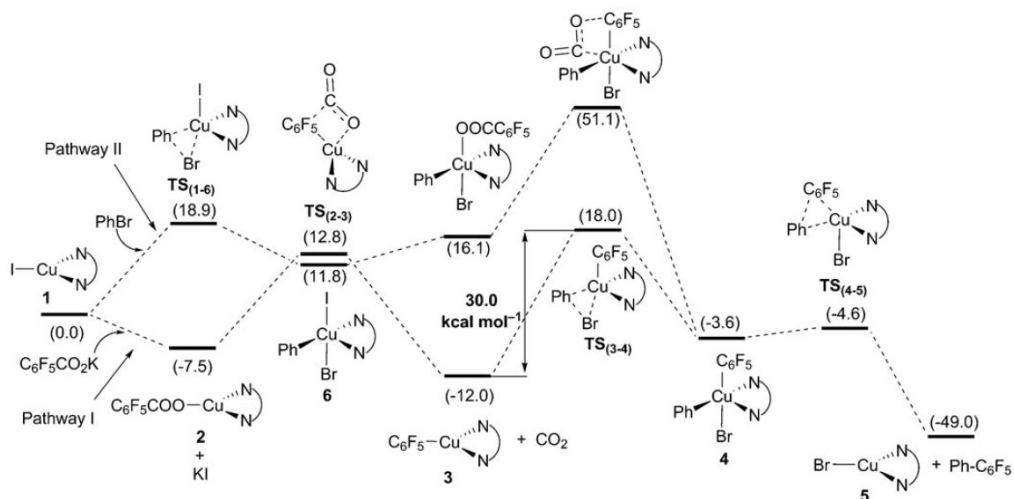


Figure 1.2: Shang and Liu's potential reaction pathways, calculated via DFT. All energies are given in kcal.mol<sup>-1</sup><sup>33</sup>.

It has been shown that copper catalysed decarboxylative cross-coupling is not simply limited to the formation of biaryls. Mu *et al.* report the successful formation



In all cases, C-H functionalisation was suppressed in favour of decarboxylative cross-coupling, even if coupling at the carboxylate position represented the more sterically demanding point of attack. However, in contrast to other decarboxylative cross-coupling protocols, if the benzoic acid substrate contains a C-H bond in the position adjacent to the carboxylic acid functionality, the aryl iodide coupling partner could also insert into this bond, leading to a mix of products. Due to this side product formation, they propose that having acquired the coupling partner moiety *via* an oxidative coupling, the palladium catalyst then binds to the heterocyclic 2-carboxylic acid in the 3 position. A divergent path then presents itself: If the 3-position does not contain a C-H bond, the palladium migrates to the 2-position, eliminating CO<sub>2</sub>, which is then followed by a reductive elimination to yield the desired biaryl product (see Figure 1.3 Path 1); If the 3-position contains a C-H bond, deprotonation occurs, followed by a reductive elimination to generate the 3-aryl heterocyclic 2-carboxylic acid (see Figure 1.3 Path 2). This product can then re-enter the cycle and react *via* Path 1, resulting in the mixture of products observed<sup>35</sup>.

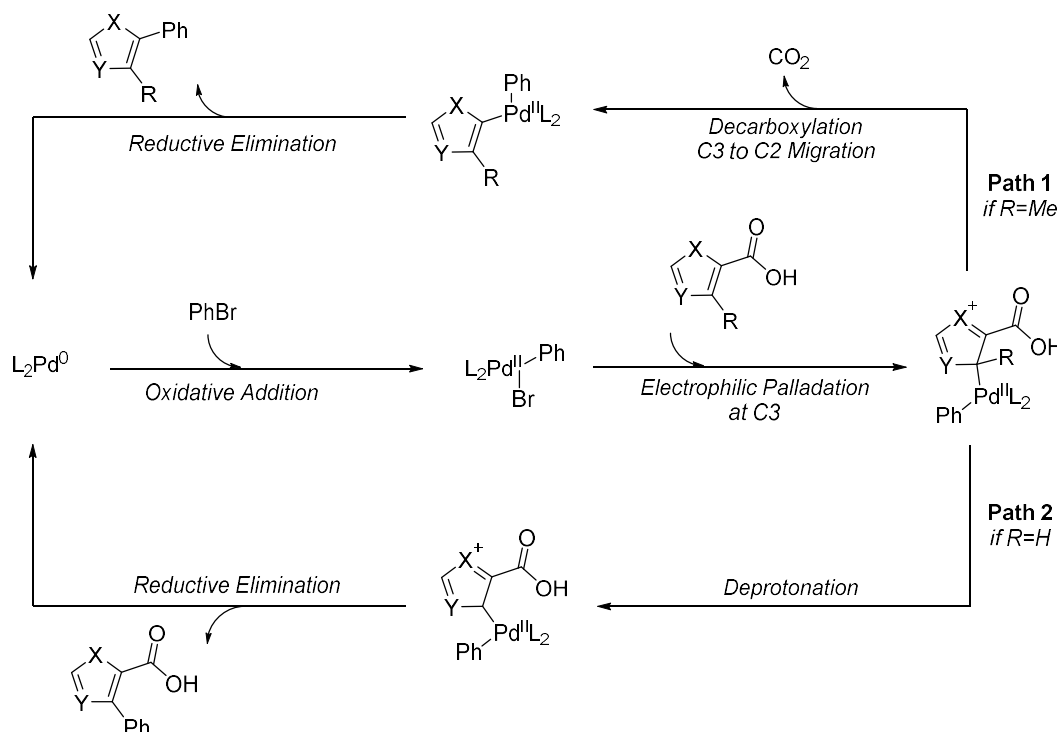
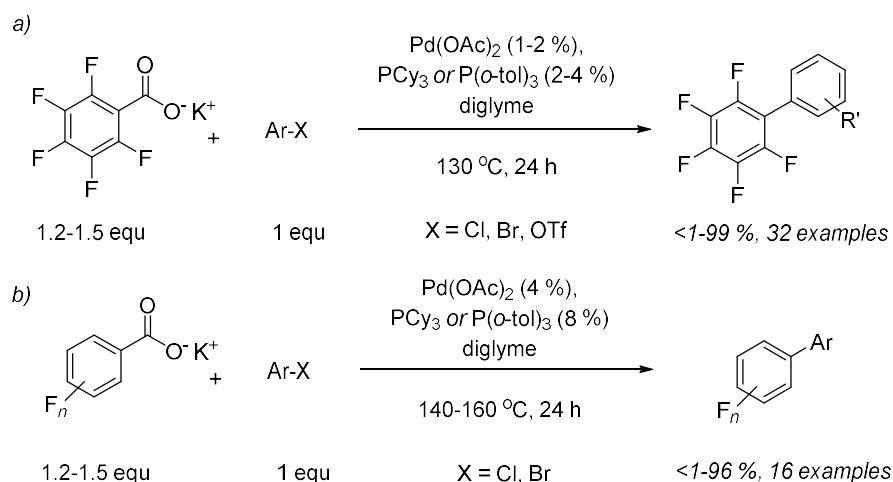


Figure 1.3: Forgiione's proposed mechanism<sup>35</sup>.

Liu *et al.*, building on their previous work surrounding copper catalysed decarboxylative chemistry, have shown that palladium monometallic catalyst systems are also able to promote cross-coupling between potassium polyfluorinated benzoates and aryl bromides, chlorides and triflates (See Scheme 1.11a)<sup>36</sup>. Their protocol calls for 1-2 mol% Pd(OAc)<sub>2</sub> along with 4 mol% PCy<sub>3</sub> or P(*o*-Tol)<sub>3</sub> as ligands, at 130 °C in diglyme (OAc: acetate, Cy: cyclohexyl, *o*-Tol: *ortho*-tolyl). Monofluorinated benzoates proved challenging to couple however, yielding trace product unless the fluoro- group was in an *ortho*-position to the carboxylate, with the other *ortho*-position containing a chloro- or trifluoromethyl- group. This may be indicative of a similar effect observed by Goossen in aryl halide systems, wherein coordinating *ortho*-groups allowed the substrate to displace halide ions released by the reaction and bind to the catalyst<sup>13,17,32</sup>. However, Liu *et al.* did not include aryl triflates when screening benzoates of varying fluorination, which may have helped to elucidate this, instead focusing on aryl bromide and chloride coupling partners (see Scheme 1.11b)<sup>36</sup>.



*Scheme 1.11: Palladium-catalysed decarboxylative cross-coupling of polyfluorinated potassium benzoates and aryl chlorides, bromides and triflates*<sup>36</sup>.

The group also performed DFT calculations to gain insight on the potential mechanism of palladium-catalysed decarboxylative cross-coupling, and found that as Forgone predicted<sup>35</sup>, oxidative addition of the aryl halide coupling partner occurs first, confirming that palladium catalysed decarboxylative cross-coupling proceeds *via* a different mechanism to what the group predicted for the copper-catalysed system previously studied (see Figure 4)<sup>33</sup>. However, their calculations predict that

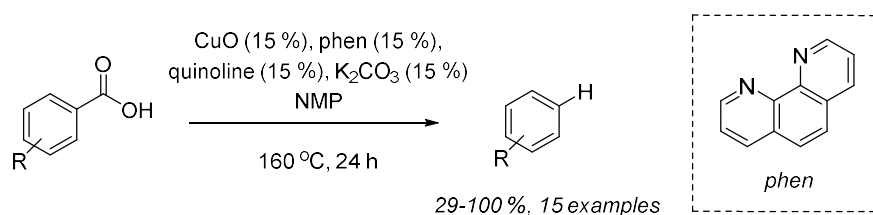
the palladium complex then associates to the carboxylate anion before decarboxylation occurs, yielding a Pd-C bond<sup>36</sup>. This is in contrast to Forgione's proposed mechanism, and instead agrees with the calculations of Su *et al.*, who also report that the palladium catalyst associates with the carboxylate ion, and not a position adjacent<sup>37</sup>. However, both Lin's group and Su's were considering aryl carboxylic acids, whereas Forgione was studying heterocyclic carboxylic acids. This may suggest the potential of a differing mechanism based upon substrate choice.

#### 1.2.4. Protodecarboxylation

When it comes to understanding the mechanism behind decarboxylative cross-coupling chemistry, the importance of the decarboxylation step itself cannot be overstated. The extrusion of CO<sub>2</sub> from most carboxylic acid substrates, including carboxylate salts, generally requires forcing conditions to induce, which is reflected not only in the protocols reported by Nilsson<sup>16,19</sup>, but even in the bimetallic solutions of Goossen<sup>13,38</sup> and Larrosa<sup>39</sup>. Under such conditions, side reactions are a pressing concern, and indeed Nilsson noted that a consistent side product in his reaction was the formation of protonated starting material<sup>16</sup>. However as many commercially available substrates and natural products contain carboxylic acid functionality, controlled decarboxylation to yield the corresponding protonated compound, or 'protodecarboxylation', is a valuable transformation – particularly in cases where carboxylic acid functionality is used as a directing group in complex molecules, but not desired in the end product<sup>40</sup>. It is in targeting the intentional protodecarboxylation of substrate that monometallic group 11 catalyst systems excel, as although the works of Shang and Liu *et al.*<sup>33,36</sup>, Forgione *et al.*<sup>35</sup> and others have shown that monometallic copper and palladium systems are viable, their works are all limited in scope and broader applicability, be it in restrictions on the choice substrate, reaction temperature, solvent or ligand. When considered alongside competing copper/palladium and silver/palladium systems, it is clear that monometallic systems are good choices for inducing decarboxylation and generating organometallic intermediate, but the task of handling cross-coupling and biaryl formation is better left to palladium. It is also worth noting that protodecarboxylation and decarboxylative cross-coupling represent divergent paths from a common organometallic intermediate<sup>13,16</sup>, and therefore interest in directly

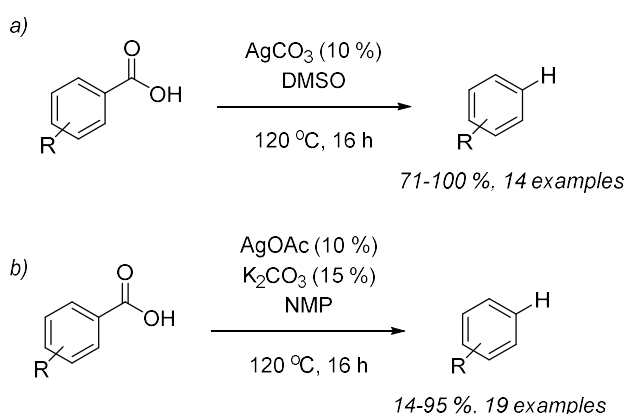
pursuing protodecarboxylation is also rooted in attempting to understand the nature of the decarboxylation step.

Goossen *et al.* report that their copper(I) phenanthroline (phen) quinolone complex in catalytic amounts (15 mol%, generated *in situ*) was able to promote the protodecarboxylation of a variety of substituted aromatic carboxylic acids, with *ortho*-substitution fairing best (see Scheme 1.12)<sup>13</sup>.



Scheme 1.12: Copper-catalysed protodecarboxylation<sup>13</sup>.

The protodecarboxylation of both heteroaromatic and vinylic carboxylic acids was also possible. They also noted that when halide ions that would have been released during a cross-coupling mechanism were artificially added, the rate of protodecarboxylation of these carboxylic acids was dramatically reduced (see Scheme 1.5)<sup>13,27</sup>. This suggests that halide ions directly compete with the carboxylic acid substrate for coordination sites on the copper centre.



Scheme 1.13: Silver-catalysed protodecarboxylations<sup>38,41</sup>.

Protodecarboxylation is not only limited to copper mediation, however. Larrosa *et al.* have reported a silver(I)-catalysed method to protodecarboxylate *ortho*-

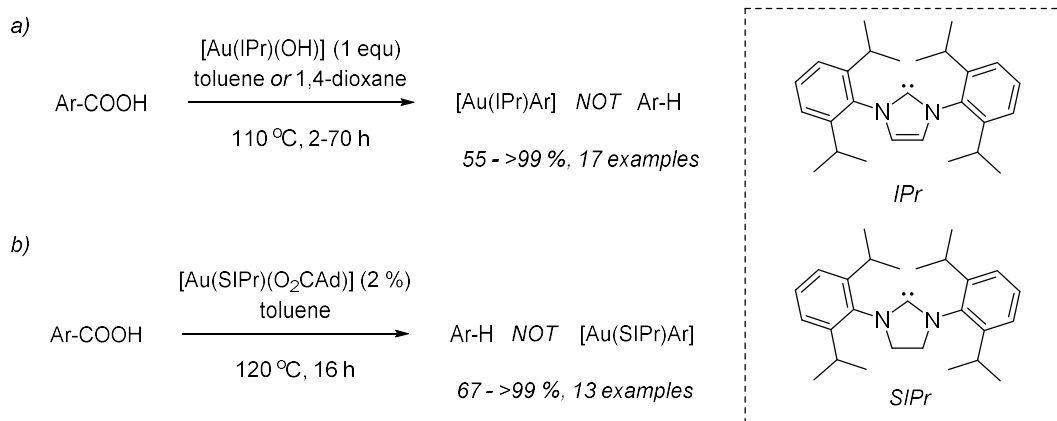
substituted benzoic acids with yields ranging from between 71-100 %, with many examples of >95 % yield (see Scheme 1.13a)<sup>41</sup>. This was achievable at temperatures as low as 120°C, a significant improvement on the copper-catalysed method reported by Goossen. Larrosa notes that the choice of *ortho*-substituted functionality on the target substrate is of considerable importance as it is only electron-withdrawing and alkoxy groups that promote the reaction.

The pattern of *ortho*-substituted carboxylic acids having a greater activity for decarboxylative protocols, both protodecarboxylation and cross-coupling, is also present in the work of Goossen concerning copper decarboxylation reactions<sup>8,13</sup>, as well as in his own studies into silver-catalysed protodecarboxylations (see Scheme 1.13b)<sup>38</sup>. Larrosa hypothesises that this is due to “electronic reasons”<sup>41</sup>, presumably with electron-withdrawing groups able to stabilize the development of negative charge during the decarboxylation step. In later studies on dicarboxylic acids<sup>41</sup>, they found that the carboxylic acid group with an electron-withdrawing *ortho*-substituent is selectively removed. However, they note that adjacent carboxylic acid groups do not seem to activate each other. Within the confines of *ortho*-substitution the protocol is robust, with it later becoming apparent that the heteroatoms of a variety of heteroaromatic carboxylic acids were also able to promote protodecarboxylation with near quantitative yields providing the heteroatom was in the  $\alpha$ -position to the carboxylic acid group<sup>42</sup>.

The milder conditions reported by Larrosa imply that silver(I) salts are more effective than their copper analogues, an observation backed up by the DFT calculations of Goossen who reported that the activation energy of a typical silver promoted protodecarboxylation was predicted to be 1.8 kcal.mol<sup>-1</sup> lower than the corresponding copper system<sup>27</sup>, translating to an almost 10-fold increase in the rate of reaction.

With this trend in mind, it would be logical to assume that gold may fare even better in promoting decarboxylation. However, there are far less instances of investigations into golds ability as a protodecarboxylation catalyst. Dupuy and Nolan have explored this area a great deal, reporting that the strongly basic gold(I) complex [Au(IPr)(OH)] (IPr = 1,3-bis(2,6-diisopropyl)-phenyl-imidazol-2-ylidene) was able

to promote decarboxylation of a large variety of benzoic acids and heteroaromatic carboxylic acids in 1,4-dioxane or toluene at 110 °C with yields >95 % for all but one substrate, *ortho*-nitrobenzoic acid, yielding 55 % product over 24 hours (see Scheme 1.14a)<sup>43</sup>.



Scheme 1.14: Gold-promoted decarboxylations of aromatic and heteroaromatic carboxylic acids<sup>40,43</sup>

Such results seem to confirm that gold shows an even stronger affinity for decarboxylation, especially as it was even capable of promoting the near-quantitative decarboxylation of *para*-methoxybenzoic acid, albeit at 120 °C over 70 hours. However, an interesting observation is that in all cases reported by Dupuy and Nolan with this catalytic system the protodecarboxylated product was never isolated, the reaction instead stopping at the formation of a gold(I)-aryl compound. They explained this in terms of the relatively high stability of the carbon-gold bond in comparison to their copper and silver analogues<sup>43</sup>.

In later studies with a second generation gold(I) catalyst [Au(SIPr)(O<sub>2</sub>CAr)] (SIPr = 1,3-bis(2,6-diisopropylphenyl)-4,5-dihydroimidazol-2-ylidene ; O<sub>2</sub>CAr = adamantane-1-carboxylate) true protodecarboxylation was achieved for a variety of electron-rich *ortho*-substituted benzoic acids and heteroaromatic acids, utilising anhydrous toluene at 120 °C over 16 hours, with yields ranging from 67->99 % (see Scheme 1.14b)<sup>40</sup>. This development was due to the O<sub>2</sub>CAr<sup>-</sup> ligand, which forms adamantane-1-carboxylic acid *in situ*, which is suggested to act as a source of protons, and able to cleave the strong carbon-gold bond formed during decarboxylation (see Figure 1.4).

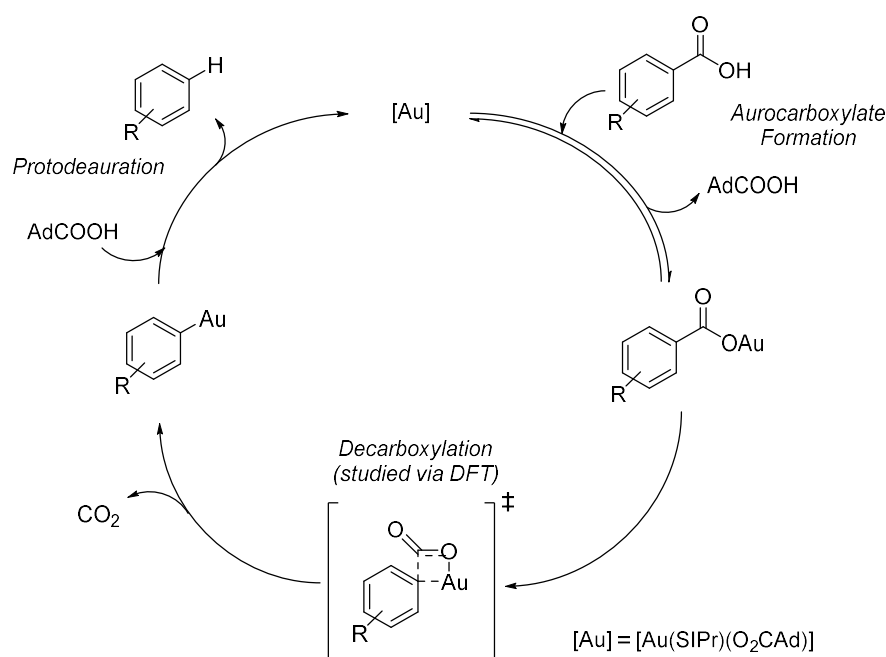


Figure 1.4: Dupuy and Nolan's proposed gold-catalysed protodecarboxylation mechanism

26.

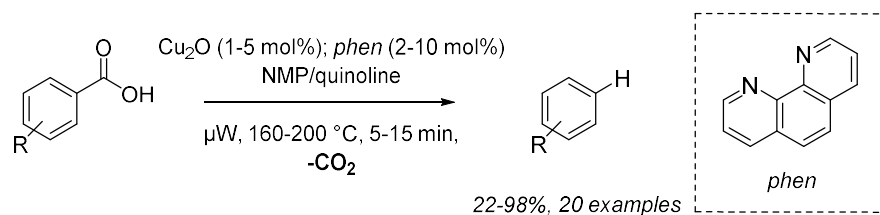
Dupuy and Nolan note that, whilst their gold(I) catalysts showed excellent reactivity towards decarboxylation, there appeared to be a considerable difference in the chemistry of gold(I) compared to copper(I) and silver(I) in that electron-withdrawing substituents seemed to have a deactivating effect upon the substrate towards decarboxylation with gold(I) – even in the *ortho*-position<sup>40,43</sup>. This was especially surprising in the case of *ortho*-nitrobenzoic acid, a substrate that fares well in copper<sup>8,13</sup> and silver<sup>41</sup> mediated reactions but only 61 % product was obtained under their optimised conditions over 16 hours. Protodecarboxylation could still be driven to completion, but required much greater reaction times<sup>40</sup>.

This result hints at the possibility of gold(I) catalysed decarboxylation of benzoic acids following a different mechanism to copper(I) and silver(I). The group later explored the mechanism *via* DFT calculations, and were able to confirm that in the case of gold(I) catalysed protodecarboxylations, the presence of electron-donating *ortho*-substituents substantially reduced the activation energy for the decarboxylation step<sup>26</sup>. Positioning of the substituents on the ring relative to the carboxylic acid group, as with copper and silver systems, is still of great importance,

with all substituents having a much greater influence upon activation energy of decarboxylation in the *ortho*-position, compared to *meta* and *para* <sup>26</sup>. Their calculations also elucidated the nature of the transition state. Formation of the Au-C bond and cleavage of the Au-O bond occur in a concerted step, consistent with Goossen's DFT calculations for Ag and Cu systems <sup>27</sup>. However, the gold-oxygen bond is essentially fully cleaved (the Au-O bond being  $>2.7$  Å) and no strong interaction between the gold and leaving CO<sub>2</sub> moiety is observed <sup>26</sup> – in contrast to the predicted transition states for copper and silver systems by Goossen. This suggests a shift from an ideal concerted mechanism towards a step-wise style electrophilic aromatic substitution of the carboxylate group by the catalytic metal. This, coupled with the propensity for electron-donating substituents accelerating the rate of gold mediated decarboxylation, also suggests that mesomeric effects have a greater effect than observed in copper and silver mediated decarboxylation.

#### 1.2.5. The *Ortho*- Effect

It is noted by several key investigations in the literature that transition metal promoted decarboxylative cross-couplings and protodecarboxylations show significantly improved reactivity when an aromatic carboxylic acid substrate is chosen that bears functionality in the positions *ortho* to the carboxylic acid group. Goossen *et al.* report that, concerning the scope of carboxylic acid substrate towards palladium-catalysed protodecarboxylation, yield of decarboxylated product is substantially higher when functionality is located in the *ortho*-position regardless of whether that functionality was electron rich or electron deficient <sup>8</sup> and his related studies in cross-coupling that employ *ortho*-substituted carboxylic acids typically enjoy good yields <sup>17,44</sup>. Shang and Liu observed that *ortho*-substitution of carboxylic acid substrate was well tolerated in their copper-promoted decarboxylative cross-coupling protocol, although their exploration of polyfluorinated carboxylic acid substrate omits any examples that lacked *ortho*-substitution <sup>33</sup>. Indeed, much investigative work done in this field has explicitly used *ortho*-substituted carboxylic acids such as 2-nitrobenzoic acid, 2-methoxybenzoic acid, 2-fluorobenzoic acid and so on because of this proven reactivity.



*Scheme 1.15: Goossen and Manjolinho's microwave-assisted protocol for broad-spectrum decarboxylation of functionalised benzoic acids.*<sup>45</sup>

Copper systems have been shown to catalyse decarboxylation in a broad scope of *ortho*-, *meta*- and *para*-substituted carboxylic acids<sup>46</sup> but Goossen and Manjolinho showed that, using a typical copper(I) oxide/1,10-phenanthroline catalyst system, reaction temperatures of 190-200 °C were required to develop conditions generally applicable to all substrates (see Scheme 1.15)<sup>45</sup> – 40 °C higher than Goossen's optimised copper system utilising only *ortho*-substituted starting material<sup>13</sup>. Goossen and Manjolinho's general approach utilised microwave heating over a 15 minute timeframe whereas Goossen's original protocol utilised conventional heating over 24 hours, thus making a direct comparison difficult. However, Goossen and Manjolinho showed that for the *ortho*-substituted compounds they screened, temperature, reaction time and catalyst loading could be reduced significantly<sup>45</sup> – confirming the requirement for forcing conditions when utilising *meta*- and *para*-substitution patterns.

As the field of decarboxylative cross-coupling has evolved, much interest has shown in exploring the reasoning behind this '*ortho*-effect'. In a DFT study on the decarboxylation step of both copper and silver catalyst systems, Xue, Su and Lin show that *ortho*-substituted carboxylic acids do indeed exhibit lower activation energies for decarboxylation relative to their *meta*- and *para*- analogues in all cases<sup>47</sup>. However, there is no correlation between the size of the energy barrier and the electronic properties of the substituent in their calculated data. From this, Xue *et al.* concluded that the *ortho*-effect is mainly steric in nature, with the *ortho*-functionality destabilising the metal-carboxylate complex and therefore resulting in a lower activation energy<sup>47</sup>. This finding is in contrast to the hypothesis put forward by Goossen that the improved reactivity observed when using substrates such as *o*-nitrobenzoic acid or *o*-methoxybenzoic acid is due to coordination between the

*ortho*- substituent and the transition metal catalyst <sup>13</sup>. This would lower the energy of the decarboxylation transition state and therefore lead to a lower activation energy of decarboxylation. Xue *et al.* address this, observing that certain *ortho*- substituents capable of coordination, such as *o*-NO<sub>2</sub> and *o*-OMe, did indeed stabilise the transition state. However this was not consistent across the data set, with *o*-NH<sub>2</sub> and *o*-OH displaying the largest energy barriers in the *ortho*- data set, a finding consistent with similar DFT studies <sup>46</sup>. Xue therefore reason that coordination is a secondary effect, with sterics playing the dominant role <sup>47</sup>.

Goossen *et al.*, in their own DFT study on group-11 catalysed decarboxylation report a trend that more potent electron-withdrawing *ortho*- substituents lead to lower calculated free reaction energies <sup>27</sup>, a finding backed up by the trends in reactivity reported in the literature <sup>13,17,27,31,33</sup>. From this they reason that the reactivity of benzoic acid derivatives towards decarboxylation is dominated by short-range inductive effects through the  $\sigma$ -backbone of the aryl ring, with longer range mesomeric effects through the  $\pi$ -system from *para*- substituents being significantly less important <sup>27</sup>. They do not address the role sterics plays in destabilising the starting intermediate, however, which would also lead to a reduced calculated free reaction energy.

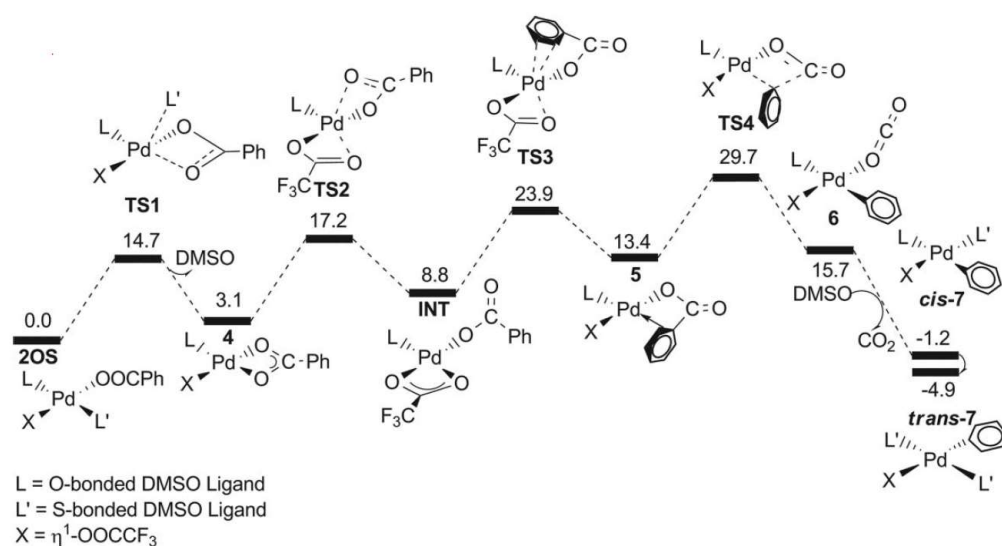


Figure 1.5: Xue *et al.*'s full calculated reaction pathway for palladium-catalysed decarboxylation of carboxylic acids. Energies are given in kcal.mol<sup>-1</sup> <sup>37</sup>.

This is in contrast to their findings when exploring group-10 catalysed protodecarboxylations, wherein electron-donating *ortho*- substituents also lead to improved reactivity<sup>8</sup>. Xue, Su and Lin explain this in their DFT study on the mechanism of palladium-catalysed decarboxylations, which proceeds *via* a 4-membered ring transition state, shown in Figure 1.5 as “TS4”<sup>37</sup>. As the aryl-carboxylate and aryl-palladium bonds are broken and formed in one concerted step, there would be limited build-up of charge on the carbon *ipso*- to the carboxylate group. Therefore steric effects largely explain the observed *ortho*-effect in palladium catalysed systems<sup>37</sup>. This is in contrast to the calculated decarboxylation transition state for copper systems shown in Figure 1.2 TS<sub>(2-3)</sub>, wherein the aryl-carboxylate bond is shown to break after the formation of a copper-aryl bond. The presence of *ortho*- substitution, be it electron-withdrawing or electron-donating, helps to destabilise the palladium-carboxylate reaction intermediate and therefore lower the calculated activation energy for decarboxylation. Assuming decarboxylation is rate determining, this would go on to explain Goossen’s experimental findings.

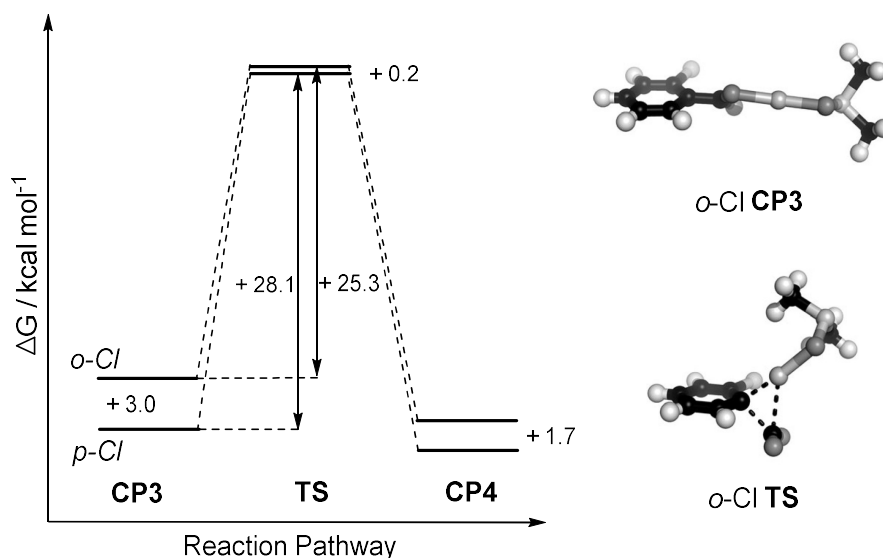


Figure 1.6: Larrosa’s calculated reaction pathway for silver-catalysed decarboxylation for *ortho*- and *para*-chlorobenzoic acid<sup>46</sup>. CP3 represents the silver-carboxylate complex, whereas CP4 represents a silver-aryl complex. Not drawn to scale.

In a more recent DFT study on the silver-catalysed protodecarboxylation of carboxylic acid substrates with varying substitution patterns, Larrosa agrees with Xue *et al.*, reporting that *ortho*- substitution exhibits steric clashing with the

carboxylate group in the silver-carboxylate reaction intermediate, destabilising it and therefore lowering the activation energy of decarboxylation <sup>46</sup>. Interestingly, however, they noted that the difference between the energies of the transition states of *ortho*- and *para*- systems was much less pronounced, and in some cases identical. This is due to the structure of the calculated transition state itself, depicted in Figure 1.6 labelled ‘*o*-Cl TS’ with the carboxylate group laying perpendicular to the aryl ring, resulting in significantly less steric clashing <sup>46</sup>.

However, whereas Xue *et al.* report no correlation between electronics and activation energy <sup>47</sup>, Larrosa disagrees. Studying the transition state itself, they found that there was a significant build-up of negative charge on the carbon *ipso* to the carboxylate group. When comparing two groups of similar steric bulk but vastly different electronic properties, *o*-Me and *o*-Br, they found the silver-carboxylate intermediates to exhibit similar energies, but a notable difference in activation energies. The electron-withdrawing *o*-Br group yielding a reduction in activation energy by  $-0.2 \text{ kcal mol}^{-1}$  and the electron-donating *o*-Me group yielding an increase in activation energy by  $3.6 \text{ kcal mol}^{-1}$ , compared to their *para*- analogues <sup>46</sup>. This follows, as the presence of electron-withdrawing substituents *ortho*- to a build-up of negative charge would lead to stabilisation *via* short range inductive effects and *vice versa* for electron-donating substituents, a finding that falls in line with the work put forward by Goossen <sup>27</sup>.

Whilst notable, however, these differences in transition state energies due to electronic effects are lower than the differences observed due to silver-carboxylate intermediate destabilisation *via* steric clashing. As such Larrosa *et al.* reason that the *ortho*- effect is largely steric in nature, with electronics having a milder influence <sup>46</sup>. Considering the breadth of research on the topic, it is likely that the observed *ortho*-effect in group-11 catalysed decarboxylations is comprised of three key factors: destabilisation of the metal-carboxylate starting intermediate *via* steric clashing, stabilisation of the decarboxylation transition state *via* short range inductive effects and stabilisation of the decarboxylation transition state *via* coordination between *ortho*- substituents and the transition metal catalyst. When considering all of these factors contributing to a wider effect, reported trends both in calculated data and experimental data begin to make sense. Throughout Xue’s <sup>47</sup>, Goossen’s <sup>27</sup> and

Larrosa's <sup>46</sup> calculations *o*-NO<sub>2</sub> is shown to exhibit the smallest free energy of reaction. In this case, all three factors are in play: -NO<sub>2</sub> is a relatively bulky, electron-withdrawing group with the capability to coordinate to the transition metal catalyst. *Ortho*- halogen groups are also a popular choice in the literature <sup>17,31,33,36,44</sup>, and Goossen predicts them to be just behind nitro groups in reactivity in his calculations <sup>27</sup>. They are electron-withdrawing, and can coordinate, but possess less steric bulk than the nitro group – leading to stabilisation of the transition state but a lesser degree of destabilisation of the initial metal-carboxylate complex.

### 1.3. Metallic Nanoparticles

Strictly speaking, the term 'nanoparticle' defines a type of ultra-fine particle, with dimensions between 1-100 nm. However, nanoparticle is a very broad phrase, encompassing many kinds of systems with differing physical and chemical properties: metallic nanoparticles, quantum dots and even nanoparticles made of biological matter <sup>48</sup>. In an even broader sense, the term nanoparticle can be considered alongside 'nanotechnology' – the use of sophisticated synthetic and analytical techniques to create materials that either contain discrete nanometre-scale structure, or are nanometre sized themselves. The field of nanoparticle chemistry is diverse, embracing influences from physics, maths and biology, as well as engineering and material sciences <sup>49</sup>. This has led to several astonishing developments: functioning guitars only a few microns long <sup>50</sup>; nanometre-scale devices capable of moving under their own traction <sup>51</sup>, even novel therapeutic techniques for cancer treatment <sup>52,53</sup>. A discussion of advanced nanotechnology, however, falls outside the scope of this project, so instead focus will be drawn towards various metallic nanoparticle systems, techniques for their synthesis and their applicability. Metallic nanoparticle chemistry is of paramount importance to the project, particularly in their catalytic applications, and attention is also drawn to the challenges of preventing agglomeration – the 'clumping' of individual nanoparticles into larger macrostructures – and control of the size distribution, or dispersity, during metallic nanoparticle synthesis.

In some ways, the production of nanometre scale material is not a new process – the production of clusters of gold and silver atoms has been known for over 2000 years, and found use in the production of coloured glass and ceramics, producing rich red

and yellow hues respectively<sup>54</sup>. The craftsmen were unwittingly taking advantage of the unique, size dependant electronic properties of gold and silver when the bulk material was reduced to small clusters of atoms. Pioneering research done by Nimtz *et al.* found that, as bulk metals are reduced down to clusters a few nm in diameter the dense continuum of orbitals that make up their band structure splits out into orbitals far enough apart for quantisation – the transition from continuum to a discrete set of energy levels – to be observed<sup>55</sup>, similar to what was observed by Brus *et al.* in their investigations into the electronic structure of quantum dots<sup>56</sup>. This is referred to as the size-induced metal to insulator transition (SIMIT) and occurs when the size of the particle begins to approach the De Broglie wavelength scale. SIMIT has profound implications for the properties of metallic materials as they are reduced to the nanoscale. Nimtz *et al.* proved that electrical conductivity was dependant on system size, finding that indium particulate greater than a micrometre in size displayed conductivity similar to bulk indium metal. However, as the particulate approached sizes of 20 nm conductivity drastically receded<sup>55</sup>. They therefore postulate that this is due to the weaker overlap between the conductance band orbitals and valence band orbitals resulting from SIMIT. The electrons become quantum confined within the structure of the nm sized particles. These results are reinforced by later studies into the electronic structures of quantum confined systems<sup>56–59</sup>.

Conductance is not the only property affected by SIMIT. The phenomena that make up observable magnetic behaviour such as magnetic domains and exchange coupling take place between the micro and nanometre scale. As magnetic materials approach this scale in size, the effects of quantum confinement are observed<sup>60</sup>. Bulk magnetic material is comprised of ‘domains’ – areas of the structure in which each individual structural unit’s magnetic moment is aligned in the same direction<sup>61</sup>. If these domains have a random orientation with respect to each other, the material exerts no magnetic field as the random orientation of the various magnetic moments cancels itself out, and the material is said to exhibit ‘paramagnetic’ behaviour. These domains will still respond to an external magnetic field however, as they can rotate to align with an external field, at which point they are said to exhibit ‘ferromagnetic’ behaviour<sup>62</sup>. Magnetisation is inversely proportional to temperature according to the Curie law. As the material approaches a value known as the ‘Curie temperature’, it

loses its intrinsic magnetism and becomes paramagnetic<sup>61</sup>. This is due to the fact that, at higher temperatures, the system has more energy, allowing for the domains to overcome the energy barrier of becoming unaligned from its neighbours. If a material is ferromagnetic at a given temperature, its domains will remain aligned in the direction of the external field even after it is removed. As the typical size for a magnetic domain is in the order of nanometres<sup>60,63</sup> a bulk material that displays ferromagnetism divided finely enough will be comprised of particles with only one domain – the exact size depending upon material type. On this scale, an interesting mix of properties occurs. The particles retain their magnetic susceptibility, as they are made of the same material, however, they also behave paramagnetically, retaining no magnetic field<sup>64</sup>. This is because the domains are no longer bound within a solid structure having to overcome strong magnetic forces to move towards a random distribution, the particle itself can simply rotate and tumble in solution. This kind of phenomenon is referred to as superparamagnetism<sup>65</sup>, and it has some interesting implications for magnetically catalysed reactions and induction heating.

The literature surrounding the field of metallic nanoparticles concerns itself mainly with the investigation of noble metal nanoparticles, such as palladium, gold, ruthenium and rhodium. This is due to the fact that they make excellent, easily recoverable catalysts for a wealth of chemistry. In particular, palladium nanoparticles show a high catalytic activity for carbon-carbon cross-coupling chemistry<sup>66-69</sup>, and gold nanoparticles find use as highly efficient oxidation catalysts under aerobic conditions<sup>70-73</sup>. In recent years, however, nanoparticles of metallic species such as iron oxide have become attractive due to their potential as magnetically recoverable catalysts<sup>67,69,74-76</sup>. Multimetallic systems have also been attracting attention, bringing the promise of improved selectivity and catalytic stability<sup>77</sup>.

### 1.3.1. Routes to Synthesis

When it comes to metallic nanoparticles, the dominant synthetic methods follow a wet-chemistry colloidal route in some form or another, wherein nanometre scale nanoparticles are grown from precursors in solution. This is due to the fact that interest in these particles comes from their catalytic applications. As a result, there is a desire to produce chemically significant quantities of these particles, with room to

scale up if required. So, whilst methods utilised more frequently in other areas of nanotechnology, such as molecular beam epitaxy, are also capable of producing metallic nanoparticles<sup>54</sup>, they will not be considered here due to difficulties with scale-up. Similarly, the principles surrounding colloidal methods differs little between different metallic systems, so synthetic methods will be considered as a whole, rather than for each individual species. The hallmarks of an acceptable metallic nanoparticle synthesis are low degrees of polydispersity (that is to say that the particles are of a similar size) and control of particle shape, as both of these properties have implications for catalytic activity. It is here where metallic nanoparticle synthesis becomes non-trivial, as metallic particulate of this size shows a tendency to agglomerate *via* van der Waals forces into bulk structures. It does this so as to minimise the surface energy of individual nanoparticles, whose surface atoms make up for a significant portion of their total mass. This is typically overcome *via* the incorporation of a polymer, surfactant or ligand into the synthesis, which reversibly adsorbs onto the surface of the freshly formed nanoparticles, inhibiting agglomeration.

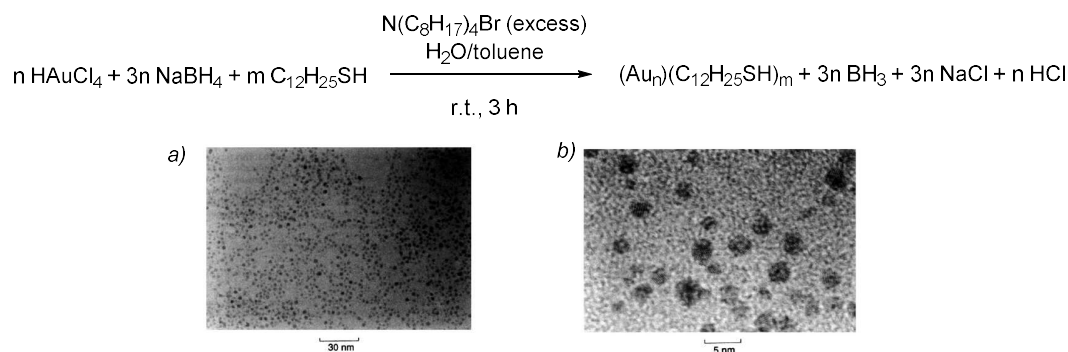


Figure 1.7: Biphasic synthesis of gold nanoparticles. a) low magnification b) high magnification transmission electron microscopy (TEM) image<sup>78</sup>.

Of all the methods of producing metallic nanoparticles *via* colloidal routes, the reduction of metal salt precursors is the most widely reported<sup>54</sup>. A large library of reducing agents exists, and typically they are interchangeable from metal to metal. Brust *et al.* were able to synthesis gold nanoparticles *via* the reduction of simple gold salts by sodium borohydride in a dual-phase system (water/toluene)<sup>78</sup>. This was done in the presence of thiol-containing compounds that acted as an anti-agglomeration agent, and tetraoctylammonium bromide as a phase transfer agent

(see Figure 1.7). By altering the amount of thiol within the reaction, particles between 2-5 nm in size were produced, with a high degree of monodispersity. Borohydride reduction has also found use in the production of more exotic bimetallic nanoparticles. Lu *et al.* were able to produce various copper-iron nanoalloys *via* the one-pot reduction of an aqueous solution containing iron(II) chloride and copper(II) chloride *via* sodium borohydride <sup>79</sup>. They found that by simply altering the stoichiometry of the two salts, they could reliably produce nanoparticles with differing copper to iron ratios, confirmed by inductively coupled plasma mass spectrometry measurements. This produced particulate sizes of 3 nm or less, though a high degree of agglomeration was observed, likely due to the magnetic properties of these nanoparticles.

Moving away from aqueous chemistry, it is possible for solvent and reducing agent to be the same compound. Pioneering work by Hiari *et al.* found that alcohol containing compounds were capable of the reduction of metal salts, producing nanometre sized particulate of the metal as well as the carbonyl analogue of the alcohol <sup>80</sup>. Organic polymers such as poly(vinylpyrrolidone) (PVP) were used to bind to the fresh nanoparticles and prevent agglomeration. Their early work focused upon rhodium nanoparticles and resulted in aggregated particulate of between 3-7 nm in size. Later work however improved this markedly, in which they refluxed rhodium(III) chloride and methanol in the presence of poly(vinyl alcohol), yielding particulate 8 nm in size <sup>81</sup>. Hiari *et al.*'s colloidal alcohol reduction method has proven to be a robust and general approach to metallic nanoparticle synthesis, capable of the generation of not just rhodium but other metals as well: Toshima *et al.* were able to produce Au, Pt, Pd, Rh and Ru monometallic particles, as well as Au/Pt, Au/Pd, Au/Rh and Pt/Ru clusters <sup>82</sup>. Particle size for these systems was reported to be between 2.6-1.9 nm, with standard deviations of between 0.8-1.6 nm, depending on the particle systems under investigation. Lu *et al.* were also able to adapt the method to create nickel/palladium nanoalloys <sup>83</sup>. Interestingly however it was determined *via* extended x-ray absorption fine structure (EXAFS) analysis that, when used to synthesise bimetallic nanoparticles, Hiari's alcohol reduction had a propensity to generate core-shell structures rather than true nanoalloys (see Figure 1.8) <sup>82</sup>.

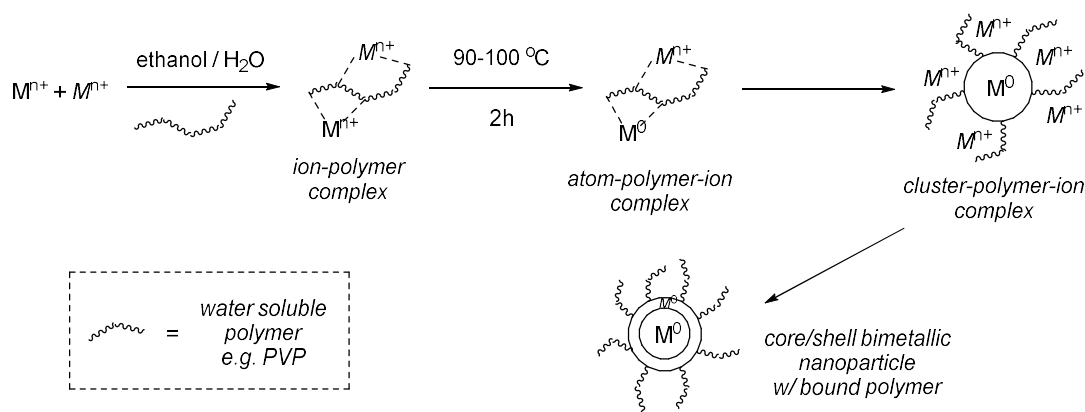


Figure 1.8: Synthesis of core/shell structured nanoparticles via colloidal alcohol reduction<sup>82</sup>.

It is also possible to replace the need for a chemical reductant with electrochemistry. M. T. Reetz and W. Helbig have displayed that, with an inexpensive two electrode set-up in solutions of metal salts, electrochemistry could be used to produce nanoparticulate with excellent size selectivity (see Figure 1.9)<sup>84</sup>. They found that the electrochemical reduction at the cathode leads to the generation of individual atoms at the cathodic surface. Rapid agglomeration occurs between these ‘adatoms’, mediated by the reversible adsorption of tetraalkylammonium salts present in the electrolyte. Reetz *et al.* observed a negative correlation between electrode charge density and particulate size, which can be exploited to control the growth of the nanoparticles (see Figure 1.9a-c)<sup>84,85</sup>. Their initial work focused on the electrochemical reduction of palladium and nickel, the resulting nanoparticles found to have typical size distributions of  $\pm 2$  nm. This method has been expanded, with reports of the synthesis of Ti, Fe, Co, Pt, Ag and Au monometallic nanoparticles<sup>54</sup>, as well as Ni/Pd, Fe/Co and Fe/Ni nanoalloys<sup>85</sup>. The work of Toshima *et al.* and Reetz *et al.* serves to highlight the generality of metal salt reduction methods, a wide variety of catalytically interesting nanoparticles can be synthesised with small particulate size and narrow size distribution, simply by altering the composition and stoichiometry of the metal salt precursor(s).

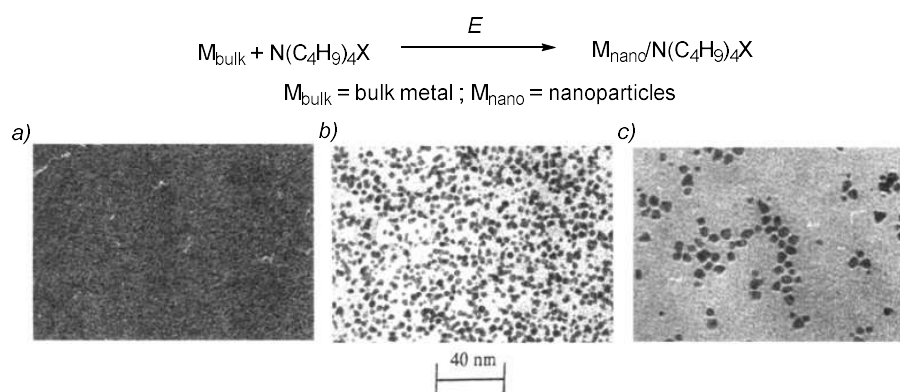


Figure 1.9: Synthesis of metal nanoparticles via electrochemical redox.  
 a) TEM of Pd nanoparticles generated at  $5 \text{ mAcm}^{-2}$ ; b)  $0.8 \text{ mAcm}^{-2}$ ; c)  $0.1 \text{ mAcm}^{-2}$  <sup>84</sup>

Many organometallic compounds are unstable with respect to decomposition *via* heat, light or ultrasound, yielding metal and organic products. The conditions required to achieve such reactions are typically quite mild, and can be exploited to produce metallic nanoparticles <sup>54,86</sup>. Bradley *et al.* have produced Pd, Pt and PdCu nanoparticles by taking solutions of the corresponding metal acetates and heating them to reflux for 2 hours in the presence of poly(vinylpyrrolidone) as a stabiliser <sup>87</sup>. The resulting average particulate size was found to vary between batches from 30-50 nm, but in each batch a size distribution of  $\pm 10\%$  was observed. Energy-dispersive X-ray (EDX) measurements confirmed that, in the case of the PdCu alloy, the stoichiometry of palladium and copper acetates used was represented in the composition of the nanoparticles. However, infrared spectroscopy performed on the nanoparticles in a carbon monoxide atmosphere revealed that, unless the copper content of the particles exceeded 50%, the Pd-CO vibration was largely dominant <sup>87</sup>, suggesting that the surface of these particles is mainly comprised of palladium. This result is unfavourable if a homogenous alloy is desired. This was later expanded upon by Yu *et al.* who were able to produce poly(vinylpyrrolidone)-stabilised palladium nanoparticles only a few nanometres in size from simple palladium complexes <sup>88</sup>. This was achieved *via* the use of microwave heating, which was able to apply energy to the reaction uniformly throughout the mixture. This has the benefit of homogenous nucleation and quick reaction times, on the scale of a few minutes – a marked improvement on Bradley *et al.*'s synthesis. With 50 mol% poly(vinylpyrrolidone), the resulting particulate was  $3 \pm 0.5 \text{ nm}$ , a narrower size distribution than what they observed with conventional heating *via* oil bath:  $2.7 \pm$

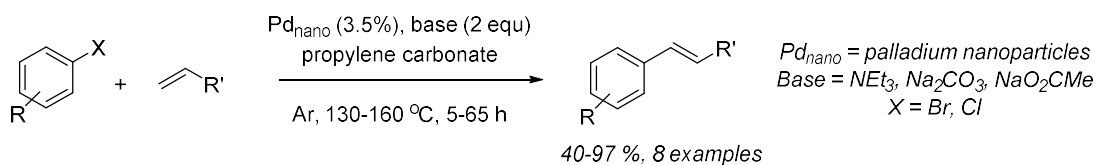
0.74 nm. As with Brust *et al.*'s salt reduction method<sup>78</sup>, a negative correlation was observed between stabiliser concentration and particle size.

Gedanken *et al.* have shown that ultrasound is capable of producing palladium nanoparticles from palladium acetate in THF<sup>89</sup>. This works by causing the formation of cavities within the solvent, in which temperatures (>5000 °C) and pressures (>20 MPa) are much higher than the surrounding solvent<sup>90</sup>. At the cavity-solvent barrier, the stabilising compounds and solvent are subjected to rapid pyrolysis into radical species. These radicals go on to reduce the palladium alkyl into nanoscale palladium (0) particulate. TEM analysis revealed the resulting particles to be spherical in nature, with a size distribution of between 10-20 nm<sup>89</sup>. With this method they also produced nickel nanoparticles with a size distribution of 5-20 nm<sup>91</sup>, and silver nanoparticles 20 nm in diameter (no distribution stated)<sup>92</sup>. Therefore, whilst ultrasonic generation of nanoparticles is possible for a variety of metals, the lack of control over particulate size leaves a lot to be desired.

### 1.3.2. Monometallic Nanoparticles in Catalysis

The catalytic properties of metallic nanoparticles have gained significant interest over the last 15 years. Metal nanoparticles can be considered to be very finely divided bulk metal, and therefore it holds that they display vastly increased catalytic activity compared to bulk metal, owing to their increased surface area. They also have an advantage over homogeneous catalysts in that they are comparatively easier to extract from reaction mixtures post-reaction, either through filtration<sup>93</sup> or through the use of an external magnetic field<sup>65</sup>. This helps reduce the contamination of end product with transition metal catalyst and enables the recycling of the catalyst for future use.

It can be argued that reactions forming carbon-carbon bonds are some of the most important reactions to modern organic chemistry, allowing for the synthesis of everything from pharmaceuticals to pesticides<sup>66</sup>. Whilst many metals are capable of catalysing the formation of new carbon-carbon bonds, the most firmly established and investigated techniques use palladium. Of particular prevalence are the Heck, Suzuki, Sonogashira, Stille and Negishi reactions, which all find use industrially as well as academically<sup>94</sup>.



*Scheme 1.16: Reetz et al.'s colloidal palladium-catalysed Heck reaction*<sup>95</sup>

The use of palladium nanoparticles in the Heck reaction has been largely explored by Reetz *et al.*, who were able to take their electrochemically synthesised particles and incorporate them directly into typical Heck protocols (see Scheme 1.16)<sup>95</sup>. As expected, they found the greatest reactivity using substrates with weak carbon-halogen bonds, with yields between 70-100 % being observed when triethylamine was used as a base, and 3.5 mol% loadings of palladium nanoparticles. Interestingly, they were able to achieve yields of up to 55 % with chlorobenzene as a substrate. However, aryl chlorides required reaction times of 65 hours, which weakens the reactions applicability in that regard. In later studies, they observed that palladium nanoparticle catalysed Heck reactions follow the typically observed mechanism at the particle surface, beginning with oxidative addition of the aryl halide onto the particle<sup>96</sup>.

Bradley *et al.* expanded upon these investigations, finding that there is a negative correlation between the average size of palladium nanoparticles used, and the initial rate of reaction<sup>97</sup>. As particle size decreases, a higher proportion of the surface area is made up of palladium atoms with low coordination. These sites show increased reactivity, as low levels of coordination is energetically unfavourable. They therefore postulate that it is these low coordination sites that are catalytically active to the Heck reaction. Li *et al.* have reported the successful use of poly(vinylpyrrolidone)-stabilised palladium nanoparticles in the Suzuki reaction, investigating a wide range of aryl boronic acids and aryl iodide substrates<sup>98</sup>. Yields as high as 95 % were reported. They attribute the high reactivity observed to the large surface area of the nanoparticle catalyst and observed that the initial rate of the reaction was linearly dependent upon the catalytic loading. Li *et al.* therefore draw the conclusion that the reaction is occurring directly upon the particle surface itself. Their synthesis is attractive as they were able to perform it in aqueous media which,

when considered alongside the easily recoverable nanocatalyst, has positive implications for industrial use where it would be favourable to avoid the use of large volumes of volatile, harmful solvents.

It is known that trace amounts of palladium are capable of sufficiently catalysing cross-coupling reactions<sup>93</sup>. Therefore, there is much discussion in the literature surrounding palladium nanoparticles as to whether or not their catalytic activity is due to the leaching of trace amounts of palladium ions into solution<sup>66,93</sup>. This would mean that the true catalytic mechanism would be homogeneous in nature, not heterogeneous. Palladium nanoparticle leaching is a widely reported phenomenon, and although it has been observed occurring in neat coordinating solvent it is typically reported when palladium nanoparticles are used alongside aryl halides<sup>93</sup>. Rothenberg *et al.* observed *via* TEM analysis that, as their palladium nanoparticle-catalysed Sonogashira reaction progressed, the average diameter of their nanoparticle catalyst decreased<sup>99</sup>. From this, they hypothesise that the mechanism of depletion of the palladium metal from the particulate proceeds *via* the oxidative addition of aryl halide to the particle surface, forming a soluble Pd<sup>II</sup> species which then enters the catalytic cycle. This is contested by a study performed by Reimann *et al.* wherein Quick Extended X-ray Absorption Fine Spectra (Quick EXAFS) was used to simultaneously monitor a fixed-bed of alumina-supported palladium nanoparticles and the reaction mixture during a typical Heck reaction for palladium-containing species<sup>100</sup>. During the active phase of catalysis, after heating to 150 °C, palladium colloids are observed in solution; it is only at reaction completion that palladium halide species ( $[\text{PdX}_4]^{2-}$ ,  $[\text{Pd}_2\text{X}_6]^{2-}$ ) are found in significant quantity<sup>100</sup>. The prevalence of colloidal palladium species during the active phase suggests that they may play a significant role in the reaction mechanism besides simply serving as a reservoir for leached homogeneous catalysts. However, studies have shown that after performing a typical palladium nanoparticle-catalysed cross-coupling reaction, one can remove any remaining particulate *via* hot filtration, spike the supernatant solution with fresh reagent and see reactivity<sup>93</sup>. Therefore, catalysis by leached palladium ions and catalysis upon particulate surface are likely competing processes.

The catalytic application of iron nanoparticles is not simply limited to serving as a support for other catalytically active metals, with various reactions reported to be

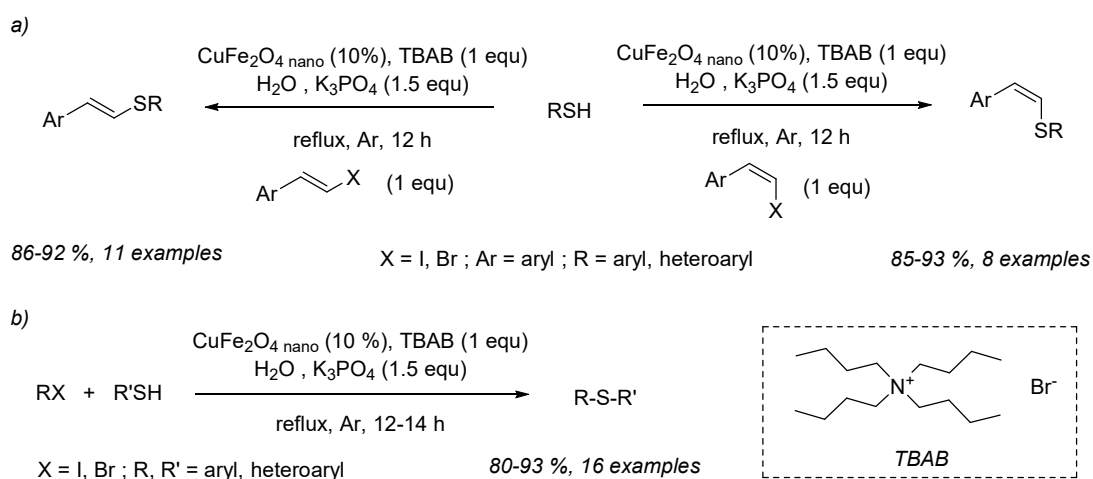
directly catalysed by the particles themselves, such as aminolysis of epoxides <sup>101</sup>, borylation of alkynes <sup>102</sup> and the aqueous reduction of nitroarenes <sup>103</sup>. These examples all display a very high degree of regio- and stereoselectivity. Notably however, Yang *et al.* have recently reported success in using Fe<sub>3</sub>O<sub>4</sub> nanoparticles as a catalyst in the radical-promoted decarboxylative cross-coupling reaction between cinnamic acid derivatives and toluene <sup>104</sup>. A modest number of substrates were screened, with yields between 67-85 % reported – significantly higher than observed with the use of simple iron salts. Greater yields were shown in the cases where electron-withdrawing groups were present on the cinnamic acid derivative, or electron-donating groups on the toluene derivative. *Via* use of an external magnetic field they were able to separate the catalyst and recycle it, with reactivity dropping from 85-75 % in a typical reaction over 7 runs.

### 1.3.3. Bimetallic Nanoparticles in Catalysis

Mixed metal nanoalloys represent an interesting class of metallic nanoparticles because the choice of metals, and their ratios in the end product can have a pronounced effect upon their electronics and catalytic activity <sup>77,105</sup>. This was alluded to in Reetz *et al.*'s exploration into the use of electrochemically synthesised nanoparticles in the Suzuki reaction <sup>106</sup>. They observed that the Ni/Pd nanoalloy showed a greater catalytic activity compared to their palladium monometallic nanoparticles. Indeed, they found that the Ni/Pd nanoalloy was even able to promote coupling between aryl chlorides and boronic acids, although with a much lower turnover compared to aryl bromides – similar to their work on the Heck reaction <sup>96</sup>. However, there is little direct literature addressing the use of these materials as catalysts in organic chemistry. This is likely due to the fact that reactions requiring two or more transition metal catalysts are relatively uncommon, meaning only one of the metals in the alloy will be acting as a catalyst. The reactivity of these materials would then be dependent upon the number of exposed catalytic metal, a parameter that is difficult to control without simply forming a core/shell structure.

Kundu *et al.* have found nanoscale CuFe<sub>2</sub>O<sub>3</sub> to be an excellent catalyst for the formation of carbon-sulfur bonds between thiols and either styrenyl halides (see Scheme 1.17a) or aryl/heteroaryl halides (see Scheme 1.17b) <sup>107</sup>. Classical approaches to these reactions typically utilised complexes of metals such as Fe, Cu,

Ni, Co or Pd<sup>108,109</sup>. Reportedly however, the catalysis of styrenyl halides with these catalysts has proven challenging, particularly when it comes to stereoselectivity<sup>107</sup>. Kundu *et al.*, after reaction optimisation, screened a vast library of styrenyl halides against the reaction, with differing halide choice, symmetry, steric hindrance, and substituents. Yields between 80-93 % are reported, with excellent selectivity in each case. The catalyst even proved amenable to the synthesis of bisulfides *via* di-substituted reagents, although yields were poorer, ranging from 65-86 %. Catalyst recyclability was investigated against a typical reaction, with yields falling from 85 % to 80 % over 10 runs. The particles themselves were analysed after each run, and it was observed that they showed a tendency to agglomerate, becoming successively larger as they are recycled. This gives insight into the mechanism of nanoparticle catalyst deactivation – an inherent tendency to agglomerate reducing the total catalytic surface area of the system.



*Scheme 1.17: CuFe<sub>2</sub>O<sub>4</sub> nanoalloys as catalysts for the coupling of thiols and halide coupling partners<sup>107</sup>.*

Handa *et al.* have recently exemplified the properties these nanoalloys possess in a novel synthesis of an iron/palladium alloy from cheap, commercially available iron(III) chloride, which naturally contains parts-per-million (ppm) levels of palladium<sup>110</sup>. This catalyst was found to be highly reactive in Suzuki cross-couplings, in the presence of ligand and with water as a solvent. When an amount of Pd(acac)<sub>2</sub> identical to the ppm levels in the catalyst was used, no reactivity was observed. Nor did the reaction proceed in the presence of the starting materials used to create the catalyst. It required the palladium to be specifically bound to the iron in

the form of a nanoalloy, highlighting the fact that alloy formation can have interesting implications for catalytic activity. A yield of 98 % was reported using the nanoalloy with SPhos as a ligand, however the yield varied greatly with ligand choice, falling as low as 28 % with  $\text{PPh}_3$ <sup>110</sup>. This increased reactivity resulting from the incorporation of palladium into nanometre scaled alloys reinforces the results reported by Reetz *et al.*<sup>106</sup>.

#### 1.4. Project Aims

The core aim of the research presented is to build up upon the wealth of investigations found in the literature surrounding DCC chemistry and develop a low temperature DCC protocol. Initially, focus will be drawn towards copper-catalysed monometallic decarboxylative cross-coupling methods due to their relative simplicity compared to their state-of-the-art bimetallic counterpart protocols <sup>17</sup>. A model reaction will be chosen and parameter such as catalyst choice, loading, solvent and reaction temperature will be manipulated with the objective of gaining understanding of the system and identifying conditions that will be carried forward into further investigations.

With monometallic investigations in hand, research into the development of a bimetallic approach will begin in earnest. Whilst homogeneous catalyst systems for DCC chemistry have been well reported, methodology utilising nanoparticles as catalysts have received little attention. Bimetallic nanoparticles are an attractive target for catalysis design as their performance as catalysts is dependent on a number of properties that are determined by the route used for their synthesis. This includes but is not limited to: particulate size; particulate shape; metal content; capping agent and distribution of metal throughout the particulate <sup>105</sup>. Bimetallic DCC approaches utilise palladium coupled with either copper or silver catalysts. As such, a wide library of group 10/group 11 bimetallic materials, as well as monometallic counterparts for comparative purposes, will be both synthesised and characterised before being screened against the conditions elucidated by the prior monometallic investigations. This library will be designed in such a way that various combinations of nanoparticle properties will be placed under investigation.

A broader aim of this research is to investigate the scope for improving the overall viability of DCC chemistry. Developing a successful low-temperature protocol is part of this goal, but this does not address the widespread use of toxic and harmful solvents in reported DCC research. To this end two approaches will be investigated: direct replacement of problem solvents *via* principle component analysis (building upon the work of Murray <sup>111</sup>; and the replication of the proven efficacy of problem solvents *via* the use of chemically similar but innocuous additives to improve reactivity in desirable but underperforming solvent systems.

## 2. Investigations in Copper-catalysed Decarboxylative Cross-coupling

### 2.1. Introduction

Carbon-carbon bond forming reactions are a highly valuable tool in the modern chemist's toolbox, enabling the synthesis of complex and valuable molecules. In particular, two aromatic rings joined by a single carbon-carbon bond is a recurring motif in a plethora of natural and man-made compounds such as pharmaceuticals <sup>112</sup>, agrochemicals <sup>94</sup>, and other fine chemical applications <sup>113</sup>. Therefore, reactions that facilitate such transformations are in high demand, both in industry and academia <sup>114</sup>. Traditionally this has been achieved *via* the reaction of two aromatic starting materials and mediated by a transition metal in either a catalytic or stoichiometric quantities <sup>115</sup>. These are referred to as cross-coupling reactions. In recent years, one such route to carbon-carbon bond formation has found itself the subject of numerous studies as an attractive alternative to popular cross-coupling reactions – decarboxylative cross-coupling (DCC) <sup>17,31,44</sup>.

Derived from the copper-catalysed Ullmann reaction <sup>16</sup>, DCC is concerned with the copper-mediated reaction between aryl halides and carboxylic acids or carboxylate salts. Carboxylic acids and their derivatives are found in numerous natural products and compounds that contain carboxylic acid functionality are widely available on a commercial scale <sup>17,116</sup>. They also have the benefit of being easy to handle and store <sup>17</sup>. It is for these reasons that interest in DCC has arisen, as competing cross-coupling reactions such as the Suzuki-Miyaura, Negishi, Kumada and Stille reactions all require starting materials with lengthy and, in some cases, challenging syntheses and that also require special considerations when it comes to storage and handling <sup>31,94,117</sup>.

As the name would suggest, DCC proceeds *via* the decarboxylation of carboxylic acids *via* interaction with a transition metal catalyst (typically based around copper, silver or palladium), forming a highly reactive organometallic intermediate *in-situ* which then goes on to react with an aryl halide, yielding a new carbon-carbon bond. However, the challenge in utilising DCC as a route to these desired transformations lies in bringing about the decarboxylation step itself, as it requires harsh and forcing

conditions to induce <sup>17</sup>. Such conditions are wasteful, limit functional group tolerance and can promote unwanted side reactions.

The work presented in this chapter is concerned with a number of studies aimed at investigating DCC and probing solutions to its shortcomings. These include:

- Adapting literature protocols for DCC with the aim of reducing required reaction temperatures and catalyst loadings.
- Investigating the role solvent plays in the DCC reaction, in particular the hazardous solvent diethylene glycol dimethyl ether (diglyme).
- Utilizing induction heating as a novel approach to energy delivery, potentially allowing for the direct targeting of DCC over undesirable side reactions through magnetically susceptible heterogeneous catalyst.

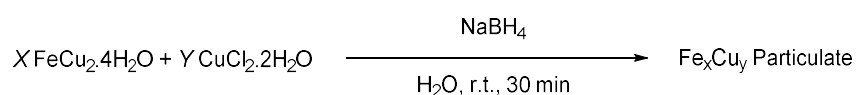
Although cutting edge research in this field is largely focused on the use of bimetallic catalyst systems containing group 11 metals (*e.g.* copper or silver) and the group 10 metal palladium <sup>17,44</sup>, this introduces additional layers of complexity to the DCC reaction. This is because it requires two separate transition metal catalytic cycles to work in tandem. Given the broad-spectrum nature of the investigations presented in this chapter it was therefore decided to focus on monometallic DCC protocols utilising copper. There is significant literature precedent for copper-catalysed approaches <sup>17,31</sup> and avoiding the use of palladium altogether in catalysis has been highlighted as desirable due to economic concerns such as the added cost of extraction steps so as to ensure end products are not contaminated with palladium <sup>118–120</sup>.

## 2.2. Synthesis and Characterisation of Copper-containing Heterogeneous Catalysts

Even when limited to a monometallic approach focusing on copper-based transition metal catalysts, there are numerous choices available to the researcher. A popular literature catalyst in the field of copper-catalysed DCC is copper(I) iodide (CuI) <sup>17,31,33</sup>, though there are also examples using copper oxides and even metallic copper itself <sup>16,20,22</sup>. However, as direct heating of catalytic material *via* induction heating is a primary interest of the work presented, none of these choices are suitable. Eddy

currents can be induced within metallic copper, but as particle size is reduced from bulk scale towards micrometre and nanometre regimes size-induced metal to insulator transition (SIMIT) effects begin to inhibit the flow of electrons throughout the material <sup>55</sup>. This would likely result in poor overall performance. The catalyst needs to retain the chemical reactivity of copper but also possess susceptibility to an external magnetic field. This would allow for the material to be heated *via* magnetic hysteresis loss if particle size was large or *via* Neel and Brownian relaxation if the resulting material was comprised of particles small enough to contain only one magnetic domain.

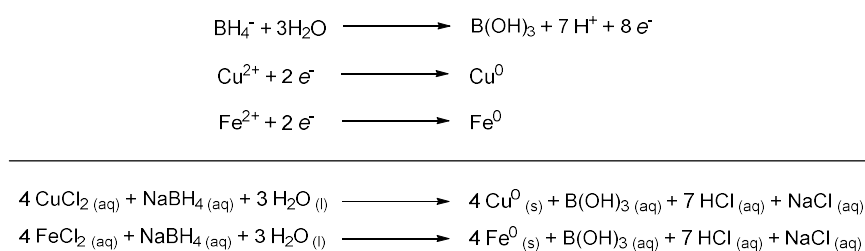
The approach put forward within this work is to utilise an alloy of catalytically active copper and magnetically susceptible iron. Small particle size is desirable to maximise the exposure of copper active sites within the catalyst, however Ghosh *et al.* report that in the case of using induction to heat iron oxide nanoparticles of various sizes, larger particles were significantly more receptive to the inductive field, resulting in greater system temperatures over a 10 minute period <sup>52</sup>. Indeed, prior work by Nguyen found that when using induction heating to directly heat iron/palladium bimetallic nanoparticle catalysts that the inclusion of capping agents in the nanoparticle synthesis resulted in reduced catalyst performance <sup>121</sup>. Such capping agents would serve to arrest agglomeration and therefore lower effective particle size.



*Scheme 2.1: Synthesis of iron/copper catalytic material, adapted from Lu et al. <sup>79</sup>.*

Iron/copper alloys and their synthesis have been reported in literature, and for this work the preparation put forward by Lu *et al.* was chosen as the basis of this investigation <sup>79</sup>. Metal salt reduction routes to heterogeneous and nano-scale catalysts are popular due to their relative ease of both synthesis and scale-up compared to competing methods such as electrolysis and molecular beam epitaxy <sup>122</sup>. It is for these reasons, coupled with the lack of a requirement for capping agent, that Lu *et al.*'s method was chosen (Scheme 2.1).

Three iron/copper materials of varying iron to copper ratios were synthesised by varying the molar quantities of iron(II) chloride tetrahydrate and copper(II) chloride dihydrate used in the synthesis: **Fe<sub>2</sub>Cu**, **FeCu<sub>2</sub>** and **Fe<sub>4</sub>Cu**. For comparative purposes, monometallic copper material, **Cu(mono)**, was also synthesised under the same conditions by simply omitting the iron salt precursor. In all cases, upon the dropwise addition of the aqueous solution of copper(II) and iron(II) salts to reducing agent sodium borohydride, vigorous effervescence and the formation of a fine black precipitate was observed. This precipitate was collected *via* centrifugation, washed with deionised water and acetone before finally being dried *in vacuo* and stored under nitrogen. The relevant half-equations and full equations for the redox processes are shown in Scheme 2.2. These materials were then analysed *via* atomic absorption spectroscopy (AAS) to determine their copper content by weight, the results of which are displayed in Table 2.1.



*Scheme 2.2: Half-equations and full equations for the redox processes between aqueous copper/iron ions and sodium borohydride under aqueous conditions.*

The AAS data displayed in Table 2.1 reveals a good agreement between the observed amount of copper by weight in the resulting materials and what was expected, given the loadings of copper and iron precursor salts in the synthesis. In all cases, however, the observed copper content by weight was found to be slightly lower than expected, suggesting a degree of impurity in the resulting materials.

Given the lack of capping agents to arrest particle growth and agglomeration, nanoscale material was not expected in any of the catalysts. Therefore, to characterise the size and shapes of the resulting particulate, scanning electron microscopy (SEM) was used in favour of transition electron microscopy (TEM) as the typical resolution of the micrographs gathered *via* SEM would be more than adequate. Micrographs at multiple resolutions were captured for each catalyst,

alongside energy-dispersive X-ray spectroscopy (EDX) data, the results of which are displayed in Figure 2.1 to Figure 2.4.

*Table 2.1: AAS characterisation for the Fe/Cu catalyst series. Values rounded to nearest whole number for clarity.*

<b>Catalyst</b>	<b>Ideal Iron Content (wt%)</b>	<b>Ideal Copper Content (wt%)</b>	<b>Observed Copper Content (wt%)</b>	<b>Remaining Mass (wt%)</b>
Cu(mono)	0	100	93	7
FeCu <sub>2</sub>	31	69	67	33
Fe <sub>2</sub> Cu	64	36	35	65
Fe <sub>4</sub> Cu	78	22	20	80

The EDX spectra displayed in the aforementioned figures show clear emissions at 0.930 keV, 8.048 keV and 8.905 keV corresponding to copper L<sub>α</sub>, K<sub>α</sub> and K<sub>β</sub> emissions respectively. Also, in all samples expected to contain iron, emissions at 0.705 keV and 6.398 keV corresponding to iron L<sub>α</sub> and K<sub>α</sub> emissions were also observed. Besides this, an emission at 0.705 keV corresponding to an oxygen K<sub>α</sub> emission is observed in all samples, suggesting a degree of oxidation is present. This is to be expected, given the aerobic conditions of their synthesis. The small emission at 2.621 keV in the EDX spectra of catalyst **Fe<sub>2</sub>Cu** (see Figure 2.3) suggests that chlorine-containing impurities resulting from the synthesis (such the metal chloride precursors or expected side-product sodium chloride) persisted despite rigorous washing steps. Emissions at 0.227 keV and 1.739 keV are present in all spectra and correspond to carbon K<sub>α</sub> and silicon K<sub>α</sub> emissions, respectively. They are present due to the media upon which the samples were mounted and can therefore be safely disregarded.

The size and peak area of EDX emissions are proportional to the amount of that element in the sample under analysis. However, unlike AAS which analyses a homogenous solution of dissolved sample, EDX analyses the surface layer of a chosen area of a sample in the solid state. Therefore, these peak areas are subject to bias and the resulting peak areas and ratios will be influenced by the distributions of the elements under investigation throughout the material.

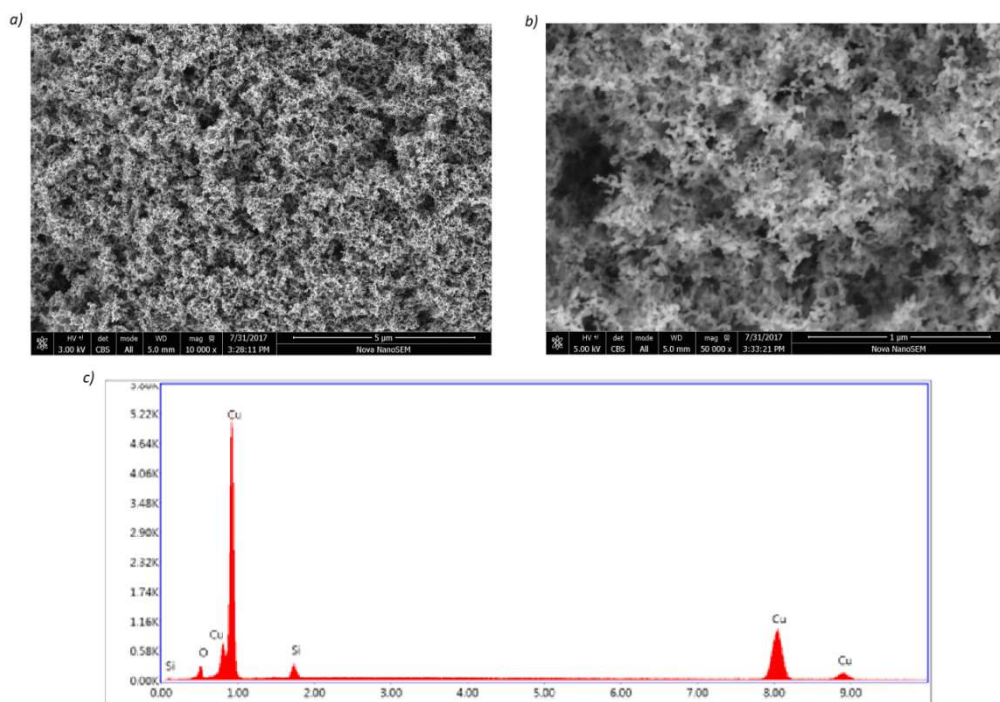


Figure 2.1: Structural analysis of catalyst **Cu(mono)**. a) SEM at 5 μm resolution. b) SEM at 1 μm resolution. c) EDX spectra. Sample mounted on a silicon wafer with carbon tape.

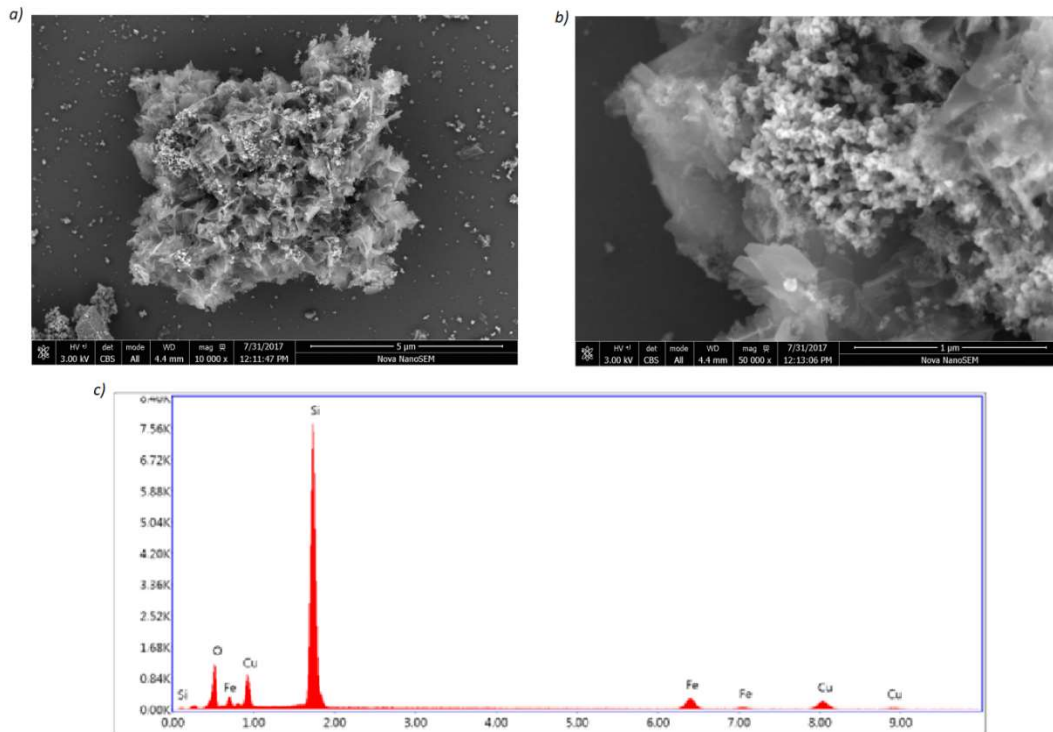


Figure 2.2: Structural analysis of catalyst **FeCu<sub>2</sub>**. a) SEM at 5 μm resolution. b) SEM at 1 μm resolution. c) EDX spectra. Sample mounted on a silicon wafer with carbon tape.

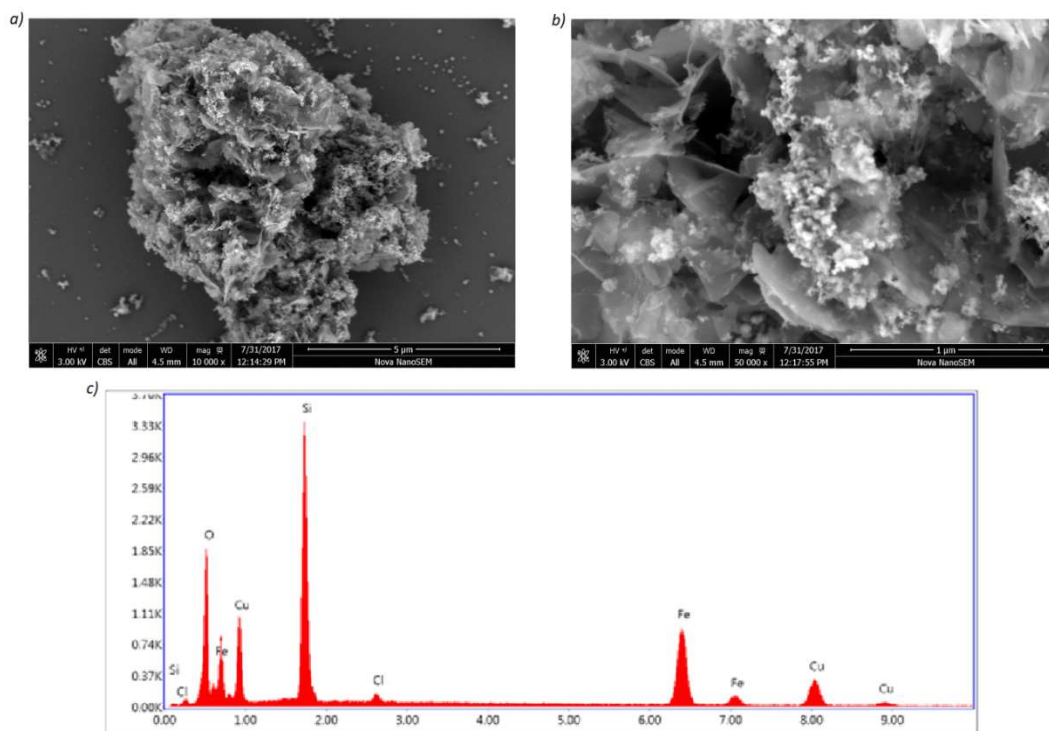


Figure 2.3: Structural analysis of catalyst  $Fe_2Cu$ . a) SEM at  $5\ \mu m$  resolution. b) SEM at  $1\ \mu m$  resolution. c) EDX spectra. Sample mounted on a silicon wafer with carbon tape.

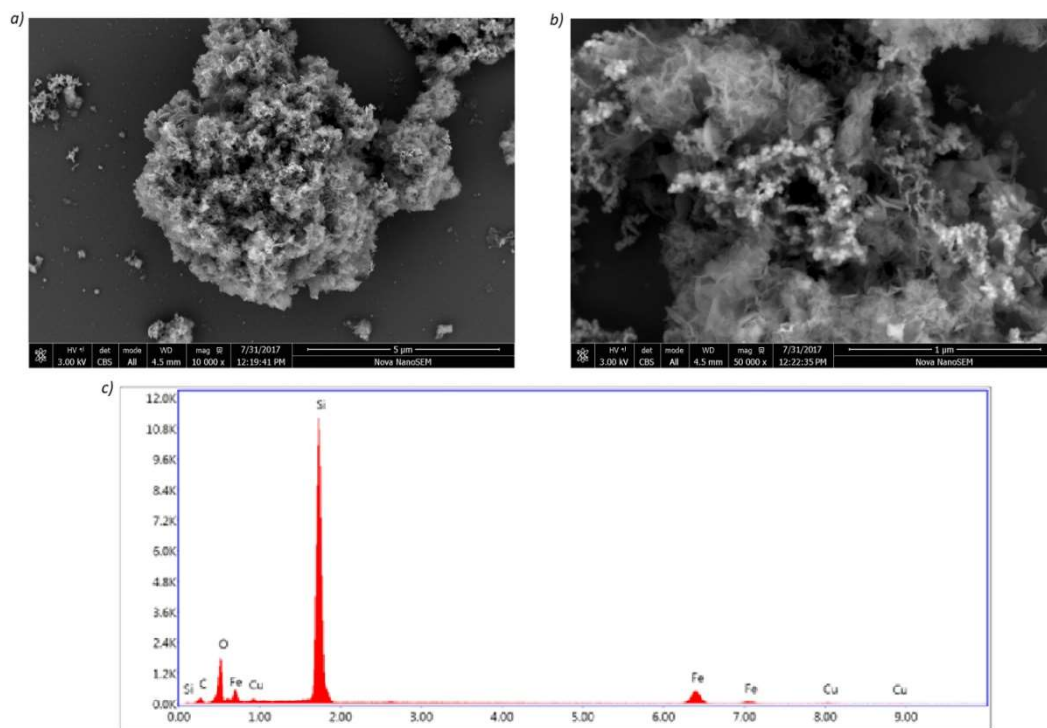


Figure 2.4: Structural analysis of catalyst  $Fe_4Cu$ . a) SEM at  $5\ \mu m$  resolution. b) SEM at  $1\ \mu m$  resolution. c) EDX spectra. Sample mounted on a silicon wafer with carbon tape.

While in theory it would be possible to use EDX to characterise the elemental content of the iron/copper catalyst series, due to these aforementioned factors in practice EDX can only give qualitative information in this case. Despite this, when comparing the ratios of the iron and copper  $K_{\alpha}$  peaks, the expected trend is observed (see Table 2.2). Higher iron-to-copper ratios are observed in samples that were observed to contain lower copper content by weight *via* AAS analysis. However, as the observed ratios between these peaks differ from what would be expected given the loading of precursors in their synthesis, it is possible there is an uneven distribution of iron and copper throughout the bimetallic materials.

*Table 2.2: Table comparing the observed ratios of iron and copper  $K_{\alpha}$  peak areas of Fe/Cu catalyst series to the expected ratio given the loading of precursors. <sup>a</sup> Iron wt% divided by copper wt%.*

Catalyst	Ideal Fe/Cu Ratio <sup>a</sup>	Observed Fe/Cu Ratio <sup>a</sup>
FeCu <sub>2</sub>	0.44	0.67
Fe <sub>2</sub> Cu	1.76	1.46
Fe <sub>4</sub> Cu	3.52	3.14

When analysing the iron/copper bimetallic catalysts *via* SEM, distinct particulate is observed with a diameter of roughly 5 micrometres. However, when observed at a higher magnification it becomes clear that these materials are comprised of two distinct types of structures: large, thin flakes and smaller, rod-like particles that cluster on the edges of the flakes. When compared to the micrographs of monometallic catalyst **Cu(mono)** (see Figure 2.1), synthesised under the same general conditions as its bimetallic analogues, we can see that these rod-like particles bear a striking resemblance to the structure of **Cu(mono)**. Such an observation supports the hypothesis that the synthesised iron/copper bimetallic materials are not a homogeneous iron-copper alloy but rather that they are comprised of particles that contain regions of high iron or copper concentration.

To probe this hypothesis further EDX mapping techniques were also employed, enabling for the direct visualisation of elemental content on the surface of the materials under observation. Catalysts **FeCu<sub>2</sub>** and **Fe<sub>2</sub>Cu** were analysed using this technique, looking for regions of iron, copper and oxygen. The results of the EDX

mapping experiments, as well as the corresponding SEM image of the sample area under investigation, are displayed in Figure 2.5 and Figure 2.6, respectively.

In the case of catalyst  $\text{FeCu}_2$  it can be observed that iron, copper and oxygen are well dispersed throughout the majority of the sample area under investigation, except for a region at the top of the structure where a high degree of copper is observed. When comparing the mapping data to the corresponding micrograph it is noted that this area of high copper concentration does coincide with an area that contains small, rod like structures similar to those observed in catalyst  $\text{Cu}(\text{mono})$  (see Figure 2.1).

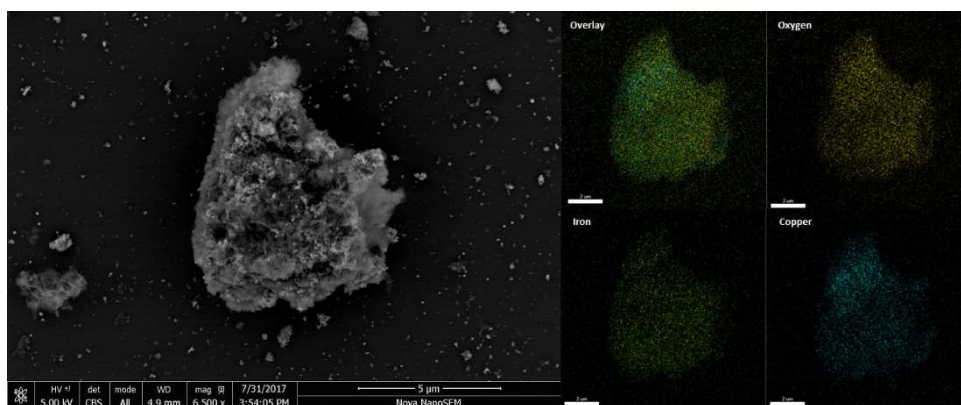


Figure 2.5: EDX mapping analysis of catalyst  $\text{FeCu}_2$  for oxygen, iron and copper, captured over 10 minutes.

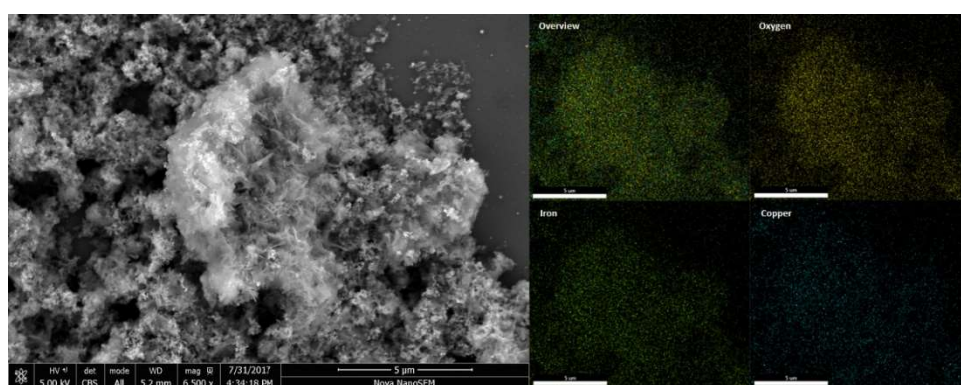
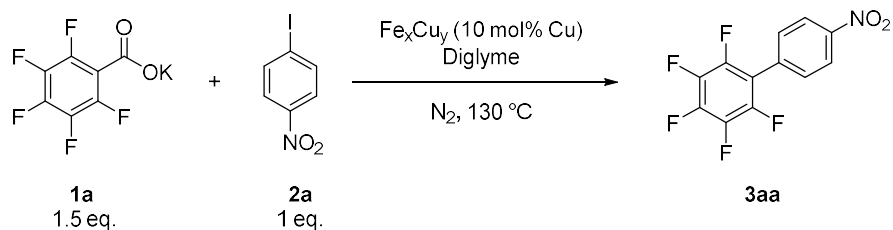


Figure 2.6: EDX mapping analysis of catalyst  $\text{Fe}_2\text{Cu}$  for oxygen, iron and copper, captured over 10 minutes.





Scheme 2.4: Model DCC reaction.

High performance liquid chromatography (HPLC) was chosen as the means to follow this reaction and for this it was required to draw samples from the reaction mixture. However, Shang *et al.*'s DCC conditions call for high reagent concentrations<sup>33</sup>. **1a** displays poor solubility in reaction solvent diglyme and under such conditions the reaction mixture remains a viscous slurry of solvent and undissolved **1a**. Therefore, it was decided to reduce the concentration of reagents by increasing solvent volume four-fold. This would result in a slower rate of reaction, but as concentrations are not varied within the catalyst screening the results are internally consistent.

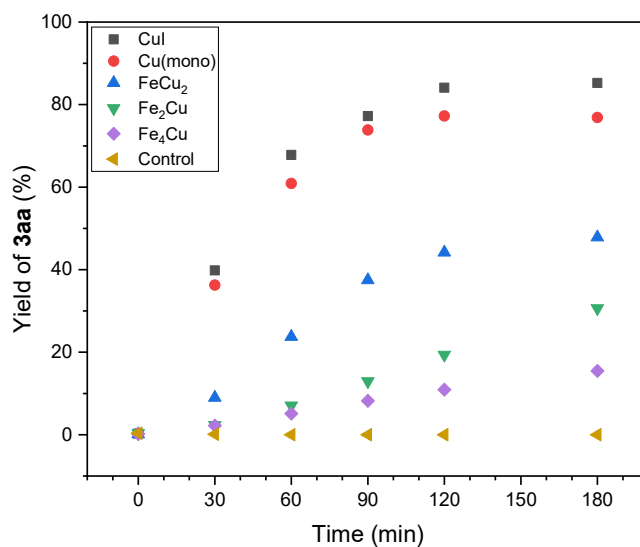


Figure 2.7: A plot comparing the performance of various catalysts in the coupling of **1a** and **2a** at 130 °C. Loading of nanoparticle catalysts 10 mol% with respect to copper content. Yields determined via HPLC.

Using these modified reaction conditions, the copper containing catalyst series was screened over a 3-hour timeframe, alongside popular literature catalyst CuI and a control reaction containing no catalyst for comparative purposes. Using the metal

content data derived *via* AAS (see Table 2.1), catalysts were loaded such that the system contained 10 mol% copper so as to ensure consistency between experiments. The results of this are displayed in Figure 2.7.

The data from this series of screening experiments reveals a correlation between the rate of formation of product **3aa** and the copper content of the heterogeneous catalysts employed. As copper content of the catalysts decreases, so too does the initial rate of reaction and the yield of product **3aa** after 3 hours. It is hypothesised that this trend is because as copper content is reduced, the number of catalytically active copper sites in the system is also reduced creating a kinetic bottleneck and throttling the rate of reaction. EDX mapping experiments of catalysts **FeCu<sub>2</sub>** and **Fe<sub>2</sub>Cu** help corroborate this (Figure 2.5 and Figure 2.6 respectively). There is a greater concentration of copper on the surface of catalyst **FeCu<sub>2</sub>** when compared to **Fe<sub>2</sub>Cu**, and **FeCu<sub>2</sub>** was found to perform better as a catalyst – displaying a faster initial rate of reaction and a higher yield of product **3aa** after 3 hours.

Predictably this resulted in monometallic catalyst **Cu(mono)** performing the best out of all heterogeneous catalysts synthesised in Section 2.2, reaching a yield of product **3aa** of 77 % after 3 hours. However, even **Cu(mono)** performed worse than its homogeneous competitor CuI despite the loading of copper remaining equal. Again, this is possibly due to a disparity in the number of catalytically active copper sites between the two catalysts. Due to its heterogeneous nature, a proportion of the copper content of catalyst **Cu(mono)** lies in the centre of individual particles – unable to interact with reactants in any meaningful way. Considering the AAS and EDX data for **Cu(mono)** it is also clear that it is oxidised to an extent which would further obscure catalytically active copper sites on the surface of **Cu(mono)** particulate.

A point to note about all catalysts analysed is the lack of total conversion of starting material **2a** to product **3aa**, even after a 3-hour period. When the data for catalyst **FeCu<sub>2</sub>** depicted in Figure 2.7 is considered alongside an analysis of the rate of consumption of starting material **2a**, it becomes clear that the observed quantities of **2a** and **3aa** do not fully account for the quantity of **2a** observed at time = 0 minutes (see Figure 2.8). Homocoupling of starting material **2a** to yield side-product 4,4'-

dinitrophenyl (**4a**) was hypothesised to be the reason for this discrepancy and so, to investigate, this experiment was repeated under the same conditions with a sample drawn off after 1 hour, diluted in deuterated chloroform (CDCl<sub>3</sub>) and analysed *via* proton nuclear magnetic resonance (<sup>1</sup>H NMR). The conditions of this reaction are depicted in Scheme 2.5 and the resulting NMR spectra of the crude reaction mixture after 1 hour is displayed in Figure 2.9.

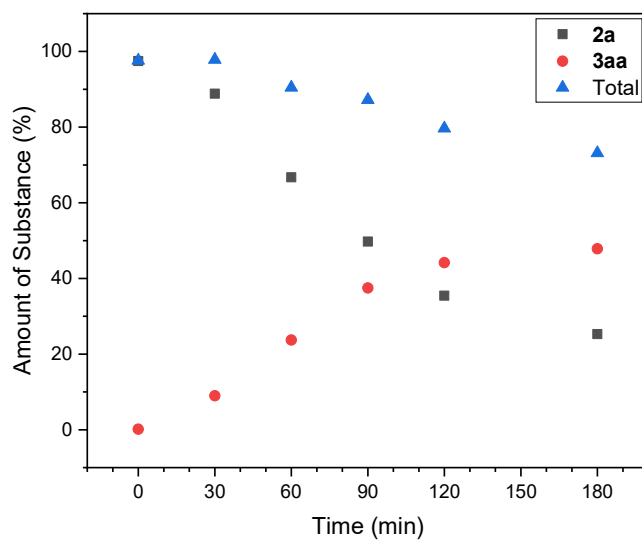
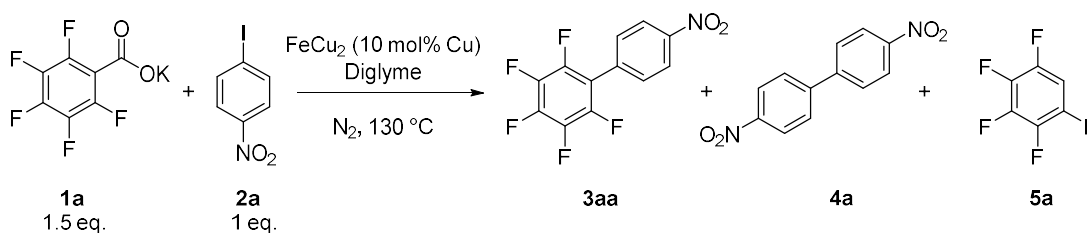


Figure 2.8: Kinetic profile of the DCC reaction of **1a** and **2a**, catalysed by heterogeneous catalyst **FeCu<sub>2</sub>** under the conditions depicted in Scheme 2.4. Values determined via HPLC.

Using literature values for <sup>1</sup>H NMR characterisation of compounds **2a**<sup>124</sup>, **3aa**<sup>33</sup>, **4a**<sup>125</sup> and **5a**<sup>126</sup>, as well as reference compounds, full assignment of the NMR trace displayed in Figure 2.9 was achieved. Comparing the integrals for the peaks corresponding to compounds **2a**, **3aa** and **4a** it is observed that these compounds are present at time = 1 hour in the ratio of 70:27:3, showing good agreement with the kinetic profile displayed in Figure 2.8.



Scheme 2.5: **FeCu<sub>2</sub>**-catalysed DCC reaction between **1a** and **2a**, depicting observed side products **4a** and **5a**.

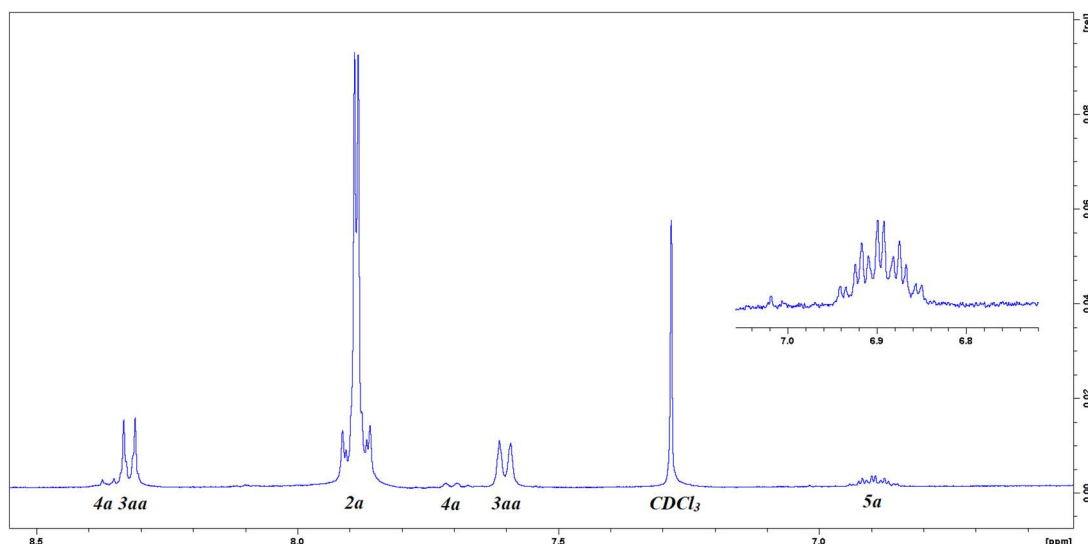
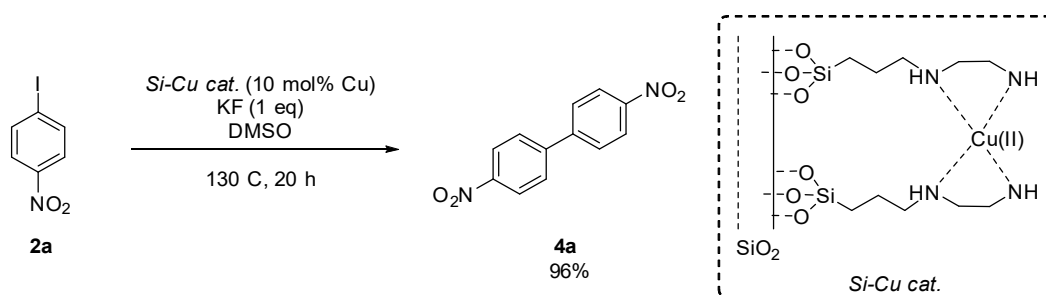


Figure 2.9: Fully assigned  $^1\text{H}$  NMR of reaction depicted in Scheme 2.5 after 1 hour (400 MHz,  $\text{CDCl}_3$ ). Inset: characteristic triplet of triplet of doublets (ttt) arising from coupling between  $^1\text{H}$  and  $^{19}\text{F}$  spin  $\frac{1}{2}$  nuclei of side-product **5a**.

Given the presence of copper in the catalyst chosen for this reaction, the presence of compound **4a** is likely due to the copper-catalysed Ullmann homocoupling of starting material **2a**. Such a reaction is typical of Ullmann coupling<sup>1,2</sup> and the homocoupling of **2a** has been reported in the literature under very similar conditions to those used in Scheme 2.5 (see Scheme 2.6)<sup>127</sup>.

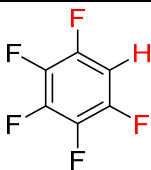
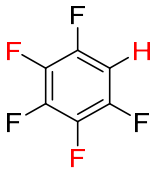


Scheme 2.6: Wu's copper-catalysed Ullmann homocoupling of **2a** in the presence of a potassium base at 130 °C<sup>127</sup>.

Interestingly, the  $^1\text{H}$  NMR trace displayed in Figure 2.9 reveals the presence of another side-product. A peak with a multiplet pattern of a triplet-of-triplet-of-doublets is observed at 6.89 ppm, corresponding to the single proton of pentafluorobenzene (**5a**) coupling with the various  $^{19}\text{F}$  nuclei on the aromatic ring. Analysis of this multiplet is shown in Table 2.3.

**5a** is present as a side-product under these conditions due to catalyst **FeCu<sub>2</sub>** also promoting the protodecarboxylation of starting material **1a**. This phenomenon has been widely reported in the literature <sup>16,19,27,27,45</sup>. Indeed, it has been reported by Goossen that highly activated carboxylates such as **1a** show a particular tendency to undergo protodecarboxylation, even in the absence of a transition metal catalyst <sup>17</sup>. It is worth noting however that while Figure 2.9 allows for the qualitative assertion that protodecarboxylation side-product **5a** is present, the data cannot be utilised in a quantitative manner. This is because **5a** is a volatile compound with a boiling point of 85 °C meaning that under the conditions of the experiment (see Scheme 2.5) **5a** would rapidly boil off.

Table 2.3: Analysis of the first order multiplet observed at 6.89 ppm in the <sup>1</sup>H NMR trace displayed in Figure 2.9.

Assignment	Multiplet	Observed Coupling Constant (Hz)
	<sup>3</sup> J <sub>H-F</sub> Triplet	10.0
	<sup>4</sup> J <sub>H-F</sub> Triplet	6.8
	<sup>5</sup> J <sub>H-F</sub> Doublet	2.8

For protodecarboxylation to occur, there must be a source of labile protons available within the system. As care has been taken to eliminate such protons from chosen reagents and solvents, the prime suspect would be the presence of trace amounts of water within the reaction mixture. At the time of experimentation, anhydrous diglyme was not commercially available, and therefore the diglyme used for the experiments described within this work was dried and stored over activated molecular sieves with an average pore size of 4 angstroms under an atmosphere of inert gas such as nitrogen or argon. Samples before and after this drying process

were collected and analysed *via* Karl Fischer titration to determine water content, the results of which are displayed in Table 2.4.

*Table 2.4: Effectiveness of drying diglyme over 4 Å molecular sieves, determined via Karl Fischer titration.*

	Sample Weight (g)	Observed H <sub>2</sub> O (g)	H <sub>2</sub> O Content (%)
<b>Before Drying</b>	2.0404	0.0007	0.03
<b>After Drying</b>	2.4816	0.0003	0.01

The drying method was observed to be successful, with a total reduction in water content observed in the sample of 67 %. However, trace quantities of water remained.

### 2.3.1. Reaction Optimisation

The presence of Ullmann homocoupling as a side-reaction, even in the case of the best performing catalysts CuI and **Cu(mono)**, was an undesirable outcome. However, the rate of homocoupling compared to that of the desired DCC reaction was observed to heavily favour DCC (see Figure 2.9). Therefore, it was hypothesised that with modifications to the initial reaction conditions it may be possible to suppress Ullmann homocoupling altogether. To investigate this, two studies were performed where reaction temperature and catalyst loadings were varied, keeping all other variables constant. The catalyst chosen for these investigations was the iron/copper bimetallic catalyst **FeCu<sub>2</sub>** as the potential to find conditions that allow for successful DCC reactions at lower temperatures would be of significant relevance to induction heating focused studies, where heat and energy transfer would be a primary concern. These experiments were monitored by HPLC over 5 hours and the results are displayed in Figure 2.10 and Figure 2.11 respectively.

As can be inferred from Figure 2.10, successful DCC reactivity is observed at temperatures lower than reported in the literature<sup>33,123</sup>, although as temperature is reduced so too is the initial rate of reaction. Figure 2.11 shows that increasing the loading of copper catalyst in the reaction lead to faster initial rates of reaction, with

30 mol% copper yielding 54 % **3aa** after just 1 hour – outperforming the 10 mol% system even after 5 hours.

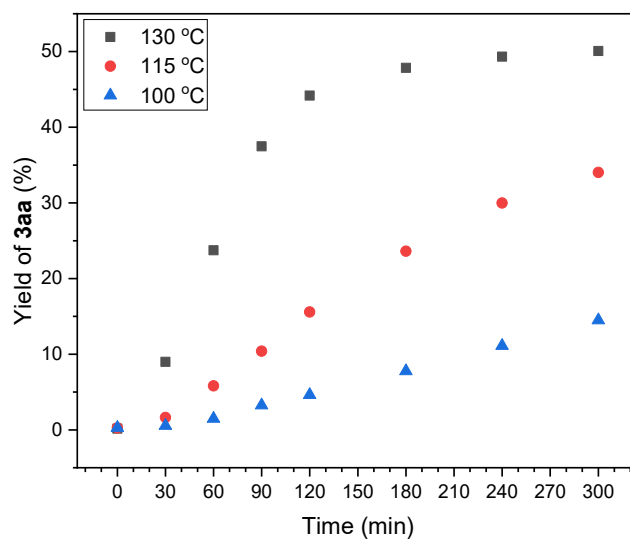


Figure 2.10: Plot describing the effect varying reaction temperature has upon the yield of product in a standard DCC reaction. Conditions: **1a** (1.5 mmol), **2a** (1 mmol), **FeCu<sub>2</sub>** (0.1 mmol Cu), diglyme (4 mL) and biphenyl (0.1 mmol) as internal standard.

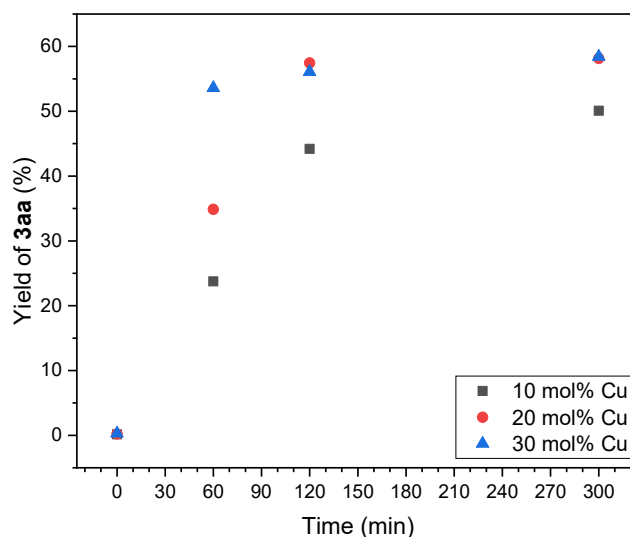
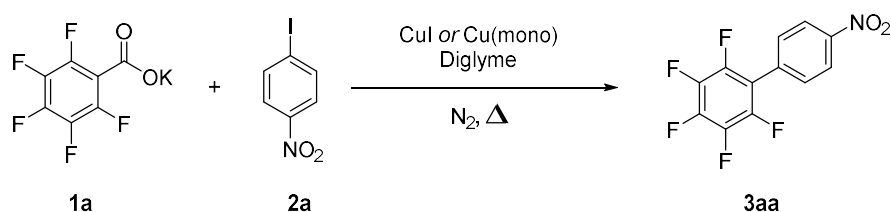


Figure 2.11: Plot describing the effect varying the loading of copper-containing catalyst has upon the yield of product in a standard DCC reaction. Conditions: **1a** (1.5 mmol), **2a** (1 mmol), **FeCu<sub>2</sub>** (0.1-0.3 mmol Cu), diglyme (4 mL) and biphenyl (0.1 mmol) as internal standard. Temperature was held at 130 °C.

With these results in hand the next logical step was to revisit the conditions described in Scheme 2.4 and modify them, reducing reaction temperatures from 130

°C to 100 °C and increase loadings of copper from 10 mol% to 30 mol% in an attempt to compensate for the loss of reactivity caused by lowering temperatures. The best performing copper catalysts, CuI and **Cu(mono)**, were chosen for this investigation, the results of which are displayed in Table 2.5

Table 2.5: A comparison between high temperature and low temperature approaches. Reaction conditions: **1a** (1.5 mmol), **2a** (1 mmol), diglyme (4 mL), performed under nitrogen. <sup>a</sup> Determined via HPLC using biphenyl (0.1 mmol) as an internal standard. <sup>b</sup> Between **2a** and **3aa**.



Entry	Catalyst	Loading (%)	Temp. (°C)	Time (h)	<b>2a</b> Remaining (%) <sup>a</sup>	<b>3aa</b> Yield (%) <sup>a</sup>	Total (%) <sup>a b</sup>
1	CuI	10	130	5	4	86	90
2	CuI	30	100	5	17	81	98
				24	11	75	86
3	Cu(mono)	10	130	5	13	75	88
4	Cu(mono)	30	100	5	56	42	98
				24	19	75	94

In the case of popular literature catalyst CuI, a comparison between entries 1 and 2 from Table 2.5 reveals that the modifications to catalyst loadings and temperature do have a negative impact on the production of **3aa** after 5 hours, with a 5 % decrease in observed yield. However, when considering **3aa** yield alongside remaining starting material **2a** it becomes apparent that the modified reaction conditions have achieved their goal – side reaction prevalence has been reduced. Knowing that lower reaction temperatures lead to a slower rate of DCC (see Figure 2.10) it was decided another sample after 24 hours should be taken to gain insight into the end point yield under these modified conditions. Curiously, this revealed that product **3aa** is slightly unstable under the conditions shown in entry 2, with the yield of **3aa** falling 6 % during this time.

A much more pronounced difference between initial and modified conditions was observed when utilising the heterogeneous copper catalyst **Cu(mono)**. Comparing entries 3 and 4 from Table 2.5 it can be observed that after 5 hours the yield of **3aa** is considerably lower under the modified conditions. However, as with the literature catalyst CuI a dramatic improvement in side-reaction prevalence is observed, with the sum of the observed molar quantities of **2a** and **3aa** accounting for 98 % of the initial loading of starting material **2a**. Unlike the CuI system, however, greater suppression of side reactions compared to the initial conditions is observed even after 24 hours. **3aa** yield was also observed to increase during this time, reaching parity with **3aa** yield under the initial conditions.

Such findings confirm the hypothesis that pursuing reaction conditions that utilise lower reaction temperatures would yield greater suppression of the unwanted Ullmann homocoupling side reaction.

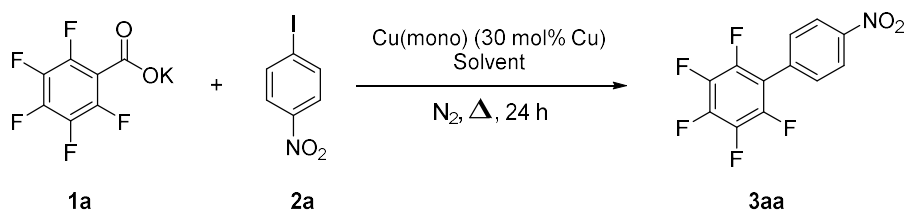
### 2.3.2. Solvent Scope and the Role of Diglyme

A notable observation in the literature surrounding DCC chemistry is the sensitivity it displays towards changes in reaction conditions, particularly solvent choice. Shang reports that the coupling of polyfluorobenzoate **1a** proceeds particularly well in the polar aprotic solvent diglyme. Deviation from this solvent with this substrate was observed to dramatically reduce product yields<sup>33</sup>. This finding is supported in the literature<sup>123</sup>. Given its polar aprotic nature, coupled with its high boiling point (168 °C), it is not surprising that diglyme serves as a good solvent for DCC protocols given the high reaction temperatures demanded and sensitivity of the organo-copper reaction intermediate to labile protons. However, there are a variety of solvents that display similar parameters and yet diglyme is observed to be superior. Zhao posits that the reason behind this is due to the structure of diglyme enabling it to coordinate to potassium ions and thus facilitating the coordination between copper catalyst and benzoate anion<sup>123</sup>, an assumption also adopted in Shang's original study<sup>33</sup>. Tang *et al.* corroborate this hypothesis reporting that diglyme, due to its structural similarity to crown ethers, displays a particular affinity for chelating small cations<sup>128</sup>.

However, the use of diglyme introduces several health concerns. It causes minor irritation in contact with skin, and shows low levels of acute toxicity after exposure

due to inhalation or oral intake <sup>128</sup>. The main danger surrounding the use of diglyme, however, is that it displays high degrees of reproductive toxicity towards males and is a known teratogen, causing a variety of dose-dependent effects on the unborn foetuses of rats, rabbits and mice such as reduced foetus weight, resorption and malformation of foetal tissues <sup>129</sup>. Exposure to similarly structured solvents such as ethylene glycol dimethyl ether (glyme) has been linked to atrophy of the thymus gland, bone marrow suppression and degeneration of testicular tissues <sup>130</sup>. Indeed, the risks surrounding the use of solvents within the ‘glyme family’ were deemed severe enough that notable government bodies around the world have placed severe restrictions and regulations on their use <sup>128,131</sup>. With these concerns in mind, the use of alternative solvents is a highly desirable prospect.

Table 2.6: Exploring solvent scope. Reaction conditions: **1a** (0.75 mmol), **2a** (0.5 mmol), **Cu(mono)** (0.15 mmol Cu), solvent (2 mL). <sup>a</sup> Determined via HPLC using biphenyl (0.05 mmol) as an internal standard. <sup>b</sup> Performed under reflux.



Entry	Solvent Choice	Temperature (°C)	Time (h)	3aa Yield (%) <sup>a</sup>
<b>1</b> <sup>b</sup>	1,4-Dioxane	100	5	0
			24	1
<b>2</b>	DMF	100	5	7
			24	8
<b>3</b>		130	5	5
			24	5
<b>4</b>	DMSO	100	5	20
			24	19
<b>5</b>		130	5	16
			24	11

When choosing alternative solvents, there were several issues to consider. The solvent had to be aprotic so as to suppress protodecarboxylation. Solvent choice was also limited by the reaction temperature of 100-130 °C. Working within these constraints, three solvents were chosen to investigate: 1,4-dioxane, dimethylformamide (DMF), dimethyl sulfoxide (DMSO). Dioxane was chosen

primarily due to its structural similarities to diglyme, containing ether groups that may coordinate to potassium ions and help facilitate the formation of the copper-benzoate complex per Zhao's hypothesis. DMF and DMSO on the other hand were chosen due to being polar aprotic solvents with less severe health risks than diglyme. These were screened at both 100 °C and 130 °C, utilising **Cu(mono)** at 30 mol% loading as catalyst. The results of these experiments are summarised in Table 2.6.

Of the three solvents chosen, DMSO was observed to perform the best, reaching a yield of DCC product **3aa** of 20 % after 5 hours under the low temperature conditions developed from Table 2.5. Indeed, both DMSO and DMF solvated systems were observed to perform better under the low temperature protocol when compared to 130 °C. Due to the boiling point of 1,4-dioxane (101 °C), it was not possible to study the solvent system under the high temperature conditions. As was noted in Table 2.5, reduction in observed yield of DCC product **3aa** over time was observed when utilising DMSO as solvent. Crucially, it's worth noting that all systems investigated underperformed relative to their literature analogue, diglyme, with all other variables held constant (see Table 2.5, entry 4).

These findings would seem to lend credence to the observations of Zhao that diglyme serves a special function during the DCC reaction that enables greater reactivity in DCC protocols. Zhao hypothesises that this is due to the chelating properties of diglyme enabling it to abstract potassium ions from potassium benzoate substrate **1a**<sup>123</sup>, facilitating the formation of the copper-benzoate complex **Int. 1** (see Figure 2.12). Using density functional theory (DFT) calculations, Shang reports that decarboxylation of metal-benzoate complexes to yield organometallic intermediate species with structures similar to **Int. 2** is the rate determining step for copper DCC chemistry<sup>33</sup>. Therefore, the rate of reaction would depend on the concentration of reaction intermediate **Int. 1**. It would then follow that, assuming the concentration of starting material **1a** wasn't limited by solubility, an increase in the rate of the coordination step would result in a greater concentration of **Int. 1** and therefore a faster rate of overall reaction.

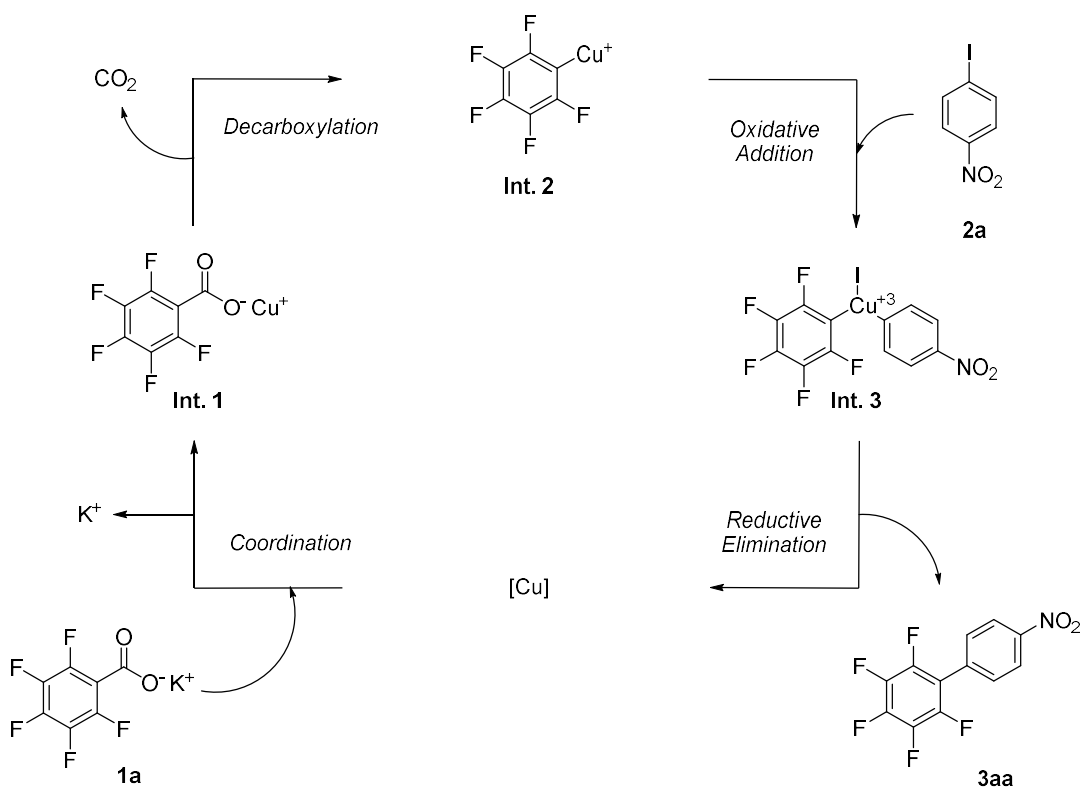


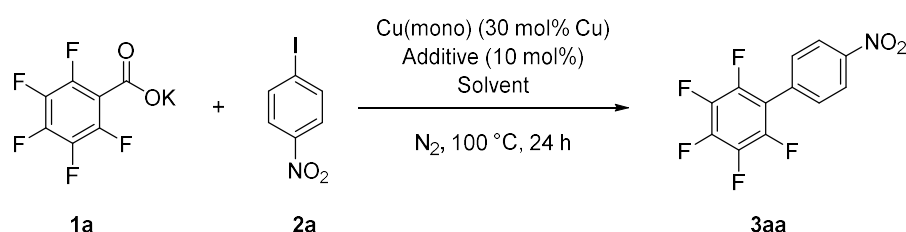
Figure 2.12: Hypothetical mechanism for the copper catalyzed DCC reaction of **1a** and **2a**, adapted from DFT studies performed by Shang et al.<sup>33</sup>.

To investigate further, DMF and DMSO solvent systems were revisited under the same conditions, save for the inclusion of 10 mol% diglyme as an additive. If diglyme truly facilitates the formation of reaction intermediate **Int. 1** then it would be expected to improve reactivity in these systems. Further, it would follow that any additive capable of abstracting potassium ions would elicit a similar improvement in reactivity. To test this hypothesis, experiments including 10 mol% of the crown ether 1,4,7,10,13,16-hexaoxacyclooctadecane (18-crown-6) as additive were also performed. This compound was chosen as it has been well documented to display an affinity for potassium ion coordination<sup>132</sup>. These investigations were performed at 100 °C and the results are displayed in Table 2.7.

Comparing Table 2.7, entry 3 to Table 2.6, entry 4 it is clear that the inclusion of diglyme as an additive in the DMSO solvated system has improved reactivity, with observed yields of DCC product **3aa** increasing two-fold. Reactivity is improved further when 18-crown-6 is utilised, reaching 60 % yield of **3aa** after 5 hours. In contrast to this, the DMF solvated system displayed minor changes in reactivity.

Alongside these experiments a control reaction was performed where 18-crown-6 was utilised as an additive alongside the use of diglyme as solvent. It was hypothesised that this would lead to a negligible change in reactivity compared to the results shown in Table 2.5 as potassium-abstracting additive diglyme would be in vast excess compared to 18-crown-6. As Table 2.7, entry 5 shows, after 5 hours the observed yield of product **3aa** is identical to the yield observed when no additive is utilised.

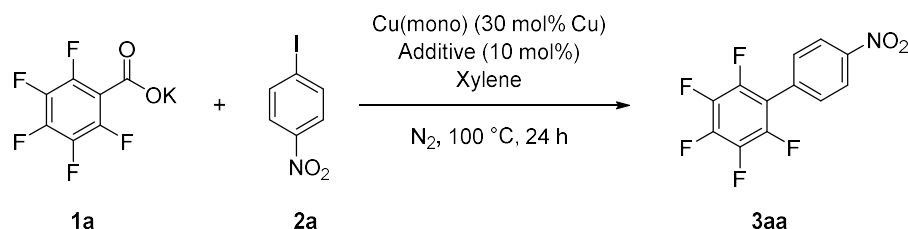
Table 2.7: Probing the role diglyme plays in DCC reactivity. Reaction conditions: **1a** (0.75 mmol), **2a** (0.5 mmol), **Cu(mono)** (0.15 mmol Cu), additive (0.05 mmol), solvent (2 mL). <sup>a</sup> Determined via HPLC using biphenyl (0.05 mmol) as an internal standard.



Entry	Solvent Choice	Additive	Time (h)	<b>3aa</b> Yield (%) <sup>a</sup>
1	DMF	Diglyme	5	4
			24	4
2		18-Crown-6	5	9
			24	11
3	DMSO	Diglyme	5	43
			24	43
4		18-Crown-6	5	60
			24	54
5	Diglyme	18-Crown-6	5	42
			24	48

Use of these potassium-chelating additives was found to promote reactivity even when the non-polar solvent xylene was utilised. This solvent was chosen expressly because its non-polar nature would make dissociation of the potassium ion from the benzoate substrate unfavourable. As is displayed in Table 2.8, modest improvements in yield of **3aa**, compared to a control reaction with no additive, were observed, with a similar trend to the dipolar aprotic solvent experiments (see Table 2.7)

Table 2.8: Chelating additives promoting DCC reactivity in non-polar solvent. Reaction conditions: **1a** (0.75 mmol), **2a** (0.5 mmol), **Cu(mono)** (0.15 mmol Cu), additive (0.05 mmol), xylene (2 mL). <sup>a</sup> Determined via HPLC using biphenyl (0.05 mmol) as an internal standard.



Entry	Additive	Time (h)	3aa Yield (%) <sup>a</sup>
<b>1</b>	No Additive	5	22
		24	23
<b>2</b>	Diglyme	5	27
		24	24
<b>3</b>	18-Crown-6	5	37
		24	34

To rule out the possibility that this improved reactivity was resulting simply due to improved solubility of starting material **1a** in diglyme compared to best performing competitor DMSO, two experiments were set up wherein **1a** and either diglyme or DMSO were heated to 100 °C per the conditions used in Table 2.6 and Table 2.7 for 1 hour. The reaction mixture was then allowed to settle before samples were drawn off and diluted in deuterium oxide (D<sub>2</sub>O) spiked with a known concentration of sodium fluoride. These samples were then analysed *via* <sup>19</sup>F NMR to determine the solubility of **1a** under DCC reaction conditions. The results of this investigation are displayed in Table 2.9, and clearly show that observed solubility of **1a** in diglyme is considerably poorer than in DMSO. Such a finding is supported by the anecdotal observation that, when utilising diglyme as solvent, the reaction mixture is not a clear solution, rather an opaque, viscous slurry (see Figure 2.13).

Table 2.9: Determining solubility of **1a** in various solvents. Conditions: **1a** (0.75 mmol), solvent (2 mL), heated to 100 °C for 1 hour before being sampled. Followed by <sup>19</sup>F NMR (376 MHz, D<sub>2</sub>O) utilising sodium fluoride as an internal standard.

Entry	Solvent	Theoretical Maximum Conc. (M)	Observed Conc. (M)
<b>1</b>	Diglyme	0.375	0.003
<b>2</b>	DMSO	0.375	0.272

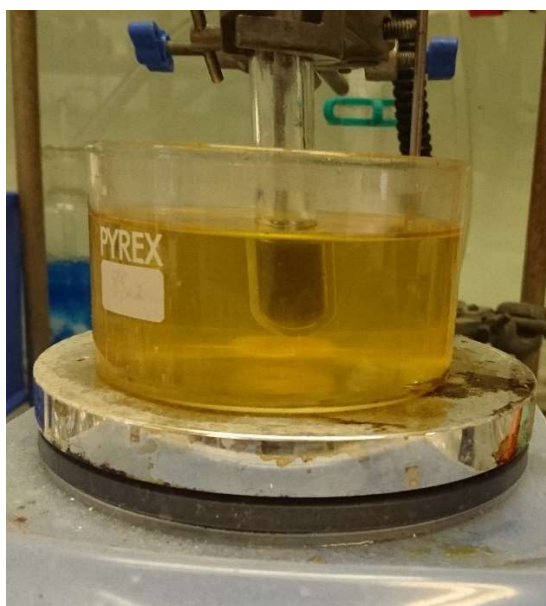
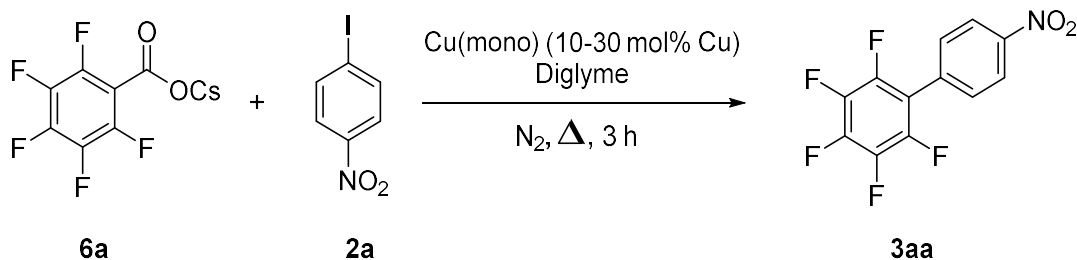


Figure 2.13: Typical diglyme-solvated DCC reaction in progress. Note the opaque colouration of the reaction mixture.

### 2.3.3. Exploring the Effect of Varying Substrate Counter-ion

With evidence pointing towards the idea that facilitating the coordination step to produce copper benzoate complex **Int. 1** (see Figure 2.12) leads to better DCC reactivity, and therefore higher yields of product, it was prudent to explore a variety of routes towards improving this reaction step. The use of chelating solvents such as diglyme was found to have a pronounced effect on reactivity, but this is not the only way of achieving this result. Another approach would be to switch the counter-ion of the benzoate substrate from potassium to caesium. Given the lower charge density of the caesium cation compared to the potassium cation, it can be expected that the activation energy of the dissociation of caesium benzoate would be lower than that of potassium benzoate, leading to a comparatively faster rate of dissociation.

To investigate this, caesium pentafluorobenzoate (**6a**) was incorporated into the model DCC reaction with **2a** to yield product **3aa** that has been investigated throughout this work (see Scheme 2.7). This allows for direct comparison between potassium and caesium containing systems. **Cu(mono)** was chosen as the catalyst for these investigations, and both reaction temperatures and catalyst loadings (with respect to copper content) were varied. These experiments were followed *via* HPLC and the results are displayed in Figure 2.14 and Figure 2.16.



*Scheme 2.7: Model DCC protocol utilising caesium benzoate substrate*

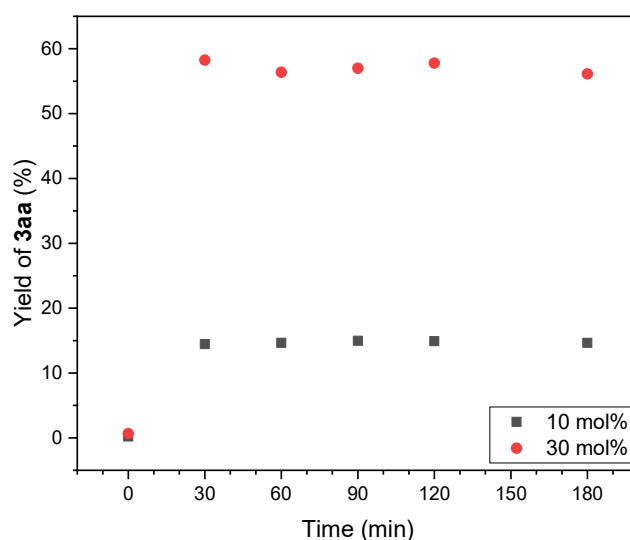


*Figure 2.14: Kinetic profiles for the reaction of **6a** and **2a** at 130 °C with differing loadings of catalyst. Values determined via HPLC. Conditions: **6a** (0.75 mmol), **2a** (0.5 mmol), **Cu(mono)** (0.05-0.15 mmol), diglyme (2 mL) and biphenyl (0.05 mmol) as an internal standard.*

At 130 °C, it was observed that the use of caesium substrate **6a** led to a dramatically increased initial rate of reaction compared to its potassium analogue **1a**. Irrespective of catalyst loading, the reaction was observed to cease after only 30 minutes (see Figure 2.14). This reaction time is comparable to the use of **1a** at 130 °C, utilising **Cu(mono)** as catalyst (10 mol% loading with respect to copper), in which reaction completion was reached after 120 minutes (see Figure 2.7). Interestingly, this improved reaction rate did not also manifest as an improved end-point yield of DCC product **3aa**. Utilising 10 mol% **Cu(mono)**, end-point yield was observed to be 15 %, a fivefold decrease in observed yields compared to similar conditions utilising potassium substrate **1a** (see Figure 2.7). Increasing catalyst loading improved this

figure, however performance with respect to **3aa** yield still fell below the potassium containing reaction system.

The apparent cessation of DCC reactivity after 30 minutes is not caused by complete consumption of reagent **2a**, however. A thorough examination of the experiment performed at 130 °C, catalysed by 30 mol% of **Cu(mono)**, reveals that at the 30-minute mark, 33 % of the initial loading of **2a** is observed within the reaction mixture. After 30 minutes the observed concentration then falls at a slow rate, relative to the sharp reduction in concentration observed from experiment start to the 30-minute mark. Using the sum of the observed quantities of **2a** and **3aa** as a gauge on Ullmann homocoupling side reaction prevalence it can be observed that, as when utilising potassium substrate **1a**, consumption of **2a** through side processes is present. But at the 3-hour mark, 27 % of the initial loading of **2a** is present even with the consumption of **2a** through side reactions. Such an observation suggests that, by the 30-minute mark the reaction is halts because the system has run out of caesium substrate **6a**, despite the fact that **6a** is present in excess at reaction start.

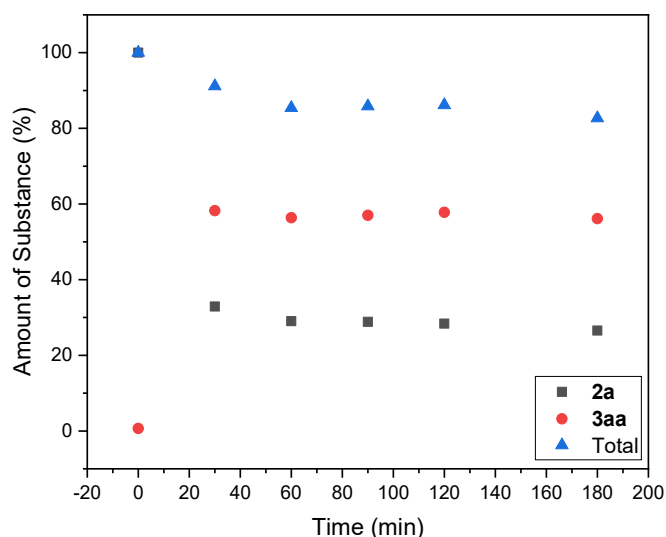


*Figure 2.15: Kinetic profile of the DCC reaction of **6a** and **2a** at 130 °C, catalysed by the heterogeneous catalyst **Cu(mono)**. Values determined via HPLC. Conditions: **6a** (0.75 mmol), **2a** (0.5 mmol), **Cu(mono)** (0.15 mmol Cu), diglyme (2 mL) and biphenyl (0.05 mmol) as an internal standard.*

To attempt to remedy this, reaction temperatures were reduced from 130 °C to 100 °C. However, as was observed in Figure 2.10, this led to substantial decreases in

DCC reactivity. The results of these experiments are displayed in Figure 2.16. Thermal decomposition of carboxylic acids is a known phenomenon. As Goossen observed, potassium substrate **1a** shows reactivity towards protodecarboxylation when in the presence of acidic protons and heat, even in the absence of a catalyst<sup>17</sup>. Yakerson, whilst studying the decomposition of various acetate salts observed that the decomposition point for calcium, strontium and barium acetates were 407, 358 and 328 °C respectively<sup>133</sup>, highlighting a negative correlation between counter-ion size and energy required for decomposition. It therefore follows that in switching the counter-ion of the pentafluorobenzoate substrate from potassium (**1a**) to caesium (**6a**), loss of the benzoate substrate due to thermal decomposition *via* protodecarboxylation could be accelerated.

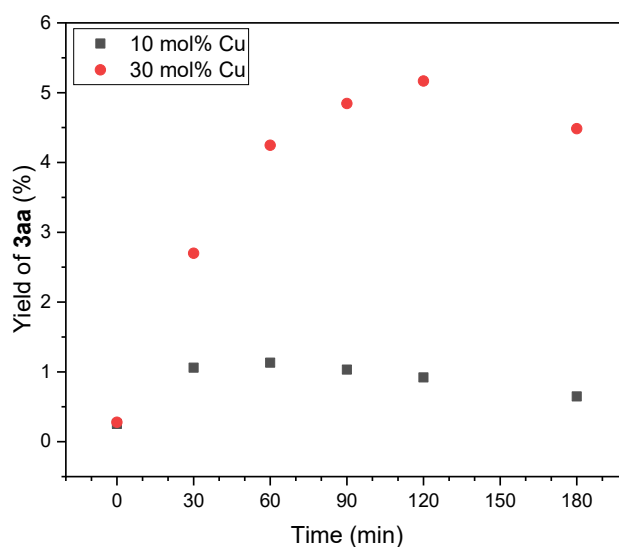


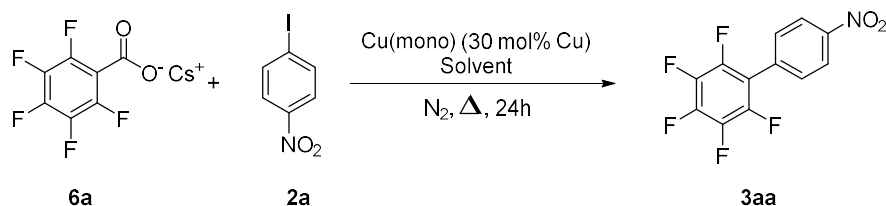
Figure 2.16 Kinetic profiles for the reaction of **6a** and **2a** at 100 °C with differing loadings of catalyst. Values determined via HPLC. Conditions: **6a** (0.75 mmol), **2a** (0.5 mmol), **Cu(mono)** (0.05-0.15 mmol Cu), diglyme (2 mL) and biphenyl (0.05 mmol) as an internal standard.

It is worth noting that these experiments were performed utilising diglyme as a solvent. Diglyme has been noted in the literature for its affinity towards coordination to alkali metal cations, further promoting dissociation of cation and anion, and therefore improving anion reactivity<sup>134</sup>. It is therefore possible that the rapid consumption of caesium substrate **6a** seen in Figure 2.14 is due to the combination of the caesium counter-ion and chelating solvent diglyme. Both of these factors would encourage the dissociation of the benzoate salt and therefore with both factors

working in tandem they could be producing too great a dissociative effect. As Table 2.6 displayed, moving away from diglyme to other solvents had a tempering effect on the reactivity of the system towards DCC, resulting in substantially lowered yields of DCC product **3aa** in the given timeframe. Addition of chelating compounds such as diglyme or 18-crown-6 was required in order to improve reactivity in these cases. To investigate whether the use of caesium as a counter-ion could be used to replace these additives, the reaction of **2a** with caesium substrate **6a** was screened against the same solvents as shown in Table 2.6. This was not observed to be the case. As Table 2.10 shows, low reactivity was observed in all cases, comparable to the results of Table 2.6. Such findings support the idea that the use of caesium benzoate substrates is not amenable to DCC coupling compared to using their potassium analogues.

Table 2.10: Exploring solvent scope with caesium activated substrate.

Reaction conditions: **6a** (0.75 mmol), **2a** (0.5 mmol), **Cu(mono)** (0.15 mmol Cu), solvent (2 mL), performed under nitrogen. <sup>a</sup> Determined via HPLC using biphenyl (0.05 mmol) as an internal standard.



Entry	Solvent Choice	Temp (°C)	Time (h)	3aa Yield (%) <sup>a</sup>
<b>1</b>	1,4-Dioxane	100	5	1
			24	9
<b>2</b>	DMF	100	5	5
			24	9
<b>3</b>		130	5	8
			24	7
<b>4</b>	DMSO	100	5	17
			24	14
<b>5</b>		130	5	12

#### 2.4. Induction Heating as a Novel Approach to Decarboxylative Cross-coupling

The decarboxylative cross-coupling experiments discussed in Section 2.3. all utilised passive heating *via* an oil bath and hot-plate as the source of energy, or

'conventional heating' as it will be referred henceforth. This represents standard operating procedure and is an easy and effective way of applying energy to a reaction. However, as it relies on the passive diffusion of heat throughout the reaction mixture, it is indiscriminate and unselective, requiring the need for an efficient mechanical agitating solution for effective distribution of the radiant energy throughout the reaction mixture. There exist alternative heating methods that display selectivity, applying energy directly where the chemist wishes it to be. Microwave irradiation is one such technique, and there have been several reports highlighting the improvements such an energy source can have upon an organic reaction. It differs fundamentally from conventional heating in that energy transfer is derived from the interaction of electromagnetic radiation with molecules containing a dipole moment. It is therefore a selective energy transfer method, in that only polar compounds will interact with the irradiation in any meaningful way. This has been exploited to selectively heat reaction solvents or even polar catalysts.

Induction heating is another selective method, in that it uses an oscillating electromagnetic field to bring about a rise in temperature within magnetically susceptible materials. However, harnessing this phenomenon for organic reactions is non-trivial. Ceylan has reported a successful approach harnessing induction heating in organic chemistry. The method involves passing reaction mixture through a column packed with ferromagnetic material. The column is placed within an induction coil, and *via* the application of an oscillating electromagnetic field, the reaction mixture is rapidly heated as it passes through the column. This has been utilised both with inert and catalytically active ferromagnetic material and increases in the rate of reaction relative to conventional methods were reported, owing to the increased efficiency of the heat transfer. However, although the energy transfer to the reaction mixture is selective in principle, it is indeed the ferromagnetic material and not the reaction mixture that is heated by the induction field, the method of energy transfer from ferromagnetic material to reaction mixture is unselective – energy radiates from the packed bed, heating the reaction mixture as it passes through. The approach hypothesised in this work is to marry the concepts of induction heating as a selective energy transfer technique and the design of a catalyst to be susceptible to such a selective approach. This would then allow for the

direct and selective promotion of catalysed reactions *via* the use of an inductive field.

In a bulk magnetically susceptible metal, the increase in temperature due to induction heating is caused two phenomena: the generation of eddy currents and magnetic hysteresis losses. As the electromagnetic field oscillates around the metal, it induces small localised currents of electrons within the metallic structure, otherwise known as ‘eddy currents’. These electrons, now flowing, collide into atoms and release energy as heat<sup>135</sup>. If the metallic material also contains magnetic domains, then the oscillating electromagnetic field will cause these domains to reorient themselves. The magnetisation of the material, a vector value that describes the sum of magnetic domain orientation, will increase as the field strength increases until it reach a maximum, known as the magnetisation saturation ( $m_s$ )<sup>136</sup>, wherein all of the domains are aligned with the field (see Figure 2.17).

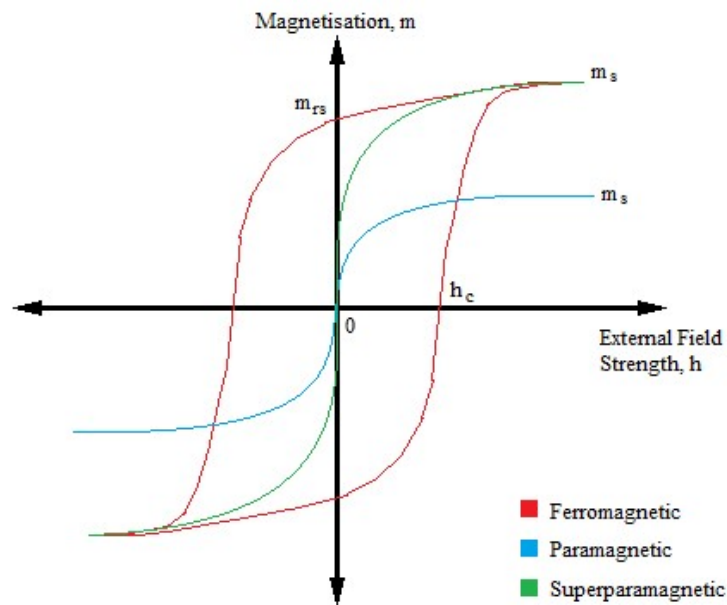


*Figure 2.17: Hypothetical hysteresis loops for ferromagnetic, paramagnetic and superparamagnetic materials for illustrative purposes<sup>137</sup>.*

As the field then begins to oscillate, magnetisation falls, and then becomes increasingly negative. This cycle is known as a magnetic hysteresis loop. In ferromagnetic materials, some degree of magnetisation is retained when the external field strength reaches zero, known as the remnant magnetisation saturation ( $m_{rs}$ )<sup>136</sup>. The energy required to destroy this magnetic ordering is described as the coercivity

( $h_c$ )<sup>138</sup>. As these domains reorient themselves within the metallic structure in response to the alternating electromagnetic field, there is friction between neighbouring domains, which results in loss of energy *via* heat<sup>138</sup>. This heat loss, or ‘magnetic hysteresis loss’, is proportional to the area of the hysteresis loop (the values of  $m_{rs}$  and  $h_c$  describing the degree of friction between domains). Magnetic hysteresis loss is only relevant for magnetic materials below their Curie temperature. This is because as the temperature of the system exceeds the Curie temperature of the metal, the domains within the system have enough energy to fall into a random distribution of alignments – the material becomes paramagnetic, and as a result  $h_c$  and  $m_{rs}$  fall significantly<sup>136</sup>.

When the size of the metal is reduced down to nanometre scale, such as with superparamagnetic iron nanoparticles, an oscillating magnetic field will still bring about a rise in temperature. However, it does so through different mechanisms, referred to as Neel relaxation and Brownian relaxation<sup>52,64</sup>. Neel relaxation is closely related to magnetic hysteresis loss; however it describes the loss of energy as heat as the single domain of a superparamagnetic nanoparticle physically rotates in response to an oscillating electromagnetic field, causing internal structural changes that result in the loss of energy *via* heat<sup>52</sup>. As the system is now comprised of several isolated domains, it becomes possible for the domains to reorient themselves *via* rotation of the particle itself. As a result, an oscillating electromagnetic field causes magnetic nanoparticles to roll and tumble in solution, causing loss of energy as the nanoparticles collide with solvent molecules, a process known as Brownian relaxation<sup>139</sup>. Of course, eddy current and hysteresis loss effects are still present on the nanometre scale. However, quantum confinement inhibits the flow of electrons, giving these particles high resistivity and therefore diminishes the effects of eddy currents. Also due to the superparamagnetic properties of single domain nanoparticles, losses due to magnetic hysteresis are also negligible<sup>52</sup>.

The dominant relaxation pathway is dependent upon the size of the nanoparticles themselves. Fannin and Charles have observed this dependency whilst measuring Neel relaxation times<sup>140</sup>. They report that for magnetite nanoparticles dispersed in a hydrocarbon, only Neel relaxation is observed below 5 nm in size. As particles increase in size beyond this, Brownian effects dominate. Parmar *et al.* have

elaborated upon this in greater detail. They took magnetite nanoparticles of 13 nm and 20 nm in size and dispersed them in viscous glycerol, so as to effectively remove Brownian relaxation contributions to the heat output of the particles<sup>139</sup>. They found the smaller particles to display a much higher specific loss power and, as previous x-ray diffraction experiments had revealed the larger particles to have a disparate crystalline structure (72 % magnetite, 28 % maghemite), they conclude that Neel relaxation becomes dominant below a critical particle size. This critical point is dependent on material, and below it particles display relatively low levels of magnetic anisotropy.

Ghosh *et al.* have probed even further, in a study on the heating efficacy of various magnetite nanoparticles in aqueous media<sup>52</sup>. They synthesised bare magnetite nanoparticles (particle size 20 nm), and magnetite nanoparticles capped with polyethylene glycol (particle size 10 nm) and oleic acid (particle size 5 nm). As to be expected, the inclusion of anti-agglomeration agents produced a smaller average particle size, though it should be mentioned that Ghosh *et al.* only report the size distribution of the oleic acid nanoparticles, which ranges from 3-25 nm, with 5 nm being the most observed. They subjected 100 milligram samples of these particles, suspended in water, to alternating electromagnetic fields, with amplitudes ranging from 100-600 A over 10 minutes. The larger particles significantly outperform the smaller particles at every amplitude bar 100 A, where the smaller particles lead to a 2 °C increase in temperature over the larger system. The higher performance of the larger particles suggest that the Brownian relaxation, predicted to be dominant by the works of Fannin, Charles and Parmar *et al.*<sup>139,140</sup> for nanoparticles of this size, is dependent upon particle size. Ghosh *et al.* also hypothesise that the result could be due to the fact that the 100 milligram sample of the largest particles simply contained more iron, as their surfaces are not coated<sup>52</sup>. However, the polyethylene glycol coated particles show a larger rise in temperature over 10 minutes compared to the smaller oleic acid coated particles, further alluding to the size dependence of Brownian relaxation.

#### 2.4.1. Reactor Design

It was decided to test this hypothesis on the DCC chemistry investigated in Section 2.3. However, in order to utilise induction heating for this use-case, modifications to

the reactor design was necessary. The model DCC protocol calls for the use of an inert atmosphere and anhydrous reaction solvents, as the presence of water would provide an ample source of labile protons for undesirable protodecarboxylation side reactions. The reactor also needs to be able to be placed within an electromagnetic field. Finally, mechanical agitation that does not rely on a rotating magnetic field as is typical in conventional heating methods is required. This is because such an approach requires the use of a ‘stirrer bar’ – a piece of Teflon-coated magnetic material – placed within the reaction mixture. This would be rapidly heated in the presence of an inductive field, potentially causing damage to the stirrer bar or reactor, and would also lead to undesirable radiative heating per Ceylan’s method.

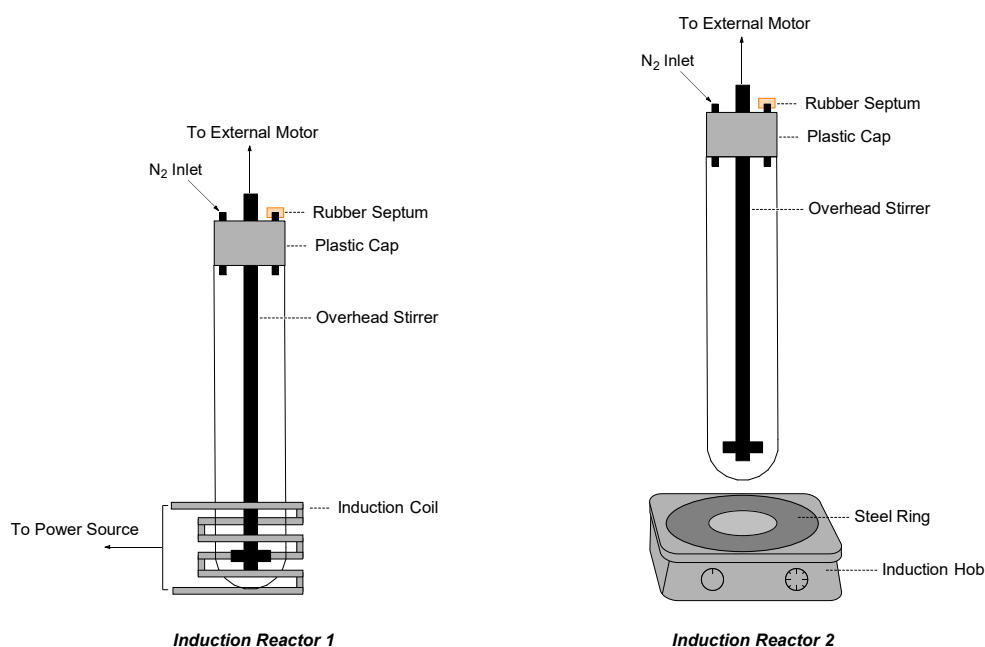


Figure 2.18: Induction heating reactor designs.

To meet these needs, two reactors were investigated which aim to place the reaction system within the magnetic flux of the induction coils. The designs of these reactors are summarised in Figure 2.18. Induction Reactor 1 places the reaction vessel directly within the coils of the induction heater itself, maximising the degree of magnetic flux that the reaction experiences. Mechanical stirring is provided *via* an overhead motor connected to a rod comprised of Teflon, with fins that agitate and move material within the reaction mixture. The coil is powered by an external source supplying 117 W of power. While capable of providing more power, 117 W

represents the safe operational limit of this reactor. The use of higher wattages causes the temperature of not only the power supply unit but the coil (which is internally water cooled) to rise to levels deemed unsafe over the timescales of typical decarboxylative cross-coupling protocols.

With Induction Reactor 2, the low power induction coils are replaced with a commercially available VonShef 2000 W induction hob. The induction coil is contained within the unit and is cooled *via* an internal fan. Whilst allowing for much higher power levels, the unit has a safety feature that prevents the coils receiving power if a significant amount of inductively responsive material is not detected above the unit. To bypass this feature, a steel ring with a diameter comparable to the dimensions of the surface of the hob is placed upon it. The reaction vessel is then suspended above the steel ring, the shape of which allows for some degree of magnetic flux to pass through the vessel without first striking the ring. Although capable of supplying 2000 W of power, this was limited to a maximum of 600 W over a 60-minute timeframe for the scope of these investigations, as higher levels of power caused rapid overheating of the steel ring, triggering a safety cut out. At power levels higher than 600 W, the steel ring was also observed to be moved by the induction field.

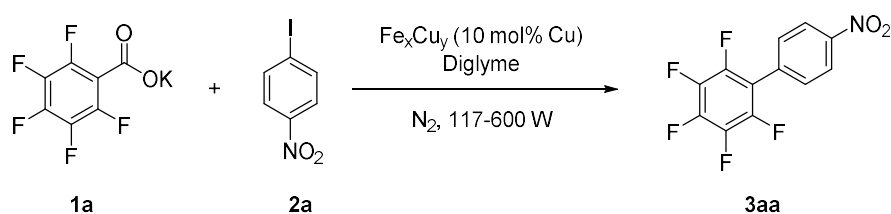
#### 2.4.2. Initial Investigations and Discussion

When choosing what reaction and conditions to target for the initial investigations, the reaction between substrate **1a** and coupling partner **2a** in diglyme (see Table 2.11) represented the best choice, as it has consistently performed better in terms of yield of DCC product **3aa**. However, the reaction is catalysed by copper active sites, which is not an ideal material to use as a vector for induction heating due to its lack of ferromagnetism. As such, pure copper particulate would serve as a poor candidate for these induction heating studies. To alleviate this concern, bimetallic particulate comprised of both catalytically active copper and magnetically susceptible iron were used. The iron would respond to the inductive field, and the heat generated would be transferred to the surrounding copper active sites, promoting reaction.

Iron/copper bimetallic catalysts **Fe<sub>2</sub>Cu**; **FeCu<sub>2</sub>**; and **Fe<sub>4</sub>Cu** were therefore chosen, and these materials were screened against the coupling of **1a** and **2a** utilising

**Induction Reactor 1**, as well as a control reaction wherein the glass vessel containing the reaction mixture was not placed in any induction field, instead being stirred at room temperature for the designated reaction time (see Table 2.11). From these experiments it was observed that over a 5 hour timescale, no reaction is observed to occur using this experimental set-up, no matter the ratio of iron to copper in the catalyst.

Table 2.11: Comparing the performance of various Fe/Cu bimetallic materials as inductively heated catalysts. Reaction conditions: **1a** (1.5 mmol), **2a** (1 mmol),  $Fe_xCu_y$  catalyst (0.1 mmol Cu), diglyme (4 mL), Induction Reactor 1 – 117 W, performed under nitrogen. <sup>a</sup> Determined via HPLC using biphenyl (0.1 mmol) as an internal standard.



Entry	Catalyst Choice	Reactor Choice	Power (W)	Time (h)	3aa Yield (%) <sup>a</sup>
1	<b>Fe<sub>2</sub>Cu</b>	Induction Reactor 1	117	5	0
2	<b>FeCu<sub>2</sub></b>	Induction Reactor 1	117	5	0
3		No Reactor	n/a	24	0
4	<b>Fe<sub>4</sub>Cu</b>	Induction Reactor 1	117	5	0

Given the data displayed in Table 2.11, the first possible explanation is that despite containing an observable quantity of iron (see Table 2.1) the iron/copper bimetallic materials synthesised for use in this work were not susceptible to an electromagnetic field and therefore are unable to be heated *via* induction. To investigate this, the series of materials were analysed using a Guoy balance, which measures the change in sample weight upon the application of an external field, a value which can be extrapolated to determine magnetic susceptibility with respect to mass (see Table 2.12). Samples were measured as a 2 wt% suspension in magnesium sulphate so as to avoid over saturation of the balance.

Table 2.12: Magnetic susceptibility measurements of the iron/copper bimetallic catalyst series compared to known ferrimagnetic iron oxide, magnetite. <sup>a</sup> Measured as a 2 wt% suspension in magnesium sulphate.

Material	Mass Susceptibility, $\chi_g$ (cm <sup>3</sup> g <sup>-1</sup> ) <sup>a</sup>
Magnetite powder (Fe <sub>2</sub> O <sub>3</sub> )	0.0217
<b>FeCu<sub>2</sub></b>	0.0077
<b>Fe<sub>2</sub>Cu</b>	0.0215
<b>Fe<sub>4</sub>Cu</b>	0.0169

To provide context for these measurements, a sample of pure magnetite powder was also analysed as a 2 wt% suspension. As the data shows, in all cases the mass susceptibility is observed to be positive. This indicates that all of the materials investigated are attracted to an external electromagnetic field.

Stirring the reaction at room temperature under nitrogen for 24 hours yields similar results (Table 2.11, entry 3), therefore another possible explanation for this is that 117 W of power is insufficient to drive the energetically demanding decarboxylation step. To test this theory the reaction system utilising catalyst **Fe<sub>2</sub>Cu** was screened at higher power levels with **Induction Reactor 2**. **Fe<sub>2</sub>Cu** was chosen as the catalyst of choice for these investigations as it was observed to possess the greatest magnetic susceptibility (see Table 2.12). As previously discussed, the high-power experiments were limited to between 200-600 W of power over a 1-hour time frame, due to overheating issues with **Induction Reactor 2**. The results of these experiments are summarised in Figure 2.19. Again, the application of an inductive field was unable to drive the decarboxylative cross-coupling reaction. Comparing these results to their conventional heating analogue over similar timeframes reinforces this point (see Figure 2.19).

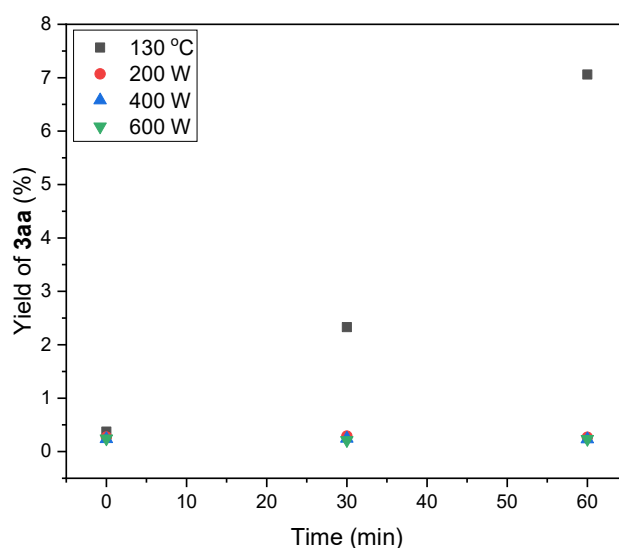


Figure 2.19: A plot comparing the use of conventional heating at 130 °C with induction heating at power levels from 200-600 W for catalyst  $\text{Fe}_2\text{Cu}$  over a 1-hour timeframe. Values determined via HPLC.

## 2.5. Conclusions and Future Work

DCC and associated decarboxylative transformations, both in terms of copper-catalysed systems and more exotic bimetallic catalyst systems, has been routinely identified in the literature as a reaction that shows great promise but is held back by the forcing conditions required to promote it<sup>32,41,141</sup>. Reaction temperatures are typically high relative to other cross-coupling transformations, even in the case of the state of the art copper/palladium and silver/palladium bimetallic catalyst systems investigated by Goossen<sup>13,32</sup> and Larrosa<sup>39</sup>. Catalyst loadings, particularly in the case of copper-catalysed DCC, remain high with 10 mol% loadings of copper being a common reaction condition and loadings greater than 10 mol% being reported less frequently but being reported none the less<sup>17,31,44</sup>. In undertaking this work, the central aim was to glean a deeper, richer knowledge of the DCC reaction and in so doing develop potential solutions to these shortcomings.

To this end, popular and well-cited literature conditions for copper-catalysed DCC were adopted and investigated. Prevalence of side reactions under these conditions was observed and characterised – particularly the presence of an undesirable Ullmann homocoupling of aryl iodide **2a**. Through simple and rudimentary reaction optimisation with regards to reaction temperature and catalyst loadings, it was found

that DCC chemistry could be driven 30 °C lower than reported in literature. Under these low temperature conditions, it was observed that the homocoupling side reaction of reagent **2a** was suppressed considerably. This marks a substantial step forwards for DCC chemistry and will form the basis of future investigations put forward in this thesis. However, this reduction in reaction temperature was observed to reduce the rate of reaction significantly. To compensate, catalyst loading was increased threefold to 30 mol% (with respect to copper). It would therefore be possible to view this as a partial success, one step forwards and one step backwards. Both reaction temperature *and* catalyst loading were identified as problem points, after all, and to reduce one whilst still maintaining acceptable reactivity the other must be exacerbated. However, from these investigations it is clear that, of the two parameters it is temperature that plays the greater role in reducing the viability of the DCC reaction. In lowering reaction temperatures, side reactions are suppressed, leading to greater efficiency. Whilst a threefold increase in catalyst loading is substantial, popular literature catalyst CuI is inexpensive and readily commercially available. As an alternative, the copper heterogeneous material synthesised for this work, **Cu(mono)** is another easily accessible option, prepared from a simple reduction of copper salts.

Future work in this line of investigation, however, will need to focus on catalyst loading as well as reaction temperatures. It is possible that need to increase catalyst loading to compensate for lower reaction temperatures is a constraint imposed by limiting catalyst design to copper. State-of-the-art approaches to DCC chemistry pair copper or silver with palladium to great effect, boasting improved viability particularly in the case of substrate scope. These reported systems however typically display similar issues to monometallic copper approaches – high reaction temperatures and catalyst loadings. There is therefore scope to take what was learned in this work and apply it to bimetallic DCC protocols.

As well as reaction temperature and catalyst loading, solvent choice was also identified as unideal. The dipolar aprotic solvent diglyme was found in literature to be an excellent solvent for the reaction of fluorinated carboxylic acid derivative **1a** with aryl halides such as **2a**. However, the use of diglyme brings with it a number of key health concerns and there is pressure from several regulatory bodies worldwide

to reduce or eliminate the use of glyme solvents. To continue efforts to improve the viability of DCC protocols, work was performed to investigate the scope for moving away from diglyme as solvent. This work was met with mixed success. Several solvent systems were investigated, all of which underperformed considerably compared to diglyme. Switching focus from trying to replace diglyme to trying to understand its importance, it was determined that small additions of diglyme to DCC reaction mixture invariably improved reactivity. This improvement was found to not be a solubility issue and therefore suggests that the improved reaction performance observed with the addition of diglyme is due to diglyme playing a role in the reaction itself. Diglyme was observed to have a similar effect on reactivity as the crown ether 18-crown-6, and therefore it is hypothesised that diglyme plays an active role in encouraging the formation of a copper-benzoate complex that goes on to decarboxylate and participate in the wider DCC mechanism. Such a hypothesis is supported by further investigations performed wherein counter-ion identity of the benzoate substrate was varied. The larger counter-ion caesium was observed to yield reduced reaction performance compared to its smaller, less stable analogue potassium – despite the fact that such a counter-ion switch would be expected to lead to greater solubility of the benzoate substrate.

Thought this investigation was thorough, there is much scope for further work. Two counter-ions were investigated and a screening experiment looking at other counter-ions would enrich this study. Also, it is possible that the reduced reactivity observed when utilising caesium substrate **6a** compared to potassium substrate **1a** could be explained by a lack of affinity for interaction between caesium and diglyme. Crown ether 18-crown-6 is ideal for potassium abstraction due to the size of its ring structure correlating well with the size of the potassium ion. It is known in literature that the size of a crown ether influences the cations it will selectively bind to, with 15-crown-5 displaying affinity for sodium cations and 12-crown-4 selectively binding to lithium cations. Therefore, a study looking at the coupling of caesium substrate **6a** with larger crown ethers such as dibenzo-18-crown-6 or diaza-18-crown-6, as well as larger glyme-type solvents, would be a logical next step.

Finally, induction heating of magnetically susceptible catalysts was considered as a novel solution, allowing for the high energy DCC reaction to be selectively

promoted upon the catalyst surface. Such work, if successful, would find much application in other areas of chemistry. To this end a suite of iron/copper bimetallic catalyst candidates were synthesised *via* a simple co-reduction route. These catalysts were characterised *via* several techniques and were observed to display ratios of iron and copper in good agreement with what was expected given the loading of precursor salts. Oxidation was observed, however, and through a combination of SEM and EDX mapping experiments it was determined that although for the most part copper and iron were well distributed upon the catalyst surface, there existed areas of high concentration of either iron or copper. These materials were observed to elicit DCC reactivity under conventional reaction conditions but failed to promote DCC when utilising induction heating. These materials, through magnetochemistry measurements, were determined to be susceptible to influence by an external magnetic field and therefore given the findings from the EDX mapping analysis one possible explanation for this is poor thermal transfer from areas of high iron content to areas of high copper content upon the bimetallic catalysts surface.

The investigations into this subject can be considered to be preliminary, with a great deal of scope for future work. Refinement of catalyst synthesis is one key area. From prior work performed by Nguyen *et al.* it was observed that the presence of organic capping molecules designed to bind to particulate surface and control growth lead to reduced reactivity in an induction-powered Suzuki coupling utilising an iron oxide/palladium bimetallic catalyst. Therefore, the use of such compounds was omitted in this work. From SEM and EDX mapping analysis this was found to yield material with a great deal of polydispersity with respect to size, shape and distribution of metal upon the catalyst surface. Future work in this area would concern itself with incorporating capping molecules into the synthesis such as poly(vinylpyrrolidone) or poly(ethylene glycol), two polymers with a great deal of literature reports supporting their use in metal particulate growth control.

It would also be logical to further iterate on the design of the induction reactors explored within this work. Each had positive and negative traits. **Induction Reactor 1** placed the reaction mixture directly within the induction coils, ensuring maximum magnetic flux was intercepting the reaction mixture. However, cooling was inadequate, limiting the maximum power output. **Induction Reactor 2** possessed

greater potential energy output but the design of the reactor necessitated the reaction mixture be placed outside of the induction coils. A potential Induction Reactor 3 would revisit the design of **Induction Reactor 1**, maximising magnetic flux, but would utilise better cooling. The coils of **Induction Reactor 1** were water cooled, but the internal electronics passively cooled. Incorporation of air cooling may enable for greater safe energy output. Another potential induction reactor design may take inspiration from the works of Ceylan<sup>64,142</sup> and Zadrazil<sup>143</sup>, using a packed-bed type reactor comprised of a non-ferrous column containing magnetically susceptible catalyst (either unsupported or supported) placed either within **Induction Reactor 1** or over **Induction Reactor 2**. A primary concern that came out of the work presented was that the relatively minimal amount of magnetically susceptible material present within these reactions (compared to typical induction heating applications) was responsible for the poor reactivity. This would be a potential solution to that problem but runs the risk of promoting reactivity unselectively *via* passive heat diffusion from the densely packed column to the reaction mixture flowing through it.

### 3. Bimetallic Nanoparticles as Catalysts for Decarboxylative Cross-coupling

#### 3.1. Introduction

Transition metals play an extremely important role in the field of catalysis. Through them, a myriad of key chemical transformations are made achievable. Typically, they are utilised either homogeneously (in the form of transition metal complexes) or heterogeneously (in a variety of forms, including powders and metallic sponges or foams). In recent years, however, there has been a rising interest in exploring the use of nanoscale particulate of transition metals as catalysts<sup>48</sup>. When compared to their larger, heterogeneous analogues, a greater proportion of the metal atoms within a nanoparticle catalyst exist on the catalyst surface. This is often cited as reason for improved catalytic activity observed when utilising these materials as catalysts<sup>66,144</sup>. The size and shape, and therefore catalytic activity, of nanoparticles is dependent upon the conditions of their synthesis, affording them a high degree of tuneability. This combination of catalytic activity and tuneability makes nanoparticles attractive targets for catalyst design.

Decarboxylative cross-coupling (DCC) is an emerging transition metal catalysed carbon-carbon bond forming reaction<sup>17,31,44</sup>. Derived from older copper-based Ullmann chemistry, it has received much attention due to the prospect of being able to use carboxylic acids in lieu of more traditional organometallic coupling partners typically observed in carbon-carbon coupling chemistry. Carboxylic acids are easy to handle and store, as well as being cheap and widely available through both natural and synthetic routes.

Catalysts typically employed in decarboxylative cross-coupling protocols are based around copper, silver and palladium<sup>17</sup>. Through interaction with these metals, organometallic species suitable for cross-coupling are generated *in-situ via* the extrusion of CO<sub>2</sub>. Early works focused upon the use of copper<sup>16,20,22</sup>, however due to the seminal works of Goossen and his group<sup>13,32</sup> there has been a surge of interest in the use of copper-palladium and silver-palladium bimetallic catalyst systems. This approach has the advantage of transferring the burden of mediating the coupling step from copper or silver to palladium – a transition metal that is widely reported to facilitate such reactions<sup>145</sup>.

However, DCC protocols are not without their shortcomings. High reaction temperatures and loadings of homogeneous catalysts are often required to drive the DCC transformation<sup>146</sup>. Such conditions lead to reduced functional group tolerance and increased prevalence of undesirable side reactions compared to competing cross-coupling methodology. These shortcomings make decarboxylative cross-coupling an ideal class of reactions to target, as the highly tuneable size-dependant/composition-dependant properties and other unique features that nanoparticles possess give a good degree of scope for alleviating these harsh conditions and improving selectivity for DCC transformations over undesirable side reactions.

The work presented in this chapter is therefore concerned with studies aimed at marrying the concepts of DCC chemistry and nanoparticle catalysis. These include:

- The synthesis and characterisation of a library of monometallic and bimetallic nanoparticle materials, with a focus on exploring the effects of metal content, ratios and capping agent choice.
- Incorporating these materials into a model DCC reaction.
- Exploring the scope for replacing traditionally used DCC catalysts with metals such as gold or nickel, with the hypothesis that the nano-scale structure of the catalysts will improve reactivity in these cases.

### 3.2. Catalyst Synthesis and Characterisation

There are a variety of disparate and interesting techniques for synthesising nanoparticle catalysts, each displaying their own set of strengths and weaknesses. To suit the needs of this project, attractive methods would need maintain good control over resulting particle size, shape and structure, particularly in the case of bimetallic nanoparticles, where a high degree of bonding between the two metals is desirable. Other requirements would be that the method is achievable using conventional lab equipment and is capable of producing catalytically significant quantities of material. Such requirements significantly narrow the available suite of techniques. For example, a popular approach in nanotechnology fields is the use of molecular beam epitaxy, wherein the desired material is vaporised and directed towards the substrate in the form of a molecular beam, allowing for nanoscale crystals to grow in

a controlled manner *via* deposition. This allows researchers a great degree of control over the resulting materials. Despite this, there are constraints that make such an approach unsuitable for this project – given the epitaxial nature of the growth, a macroscopic crystalline substrate is required for the nanoscale materials to assemble upon. Epitaxial methods also require specialised apparatus, and typically struggle to generate substantial quantities of material as would be required for catalyst screening <sup>48</sup>.

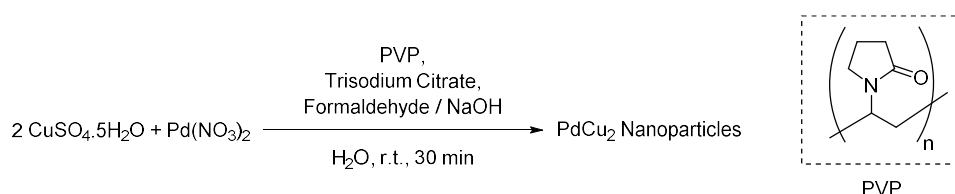
Given the demands of the project, three key approaches bear consideration: decomposition, electrochemistry and chemical reduction. Decomposition methods utilise energy in the form of heat, light or ultrasound to induce the decomposition of organometallic precursors into their respective organic and metallic components <sup>54,92</sup>. This can be performed in solution alongside the use of capping agents such as poly(vinylpyrrolidone) (PVP) or poly(ethyleneglycol) (PEG) which bind to the surface of resulting nanoscale metal and serve to inhibit further growth <sup>105,147</sup>. Specifically, in the case of pyrolytic methods, the use of heat to decompose molecules, this can also be performed in lieu of solvent by simply heating the precursor in an oven or kiln. Control in these cases is typically afforded *via* the use of a constraining environment, such as the interior of graphene nanofibers <sup>148</sup>. Literature examples of decomposition methods have shown however that control is typically challenging to achieve and necessitates careful selection and design of the metal precursor(s) to ensure that decomposition can occur under conditions mild enough to prevent decomposition of other vital components, such as the capping agent <sup>48</sup>.

Reduction methods, both chemical and electrochemical, are more forgiving in this regard, generally only requiring a salt of the metal(s) desired and a reductant potent enough to drive the redox process. Reduction methods are also typically very straightforward, being one-pot wet chemical processes with limited post-reaction work up required. These facts make reduction methods very popular in the field of metallic nanoparticle catalysis, and literature surrounding them is rich and well explored as a result <sup>54,77,149,150</sup>. Control in these reactions is afforded both through the choice of capping agent and the choice of reducing agent/conditions, the former helping to ensure control over both size distributions and particle shape, the latter

controlling the rate of particle growth – a parameter that controls average particle size.

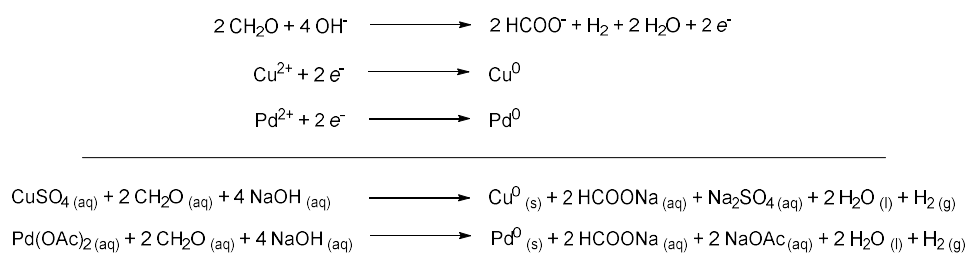
### 3.2.1. PVP-capped Palladium/Copper Catalyst Series

With reduction selected as the most attractive route to bimetallic nanoparticles, the work of Lo *et al.* was chosen as a starting point. Their approach is an aqueous co-reduction of copper and palladium ions, with the use of trisodium citrate as a complexation agent, poly(vinylpyrrolidone) as a capping agent and formaldehyde as a reducing agent (see Scheme 3.1) <sup>151</sup>.



*Scheme 3.1: Lo et al.'s citrate-aided PdCu bimetallic nanoparticle synthesis* <sup>151</sup>.

Via transition electron microscopy (TEM) analysis, they found their palladium/copper bimetallic nanoparticles to be fairly monodisperse, with particle diameters of between 3-4 nm. The only modifications to this protocol were varying the ratios of copper to palladium precursors and the substitution of palladium(II) nitrate for palladium(II) acetate due to scarcity at the time of experimentation. Palladium(II) acetate displays poor solubility in aqueous medium, typically listed as ‘insoluble’ by manufacturers and solubility databases <sup>152</sup>. However, with vigorous stirring, heating at 50 °C and the use of the complexation agent trisodium citrate, this issue was overcome.



*Scheme 3.2: Half-equations and full equations for the redox processes between aqueous copper/palladium ions and formaldehyde under basic conditions.*

Once the salts were completely dissolved, the reaction mixture was allowed to cool back to room temperature before the reducing solution of formaldehyde in 1 M NaOH was introduced. The relevant half-equations and full equations for the redox processes are shown in Scheme 3.2.

Using this modified protocol, three palladium/copper bimetallic nanoparticle systems were synthesised with differing metal ratios: Pd<sub>2</sub>Cu, PdCu and PdCu<sub>2</sub>, so as to enable the investigation into the effect varying the ratios of palladium to copper had, not only on catalyst structure but also catalytic performance. Copper and palladium monometallic particles were also synthesised *via* the same method for comparative purposes. These particles were analysed by atomic absorption spectroscopy (AAS) to determine the metal content of the resulting materials and the ratio of metals by weight in the bimetallic catalysts, and TEM to determine the average size and shapes of the catalysts. The results of these analytical investigations are summarised in Table 3.1 and Table 3.2, respectively. Energy-dispersive X-ray (EDX) spectroscopy was also performed alongside the TEM analysis, and the resulting spectra are showcased alongside their respective micrograph images in Figure 3.1.

*Table 3.1: AAS characterisation for the PVP-capped Pd/Cu catalyst series. <sup>a</sup> Palladium divided by copper. <sup>b</sup> 5ppm sample. <sup>c</sup> Rounded to nearest whole number for clarity. <sup>d</sup> Calculated without rounding.*

Catalyst	Ideal Ratio <sup>a</sup>	Ideal Ratio (by weight) <sup>a</sup>	Pd Content (%) <sup>b, c</sup>	Cu Content (%) <sup>b, c</sup>	Observed Ratio <sup>a, d</sup>	Remaining Mass (%)
Pd-PVP	Mono-metallic	---	16	---	---	84
Pd <sub>2</sub> Cu-PVP	2	3.35	26	8	3.39	66
PdCu-PVP	1	1.67	13	9	1.44	78
PdCu <sub>2</sub> -PVP	0.5	0.84	9	11	0.85	80
Cu-PVP	Mono-metallic	---	---	50	---	50

The AAS data displayed in Table 3.1 shows that there is good agreement between the observed ratio of palladium to copper by weight in the bimetallic samples and the ideal ratio expected given the loadings of palladium and copper precursors used in the synthesis. In all cases however, the percentage metal content observed represents a relatively small proportion of the overall sample mass. This implies that the particles themselves are coated in a heavy layer of capping agent and/or contain impurities, even after 3 separate methanol wash steps and subsequent centrifugation. Only in the case of catalyst Cu-PVP is this observation less true, with the sample observed to be 50 % copper by weight. When this result is compared to the observed palladium content of catalyst Pd-PVP, 16 %, it can be inferred that the capping agent PVP displays a stronger affinity for binding to palladium substrate than copper substrate.

This observation is strengthened when the TEM micrographs displayed in Figure 3.1 are also considered, wherein catalyst Pd-PVP is observed to be comprised of small spherical nanoparticles of between 3-4 nanometres (see Figure 3.1a) whereas catalyst Cu-PVP is observed to be comprised of significantly larger flake-like particulate of a size regime greater than 100 nanometres (see Figure 3.1i). Interestingly this tendency to form flake-like particulate is not observed in any of the palladium/copper bimetallic catalyst systems, which are all comprised of spherical nanoparticles of between 3-4 nanometres in diameter (see Figure 3.1c, e and g). The bimetallic systems also all exhibit behaviour not observed in the monometallic systems: the tendency to cluster together into loose spherical structures. As this agglomeration is not observed in the monometallic catalysts it may be indicative of an intramolecular interaction between the palladium/copper bimetallic nanoparticles due to unique surface chemistry brought about by the alloying of palladium and copper. Table 3.2 displays data gathered from the micrographs and while there appears to be no trend between average particle diameter and the ratio of palladium to copper in the catalyst, it can be said that the size distributions of the catalysts synthesised *via* the modified protocol are in good agreement with Lo *et al.*'s original findings<sup>151</sup>.

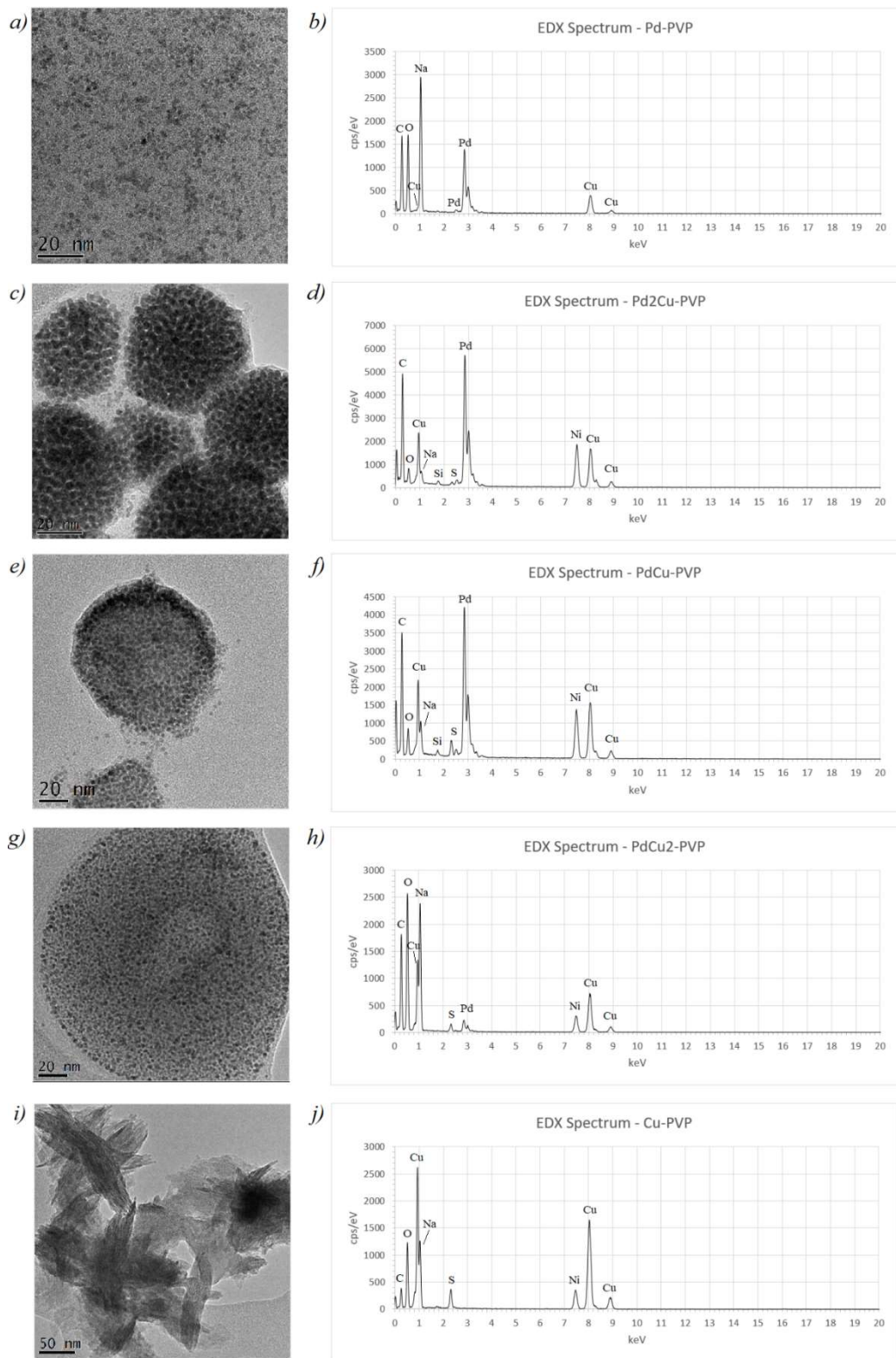


Figure 3.1: TEM micrographs and EDX spectra for Pd-PVP (a, b), Pd<sub>2</sub>Cu-PVP (c, d), PdCu-PVP (e, f), PdCu<sub>2</sub>-PVP (g, h) and Cu-PVP (i, j). EDX spectra b was taken on a copper support grid. EDX spectra d, f, h and j were taken on a nickel support grid.

Table 3.2: TEM characterisation for the PVP-capped Pd/Cu catalyst series. <sup>a</sup> Calculated from 100 measurements made over 5 distinct sample areas. <sup>b</sup> Long axis divided by short axis.

Catalyst	Average Long Axis Diameter (nm) <sup>a</sup>	Std. Dev. (nm) <sup>a</sup>	Average Short Axis Diameter (nm) <sup>a</sup>	Std. Dev. (nm) <sup>a</sup>	Average Aspect Ratio <sup>a, b</sup>	Std. Dev. <sup>a</sup>
Pd-PVP	3.2	0.5	2.9	0.4	1.1	0.1
Pd <sub>2</sub> Cu-PVP	4.1	0.6	3.6	0.5	1.1	0.1
PdCu-PVP	3.8	0.4	3.7	0.4	1.05	0.07
PdCu <sub>2</sub> -PVP	4.5	0.7	4.4	0.7	1.02	0.06
Cu-PVP	> 100	---	> 100	---	---	---

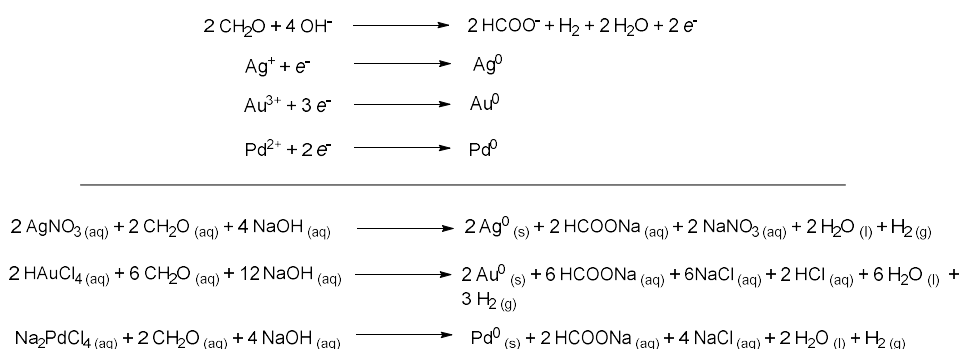
Average aspect ratio, a parameter that gives an indication on how spherical the particles are (1 representing a perfect sphere and values greater than one implying an ellipsoid shape), does appear to correlate with palladium content. Catalysts with a high palladium content (Pd-PVP and Pd<sub>2</sub>Cu-PVP) display a higher average aspect ratio than the catalysts with lower palladium content (PdCu-PVP and PdCu<sub>2</sub>-PVP).

The EDX spectra displayed in Figure 3.1 give a qualitative analysis on the atomic content of the catalysts. Firstly, it can be observed that clear palladium emissions at 2.839 keV, corresponding to the palladium L<sub>α</sub> emission, are present in all palladium containing samples. Copper emissions at 0.930 keV (L<sub>α</sub>), 8.048 keV (K<sub>α</sub>) and 8.905 keV (K<sub>β</sub>) are similarly observed in all copper containing samples. Note that in the case of catalyst Pd-PVP (Figure 3.1b), the sample was prepared upon a copper support grid, and therefore the EDX spectrum also displays these characteristic copper emissions. All other spectra were gathered upon a nickel support grid, due to the copper content of these samples, therefore Figure 3.1d, f, h and j contain a nickel emission at 7.478 keV (K<sub>α</sub>). Besides these key emissions, other notable peaks are present: carbon emissions at 0.277 keV (K<sub>α</sub>); oxygen emissions at 0.525 keV (K<sub>α</sub>); sodium emissions at 1.041 keV (K<sub>α</sub>) and sulphur emissions at 2.307 keV (K<sub>α</sub>). The source of carbon emissions is likely to be the copious amount of capping agent, suggested by AAS analysis (see Table 3.1). Likewise, the presence of the capping agent PVP could also be the source of some of the oxygen emissions present in all

spectra. However, the sodium and sulphur emissions, as well as a portion of the carbon and oxygen emissions are likely derived from the presence of sodium sulphate (Na<sub>2</sub>SO<sub>4</sub>) and sodium acetate (NaOAc) – formed from the spectator ions of the redox processes and present as a contaminant in the catalysts despite washing steps.

### 3.2.2. PVP-capped Palladium/Silver and Palladium/Gold Catalyst Series

Whilst the bulk of the literature surrounding bimetallic decarboxylative cross-coupling approaches are concerned with the use of palladium and copper, work performed by the groups of Goossen<sup>32</sup> and Larrosa<sup>39</sup> has proven the viability of palladium/silver based catalyst systems. The literature surrounding decarboxylative cross-coupling has thus far neglected the use of gold, despite reports by Dupuy and Nolan showcasing golds potential as a decarboxylation catalyst<sup>26,40,43</sup>. With this in mind, the synthesis of a suite of palladium/silver and palladium/gold materials was deemed prudent, allowing for investigations complimentary to the exploration of the use of palladium/copper bimetallic nanoparticles in decarboxylative cross-coupling protocols. Synthetic protocol has been repeatedly shown to have a strong influence on the resulting nanoparticles. Therefore, for the comparison between the different palladium/group 11 bimetallic nanoparticle catalysts to be valid care must be taken to ensure that the conditions of their synthesis remain as similar as possible.



*Scheme 3.3: Half-equations and full equations for the redox processes between aqueous silver/gold/palladium ions and formaldehyde under basic conditions.*

As such, Lo *et al.*'s palladium/copper protocol<sup>151</sup> was used once again, substituting the use of copper(II) sulphate pentahydrate for either silver nitrate or hydrogen tetrachloroaurate(III) trihydrate. Besides this, one other modification was made to

the protocol discussed in Chapter 3.2.1, sodium tetrachloropalladate(II) hydrate was used instead of the sparsely soluble palladium(II) acetate – maintaining the use of palladium 2+ ions to keep the redox chemistry the same but switching counterions for the purposes of improving aqueous solubility.

*Table 3.3: AAS characterisation for the PVP-capped Pd/Ag catalyst series. <sup>a</sup> Palladium divided by silver. <sup>b</sup> 5ppm sample. <sup>c</sup> Rounded to nearest whole number for clarity. <sup>d</sup> Calculated without rounding.*

Catalyst	Ideal Ratio <sup>a</sup>	Ideal Ratio (by weight) <sup>a</sup>	Pd Content (%) <sup>b, c</sup>	Ag Content (%) <sup>b, c</sup>	Observed Ratio <sup>a, d</sup>	Remaining Mass (%)
Ag-PVP	Mono-metallic	---	---	89	---	11
PdAg-PVP	1	0.99	31	30	1.04	39

*Table 3.4: AAS characterisation for the PVP-capped Pd/Au catalyst series. <sup>a</sup> Palladium divided by gold. <sup>b</sup> 5ppm sample. <sup>c</sup> Rounded to nearest whole number for clarity. <sup>d</sup> Calculated without rounding.*

Catalyst	Ideal Ratio <sup>a</sup>	Ideal Ratio (by weight) <sup>a</sup>	Pd Content (%) <sup>b, c</sup>	Au Content (%) <sup>b, c</sup>	Observed Ratio <sup>a, d</sup>	Remaining Mass (%)
Au-PVP	Mono-metallic	---	---	18	---	82
PdAu-PVP	1	0.54	26	17	1.52	57

*Table 3.5: TEM characterisation for the PVP-capped Pd/Ag and Pd/Au catalyst series. <sup>a</sup> Calculated from 100 measurements made over 5 distinct sample areas. <sup>b</sup> Long axis divided by short axis.*

Catalyst	Average Long Axis Diameter (nm) <sup>a</sup>	Std. Dev. (nm) <sup>a</sup>	Average Short Axis Diameter (nm) <sup>a</sup>	Std. Dev. (nm) <sup>a</sup>	Average Aspect Ratio <sup>a, b</sup>	Std. Dev. <sup>a</sup>
Ag-PVP	> 100	---	> 100	---	---	---
PdAg-PVP	11	6	10	5	1.1	0.1
Au-PVP	7	4	7	4	1.03	0.06
PdAu-PVP	7	2	7	2	1.03	0.07

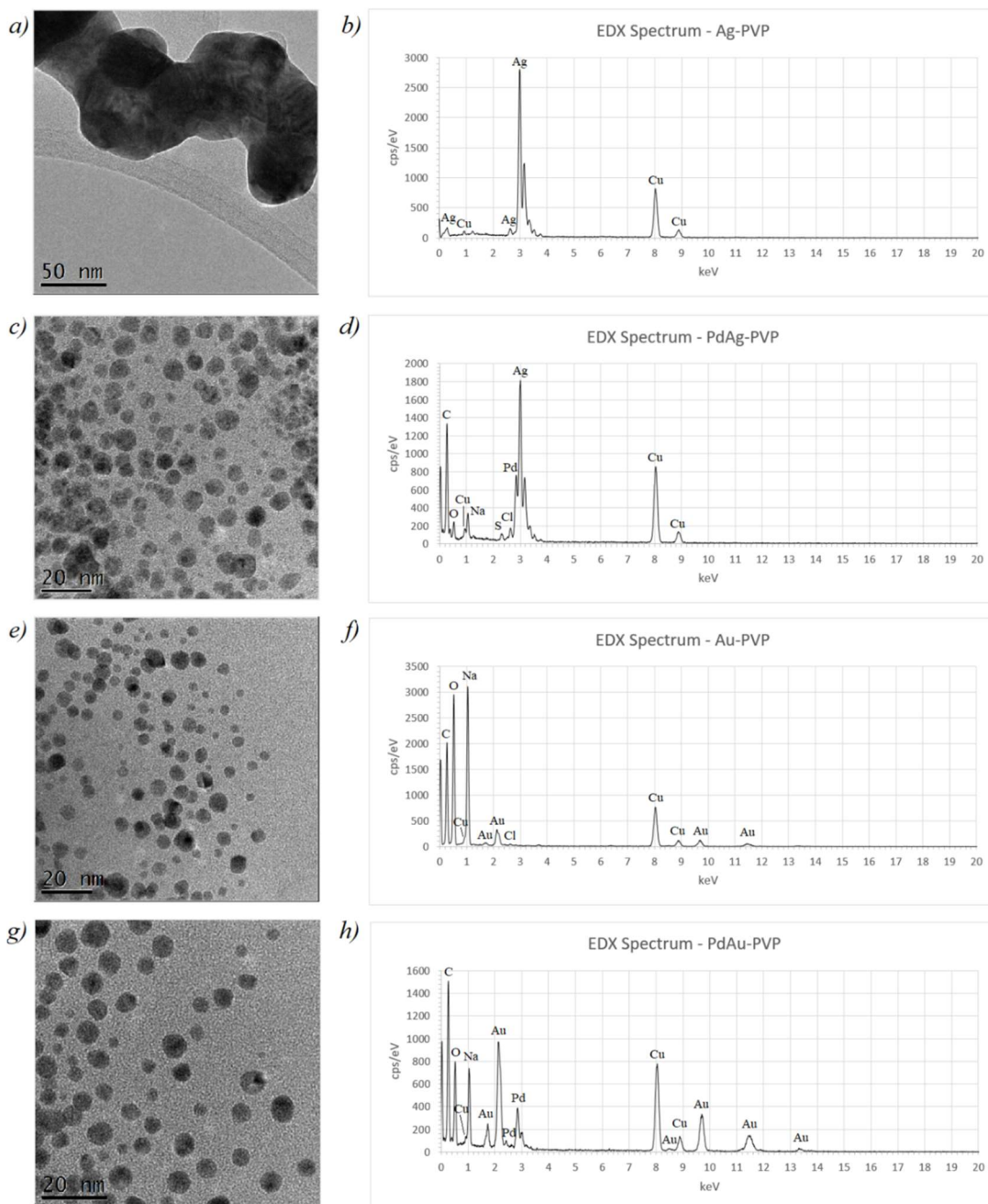
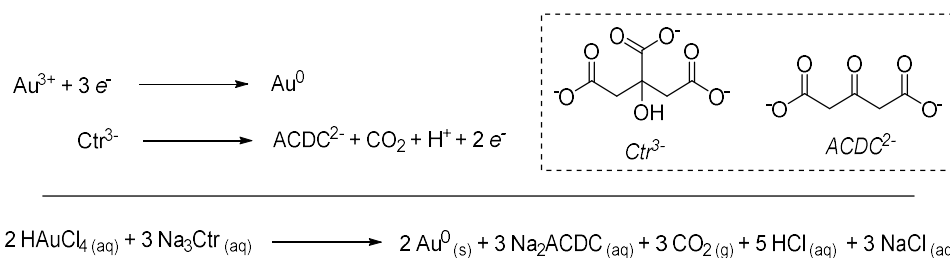


Figure 3.2: TEM micrographs and EDX spectra for Ag-PVP (a, b), PdAg-PVP (c, d), Au-PVP (e, f) and PdAu-PVP (g, h). All EDX spectra were acquired on a copper support grid.

In the case of the palladium/silver catalyst series, AAS analysis (Table 3.3) shows good agreement between the expected ratio and the observed ratio of palladium to silver by weight in the resulting bimetallic catalyst. Examining the percentage of mass not accounted for when considering both palladium and silver, it can be seen that the value is much lower for both Ag-PVP and PdAg-PVP when compared to their analogues in the palladium/copper series (see Table 3.1) This may imply that

the capping agent PVP binds even less strongly to the silver substrate than was observed with Cu-PVP. As with the palladium/copper system, suspicions raised about PVP's capping ability are reinforced *via* TEM analysis (for micrographs see Figure 3.2a and c, for derived data see Table 3.5). As with Cu-PVP, it is clear from the micrograph that Ag-PVP is not nanoscale, instead being comprised of large micrometre-scale structures. With the bimetallic catalyst PdAg-PVP, spherical nanometre-scale particles are observed with an average particle diameter of 11 nanometres. However unlike the palladium/copper series, which showed excellent control over size distributions, the palladium/silver series suffers: displaying a standard deviation in average particle diameter of 6 nanometres. This statistically significant lack of size control compared to the palladium/copper series again speaks of the fact that the conditions of the modified nanoparticle preparation derived from Lo *et al.*'s work <sup>151</sup>, such as the use of capping agent PVP, are inadequate for producing monodisperse silver and palladium/silver catalysts.

AAS analysis of the palladium/gold catalyst series (see Table 3.4) reveals further deficiencies in the modified nanoparticle preparation for palladium/group 11 bimetallic nanoparticles. Observed gold content was found to be low in the case of the monometallic catalyst Au-PVP, accounting for 18 % of the materials mass. This is similar to the findings shown in Table 3.1 for the palladium-containing catalysts and may suggest that PVP serves as a good capping agent for gold substrates – persisting even after several washing steps. However, in the case of catalyst PdAu-PVP, there is a large discrepancy between the expected ratio of palladium to gold by weight in the material (given the loadings of palladium and gold salts in the synthesis) and the observed ratio. PdAu-PVP is therefore much more palladium-rich than was desired. The reason for this was observed after reaction completion – a faint gold mirror had formed on the reaction vessel during synthesis. This is likely due to the premature reduction of aqueous gold 3+ ions by the complexation agent trisodium citrate – a well-documented process <sup>153–155</sup> for which the half equations and subsequent full equation are displayed in Scheme 3.4.



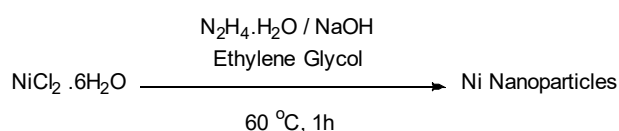
*Scheme 3.4: Half-equations and full equation for the redox process between aqueous gold ions and trisodium citrate ( $\text{Na}_3\text{Ctr}$ ).*

TEM analysis (see Figure 3.2e and g for micrographs and Table 3.5 for derived data) reveals that both the monometallic Au-PVP and bimetallic PdAu-PVP display smaller average particle diameters compared to their palladium/silver analogues, 7 nanometres in both cases, with a standard deviation of 4 nanometres in the case of Au-PVP and 2 nanometres in the case of PdAu-PVP. In the case of the palladium/group 11 bimetallic catalysts the trend observed for both average particle diameter, and degree of monodispersity is as follows: PdCu-PVP < PdAu-PVP < PdAg-PVP, with PdCu-PVP displaying both the smallest particle diameters and smallest distribution of particle diameters throughout the sample ( $3.8 \pm 0.4$  nanometres). Interestingly, the monometallic gold system Au-PVP did manifest as nanometre-scale spherical nanoparticles, a behaviour not displayed in either Cu-PVP or Ag-PVP.

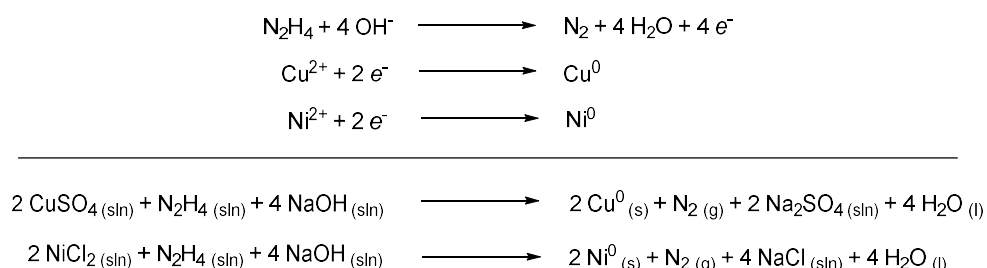
Using EDX as a qualitative tool (see Figure 3.2) it is shown that all silver containing catalysts (Ag-PVP and PdAg-PVP) display silver emissions at 2.984 keV ( $L_\alpha$ ), all gold containing catalysts (Au-PVP and PdAu-PVP) display gold emissions at 2.206 keV ( $M_{45}$ ) and 9.628 keV ( $L_\alpha$ ) and all palladium containing catalysts (PdAg-PVP and PdAu-PVP) display palladium emissions at 2.839 keV ( $L_\alpha$ ). All spectra were acquired on a copper sample grid, explaining the presence of copper emissions at 0.930 keV ( $L_\alpha$ ), 8.048 keV ( $K_\alpha$ ) and 8.905 keV ( $K_\beta$ ) despite the fact that the catalysts themselves contain no copper. As with the palladium/copper-PVP system, all other emission peaks observed within the EDX spectra can be accounted for either by the capping agent PVP or by the byproducts of the redox processes shown in Scheme 3.3 and Scheme 3.4.

### 3.2.3. EG-capped Nickel/Copper and Palladium/Copper Catalyst Series

Alongside investigations into modifying the group 11 metal content of the bimetallic nanoparticles synthesised and used in this work, investigating the effect substituting palladium for other group 10 metals was also deemed interesting – particularly as there is much interest in replacing the use of palladium in catalytic processes wherever possible. Using the same logic as in Chapter 2.1.2., Lo *et al.*'s formaldehyde reduction was again modified to suit purpose. However, this protocol was found to be unable to chemically reduce nickel salts. Therefore, a new methodology was called for – Wu and Chen's synthesis of nickel monometallic nanoparticles *via* hydrazine hydrate reduction (see Scheme 3.5) <sup>156</sup>.



Scheme 3.5: Wu and Chen's synthesis of monometallic nickel nanoparticles <sup>156</sup>.

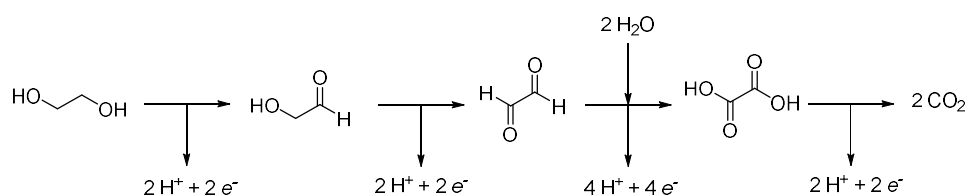


Scheme 3.6: Half-equations and full equations for the redox processes between solvated copper/nickel ions and hydrazine under basic conditions.

Their approach called for the use of ethylene glycol (EG) both as a solvent for the reaction and as a capping agent for the resulting particulate. To yield nickel copper bimetallic particulate their protocol was modified, keeping the total loading of metal salts (in mol) the same but employing an equal ratio of nickel and copper salts. Alongside this nickel monometallic material was synthesised following the same synthetic procedure, for comparative purposes. The half equations and subsequent full equations for the redox chemistry are displayed in Scheme 3.6. These materials were then analysed *via* AAS, TEM and EDX, the results of which are displayed in Table 3.6, Table 3.7 and Figure 3.3 respectively.

As key synthesis parameters such as capping agent choice, temperature and solvent had been modified compared to the protocol used for the PVP-capped catalysts, direct comparisons to the PVP-capped palladium/group 11 nanoparticles would be less valid. Therefore, using the conditions outlined by Wu and Chan, palladium/copper 1:1 bimetallic material and palladium and copper monometallic materials, were also synthesised. This also allows for investigation into the effect capping agent has both on size, shape and dispersity of the material, but also their catalytic activity compared to their PVP-capped analogues.

Reduction was observed to occur before addition of the reducing agent hydrazine hydrate in these cases. This suggests that the palladium/copper systems are amenable to the polyol process, wherein either monomeric ethylene glycol or the polymer poly(ethylene glycol), heated to specified temperatures, serve as solvent, reducing agent and capping agent for the resulting nanoscale materials <sup>105,150</sup>. Unfortunately, ethylene glycol's behaviour as a reducing agent is not fully understood and is hypothesised to have a complex reduction pathway (see Scheme 3.7) <sup>157</sup>. As such, full equations for the polyol redox chemistry have not been postulated. These materials were then analysed *via* AAS, TEM and EDX, the results of which are displayed in Table 3.8, Table 3.9 and Figure 3.4 respectively.



*Scheme 3.7: Hypothesised reduction pathway for ethylene glycol under aqueous conditions <sup>157</sup>.*

As Table 3.6 shows, copper is again found to display poor interaction with capping agent compared to its nickel counterpart. In fact, the data for Cu-EG suggests that the capping agent is entirely removed after washing steps, with copper being observed to comprise 100 % of the resulting materials mass. This suggests that EG is a weaker binding agent compared to PVP – understandable given its monomeric nature compared to the large polymeric chains of PVP. This finding is further reinforced when considered alongside the results displayed in Table 3.8, wherein

both the monometallic Pd-EG and bimetallic PdCu-EG display metal contents far in excess of the metallic content of their PVP-capped analogues Pd-PVP and PdCu-PVP (see Table 3.1).

When considering the observed ratios of nickel to copper in the EG-capped nickel/copper bimetallic system, it is clear that copper content is far greater than was desired given the initial loadings of nickel and copper salts in the synthesis. This suggests that copper reduction under these conditions occurs a greater rate compared to nickel reduction, and that when the reaction was terminated, nickel ions remained in solution. This is a somewhat expected result, however, given the harsh conditions required to induce the chemical reduction of nickel compared to copper.

*Table 3.6: AAS characterisation for the EG-capped Ni/Cu catalyst series. <sup>a</sup> Nickel divided by copper. <sup>b</sup> 5ppm sample. <sup>c</sup> Rounded to nearest whole number for clarity. <sup>d</sup> Calculated without rounding.*

<b>Catalyst</b>	<b>Ideal Ratio <sup>a</sup></b>	<b>Ideal Ratio (by weight) <sup>a</sup></b>	<b>Ni Content (%) <sup>b, c</sup></b>	<b>Cu Content (%) <sup>b, c</sup></b>	<b>Observed Ratio <sup>a, d</sup></b>	<b>Remaining Mass (%)</b>
Ni-EG	Mono-metallic	---	28	---	---	72
NiCu-EG	1	0.92	9	41	0.21	50

*Table 3.7: TEM characterisation for the EG-capped Ni/Cu catalyst series. <sup>a</sup> Calculated from 100 measurements made over 5 distinct sample areas. <sup>b</sup> Long axis divided by short axis.*

<b>Catalyst</b>	<b>Average Long Axis Diameter (nm) <sup>a</sup></b>	<b>Std. Dev. (nm) <sup>a</sup></b>	<b>Average Short Axis Diameter (nm) <sup>a</sup></b>	<b>Std. Dev. (nm) <sup>a</sup></b>	<b>Average Aspect Ratio <sup>a, b</sup></b>	<b>Std. Dev. <sup>a</sup></b>
Ni-EG	20	8	18	7	1.1	0.1
NiCu-EG	14	11	13	9	1.1	0.2

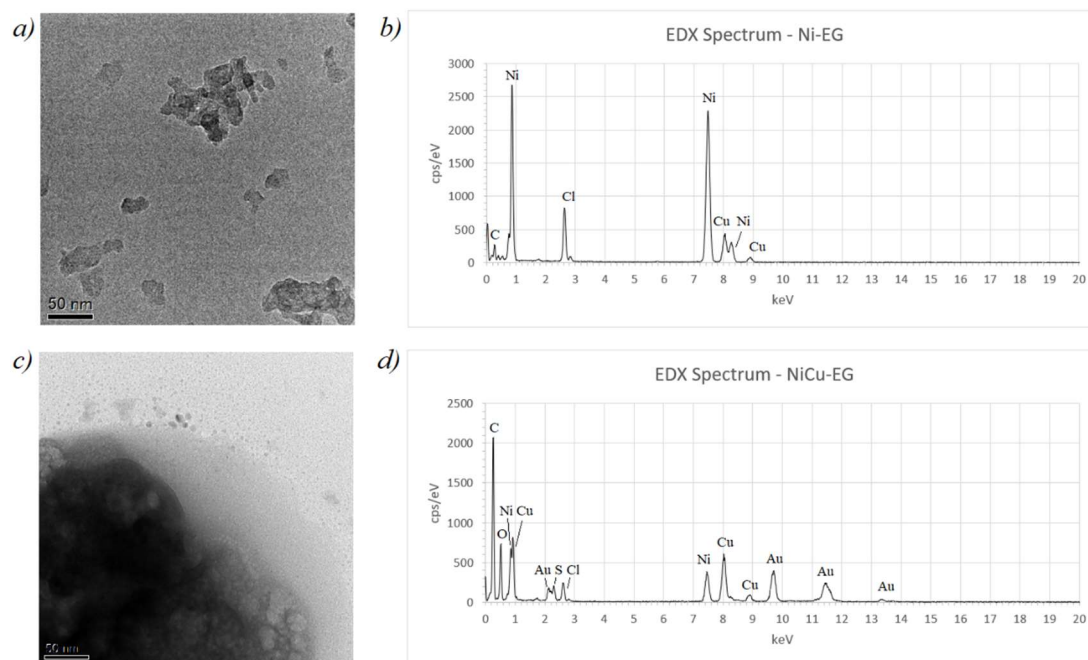


Figure 3.3: TEM micrographs and EDX spectra for Ni-EG (a, b) and NiCu-EG (c, d). The EDX spectra for Ni-EG was captured on a copper support grid. The EDX spectra for NiCu-EG was captured on a gold support grid.

In the case of the palladium/copper system, the reverse is observed, with catalyst PdCu-EG found to contain more palladium by weight than was desired. This may suggest that whilst palladium reduction under polyol conditions proceeds quickly, copper reduction is slower and copper ions remained in solution after the reaction was terminated and were subsequently lost in washing steps – depriving the catalyst of copper content.

Table 3.8: AAS characterisation for the EG-capped Pd/Cu catalyst series. <sup>a</sup> Palladium divided by copper. <sup>b</sup> 5ppm sample. <sup>c</sup> Rounded to nearest whole number for clarity. <sup>d</sup> Calculated without rounding.

Catalyst	Ideal Ratio <sup>a</sup>	Ideal Ratio (by weight) <sup>a</sup>	Pd Content (%) <sup>b, c</sup>	Cu Content (%) <sup>b, c</sup>	Observed Ratio <sup>a, d</sup>	Remaining Mass (%)
Pd-EG	Mono-metallic	---	91	---	---	9
PdCu-EG	1	1.67	61	24	2.54	15
Cu-EG	Mono-metallic	---	---	100	---	0

Table 3.9: TEM characterisation for the EG-capped Pd/Cu catalyst series. <sup>a</sup> Calculated from 100 measurements made over 5 distinct sample areas. <sup>b</sup> Long axis divided by short axis.

Catalyst	Average Long Axis Diameter (nm) <sup>a</sup>	Std. Dev. (nm) <sup>a</sup>	Average Short Axis Diameter (nm) <sup>a</sup>	Std. Dev. (nm) <sup>a</sup>	Average Aspect Ratio <sup>a, b</sup>	Std. Dev. <sup>a</sup>
Pd-EG	7	2	7	2	1.04	0.04
PdCu-EG	3.4	0.8	3.2	0.8	1.05	0.08
Cu-EG	7	2	7	2	1.06	0.09

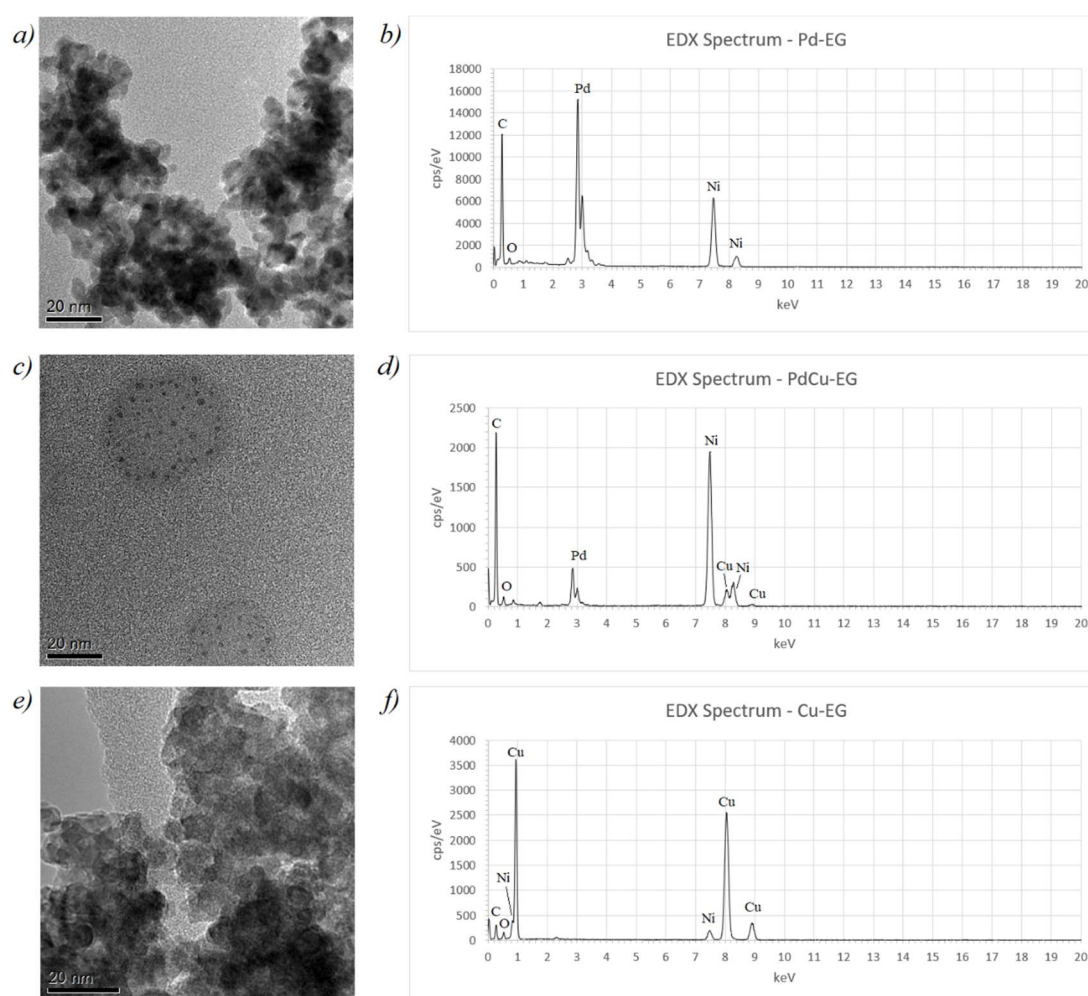


Figure 3.4: TEM micrographs and EDX spectra for Pd-EG (a, b), PdCu-EG (c, d) and Cu-EG (e, f). All EDX spectra were acquired on a nickel support grid.

TEM analysis reveals that, in the case of the nickel/copper catalyst series, average particle size correlates positively with nickel content. This is the inverse of the behaviour exhibited by the palladium/copper PVP-capped catalyst series. Of

particular note is the comparison between the catalysts Cu-EG and Cu-PVP. Where the use of PVP as capping agent for the formation of copper monometallic material resulted in highly agglomerated flake-like particles with average particle sizes far in excess of 100 nanometres, using EG as capping agent resulted in discrete spherical particulate with an average particle size of  $7 \pm 2$  nanometres. However, as Table 3.8 reveals, 100 % of the mass of Cu-EG is accounted for by copper content. This implies that, as with its PVP-capped analogue, EG is a poor binding agent for copper particulate. This is reflected in the TEM micrograph for Cu-EG (see Figure 3.4 e) where, as was observed with Cu-PVP, a great deal of particulate agglomeration is observed.

The EG-capped palladium monometallic material was found to have a larger average diameter and a higher degree of polydispersity compared to its PVP analogue, suggesting that PVP serves as a better capping agent for the control of palladium nanoparticle size. Interestingly, unlike its monometallic counterparts Pd-EG and Cu-EG who both differ greatly when compared to the PVP catalyst series, the bimetallic material PdCu-EG is remarkably similar to PdCu-PVP. The particles were observed to be small, spherical and monodisperse with an average diameter of  $3.4 \pm 0.8$  nanometres and an average aspect ratio of  $1.05 \pm 0.08$ . The particles composing PdCu-EG are also observed to form spherical clusters as was observed with the palladium/copper PVP-capped bimetallic materials. These clusters were found to vary in size greatly, with an average diameter of  $48 \pm 17$  nanometres, a figure derived from 34 measurements made over 12 distinct sample areas.

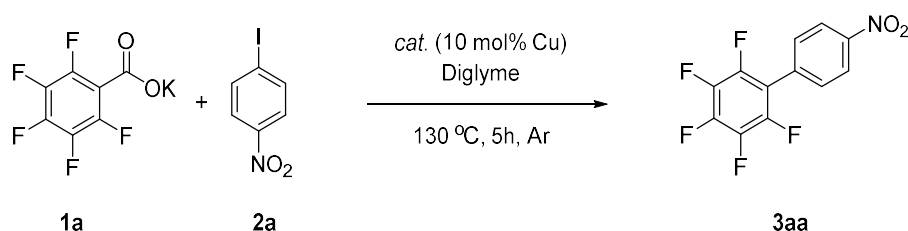
EDX analysis reveals that all nickel containing samples display characteristic nickel emissions at 0.776 ( $L_{\alpha}$ ) and 7.478 keV ( $K_{\alpha}$ ), all copper containing samples display characteristic copper emissions at 0.930 keV ( $L_{\alpha}$ ), 8.048 keV ( $K_{\alpha}$ ) and 8.905 keV ( $K_{\beta}$ ) and all palladium containing samples display characteristic palladium emissions at 2.839 keV ( $L_{\alpha}$ ). The presence of carbon emissions at 0.277 keV ( $K_{\alpha}$ ) and oxygen emissions at 0.525 keV ( $K_{\alpha}$ ) are explained by the presence of EG capping agent. Nickel, copper or gold emissions observed in spectra whose corresponding sample doesn't contain these metals is due to the choice of support grid used to mount the samples for analysis and can be safely disregarded. Of note are the presence of sulphur and chlorine emissions, at 2.307 keV ( $K_{\alpha}$ ) and 2.621 keV

(K<sub>a</sub>) respectively, in the nickel containing EG-capped samples. These are likely due to the presence of the counter ions from the metal salts used in the synthesis of these materials: SO<sub>4</sub><sup>2-</sup> resulting from CuSO<sub>4</sub>·5H<sub>2</sub>O and Cl<sup>-</sup> resulting from NiCl<sub>2</sub>·6H<sub>2</sub>O. This could imply that either byproducts containing these counter ions persisted over the various washing steps or that unreacted metal salts contaminate the final material. Given the disparity in expected and observed metal ratios revealed *via* AAS analysis (see Table 3.6) the latter explanation is most likely, however these explanations are not mutually exclusive.

### 3.3. PVP-capped Nanoparticles in Decarboxylative Cross-coupling Reactions

#### 3.3.1. Palladium/Copper Decarboxylative Cross-coupling

Following on from previous work, the target reaction and conditions were based upon Shang and Liu's monometallic copper-catalysed decarboxylative cross-coupling of fluorinated potassium benzoate salts (see Scheme 3.8)<sup>33</sup>.



*Scheme 3.8: Initial reaction conditions for palladium/copper catalyst investigations.*

Pd<sub>2</sub>Cu-PVP was initially screened under these conditions, alongside two copper monometallic catalysts: copper(I) iodide due to its prevalence as a catalyst in decarboxylative cross-coupling literature and copper(0) powder as an analogue to the zero-valent copper expected to be present in the PVP-capped palladium/copper bimetallic nanoparticles synthesised. Given the DFT studies and suggested reaction mechanisms by the groups of Liu<sup>33</sup> and Goossen<sup>13</sup>, it is hypothesised that the copper-promoted decarboxylation of the carboxylate is the rate determining step – therefore the loading of copper in all presented catalyst systems is kept constant at 10 mol%.

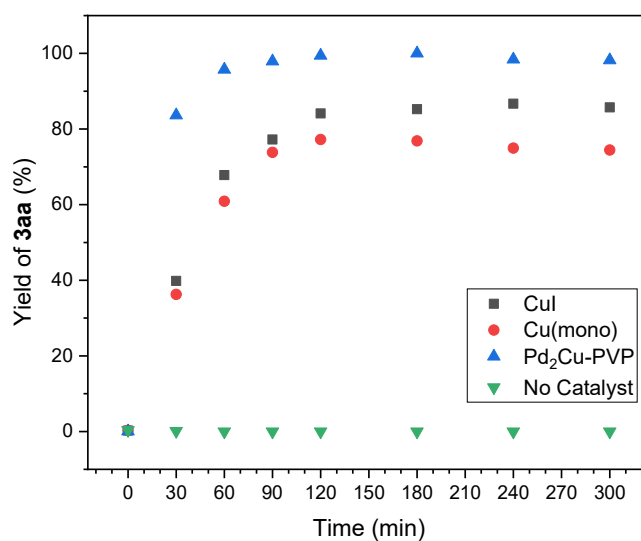


Figure 3.5: A plot comparing the performance of various catalysts in the coupling of **1a** and **2a** at 130 °C. Loading of catalysts was 10 % with respect to copper.

The bimetallic catalyst Pd<sub>2</sub>Cu-PVP was found to show improved reactivity over the monometallic catalysts (see Figure 3.5), an expected result given the proven efficiency of bimetallic approaches in decarboxylative cross-coupling chemistry. With reactivity observed under literature conditions, the temperature was then brought down to 100 °C and the whole suite of PVP-capped Pd/Cu catalysts was screened (see Figure 3.6). Even at lower temperatures, Pd<sub>2</sub>Cu-PVP continued to perform well, reaching 100 % conversion of starting material to product at 4 hours.

A clear trend can be observed in the reaction profiles displayed in Figure 3.6, with palladium rich bimetallic nanoparticles displaying faster reactivity compared to the copper rich bimetallic nanoparticles. However, when the monometallic PVP-capped palladium and copper catalyst systems were investigated, negligible reactivity was observed in both cases. These materials were both synthesised according to the same protocol as their bimetallic analogues (see Chapter 3.2.1) and therefore these findings suggest that a synergistic effect between the palladium and copper content of the bimetallic nanoparticles is operating, yielding reactivity far in excess of their constituent parts.

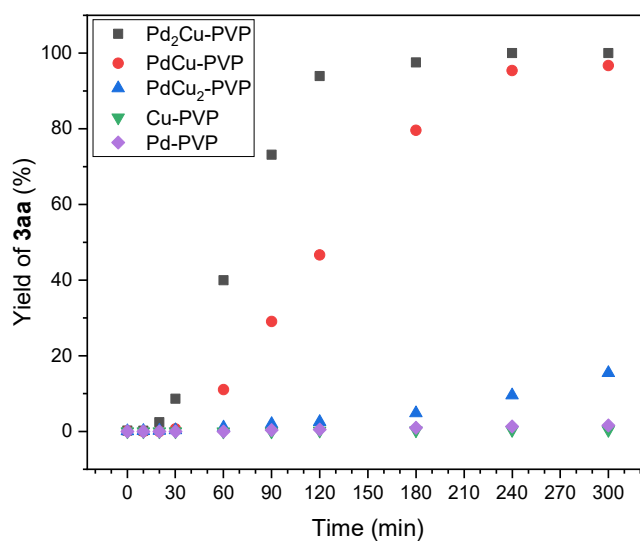
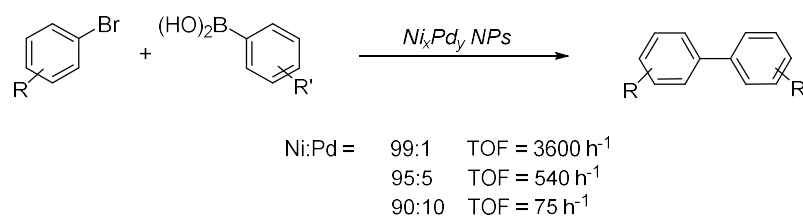


Figure 3.6: A plot comparing the performance of the PVP-capped Pd/Cu nanoparticle catalysts in the coupling of **1a** and **2a** at 100 °C. Loading of copper containing catalyst was 10 mol% with respect to copper content. Loading of Pd-PVP was 10 mol% with respect to palladium content.

A possible explanation for this observed synergistic effect may be found in the relative electronegativities of both palladium and copper. According to the Pauling scale of electronegativities, palladium possesses an electronegativity of 2.2 whereas copper's electronegativity is 1.9. Therefore, when we consider the palladium copper bimetallic materials containing a number of palladium-copper chemical bonds, we can expect the palladium sites of the particulate to be relatively electron rich and the copper sites to be relatively electron deficient. It would also follow that a positive correlation between the ratio of palladium to copper and the degree to which the copper sites would be electron deficient would exist. The relative electron deficiency of the copper active sites would result in a stronger attraction between catalyst and carboxylate anion during the coordination step of DCC reactivity. It would also result in a greater degree of polarity in the copper-oxygen and copper-carbon bonds that are broken during the decarboxylation and transmetalation steps, lowering the activation energy required to drive these transformations.

Similar charge transfer effects were observed by Rai *et al.* during their investigation into nickel/palladium bimetallic nanoparticle catalysed cross-coupling reactions<sup>158</sup>. The turnover number of the nickel/palladium catalysts during a typical Suzuki-

Miyaura coupling was found to positively correlate with the ratio of nickel to palladium (see Scheme 3.9).



*Scheme 3.9: Rai et al.'s Ni/Pd bimetallic nanoparticle promoted Suzuki coupling protocol, highlighting the correlation between the ratio of Ni to Pd and catalyst activity*<sup>158</sup>.

However, as was observed in our own investigations (see Figure 3.6), monometallic particles were observed to underperform with respect to their bimetallic counterparts<sup>158</sup>. This helped confirm the fact that the phenomenon was due to a correlation between the ratio of the two metals and catalytic activity, rather than merely a correlation between nickel content and activity. Through first principle calculations on a variety of model nanoparticle clusters of varying nickel-palladium content, Rai observed that the net negative charge accumulation occurred primarily at palladium active sites<sup>159</sup>, in keeping with the notion that charge will flow from sites with a relatively low electronegativity such as nickel (1.9) to sites with relative high electronegativity. It is these negatively charged palladium sites, they postulate<sup>158</sup>, that are the most favourable binding site for the oxidative addition of aryl halides, and therefore an increase in the ratio of Ni to Pd results in enhanced activity towards Suzuki cross-coupling.

### 3.3.2. The Potential for Nanoparticle Leaching

Where reactivity is observed in Figure 3.6 so too is the presence of an induction period – a part of a reaction profile where the rate of reaction is observed to ramp before stabilising. This could be due to two reasons, there is either a catalyst solubility issue in effect or the true catalyst is not the particles themselves but rather metal ions that leach from the particulate surface under the reaction conditions. To determine the presence of nanoparticle leaching, the Pd<sub>2</sub>Cu-PVP catalyst screening experiment was repeated at 100 °C with the addition of 200 equivalents of mercury

(with respect to the loading of copper in the catalyst used). This addition led to almost complete diminishment of reactivity over a 3 hour period (see Figure 3.7).

Such a finding may suggest that there are catalytically active ionic species in solution under the reaction conditions, and the mercury is scavenging these ions from solution – preventing catalysis. If this was true, it would imply that the catalyst Pd<sub>2</sub>Cu-PVP operates *via* a homocatalytic, rather than a nanocatalytic, mechanism. Such an eventuality would impact the feasibility of the PVP-capped Pd/Cu nanoparticles as catalysts – primarily as catalyst recovery would involve more than simply filtering and collecting the nanoparticle catalyst post reaction. It would also introduce transition metal ions into the reactions waste streams, necessitating special disposal and potentially dealing with regulation. However, these findings could also suggest that the large excess of mercury formed an amalgam with the copper component of the nanoscale material, a well-documented process<sup>160</sup>. This would also lead to catalyst destruction and reduced reactivity. As such, the findings for this experiment are inconclusive in isolation.

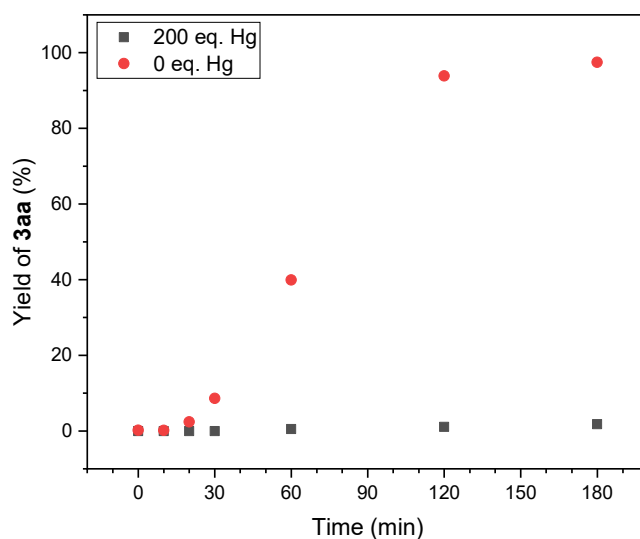


Figure 3.7: A plot depicting the effect additions of mercury have upon the performance of the Pd<sub>2</sub>Cu-PVP catalyst system in the coupling of **1a** and **2a** at 100 °C. Loading of mercury is relative to the copper content in the loading of catalyst Pd<sub>2</sub>Cu-PVP.

To further probe the potential for nanoparticle leaching, combinations of the PVP-capped monometallic palladium and copper catalysts and their corresponding homogeneous counterparts palladium(II) acetate and copper(I) iodide were

investigated at 100 °C (see Figure 3.8). The ratio of PVP-capped nanoparticle to metal salt were kept at a 1:1 molar ratio to allow for direct comparisons to the PdCu-PVP nanoparticle catalyst. If leaching is present from either the palladium or copper components of the bimetallic nanoparticles, initial reaction rates would be observed to ramp as more and more catalytically active species are released from the chemically inert nanoparticles. The findings presented in Figure 3.8 suggest that there is no significant induction period in both the Pd-PVP + CuI and the Cu-PVP + Pd(OAc)<sub>2</sub> catalysed reaction systems. Examining the data gathered during the first hour of the reaction provides further clarity, revealing the linear relationship between the observed yield of DCC product **3aa** and time in both cases (see Figure 3.9)

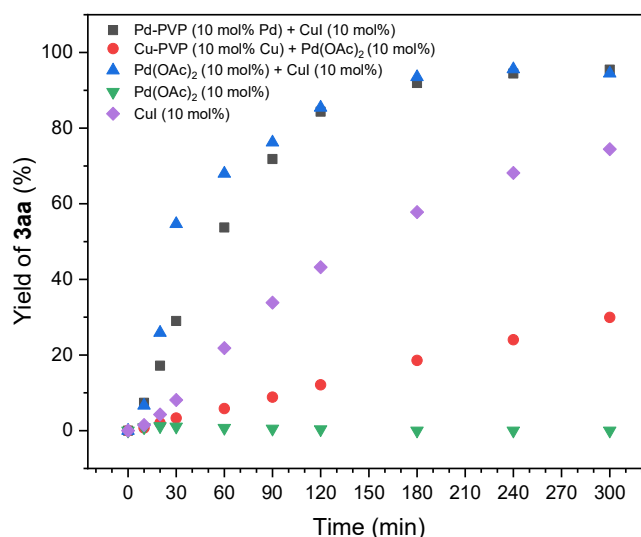


Figure 3.8: A plot comparing various catalyst systems in the coupling of **1a** and **2a** at 100 °C. Loading of Cu-PVP was 10 mol% with respect to copper content. Loading of Pd-PVP was 10 mol% with respect to palladium content.

However, whilst the data gathered shows a linear reaction profile at the outset of the reaction, it is important to recognise that the shortest interval between sampling was 10 minutes during this time. This could serve to obfuscate a minor induction period within the first 10 minutes of the reaction profile. Whilst this data can therefore not be used to completely disprove the existence of an induction period in these cases it can be said that, compared to the heterogeneous catalyst systems Pd(OAc)<sub>2</sub> + CuI and CuI, the prevalence of an induction period is greatly diminished.

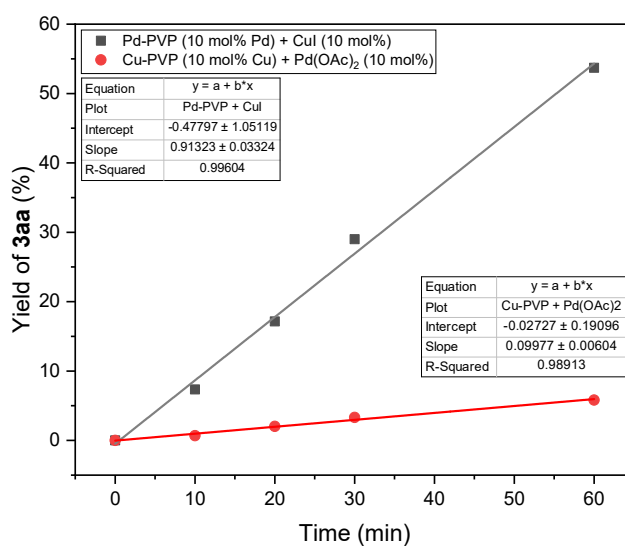


Figure 3.9: A plot showing the linear nature of the reaction profiles for the Pd-PVP + CuI and Cu-PVP + Pd(OAc)<sub>2</sub> catalysed reaction of **1a** and **2a** at 100 °C during the first hour of the reaction.

### 3.3.3. Palladium/Silver and Palladium/Gold Catalysed Decarboxylative Cross-coupling

In the case of the PVP-capped Pd/Ag and Pd/Au bimetallic nanoparticles, a synergistic effect between palladium and the group 11 metals is again observed under the standard 100 °C reaction conditions coupling benzoate salt **1a** with aryl halide **2a**. The bimetallic catalysts PdAg-PVP and PdAu-PVP perform better than their monometallic components Pd-PVP (see Figure 3.6), Ag-PVP and Au-PVP (see Figure 3.10). However, both Pd/Ag and Pd/Au catalyst systems are outperformed by their Pd/Cu analogue, PdCu-PVP, which displays dramatically faster rates of reaction and higher subsequent yields of product **3aa**. This could be due to the larger particle diameters displayed by PdAg-PVP and PdAu-PVP, leading to less exposed surface area per mole of catalyst and therefore less catalytically active sites. It could also be due to the formation of core-shell type nanoparticles rather than homogeneously mixed alloys. This would lead to surface chemistry largely dominated by either palladium or group 11 metal, which would be unfavourable given the catalytic performance of the monometallic catalysts.

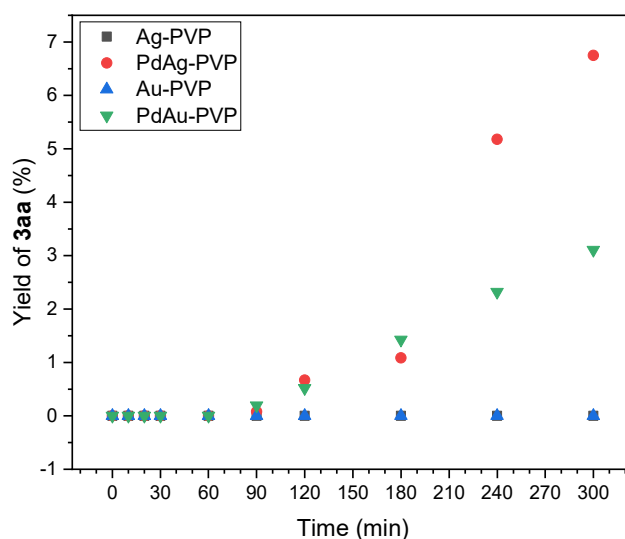


Figure 3.10: A plot comparing the performance of PVP-capped palladium/silver and palladium/gold nanoparticles in the coupling of **1a** and **2a** at 100 °C. Loading of nanoparticle catalysts was 10 mol% with respect to the group 11 metal (Ag, Au).

With the Pd/Ag system there is also the potential for catalytically active silver to be abstracted from the surface of the particles and rendered inert *via* the formation of insoluble silver halide salts as the reaction proceeds. This effect has been observed in the literature regarding homogeneous catalyst systems, with DCC protocols utilising both silver catalysts and aryl halides requiring 1-3 equivalents of silver<sup>17</sup>. Solutions to this problem require the substitution of aryl halide for non-halogenated equivalents such as aryl triflates<sup>32</sup>. However, investigation into the poisoning effects one equivalent of halide ions can have in homogeneous copper-mediated protodecarboxylation reveals that such an addition leads to the prevention of DCC product formation<sup>13</sup>. Such behaviour is not observed in the PdAg-PVP catalysed coupling of **1a** and **2a**, suggesting that halide poisoning is not present.

The Pd/Au bimetallic catalyst PdAu-PVP presented a unique case. The material itself is deeply coloured, and when dissolved produced deep purple solutions. However, this colouration was observed to develop very slowly during the catalyst screening experiment displayed in Figure 3.10. Indeed, at reaction start the colouration was barely visible at all, suggesting a catalyst solubility issue (see Figure 3.11).



Figure 3.11: Photograph depicting samples of crude reaction mixture drawn off from the diglyme-solvated DCC protocol between **1a** and **2a** at 100 °C, utilising PdAu-PVP as catalyst. From left to right the samples were drawn at time (hours:minutes) = 0:00; 0:10; 0:20; 0:30; 1:00; 1:30; 2:00; 3:00 and 4:00.

Based on prior work, DMSO was investigated as a potential alternative solvent. Substituting the literature solvent diglyme for DMSO was found to have a pronounced effect on the catalytic activity of PdAu-PVP, with product yields increased three-fold after 5 hours, and dramatically improved initial reaction rates (see Figure 3.12). Also, no induction period was observed with the use of DMSO, further reinforcing the idea that the source of induction periods in the reaction profiles of the PVP-capped catalysts is primarily due to catalyst insolubility rather than particle leaching. However, it is again important to note that the interval between samples during the initial period of the reaction was 10 minutes. Whilst Figure 3.12 suggests no induction period when using DMSO, it is possible that a short induction period (relative to the diglyme system) is being obscured.

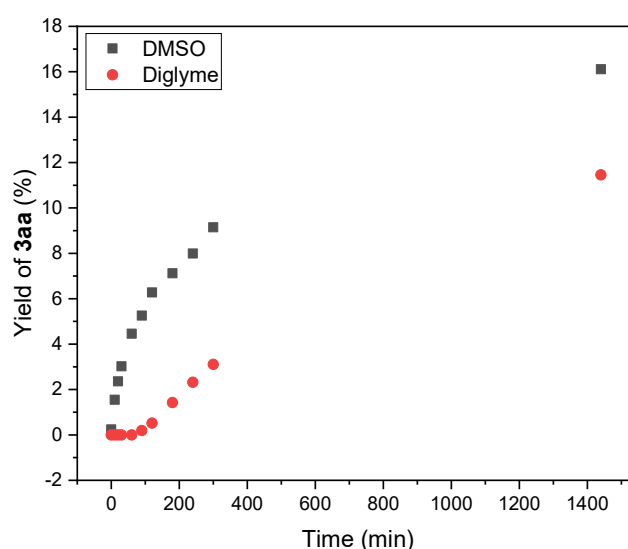


Figure 3.12: A plot detailing the effect solvent choice has upon the reactivity of PdAu-PVP in the coupling of **1a** and **2a** at 100 °C.

### 3.4. EG-capped Nanoparticles in Decarboxylative Cross-coupling Reactions

#### 3.4.1. Palladium/Copper Catalysed Decarboxylative Cross-coupling

Thus far, the investigations into the use of palladium/copper bimetallic nanoparticles have utilised particles synthesised under the same conditions. However, synthetic conditions can have pronounced effects upon reactivity of resulting nanoparticles. To investigate this, PdCu-EG bimetallic nanoparticles, as well as its monometallic components synthesised *via* the same protocol (Pd-EG and Cu-EG) were screened under standard reaction conditions at 100 °C (see Figure 3.13). It is immediately apparent when comparing the performance of the EG-capped Pd/Cu nanoparticles (Figure 3.13) to their PVP-capped analogues (Figure 3.6) that the former display greatly enhanced reactivity – with PdCu-EG reacting reaction completion in 1 hour, compared to the 4 hours required for PdCu-PVP. Reactivity is even observed in the case of the monometallic Pd-EG, reaching 15 % yield of reaction product **3aa** after 5 hours. Such reactivity isn't observed even in the case of the homogeneous catalyst Pd(OAc)<sub>2</sub> under the same conditions (see Figure 3.8). PdCu-EG doesn't reach 100 % conversion however, suggesting loss of catalytic activity after 1 hour.

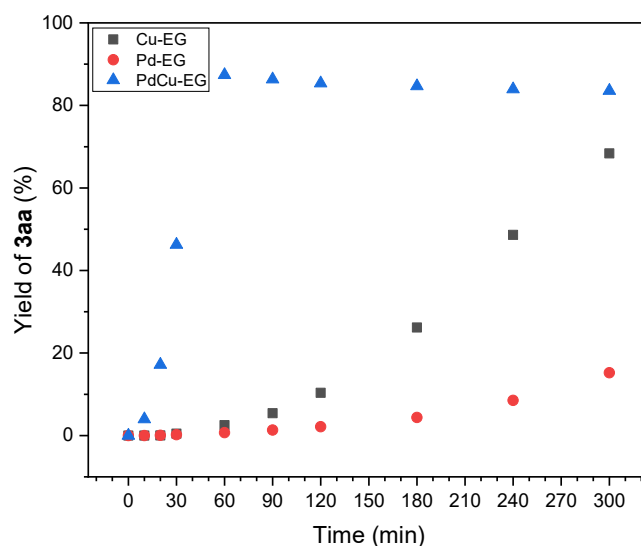


Figure 3.13: A plot comparing EG-capped Pd/Cu nanoparticles in the coupling of **1a** and **2a** at 100 °C. Loading of Cu-EG and PdCu-EG was 10 mol% with respect to copper content. Loading of Pd-EG was 10 mol% with respect to palladium content.

Comparing PdCu-EG's performance to the catalyst system Pd(OAc)<sub>2</sub> + CuI (Figure 3.8) shows that the EG-capped bimetallic nanoparticles outperform the

homogeneous system which requires 4 hours to reach reaction completion. However, PdCu-EG reaches a lower endpoint yield of product **3aa** – 87 % compared to 95 % for the homogeneous system. Despite this, it is clear that capping agent choice has a potent effect on the catalytic behaviour of the bimetallic palladium/copper catalysts. Without further characterisation data available it's hard to ascertain why the EG-capped particles perform as well as they do. Given that the AAS analysis of these materials suggested that EG is a poorer capping agent compared to PVP (see Table 3.9), a possible explanation for their performance may be that the weaker binding of the EG capping agent translates to increased lability of the capping agent, allowing for easier introduction of substrate to the catalytic surface. This is, however, speculation.

### 3.4.2. Nickel/Copper Catalysed Decarboxylative Cross-coupling

For the screening of the EG-capped nickel/copper bimetallic catalysts reaction conditions were kept as close as possible to those used in Figure 3.6. Unlike the observations made when utilising palladium/copper bimetallic particulate, no synergistic effect was found between nickel and copper. The bimetallic catalyst NiCu-EG was observed to perform better than its monometallic counterpart Ni-EG over a 5-hour period, but vastly underperformed relative to catalyst Cu-EG (see Figure 3.14).

Referring back to the analysis of these catalytic materials helps to explain the behaviour of these catalysts. TEM analysis showed that both Ni-EG and NiCu-EG exhibited a much larger average particle diameter compared to their copper monometallic analogue (see Table 3.7 and Table 3.9). These particles were also observed to display a much greater degree of polydispersity. This would result in a lower degree of catalytically active surface area compared to smaller, uniform particulate. AAS analysis revealed that catalyst NiCu-PVP contained much less nickel than was expected given the loading of nickel precursor in its synthesis. It is hypothesised that the reduction of the Ni<sup>2+</sup> ions proceeds at a slower rate than Cu<sup>2+</sup> ions under the conditions of the synthesis of NiCu-EG, which could result in core/shell style particulate with the copper active sites occluded by a layer of nickel.

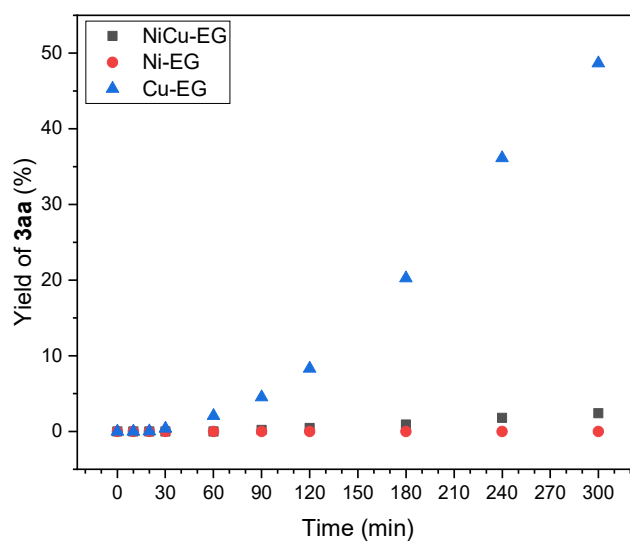


Figure 3.14: A plot comparing the performance of EG-capped nickel/copper nanoparticles in the coupling of **1a** and **2a** at 100 °C. Loading of Cu-EG and NiCu-EG was 10 mol% with respect to copper content. Loading of Ni-EG was 10 mol% with respect to nickel content.

Nickel and copper also both exhibit remarkably similar electronegativities (both 1.9 according to the Pauling scale) and therefore the flow of charge between nickel and copper regions is expected to be minimal – any copper not occluded by nickel is unlikely to be activated in the same way as is observed in palladium/copper bimetallic systems. A lack of charge distribution upon the surface of NiCu-EG may also help explain why the particulate was not observed to form spherical clusters of smaller particulate, instead simply forming a bulk agglomerate (see Figure 3.3c).

### 3.5. Conclusions and Future Work

Nanoparticles are excellent targets from a catalyst design perspective. Through manipulation of the conditions used in the synthesis of these materials the chemist is afforded a great deal of control over the properties of the resulting catalyst. Indeed, there has been much work undertaken in recent years exploring the scope for utilising these materials as replacements for conventional homogeneous or heterogeneous catalysts in a myriad of key chemical transformations<sup>48</sup>. A key aim of the work presented was to systematically investigate how manipulation of these synthetic conditions such as metal choice, metal ratios, capping agent choice and so on affects the efficacy of the resulting catalyst in a model reaction.

To accomplish this a wide library of both monometallic and bimetallic materials were synthesised according to preparations adapted from literature. Ensuring a tight distribution of particulate sizes was observed to be a challenge, particularly with the Pd/Ag-PVP and Ni/Cu-EG series of materials. Despite this, good to excellent control of size distribution was observed with the Pd/Cu-PVP, Pd/Cu-EG and Pd/Au-PVP series of materials and shape control was good across the library. In particular, PVP was found to be an excellent capping agent for controlling the growth of palladium monometallic and palladium/copper bimetallic nanoparticles, affording spherical particulate with average sizes of  $3.2-4.5 \pm 0.5-0.7$  nm, a narrow distribution. These Pd/Cu-PVP bimetallic nanoparticles were observed to agglomerate in larger, spherical clusters, a behaviour not observed in any other catalyst series save for the case of the palladium/copper bimetallic material PdCu-EG.

These palladium/copper bimetallic materials were found to be excellent catalysts when employed in a model DCC reaction. The ratio of palladium to copper was found to have a profound effect upon the performance of the nanoscale catalyst, with larger ratios performing better than smaller ratios. This is in spite of common literature wisdom which posits that DCC reactivity is rate-limited with respect to decarboxylation of the carboxylate substrate to yield an organometallic intermediate species – a copper catalysed transformation<sup>33,163</sup>. This can be explained by considering the relative differences in electronegativity between palladium and copper, 2.2 and 1.9 respectively according to the Pauling scale, and the resulting flow of charge that can be expected in a material that involves direct palladium-copper bonding. This is expected to result in electron deficient copper active sites and electron rich palladium active sites upon the surface of the nanoscale particulate, activating the copper sites towards decarboxylation and the palladium sites towards oxidative addition. Localisation of positive and negative charges upon the surface of the particulate may also help explain the ordered degree of agglomeration observed with both PVP- and EG-capped palladium/copper bimetallic systems.

Besides metal ratios, capping agent was also found to have a significant impact on the performance of palladium/copper bimetallic nanoscale catalysts, with catalyst

PdCu-EG bringing about the completion of a model DCC reaction in 1 hour, faster than its PVP-capped analogue PdCu-PVP. Future work in this area would likely take the form of expanding this palladium/copper bimetallic nanoparticle library further. There is considerable scope for modifying the ratio of palladium to copper in the materials. Indeed, working on a similar problem Rai *et al.* observed that pushing the ratio of nickel to palladium in their catalysts to the extreme (99-1 Ni:Pd) led to the most pronounced transfer of charge between nickel and palladium active sites and consequently the best performing catalyst of the series <sup>158</sup>. Therefore, it is a logical next step to produce more Pd/Cu-PVP materials with ratios of palladium to copper greater than 2:1. There is also scope for further exploring the role capping agent plays upon reactivity, not only in using different agents entirely such as poly(ethylene glycol) (PEG), but also in modifying the average molecular weights of these polymeric capping agents.

Investigations into modifying the choice of metals themselves was met with mixed success. Both the palladium/silver and nickel/copper series of catalysts were observed to underperform compared to their respective palladium/copper analogues. Both of these catalyst series were found, *via* TEM analysis, to display large average particle sizes compared to their palladium/copper analogues and, as previously discussed, a wide distribution of sizes. As such it can be said that these materials possess a smaller active surface area, which may help to explain their relative lack of catalytic activity. The PVP-capped palladium/gold catalyst PdAu-PVP, however, performed admirably. Employing PdAu-PVP in a standard DCC protocol, product yields of 20 % were reached over a 24 hour time period. Whilst Dupoy and Nolan have reported successful gold-promoted decarboxylations, they note having to use bespoke ligands and harsh reaction conditions to induce it, and cross-coupling fell outside the scope of their investigations <sup>26,40,43</sup>. At the time of writing, this work represents the first reported successful gold mediated DCC reaction and is especially exciting given the simplicity of synthesising and handling the palladium/gold bimetallic catalyst itself. Future work, therefore, would be focused on exploring the viability of palladium/gold bimetallic nanoparticulate under DCC conditions by tweaking the ratios of palladium to gold. There is also potential scope for refining the synthesis of the PVP-capped palladium/silver and EG-capped nickel/copper bimetallic materials, especially in the case of the nickel-containing catalysts given

the potential to incorporate these materials into induction heating applications. This could be achieved in several ways; for example there is good literature precedence for the use of micro-emulsions of water droplets contained within hydrophobic solvent to control the aqueous reduction of palladium, copper, silver and nickel salts and control the growth of the resulting particulate<sup>164</sup>.

## 4. Exploration of the Scope of Decarboxylative Cross-coupling under Low Temperature Conditions

### 4.1. Introduction

A common concern voiced in the literature surrounding decarboxylative cross-coupling (DCC) chemistry is the high reaction temperatures required to bring about successful decarboxylation and subsequent cross-coupling to yield biaryl product <sup>146</sup>. Such temperatures can lead to limited functional group tolerance as well as promotion of undesirable side reactions which, coupled with the increased costs associated with the conditions typical of DCC protocols (high temperatures and long reaction times) limit the real-world applicability of the chemistry. Improvements in catalyst design have been reported that bring these harsh conditions down to more acceptable levels, with prior work displaying the successful copper and copper/palladium catalysed DCC coupling of model substrate potassium pentafluorobenzoate (**1a**) at temperatures as low as 100 °C (see Figure 3.6), a 30-60 °C reduction in literature conditions <sup>17,33</sup>.

However, **1a** represents an ideal substrate for decarboxylative transformations as the potent electron-withdrawing nature of its 5 fluoro- groups leads to substantial polarisation of the aryl-carboxylate carbon-carbon bond, weakening it with respect to bond cleavage. Indeed, it is to be expected that aromatic carboxylates with aromatic rings that are more electron rich (compared to **1a**) would display stronger aryl-carboxylate bonds and therefore require harsher reaction conditions to decarboxylate. Exploring the multiple permutations of catalysts, loadings and substrate choices under these low-temperature conditions would be an exhausting task and therefore a more intelligent solution is desirable.

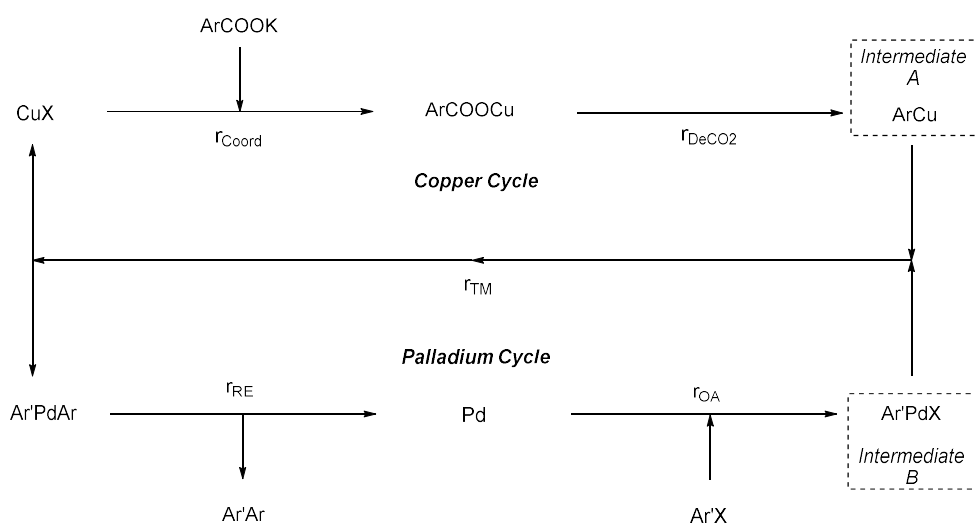
The work set out within this chapter is concerned with a number of studies exploring the scope of the DCC reaction and analysing the broader behaviour of the system under these low-temperature conditions. These include:

- The use of computational methodology to make informed decisions in selecting carboxylate substrate amenable to low-temperature decarboxylation.
- A comprehensive screening of several carboxylate and aryl halide reactants under such unconventional, low-temperature conditions.

- An exploration of the use of various homogeneous and nanoscale catalyst designs in a broader range of DCC pairings.

## 4.2. Bimetallic Catalysis and Choice of Substrate

When discussing the problems and potential solutions to poor substrate scope in a bimetallic reaction protocol, it becomes prudent to also discuss some of the challenges that accompany bimetallic catalysis approaches in general. Typically, a multi-catalyst reaction mechanism will involve a separate catalytic cycle for each catalyst. These catalytic cycles will interact with each other at one or more key reaction steps to facilitate the transfer of material. In the case of palladium/copper catalysed DCC, this has been hypothesised to occur during the transmetalation step, wherein the organocopper species Intermediate A generated in the copper catalytic cycle reacts with the organopalladium species Intermediate B generated in the palladium catalytic cycle (see Scheme 4.1).



- 1)  $r_{Coord} = k_{Coord}[CuX][ArCOOK]$
- 2)  $r_{DeCO2} = k_{DeCO} [ArCOOCu]$
- 3)  $r_{OA} = k_{OA}[Pd][Ar'X]$
- 4)  $r_{TM} = k_{TM}[Intermediate A][Intermediate B]$
- 5)  $r_{RE} = k_{Re}[Ar'PdAr]$
- 6)  $k = Ae^{\left(-\frac{Ea}{RT}\right)}$

Scheme 4.1: The hypothesised bimetallic catalyst cycle for palladium/copper DCC and associated rate equations for each step<sup>13</sup>.

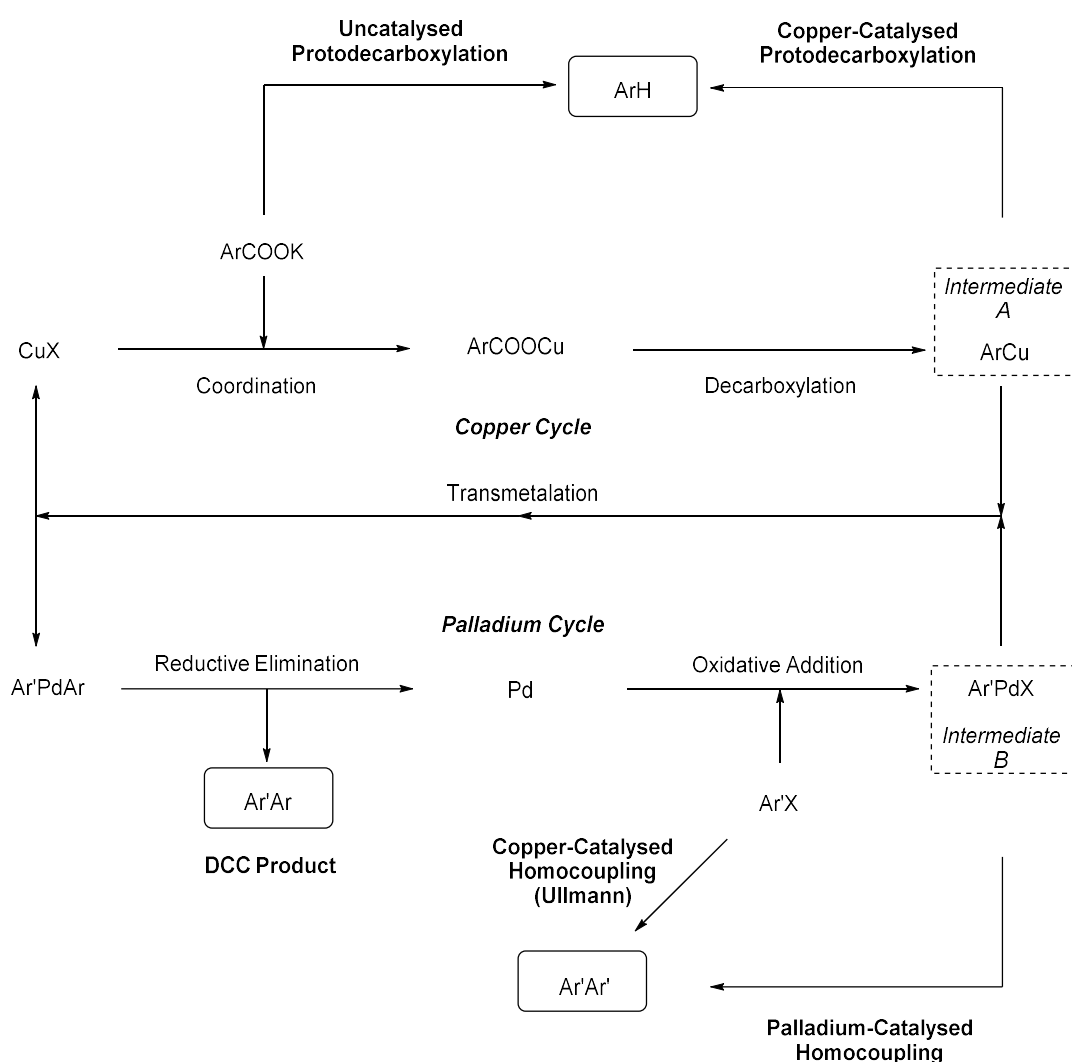
The result of this transformation is the transfer of the organic residue from Intermediate A to the palladium catalyst, regenerating the copper halide catalyst in the process<sup>13,33</sup>. This makes the transmetalation step dependent upon the rates of two separate transformations: the copper-promoted decarboxylation of carboxylate substrate and the oxidative addition of aryl halide starting material onto the palladium(0) catalyst, described by Equations 2 and 3 respectively (see Scheme 4.1).

If  $r_{\text{DeCO}_2}$  is equal to  $r_{\text{OA}}$  the two catalytic cycles are in sync. If we then assume that  $r_{\text{TM}}$  is far greater than either  $r_{\text{DeCO}_2}$  or  $r_{\text{OA}}$ , we can state that both Intermediate A and B will be consumed as they are generated; they will exist in a steady state until reaction completion. However, if  $r_{\text{DeCO}_2}$  is not equal to  $r_{\text{OA}}$  then one cycle is acting as a kinetic bottleneck for the bimetallic mechanism. For example, if  $r_{\text{DeCO}_2}$  is less than  $r_{\text{OA}}$ , the decarboxylation step would be rate limiting and we would see an increase in the concentration of Intermediate B with time. Similarly, if oxidative addition of aryl halide starting material was rate limiting,  $r_{\text{DeCO}_2}$  would be greater than  $r_{\text{OA}}$  and we would see an increase in the concentration of Intermediate A with time.

The reason this is important is that Intermediates A and B are highly reactive, unstable species. If one of the catalytic cycles is out of sync with the other, the resulting build-up of reactive organometallic intermediates translates to an increase in the prevalence of undesirable side reactions – depriving the bimetallic decarboxylative cross-coupling reaction of reagents and therefore reducing end point yields. The two most important side reactions to consider are protodecarboxylation for Intermediate A and homocoupling for Intermediate B.

This loss of starting material due to side reactions involving intermediate species is compounded by the fact that, under typical decarboxylative cross-coupling conditions, there is more than one route available to generate undesirable side products (see Scheme 4.2). The carboxylate salt starting material  $\text{ArCOOK}$  is able to protodecarboxylate even in the absence of a transition metal catalyst<sup>17</sup>. This of course has a much greater activation energy when compared to the catalysed reaction; however, for highly activated carboxylate salts such as substrate **1a** (which

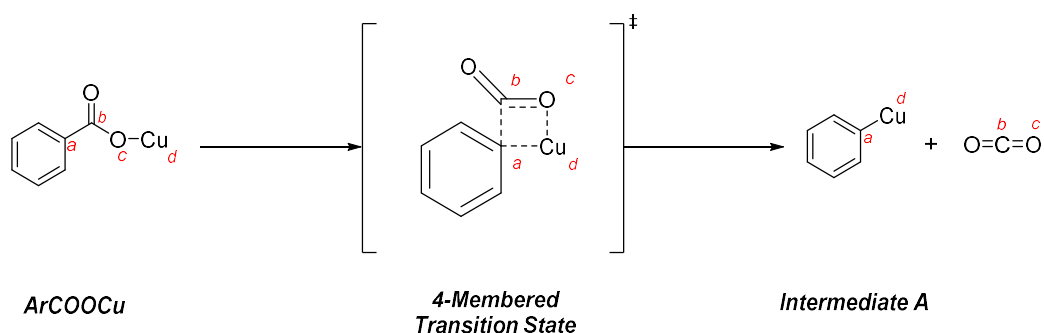
contain strong electron-withdrawing groups which help to reduce the build-up of negative charge during the uncatalysed transition state) this transformation becomes feasible at the reaction temperatures typically utilised in the literature. The aryl halide starting material Ar'X homocouples in the presence of copper. This is known as Ullmann coupling, and has been widely reported<sup>1,2,5,18,23</sup>.



*Scheme 4.2: An expanded bimetallic DCC cycle displaying competing side reactions*

Following on from the Arrhenius equation (Scheme 4.1, Equation 6), it can be observed that  $k$  is proportional to  $e^{(-Ea)}$  and  $e^{(-1/T)}$ , where  $k$  is the rate constant for a chemical transformation,  $Ea$  is the activation energy – the energy required to overcome the transformation's transition state – and  $T$  is the temperature of the system.  $A$  and  $R$  are constants. When we consider this alongside the rate equations displayed in Scheme 4.1, we can state that the rate of a particular step

depends upon three key parameters: the activation energy of the step; reaction temperature and finally the concentration of the reagents.



Scheme 4.3: The decarboxylation step – including hypothesised transition state <sup>33</sup>.

Activation energy describes the required energy that must be available to the system so as to both reach and overcome the transition state of a given transformation. We can rationalise activation energy by considering the strength of the bonds that are broken during the transformation. Assuming all other factors remain constant, the stronger the bonds, the lower the potential energy of the starting material and therefore the larger the difference between the energies of the starting material and the transition state: the activation energy. In the case of the decarboxylation step, shown in Scheme 4.3 we can see that two bonds break, *a-b* and *c-d*. Modifications to the substrate that weaken bond *a-b* will serve to destabilise the starting material, resulting in a lower activation energy and a faster rate of copper-mediated decarboxylation. Carboxylic acid substrates that contain electron-withdrawing groups capable of drawing electron density out of the aryl-carboxylate bond *a-b* will therefore help to promote the formation of Intermediate A.

In work investigating copper-promoted decarboxylation Goossen *et al.* noted that, in particular, *ortho*-substitution on the carboxylic acid or carboxylate salt substrate plays a very important role <sup>17</sup>. Evidence is provided that supports the idea that copper catalysts display a particular affinity for halide ions, such as those that would be released during decarboxylative cross-coupling with typical aryl halide coupling partners <sup>24</sup>. One solution to this problem is to employ the use of carboxylic acids that contain *ortho*- functionality capable of coordinating strongly enough to compete with the undesirable copper-halide coordination. *Ortho*- substitution also has the advantages of destabilising the aryl-carboxylate carbon-carbon bond *via* steric

repulsion and potentially electronic means if the substituents are electron-withdrawing in nature <sup>44</sup>.

This is why substrate **1a** is an ideal substrate for this transformation; it contains 5 highly electron-withdrawing groups on the aryl ring which act to draw electron density out of the *a-b* bond *via* an inductive effect, thereby weakening it. The presence of fluoro- groups in the positions *ortho*- to the carboxylate functionality further help increase the activity of substrate **1a** towards decarboxylation as they contain lone pairs of electrons, and thus can datively coordinate to the incoming copper catalyst *via* a favourable copper-halide interaction.

Whilst the low-temperature cross-coupling conditions outlined in Chapters 2 and 3 yielded excellent results, it was expected that such a dramatic reduction in reaction temperature compared to typical literature conditions would affect substrate scope – either slowing down the rate of decarboxylation dramatically or even failing to provide enough energy to overcome the activation energy required for decarboxylation to occur. Therefore, given the proven reactivity of substrate **1a** under the low-temperature conditions, it was decided to initially screen carboxylate salts with similar properties to **1a**: weak aryl-carboxylate bond and coordinating *ortho*- substitution.

To make an educated guess, computational chemistry was employed. The geometry of various fluoro-, nitro- and methoxy- containing aryl carboxylates were optimised utilising a 3-21g basis set (chosen with a consideration for computational cost). Nitro- functionality was chosen due to the increased potency of its electron-withdrawing potential compared to fluoro- groups <sup>165</sup>. Methoxy- functionality was chosen as, due to the electronegativity of oxygen relative to carbon, it is expected to display a weak inductive effect <sup>165</sup>. On top of this, it was hypothesised that the increased steric bulk of methoxy groups relative to fluoro- and nitro- groups may also help to weaken the aryl-carboxylate bond. With optimised geometries in hand, it was then possible to look through the structures for the length of the aryl-carboxylate bond. The length of a covalent bond can be used as a rough estimate for the strength of that bond, and therefore compounds that display an aryl-carboxylate

bond length similar to that observed in the optimised geometry of substrate **1a** would be potential candidates for screening.

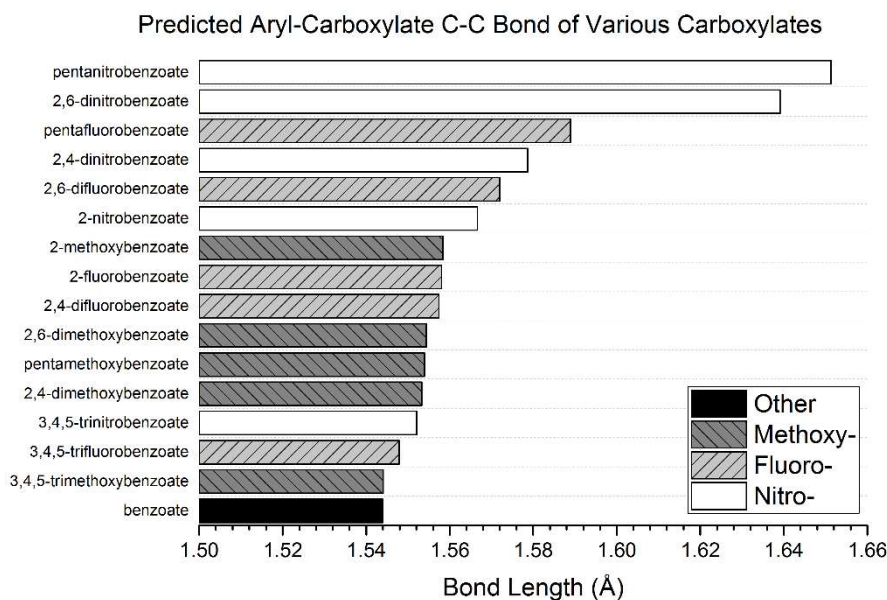


Figure 4.1: A plot comparing the length of the aryl-carboxylate carbon-carbon bond of various carboxylate anion candidates, derived from gas phase RHF 3-21g basis set optimised geometries.

As Figure 4.1 shows, two clear trends emerged. Firstly, for a given substitution pattern, the calculated length of the aryl-carboxylate carbon-carbon bond varied depending upon the identity of the functional groups: nitro- groups yielded the longest bond, followed by fluoro- groups and finally methoxy- groups. Secondly, for a given functional group identity, *ortho*- substitution was found to have the most pronounced effect on bond length; with 2,6- *diortho*- substitution typically displaying a bond length just below the idealised penta- substituted compound of its series. The methoxy- series were the only compounds to disobey this second trend. From this it can be postulated that the main factor in weakening the aryl-carboxylate bond is close-range inductive effects, with steric bulk playing a much less important role even in the *ortho*- positions. These findings agree with experimental work performed in the field by Goossen, who reported that using compounds possessing *ortho*- substituents capable of drawing electron density inductively through the  $\sigma$ -backbone of the carboxylate in their DFT calculations led to a significant reduction in the predicted Gibbs free energy for the copper-promoted decarboxylation step.

Indeed, the trend that they reported in that work is in good agreement with the trend displayed in Figure 4.1 <sup>27</sup>.

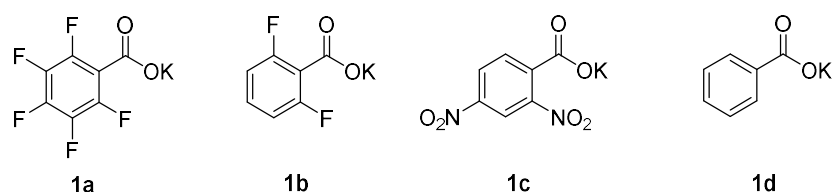


Figure 4.2: Carboxylate salts chosen.

Given the findings displayed in Figure 4.1, the following two compounds were chosen for substrate exploration: potassium 2,6-difluorobenzoate (**1b**) and potassium 2,4-dinitrobenzoate (**1c**) as they were the nearest neighbours to ideal substrate potassium pentafluorobenzoate (**1a**) and they displayed the *ortho*-substitution motif identified as important in Goossen's work. Potassium benzoate (**1d**) was also included in the screen as a baseline. Candidates pentanitrobenzoate and 2,6-dinitrobenzoate, despite being of potential interest, were not included in the screen as the carboxylic acid precursor for the former is not available commercially (likely due to the fact that it would be highly unstable and potentially dangerous to handle) and the latter was prohibitively expensive.

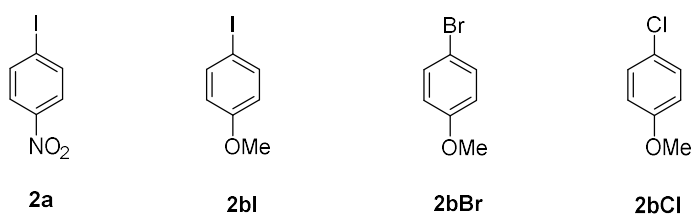


Figure 4.3: Aryl halides chosen.

To go along side these substrates two aryl halide coupling partners were implemented: 1-iodo-4-nitrobenzene (**2a**), which has seen extensive use during this project, and 4-iodoanisole (**2bI**). **2bI** was chosen as there was some concern that **2a**, owing to its strong electron-withdrawing group *para*- to the iodo- leaving group, would display a rate of oxidative addition that outpaced the rate of decarboxylation of the less activated carboxylate substrates; especially at the lower temperatures demanded by the project. This would, as previously discussed, lead to a build-up of

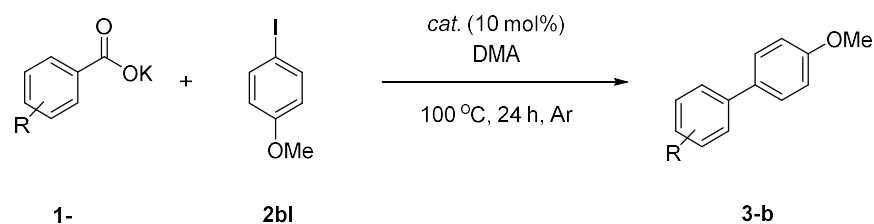
Intermediate B and potentially an increase in the prevalence of undesirable homocoupling side reactions (see Scheme 4.2). **2bI**, however, is expected to have a stronger C-I bond, and therefore a slower rate of oxidative addition, due to the weaker inductive effect displayed by methoxy- substituents <sup>165</sup>. Keeping with this theme 4-bromoanisole (**2bBr**) and 4-chloroanisole (**2bCl**) were also chosen, to further explore the effect increasing the strength of the carbon-halide bond of the coupling partner has on the reaction.

#### 4.3. Screening Substrates & Catalysts in Decarboxylative Cross-coupling Reactions

The initial conditions chosen were mainly those of the low temperature reactions outlined in Chapters 2 and 3: 100 °C and 10 mol% loading of catalyst (or 10 mol% loading of copper in the case of bimetallic systems). For each substrate pair, three types of catalyst were investigated: homogeneous, PVP-capped nanoparticles, and EG-capped nanoparticles. For each catalyst type, a 1:1 copper to palladium bimetallic system was investigated, alongside its monometallic copper and palladium counterparts for comparative purposes. The only notable changes from the low temperature conditions reported previously are the increase in reaction time from 5 hours to 24 hours and the move from diglyme to *N,N*-dimethylacetamide (DMA) as reaction solvent. Reaction time was increased as the use of less active carboxylate and aryl halide substrates was expected to result in slower rates of reaction. DMA was employed as solvent as it has been reported in the literature that for less activated carboxylate substrates, the use of DMA leads to an increase in end point yields. The results of this screen are displayed in Table 4.1.

The results of this series of experiments elucidated several things. Firstly, it is noted that the reactivity of ideal carboxylate substrate **1a** with coupling partner **2bI** is significantly poorer than was observed in prior experiments coupling **1a** with **2a**. One potential explanation for these findings is that the increase in reaction time and/or change of reaction solvent had affected the performance of the system. Diglyme has been cited in the literature as having a quality that makes it uniquely potent as a solvent for DCC reactions involving highly fluorinated carboxylate substrates <sup>33</sup> and DMA possesses completely different functionality.

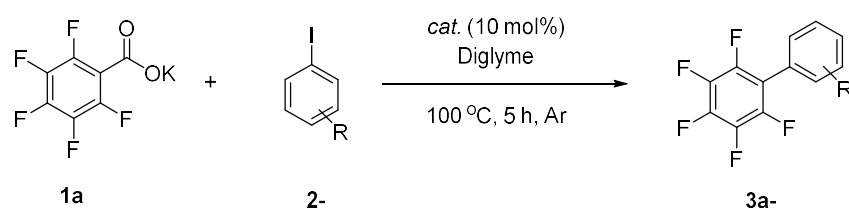
Table 4.1: Results of screening various carboxylate salts with different catalysts in a typical DCC reaction. <sup>a</sup> Determined via HPLC. Loading of catalysts: 10 mol% with respect to copper, or 10 mol% with respect to palladium if no copper was present.



Entry	Carboxylate Substrate	Catalyst	Product Yield (%) <sup>a</sup>
1	1a	CuI	4
2		Pd(OAc) <sub>2</sub>	43
3		CuI + Pd(OAc) <sub>2</sub>	85
4		Cu-PVP	0
5		Pd-PVP	28
6		PdCu-PVP	43
7		Cu-EG	0
8		Pd-EG	13
9		PdCu-EG	1
10	1b	CuI	0
11		Pd(OAc) <sub>2</sub>	48
12		CuI + Pd(OAc) <sub>2</sub>	34
13		Cu-PVP	0
14		Pd-PVP	26
15		PdCu-PVP	25
16		Cu-EG	0
17		Pd-EG	25
18		PdCu-EG	21
19	1c	CuI	2
20		Pd(OAc) <sub>2</sub>	0
21		CuI + Pd(OAc) <sub>2</sub>	4
22		Cu-PVP	0
23		Pd-PVP	0
24		PdCu-PVP	0
25		Cu-EG	0
26		Pd-EG	0
27		PdCu-EG	0
28	1d	CuI	0
29		Pd(OAc) <sub>2</sub>	0
30		CuI + Pd(OAc) <sub>2</sub>	0
31		Cu-PVP	0
32		Pd-PVP	0
33		PdCu-PVP	0
34		Cu-EG	0
35		Pd-EG	0
36		PdCu-EG	0

To test this explanation, **1a** was screened against **2bI** again, utilising the same 9 catalysts as displayed in Table 4.1 – Entries 1-9. The difference being that reaction time was brought back to 5 hours and diglyme was utilised as solvent. These results were then compared alongside the coupling of **1a** with **2a** under the same conditions. The findings from these experiments are displayed in Table 4.2.

Table 4.2: Results of screening ideal carboxylate **1a** against various aryl halides under unmodified low-temperature DCC conditions. <sup>a</sup> Determined via HPLC. Loading of catalysts: 10 mol% with respect to copper, or 10 mol% with respect to palladium if no copper was present.

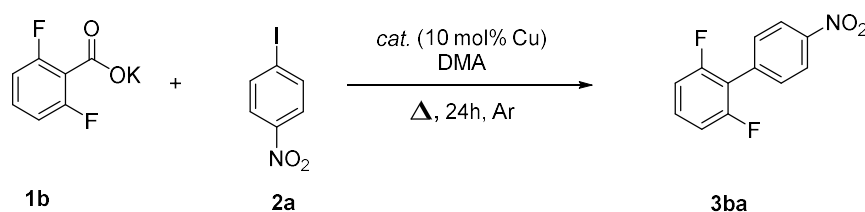


Entry	Aryl Halide Substrate	Catalyst	Product Yield (%) <sup>a</sup>
1	2bI	CuI	4
2		Pd(OAc) <sub>2</sub>	3
3		CuI + Pd(OAc) <sub>2</sub>	29
4		Cu-PVP	0
5		Pd-PVP	3
6		PdCu-PVP	Trace
7		Cu-EG	0
8		Pd-EG	0
9		PdCu-EG	Trace
10	2a	CuI	74
11		Pd(OAc) <sub>2</sub>	0
12		CuI + Pd(OAc) <sub>2</sub>	94
13		Cu-PVP	0
14		Pd-PVP	2
15		PdCu-PVP	83
16		Cu-EG	68
17		Pd-EG	15
18		PdCu-EG	77

As Table 4.2 – Entries 1-9 show, the trend of poor reactivity between ideal carboxylate **1a** and coupling partner **2bI** continued. Indeed, moving back towards the 5 hour, diglyme-solvated conditions yielded poorer results with all 9 catalysts (compare Table 4.1 – Entries 1-9 to Table 4.2 – Entries 1-9). Such findings lend

evidence against the notion that it was the change in reaction conditions that lead to poorer than expected reactivity. When substrate **2bI** was substituted for substrate **2a**, the yield of coupled product is improved dramatically in many cases (See Table 4.2 – Entries 10-18). Another explanation then presents itself: the source of poor reactivity between **1a** and **2bI** is due to the choice of substrate **2bI** itself.

Table 4.3: Results of screening various bimetallic catalysts against the DCC reaction of substrates **1b** and **2a** at different temperatures. <sup>a</sup> Determined via HPLC.

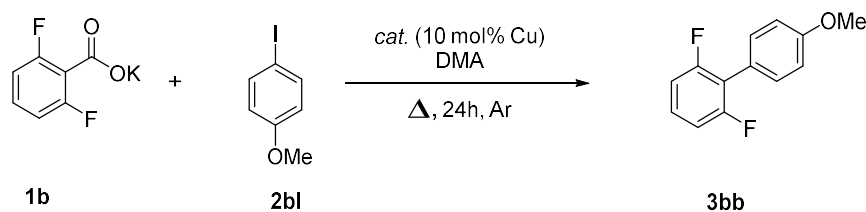


Entry	Catalyst	Temperature (°C)	<b>3ba</b> Yield (%) <sup>a</sup>
<b>1</b>	CuI + Pd(OAc) <sub>2</sub>	100	16
<b>2</b>		130	25
<b>3</b>	PdCu-PVP	100	15
<b>4</b>		130	16
<b>5</b>	PdCu-EG	100	23
<b>6</b>		130	20
<b>7</b>	Pd <sub>2</sub> Cu-PVP	100	8
<b>8</b>		130	13
<b>9</b>		160	14

However, this explanation is clouded when the coupling of **2bI** with carboxylate **1b** is brought under consideration. At first glance it would seem that, under the conditions displayed in Table 4.1, middling reactivity was again observed – the best performing catalyst palladium(II) acetate reaching a coupled product yield of 48 % after 24 hours of reactivity. But, substituting **2bI** for **2a** while keeping reaction conditions the same revealed a decrease in reactivity in all cases (compare Table 4.2 – Entries 12, 15 and 18 to Table 4.3 – Entries 1, 3 and 5, respectively). Interestingly, even under forcing conditions (increasing reaction temperatures from 100 to 160 °C and using high performing catalyst Pd<sub>2</sub>Cu-PVP in an attempt to take advantage of the synergistic effect) the yield of product **3ba** refused to improve to any significant

extent (see Table 4.3). This is directly contrary to what was observed when using carboxylate **1a**.

Table 4.4: Results of screening bimetallic catalysts against the DCC reaction of substrates **1b** and **2bI** at different temperatures. <sup>a</sup> Determined via HPLC.



Entry	Catalyst	Temperature (°C)	<b>3bb</b> Yield (%) <sup>a</sup>
<b>1</b>	CuI + Pd(OAc) <sub>2</sub>	100	34
<b>2</b>		130	93
<b>3</b>	PdCu-PVP	100	25
<b>4</b>		130	60

All the evidence gathered during these experiments points towards the following conclusion: carboxylate **1a** performs best when paired with **2a**, carboxylate **1b** performs best when paired with **2bI**. An explanation on why this might be the case harkens back to the idea of bimetallic catalyst cycles and the need to synchronise them (see Scheme 4.1).

Although displaying a mild negative inductive effect due to the relatively high electronegativity of oxygen compared to carbon, methoxy- groups are typically regarded as electron-donating groups in the literature, mesomerically donating electron density into the aromatic ring. As such it is reasonable to assume that **2bI** contains a stronger carbon-iodine bond compared to **2a**, whose nitro- functionality displays very strong negative inductive and mesomeric effects. This would equate to a relatively slower rate of oxidative addition of **2bI** onto the palladium catalyst compared to **2a**. Carboxylate **1a** has a weaker predicted aryl-carboxylate carbon-carbon bond than carboxylate **1b** (see Figure 4.1), and therefore it is reasonable to assume that under identical conditions **1a** would exhibit a faster rate of decarboxylation than **1b**. With these assumptions in mind, the conclusion becomes:

'fast' carboxylates perform best when paired with 'fast' aryl halides and *vice versa* for 'slow' carboxylates and 'slow' aryl halides.

As Table 4.4 shows, when pairing **1b** with **2bI**, the system becomes much more receptive to forcing conditions, with near complete conversion achieved at 130°C using 10 mol% copper(I) iodide and palladium(II) acetate as catalysts. The cycles are in sync, and therefore respond favourably to an increase in available thermal energy. When **1b** is coupled with **2a**, an increase in available thermal energy barely affects observed DCC product yield (see Table 4.3); the lack of synchronisation leads to a build-up of reactive intermediate that ends up being consumed by promoted side reactions.

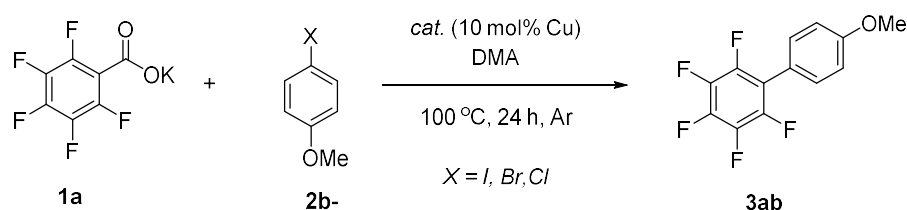
There are also the non-fluorinated carboxylate substrates to consider. As Table 4.1 shows, unfunctionalized carboxylate **1d** predictably failed to yield a successful DCC coupling with any of the catalysts under investigation using low temperature conditions. Figure 4.1 helps explain this, as it shows that **1d** was predicted to have the strongest aryl-carboxylate carbon-carbon bond. Not only would decarboxylation of **1d** be expected to be much slower than substrates such as **1a** and **1b**, it is likely that at 100 °C the system lacked the thermal energy to even overcome the decarboxylation activation energy in the first place.

**1c**, however, represents an interesting case. It was predicted to possess an aryl-carboxylate carbon-carbon bond with a length (and therefore strength) somewhere between substrates **1a** and **1b**. Yet, as Table 4.1 – Entries 19-27 show, the use of **1c** resulted in an almost complete elimination of reactivity. The best performing catalyst for this pairing was a 1:1 loading of copper(I) iodide and palladium(II) acetate, with a 4 % yield of DCC product. As previously discussed, it has been shown by other researchers in the field – particularly the research group of Lukas J. Goossen<sup>17,27</sup> – that coordinating functionality in the positions *ortho*- to the carboxylate group are vital for promoting DCC chemistry. It has also been stated in the literature that the copper catalysts typically employed in DCC protocols display a particular affinity for binding to halides<sup>17,24</sup>. Another point worth considering is that the stability of the starting material is not the only contributing factor to activation energy. Nitro- groups are bulky relative to fluoro- groups and therefore

we can expect that during the transition state there would be a greater degree of steric clashing (between the nitro groups and the rest of the system). This would raise the energy of the transition state itself, increasing the activation energy of decarboxylation.

Work reported up until this point has been concerned with the coupling of carboxylate salts with aryl iodide substrate. To investigate the effect the halogen atom has upon the reactivity of the substrate, the bromo- and chloro- analogues of substrate **2bI** were screened against typical conditions. The results of this investigation are displayed in Table 4.5. Changing the halogen atom is expected to alter the strength of the carbon-halogen bond with the following trend: I < Br < Cl. As the carbon-halogen bond strength increases, the activation energy required to break that carbon-halogen bond is also expected to increase. If we then consider the Arrhenius equation (Scheme 4.1, Equation 6) and assume that available thermal energy (reaction temperature) is held constant, we would expect that the rate of oxidative addition of the aryl halide coupling partner onto the palladium catalyst, and therefore the generation of Intermediate B, is expected to decrease; increasing the disparity of rates between the copper and palladium catalytic cycles and leading to poorer DCC reactivity.

Table 4.5: Results showing the effect varying the halogen atom of the aryl halide substrate has upon reactivity in a typical DCC reaction. <sup>a</sup> Determined via HPLC.



Entry	Aryl Halide Substrate	Catalyst	<b>3ab</b> Yield (%) <sup>a</sup>
<b>1</b>	2bI	CuI + Pd(OAc) <sub>2</sub>	85
<b>2</b>		PdCu-PVP	43
<b>3</b>	2bBr	CuI + Pd(OAc) <sub>2</sub>	6
<b>4</b>		PdCu-PVP	1
<b>5</b>	2bCl	CuI + Pd(OAc) <sub>2</sub>	Trace
<b>6</b>		PdCu-PVP	Trace

Predictably this is indeed what was observed, with substrate **2bI** vastly outperforming **2bBr** and **2bCl** resulting in a negligible conversion of starting material to product **3ab**.

#### 4.4. Conclusions and Future Work

Being able to employ the use of carboxylic acids and their derivatives as coupling partners in transition metal catalysed cross-coupling protocols is a desirable goal. Carboxylic acid functionality is abundant, both commercially and naturally. Further, they are typically cheaper other direct coupling partner analogues such as boronic acids. Because of this, developing low temperature DCC protocols dovetails nicely with the core reasons for employing this chemistry in the first place: keeping costs low and expanding the scope of substrate amenable to cross-coupling methodology.

However, decarboxylation is an energetically demanding transformation, necessitating the cleavage of a strong carbon-carbon covalent bond. High reaction temperatures are therefore, in many cases, a necessary evil to overcome the imposing decarboxylation activation energies of carboxylic acid substrate. Whilst much work has been performed exploring the applications of DCC at temperatures in excess of 130 °C, comparatively fewer studies have been undertaken below this<sup>17,31,44</sup>. Also, much of these low temperature studies resort to the use of palladium/silver bimetallic catalyst systems, which bring with them both increased costs and intolerance with respect to aryl halide coupling partners compared to their palladium/copper alternatives<sup>32</sup>. In prior work, successful palladium/copper catalysed DCC reactivity had been achieved at temperatures as low as 100 °C and therefore a key aim of the work presented in this chapter was to gain insight into the behaviour of the DCC reaction at this low-temperature frontier.

Conventionally, such a study would be performed by choosing one parameter, for example carboxylic acid substrate choice, and exploring a great deal of variations of that parameter, holding all other variables constant. This is a useful approach as it allows the researcher to screen a wide variety of substrates without needing to explore each and every combination of variables. However, such an approach fails to explore the relationships between the variables. Therefore, the methodology utilised in this study was to select a small number of viable screening candidates of

varying molecular properties with the aid of theory and DFT calculations and explore the pairings with a greater degree of rigor.

In undertaking this study, an interesting phenomenon was observed, with certain substrate pairings (**1a** and **2a**, **1b** and **2bI**) resulting in considerably greater reactivity than others. Due to the multi-metallic nature of the catalysts used it is posited that this phenomenon is due to a need to match the kinetic rates of both the copper and palladium catalytic cycles, parameters that are affected by substrate choice. This has not been mentioned in similar substrate screens in the field<sup>17,33</sup> and taking advantage of this phenomenon could allow for several interesting DCC couplings to proceed at low temperatures. As the work presents shows, however, inducing successful DCC reactivity under these relatively low temperature conditions remains a challenge when moving away from idealised DCC substrate **1a**. At this frontier, with the reaction so starved of energy, each substrate pairing necessitates re-optimisation of reaction conditions such as solvent choice and temperature in order to produce a respectable end point yield of DCC product. Because of this there is a broad scope for building upon the knowledge gained *via* this exercise.

Cornella *et al.* observed that, utilising gold(I) homogeneous catalysts, it was possible to induce decarboxylation at substantially lower temperatures when compared to copper and silver catalysed systems<sup>166</sup>. As observed by Nolan *et al.*<sup>43</sup>, they found these decarboxylations to afford stable and isolatable aryl-gold(I) complexes, rather than free decarboxylated product. However, whilst proceeding at reaction temperatures as low as 60 °C for a respectable number of substrates, stoichiometric quantities of both gold and silver mediators were required<sup>166</sup>. Utilising a bespoke, adamantyl-1-carboxylate-ligated gold(I) catalyst Nolan *et al.* was able to develop a true decarboxylation, catalytic with respect to gold; however the reaction temperatures utilised were in excess of 120 °C<sup>40</sup>. Neither Cornella nor Nolan report a successful cross-coupling, merely decarboxylation. Given the proven reactivity of PVP-capped palladium/gold catalysts towards model DCC protocols under low-temperature conditions displayed in prior work (see Figure 3.12), future work could explore the application of these palladium/gold nanoscale materials in broadening the scope of true low-temperature DCC reactivity.

Using computational calculations to both aid in the selection of substrate and inform the interpretation of the resulting data was in large part a success. However, it is clear that the rudimentary 3-21g basis set calculations were not able to account for all of the trends observed empirically, particularly in the case of the reactivity displayed by the dinitro- substrate **1c**. Selecting a basis set for DFT calculations is always a trade-off between the quality of the resulting data and the time it would take to acquire it but, time permitting, future work would benefit from revisiting these geometry optimisations with a more rigorous basis set. Beyond this, there would also be great value in attempting to model the reaction steps themselves, to gain direct insight into how substrate selection affects activation energy.

## 5. Poly(ethylene glycol) as an Additive to Promote Reactivity in Decarboxylative Cross-coupling

### 5.1. Introduction

Decarboxylative cross-coupling (DCC), as well as other decarboxylative reactions, are thriving areas of research. The novelty of bringing about meaningful carbon-carbon bond formation from cheap and widely available carboxylic acid substrate makes these processes interesting and useful and researchers are engaged in studies ranging from catalyst design to substrate scope exploration to mechanistic investigations. However, the solvents commonly utilised in these investigations leave a lot to be desired.

Typical literature protocols require the use of solvents such as quinoline, *N,N*-dimethylacetamide (DMA) or diethylene glycol dimethyl ether (diglyme)<sup>17,31,44</sup>. DMA and diglyme have both featured on the European Chemical Agency's list of substances of very high concern for authorisation of use, under the European Union's REACH regulation, due to their teratogenic properties and risk of damaging fertility<sup>167,168</sup>. Quinoline is no better, displaying acute toxicity both *via* oral and dermal exposure as well as mutagenicity and carcinogenicity<sup>169</sup>. Quinoline also presents a chronic hazard towards aquatic life, raising environmental concerns. By in large, solvent accounts for the majority of waste produced during a synthetic procedure<sup>111,170,171</sup> and therefore, in light of these properties, all of these solvents can be considered to be undesirable from a green chemistry perspective. Their replacement with suitable alternatives would go a long way in improving the overall applicability of DCC reactions to real world synthesis and production.

Replacement of these solvents, however, is a non-trivial task. Liu identified in his study on copper-catalysed DCC transformations that diglyme and DMA seemed to play important roles in the reactivity of the system. Attempts to move away from these solvents were met with dramatically reduced reactivity<sup>33</sup>. Therefore, the work presented within this chapter seeks to explore a variety of informed methods of solvent selection to solve this problem. These include:

- Using solvent mapping techniques as an intelligent way of selecting solvent candidates.

- Exploring the use of glycols as “glyme-like” additives, to replicate the effect glymes have upon DCC reactivity.
- Using design of experiment methodology as a rational approach to optimisation with multiple parameters.

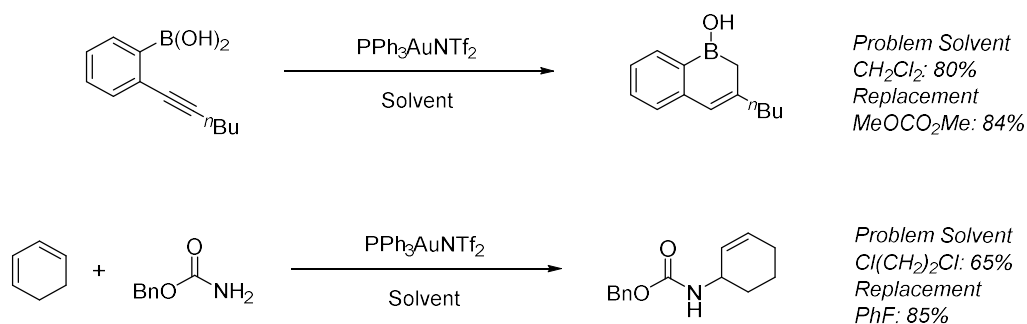
## 5.2. Applying Solvent Mapping to a Typical DCC Protocol

When approaching the task of substituting a problematic solvent with a greener, safer alternative, one approach available to the researcher would be a systematic screening of a variety of solvents. Such an approach may indeed yield results but runs the risk of being time consuming and wasteful. Instead, a more logical approach would be to look at the problematic solvent with proven reactivity and question why it works. Solvents can be defined through a myriad of properties, for example: boiling point, melting point, polarity, polarizability, viscosity, hydrogen bonding and halogen bonding. This list is far from exhaustive and yet illustrates this point well. All of these properties will play a role in the synthetic process with differing importance depending on the nature of the process itself.

Faced with the prospect of ascertaining the importance of a great number of properties in defining a good solvent for a given synthetic procedure, the researcher could be forgiven for balking slightly at the task. However, through the use of Principle Component Analysis (PCA), it is possible to derive a small number of numeric values that describe many individual properties and therefore reducing the overall dimensionality of the problem<sup>172</sup>. By considering these values, or “Principle Components” (PC) it is possible to draw meaningful comparisons between the problematic solvent and potential replacement candidates, allowing for many solvents to be discarded out of hand due to wildly differing PCs compared to the original solvent.

Such an approach was demonstrated by Murray, wherein approximately 20 physical and calculated properties of 136 commonly used laboratory solvents were rendered down into four PCs *via* PCA methodology<sup>111</sup>. By considering each solvent as a point on a plot with coordinates corresponding to its PCs, maps of the solvent space with respect to the PCs can then be derived. On such a map, the closer two points are, the greater the similarity of the solvents those points describe. This

methodology was used to great effect in substituting undesirable solvents in gold-catalysed cyclisations and hydroaminations. In all cases, the “nearest neighbour” solvents on the solvent map were found to perform similarly or better than the original solvent system (see Scheme 5.1) <sup>111</sup>.



*Scheme 5.1 Using PCA analysis to identify suitable replacements for hazardous solvents <sup>111</sup>.*

By considering each solvent described in the open access data supplied alongside Murray’s work as a point in space with four coordinates corresponding to four identifying PC’s, it is possible to calculate the distance between a starting solvent and every other solvent in the database (see Equation 5.1).

$$\sqrt{(PC1_x - PC1_y)^2 + (PC2_x - PC2_y)^2 + (PC3_x - PC3_y)^2 + (PC4_x - PC4_y)^2}$$

*Equation 5.1: Formula for determining the distance between two solvents described by four PCs. The lower the value, the closer the solvents are on the PCA derived solvent map.*

In so doing, a number of potential candidates for replacement would be revealed. For this exercise, dipropylene glycol dimethyl ether was chosen as the starting point as it represented the closest approximation to the problem solvent diglyme described within the Murray database. Using the formula displayed in Equation 5.1, the ten nearest neighbours were elucidated.

From the resulting list, candidates that contained carbonyl functionality such as acetates and ketones were discarded due to their potential reactivity under typical

DCC conditions. Dipentyl ether was, unfortunately, unavailable at the time of experimentation however this still left three potential replacement candidates: butyl butyrate, dipentyl ether and tripropylamine (see Figure 5.1). Although containing ester functionality and therefore being potentially susceptible to attack by the organocopper reaction intermediate generated during DCC, butyl butyrate was accepted as a candidate due to it being the nearest neighbour found and due to its innocuous list of hazards.

*Table 5.1: Nearest neighbour analysis of Murray's open access PCA solvent database, with the diglyme-like dipropylene glycol dimethyl ether chosen as a starting point. <sup>a</sup> Not commercially available at the time of experimentation in ethery hydrous or anhydrous forms.*

<b>Solvent</b>	<b>PC1</b>	<b>PC2</b>	<b>PC3</b>	<b>PC4</b>	<b>Distance</b>	<b>Status</b>
Dipropylene glycol dimethyl ether	2.22369	1.0575	-0.27562	2.77445	0	Starting Point
Butyl butyrate	3.07295	0.360229	0.105183	1.98061	1.408055	Selected
Methyl amyl acetate	3.06064	0.739433	-0.23613	1.60885	1.470318	Potentially Reactive
Dipentyl ether	3.93542	1.10418	-0.77128	2.32808	1.837697	Unavailable <sup>a</sup>
di-tert-butyl ketone	1.81151	1.188	-2.2443	2.36019	2.057729	Potentially Reactive
Ethyl amyl ketone	1.21835	1.14146	-1.99482	1.94809	2.157844	Potentially Reactive
Isopentyl acetate	1.96793	-0.08232	-0.38053	0.80927	2.288565	Potentially Reactive
Methyl isoamyl ketone	2.19719	-0.04491	-0.47652	0.772094	2.294736	Potentially Reactive
di- <i>n</i> -butylether	3.35797	-0.57203	-0.95389	1.39431	2.511337	Selected
tripropylamine	3.38565	0.490035	-2.45089	3.00247	2.540862	Selected
Ethyl butyl ketone	0.974324	0.529559	-1.84173	1.21951	2.590403	Potentially Reactive

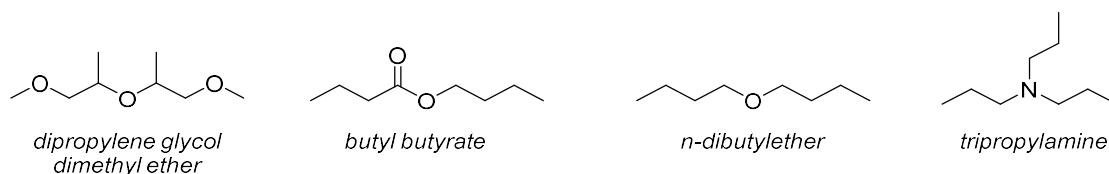
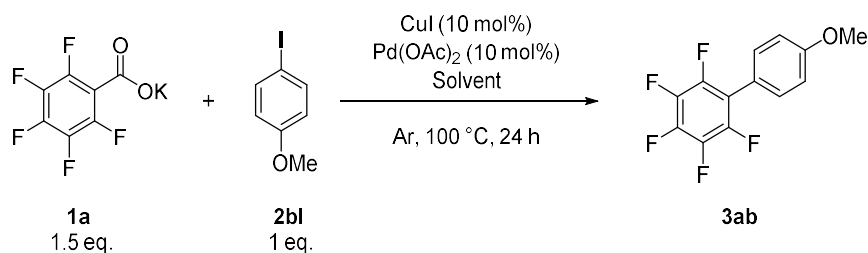


Figure 5.1: The selected replacement candidates, butyl butyrate, *n*-dibutylether and tripropylamine, displayed alongside the starting point dipropylene glycol dimethyl ether.

These solvents were then screened against a model DCC reaction between substrates **1a** and **2bI** (see Scheme 5.2). After 24 hours, the crude reaction mixture of these experiments was analysed *via* the use of  $^1\text{H}$  NMR and  $^{19}\text{F}$  NMR and compared to pure reference compounds so as to determine the efficacy of the solvent. The results of this analysis are displayed in Figure 5.2 and Figure 5.3 respectively. Examining Figure 5.2, it appears that the yield of DCC product **3ab** is so low as to be undetectable in all cases. It is only when we consider the  $^{19}\text{F}$  NMR spectra depicted in Figure 5.3 that a trace amount of **3ab**, as well as protodecarboxylation side product pentafluorobenzene (**5a**) is detected in the crude reaction mixture of the experiment solvated by butyl butyrate, the closest neighbour to the starting solvent (see Table 5.1).



Scheme 5.2: Model DCC reaction for the screening of replacement solvent candidates.

Note that in the case of the  $^1\text{H}$  NMR spectra displayed in Figure 5.2, the crude nature of the samples means that solvent effects are observed, causing drift in the observed chemical shifts of the various peaks. As such, a direct comparison of chemical shifts between crude samples and the reference compounds is not possible. The reference spectra are there merely to allow for a comparison of coupling patterns and to emphasise the fact that no peaks corresponding to DCC product **3ab**

are present in any of the crude mixtures. The doublet-triplet-doublet pattern of peaks observed between 7.2-7.8 ppm in the crude samples corresponds to biphenyl, an internal standard.

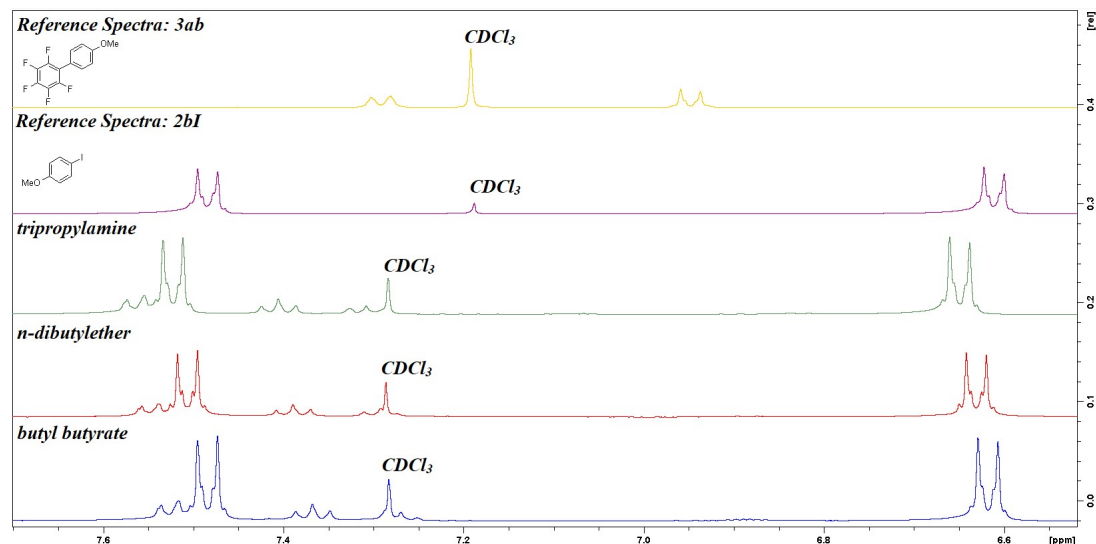


Figure 5.2:  $^1\text{H}$  NMR spectra (400 MHz,  $\text{CDCl}_3$ ) of the crude reaction mixtures of the experiments concerned with the screening of potential solvent replacement candidates under the conditions depicted in Scheme 5.2. Pure reference spectra for compounds **2bI** and **3ab** are included for clarity.

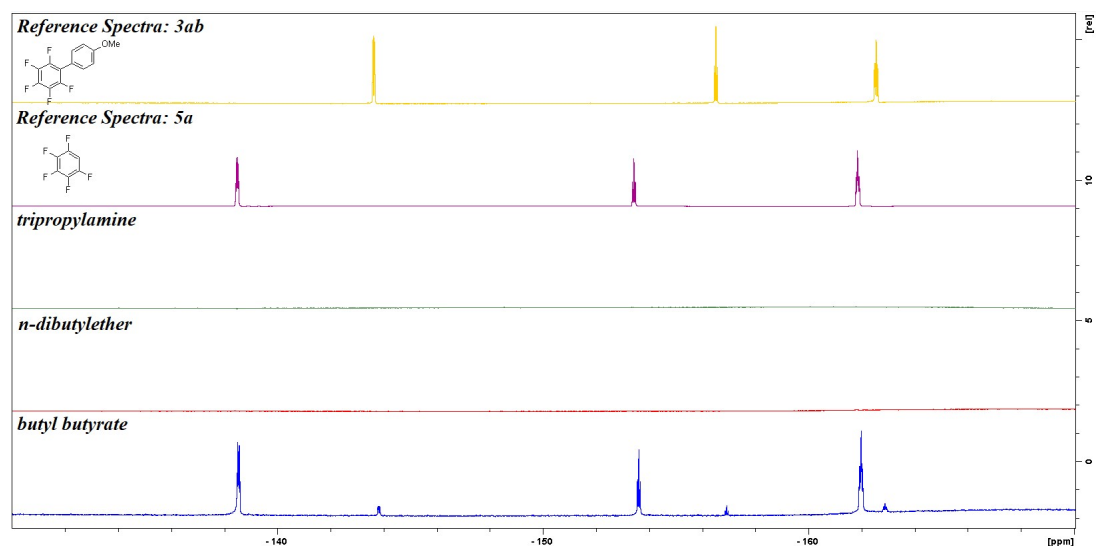


Figure 5.3  $^{19}\text{F}$  NMR spectra (376 MHz,  $\text{CDCl}_3$ ) of the crude reaction mixtures of the experiments concerned with the screening of potential solvent replacement candidates under the conditions depicted in Scheme 5.2. Pure reference spectra for compounds **3ab** and protodecarboxylation side product **5a** are included for clarity.

### 5.2.1. Using Glycols to Improve Reactivity

The results of the screening experiments displayed in Figure 5.2 and Figure 5.3 were dramatically below expectation. Under similar conditions, utilising diglyme as solvent, over a timescale of 5 hours, a yield of 29 % of DCC product **3ab** was observed (see Table 4.2, entry 3). This therefore suggests that the PCA model and associated PC's developed by Murray *et al.* do not adequately describe the properties that makes diglyme a good solvent for DCC reactions. In examining his model, Murray suggests that PC1 correlates largely with a solvents polarity, PC2 correlates largely with polarizability and PC3 correlates largely with the ability of a solvent to form hydrogen bonds<sup>111</sup>. PC4 is not commented upon and it is therefore assumed that there is no strong correlation between PC4 and a particular solvent property<sup>111</sup>. When considering all four PCs, Murray observed approximately 80 % of the solvent properties used to construct the PCA map are modelled effectively, meaning that although the vast majority of properties are accounted for by the four PCs, there is some oversight when utilising them.

Both Shang<sup>33</sup> and Zhao<sup>128</sup> have hypothesised that the quality that makes diglyme a potent DCC solvent is in its ability to chelate potassium ions. As such when a potassium benzoate substrate or potassium base is utilised, formation of a copper-carboxylate complex is facilitated *via* the extrusion of potassium ions by the glyme solvent, leading to greater concentrations of the copper-carboxylate reaction intermediate and therefore an improved rate of decarboxylation. Knowing that it is possible that this chelation property is not accounted for by Murray's PCA model, an alternative solution was instead derived from the structure of diglyme itself – poly(ethylene glycol) (PEG).

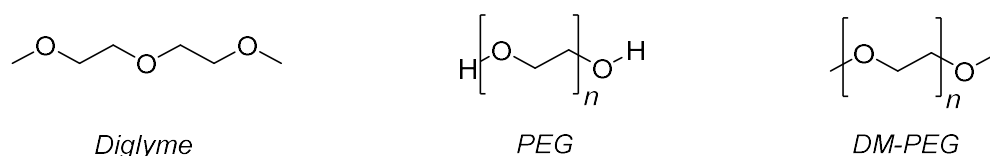
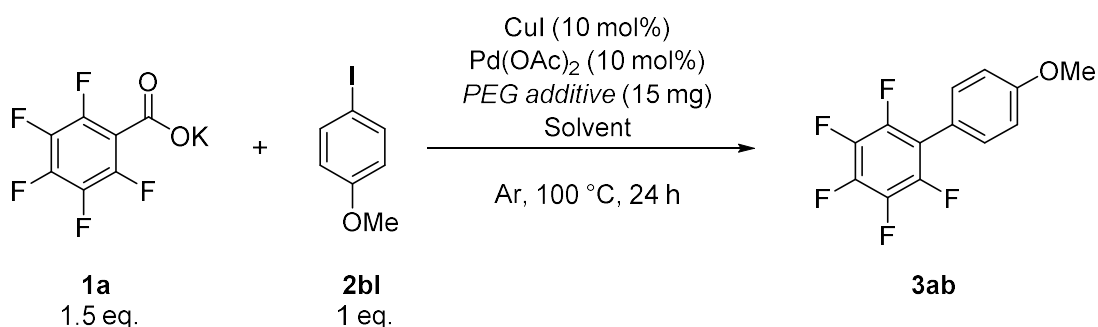


Figure 5.4: A comparison of the structural formulae of diglyme, PEG and DM-PEG.

Diglyme is comprised of two ethyl chains and two methyl terminal groups connected with ether linkages. This pattern of ethyl chains connected *via* ether

functionality is also observed in PEG and its various derivative compounds (see Figure 5.4). As such, it is hypothesised that PEG could be used as an additive in greener but unreactive solvents such as those identified by the PCA model exercise described in Subchapter 5.2. Unfunctionalized PEG, however, presents a potential problem for DCC reactivity. Each end of the PEG polymer is terminated in a hydroxy- group. This therefore provides a potential source of protons and as a result could lead to an increased prevalence of undesirable protodecarboxylation. The solution to this problem is to utilise dimethylated poly(ethylene glycol) (DM-PEG), replacing the hydroxy- capping groups with methoxy- functionality. In so doing, the structure of the resulting polymer bears such a similarity to diglyme that diglyme could be considered DM-PEG where the polymer chain length is equal to two.



*Scheme 5.3: Modified DCC protocol incorporating the use of PEG additives.*

To test this hypothesis, the PCA model-derived solvent screening experiments were repeated, differing in the inclusion of either PEG or DM-PEG as an additive. Both additives were utilised with relatively small average molecular weights, with PEG being  $\sim 300 \text{ gmol}^{-1}$  (PEG-300) and DM-PEG being  $\sim 500 \text{ gmol}^{-1}$  (DM-PEG-500). For these experiments, both additives were utilised as supplied with no further purification. They were incorporated into the model DCC reaction protocol depicted in Scheme 5.2 with a loading of 15 mg (see Scheme 5.3). The results of these experiments, as well as the results of the prior screening without additives for comparative purposes, are displayed in Table 5.2.

In all cases the addition of PEG, whether unfunctionalized or dimethylated, resulted in an improvement in observed reactivity. Such improvements were minimal with PEG-300, with only a trace of product **3ab** being observed *via* NMR analysis.

Table 5.2: Using PEG additives to improve reactivity in poor-performing solvent. Conditions: **1a** (0.75 mmol), **2bI** (0.5 mmol), CuI (0.05 mmol), Pd(OAc)<sub>2</sub> (0.05 mmol), PEG additive (15 mg), solvent (2 mL), 100 °C. <sup>a</sup> determined via <sup>1</sup>H NMR.

Entry	Solvent	Additive	<b>3ab</b> Yield (%) <sup>a</sup>
1	Butyl Butyrate	None	Trace
2		PEG-300	Trace
3		DM-PEG-500	10
4	Tripropylamine	None	0
5		PEG-300	Trace
6		DM-PEG-500	16
7	<i>N</i> -dibutyl ether	None	0
8		PEG-300	Trace
9		DM-PEG-500	8

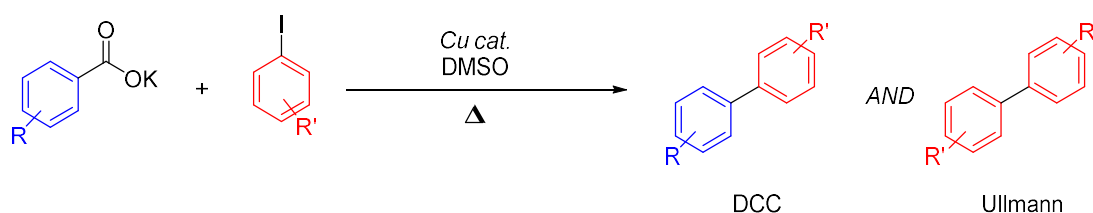
However, with DM-PEG-500, a substantial improvement was noted. In all cases, **3aa** yield is lower than was observed when utilising unfavourable solvent diglyme, but that any yields at all were observed is a marked improvement. Such findings help confirm the idea that the bare hydroxyl- functionality of PEG leads to suppression of the desired DCC reaction, when compared to its capped analogue DM-PEG.

### 5.3. Exploring the Role of Poly(ethylene glycol) in DCC Reactivity

Whilst the addition of PEG additives to the PCA map selected solvent series did lead to improved reactivity in all cases, observed yields of DCC product **3ab** were all low relative to competing solvent systems such as diglyme and dimethyl acetamide (DMA) (see Table 4.2 entry 3 and Table 4.1 entry 3 respectively). Because of this it was decided to take the lessons from this solvent screening exercise and apply them to a green solvent that has performed well in previous experiments: dimethyl sulphoxide (DMSO). The boiling point of DMSO coupled with its aprotic nature and minor safety concerns compared to competing solvent systems such as the aforementioned diglyme and DMA make it an excellent candidate for the replacement of troubling solvents in DCC protocols.

However, previous experimentation with DMSO in copper catalysed DCC revealed a significant discrepancy in the mass balance between starting material and DCC product at reaction completion (see Table 2.6). The conclusions of these

experiments, backed by similar research reported in the literature <sup>127</sup>, was that the presence of DMSO in the reaction lead to the promotion of the undesired Ullmann coupling of the aryl halide coupling partner typical of DCC protocols to yield homocoupled biphenyl product (see Scheme 5.4). Prior work found that the inclusion of diglyme as an additive to DMSO lead to improvements in DCC yield (see Table 2.7) and therefore it is logical to hypothesise that, given the results displayed in Table 5.2, DM-PEG may elicit a similar effect.



*Scheme 5.4: Use of DMSO under typical DCC conditions leads to promotion of both DCC and Ullmann homocoupling, lowering overall yields of DCC product.*

Given its polymeric nature, DM-PEG affords the opportunity to investigate the effect polymer chain length has upon the reaction. To probe this both DM-PEG-500 and the larger DM-PEG-1000 (average molecular weight 1000 gmol<sup>-1</sup>) were placed under investigation. DM-PEG molecules are expected to coordinate to potassium ions through the various ether groups that comprise its structure – therefore to ensure that the same number of coordination sites are present the loading of DM-PEG was fixed at 15 mg, per the conditions utilised in Table 5.2. This ensures the same number of ether groups (oxygen atoms) no matter the average molecular weight of DM-PEG utilised (see Table 5.3)

Under the conditions of the experiments described in Table 5.2, both PEG-300 and DM-PEG-500 were utilised as supplied. However, as the reactions progressed, vigorous effervescence was noted in both cases. DCC reactivity does produce a gaseous side product, carbon dioxide, but the presence of middling to trace observed quantities of DCC product suggests that protodecarboxylation was also being promoted under these conditions.

Table 5.3: Mathematical exercise justifying fixing the loading of DM-PEG additives by weight. <sup>a</sup> Monomer molecular weight divided by average polymer molecular weight, excluding capping groups.

Additive	Avg. Mr (gmol <sup>-1</sup> )	Avg. # of Monomers <sup>a</sup>	Avg. # of O Atoms	Loading (mg)	Loading (mmol)	Avg. Quantity of O Atoms (mmol)
<b>DM-PEG- 500</b>	500	10.30	11.30	15	0.03	0.34
<b>DM-PEG- 1000</b>	1000	21.65	22.65	15	0.015	0.34

Protodecarboxylation proceeds *via* a similar first step to DCC: decarboxylation of a carboxylate substrate to yield organocopper reaction intermediate. As such, it also produces carbon dioxide as a side product. Probing the butyl butyrate solvated reaction spiked with 15 mg of DM-PEG-500 *via* NMR techniques confirmed this suspicion. As Figure 5.5 shows, the characteristic first order multiplet caused by coupling between <sup>1</sup>H and <sup>19</sup>F spin ½ nuclei of protodecarboxylation side product pentafluorobenzene (**5a**) can be clearly observed.

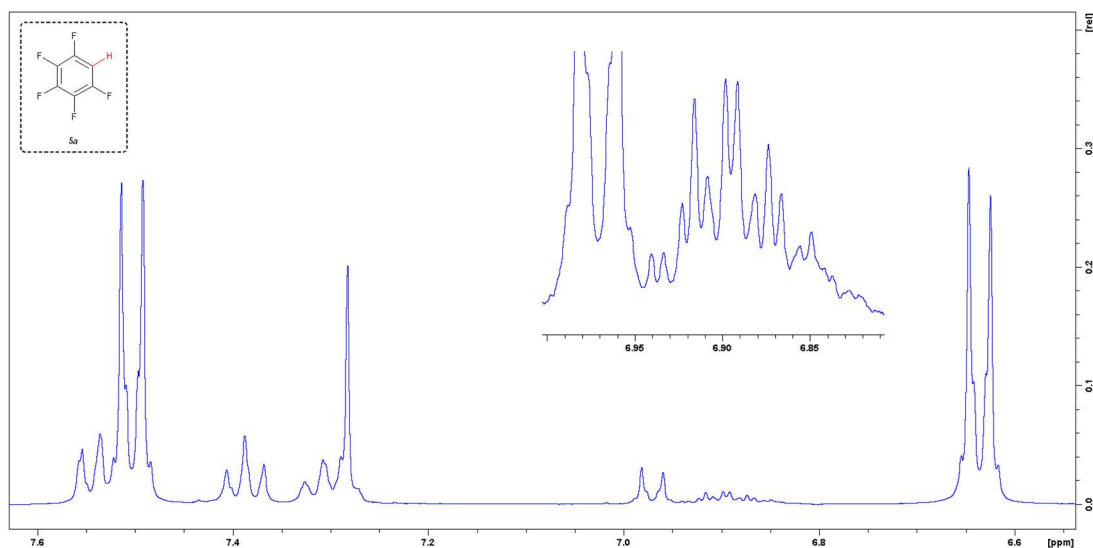


Figure 5.5: <sup>1</sup>H NMR Spectrum (400 MHz, CDCl<sub>3</sub>) of the experiment described in Table 5.2, entry 3. Inset: characteristic triplet of triplet of doublets (ttt) arising from coupling between <sup>1</sup>H and <sup>19</sup>F spin ½ nuclei of side-product **5a**.

Further analysis *via*  $^{19}\text{F}$  NMR corroborated this finding. The crude nature of the analyte did not present any solvent effects, allowing for a direct comparison to be made between reaction mixture and a pure reference sample of **5a** (see Figure 5.6). Note, however, that such analysis only allows for a qualitative observation of the presence of **5a** in the reaction mixture. This is because **5a** is a relatively volatile compound with a boiling point of 86 °C. As reaction temperatures of 100 °C were utilised in this experiment, boiling (and therefore loss) of **5a** as the reaction progressed is to be expected.

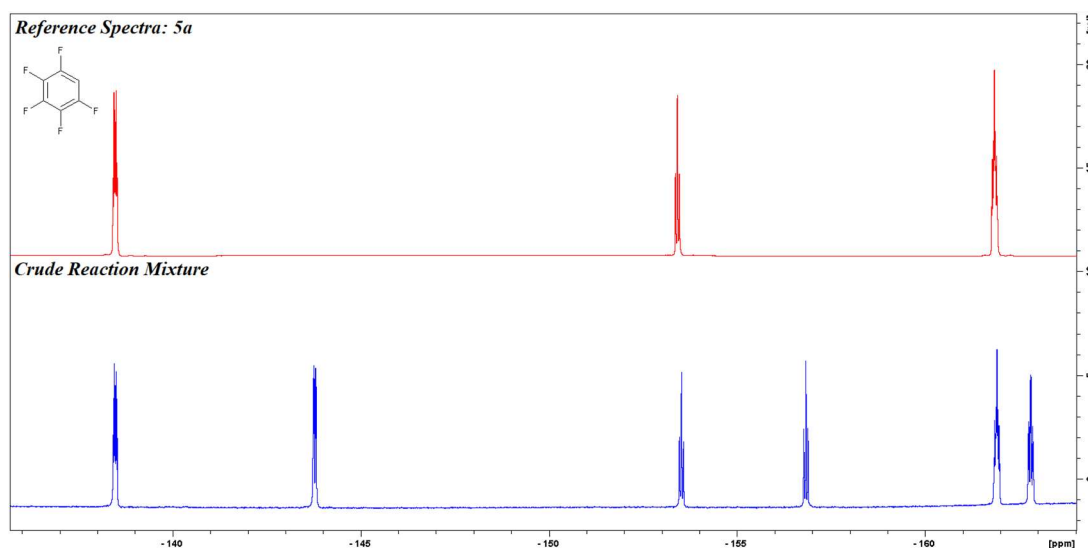


Figure 5.6:  $^{19}\text{F}$  NMR Spectra (376 MHz,  $\text{CDCl}_3$ ) confirming presence of protodecarboxylation. Top: the spectra of a pure sample of **5a**. Bottom: the spectra of the experiment described in Table 5.2, entry 3.

To eliminate the potential for DM-PEG additives to introduce water content, and therefore a source of labile protons for protodecarboxylation, both DM-PEG-500 and DM-PEG-1000 were dried over 4 Å molecular sieves for 72 hours prior to further use. Given its larger average molecular weight, DM-PEG-1000 differs from DM-PEG-500 in that it is a solid at room temperature. Therefore, whilst DM-PEG-500 was dried over molecular sieves at room temperature, DM-PEG-1000 was dried at 40 °C as a melt. Samples of DM-PEG were collected both before and after this drying process and analysed *via* Karl Fischer titration to determine the effectiveness of the procedure. The results of these titrations are displayed in Table 5.4 and show a dramatic reduction in water content in both cases. After drying, the observed water

content of DM-PEG-500 was found to decrease by 91 %. For DM-PEG-1000, a reduction of 81 % was observed.

Table 5.4: Effectiveness of drying DM-PEG over 4 Å molecular sieves, determined via Karl Fischer titration. <sup>a</sup> Prepared as a known quantity of solid dissolved in anhydrous methanol.

Sample		H <sub>2</sub> O Content (%)
DM-PEG-500	Before drying	0.1801
	After drying	0.0155
DM-PEG-1000 <sup>a</sup>	Before drying	0.4476
	After drying	0.0853

### 5.3.1. As an Additive

To investigate the effect DM-PEG additives have in a DMSO-solvated system two experiments were performed: one spiked with 15 mg of DM-PEG-500 (in keeping with prior experimentation) and a control that lacked additive. For comparative purposes similar experiments were performed in DMA, a known literature solvent, and toluene – a solvent predicted to perform poorly as its non-polar nature would inhibit solvation of potassium salt substrate **1a**. The results of these experiments, performed under the conditions displayed in Scheme 5.3, are displayed in Table 5.5.

Table 5.5: Examining the effect of DM-PEG additives on DCC reactivity in various solvents. Conditions: **1a** (0.75 mmol), **2bI** (0.5 mmol), CuI (0.05 mmol), Pd(OAc)<sub>2</sub> (0.05 mmol), PEG additive (15 mg), solvent (2 mL), 100 °C. <sup>a</sup> determined via <sup>1</sup>H NMR. <sup>b</sup> Reaction temperature 90 °C. <sup>c</sup> DM-PEG-500 loading increased to 150 mg.

Entry	Solvent	Additive	3ab Yield (%) <sup>a</sup>
<b>1</b>	DMA	None	85
<b>2</b>		DM-PEG-500	90
<b>3</b>		DM-PEG-1000	95
<b>4</b>	DMSO	None	100
<b>5</b>		DM-PEG-500	100
<b>6</b> <sup>b</sup>		DM-PEG-500	100
<b>7</b>	Toluene	None	0
<b>8</b>		DM-PEG-500	13
<b>9</b> <sup>c</sup>		DM-PEG-500	20

DMSO was found to be an excellent solvent for the DCC coupling of substrates **1a** and **2bI**, leading to 100 % yield of DCC product **3ab** both with and without the addition of DM-PEG-500 (see Table 5.5, entries 5 and 4 respectively). Indeed, DM-PEG spiked DMSO was found to be a suitable solvent even under a lower temperature regime – yielding full conversion of starting material to DCC product **3ab** at 90 °C (see Table 5.5, entry 6). This was a wonderful finding but reveals little about the efficacy of DM-PEG-500 in promoting DCC. Thankfully, this was evidenced when DMSO was substituted for alternate solvents – the addition of DM-PEG-500 improved observed **3ab** yields in both DMA and toluene. The latter case is noteworthy in that no DCC reactivity was observed to occur without the presence of DM-PEG-500. Increasing the loading of DM-PEG-500 ten-fold produced even greater yields of DCC product **3ab** when utilising toluene as solvent (see Table 5.5, entry 9), suggesting a positive correlation between **3ab** yield and PEG additive loading.

Regarding the effect polymeric chain length has upon the efficacy of DM-PEG as an additive, 15 mg of DM-PEG-1000 was incorporated into the DMA solvated model DCC reaction (see Table 5.5, entry 3). Although an undesirable solvent due to health and safety concerns, its lack of total conversion of reagent to **3ab** even when utilising DM-PEG-500 as an additive allowed for any potential increases in yield of **3ab** resulting from increased polymeric chain length to be observed. Under these conditions, DM-PEG-1000 was found to improve DCC reactivity to a greater extent than DM-PEG-500.

### 5.3.2. As a Solvent

Given the fact that both DM-PEG-500 and DM-PEG-1000 exist in a liquid state under the conditions of the model DCC reaction, it was also worth investigating the possibility of eschewing the use of other solvents and relying purely upon DM-PEG to solvate the reaction. Although similar in structure to diglyme, DM-PEG is not classified as a hazardous substance under EC regulation. Molecular sieve-dried samples of DM-PEG-500 and DM-PEG-1000 were utilised for these investigations, alongside samples that had not undergone the drying procedure so as to emphasise its importance.

Table 5.6: Examining the effect of using DM-PEG directly as a solvent with a model DCC reaction. Conditions: **1a** (0.75 mmol), **2bI** (0.5 mmol), CuI (0.05 mmol), Pd(OAc)<sub>2</sub> (0.05 mmol), DM-PEG (2 mL), 100 °C. <sup>a</sup> determined via <sup>1</sup>H NMR. <sup>b</sup> **3ab** yield divided by **4b** yield.

Entry	Solvent	<b>3ab</b> Yield <sup>a</sup>	<b>4b</b> Yield <sup>a</sup>	Ratio <sup>b</sup>
<b>1</b>	DM-PEG-500 (wet)	47	35	1.34
<b>2</b>	DM-PEG-1000 (wet)	6	94	0.06
<b>3</b>	DM-PEG-500 (dry)	71	26	2.73
<b>4</b>	DM-PEG-1000 (dry)	34	66	0.52

When utilising DM-PEG as an additive, care had been taken to ensure that the loading of DM-PEG resulted in a consistent quantity of ether functionality present in the reaction. However, when replacing conventional solvent with DM-PEG, concentration of reagents and catalysts is also an important concern. Because of this the loadings of DM-PEG were fixed by volume at 2 mL for these experiments, irrespective of average molecular weight. As the density of DM-PEG varies slightly with average molecular weight this is expected to result in differing quantities of ether coordination sites. However, keeping concentrations consistent with prior work allows for direct comparison between DM-PEG solvated experiments and other solvent choices. The findings of these experiments are detailed in Table 5.6.

In all cases, 100 % consumption of starting material **2bI** was observed, however this did not translate to 100 % conversion of **2bI** to DCC product **3ab**. Instead, significant promotion of homocoupling side reaction to yield undesired product **4b** was observed. Unlike the conclusions drawn from Table 5.5, it was observed that DM-PEG-500 performed better than DM-PEG-1000 when utilised at solvent scale. DM-PEG-500 was found to lead to greater yields of **3ab** and higher ratios of **3ab** to **4a** than its higher molecular weight analogue, both under hydrous and anhydrous conditions.

Regardless of average molecular weight, the molecular sieve drying procedure was found to dramatically improve the suitability of DM-PEG as a solvent for DCC. When utilising untreated DM-PEG-1000, it was observed that **3ab** yields had reached only 6 % after 24 hours. The remaining mass balance is accounted for by the yield of **4b**. Upon utilising DM-PEG-1000 subjected to the molecular sieve

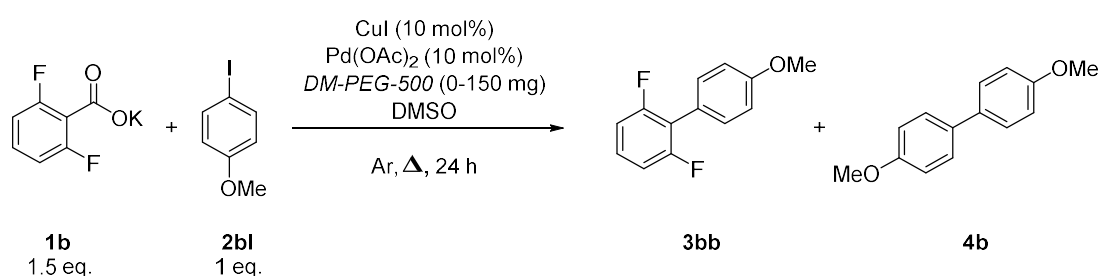
drying procedure, yields of **3ab** are increased and yields of **4b** are reduced. This is expressed in a dramatic increase in the observed ratio of **3ab** to **4b** (see Table 5.6). Similar observations were also made when experimenting with DM-PEG-500. From these findings it can be deduced that there exists a negative correlation between the water content of the DCC reaction mixture and the final yield of DCC product **3ab**. Conversely, there exists a positive correlation between water content and yield of side products. This is hypothesised to be due to the fact that an increase in water content translates to an increase in the concentration of labile protons within the reaction mixture, leading to consumption of starting material **1a** via protodecarboxylation to yield **5a**. This would reduce the concentration of **1a** in the reaction mixture, slowing the rate of DCC relative to the competing homocoupling side reaction of reagent **2bI** and therefore ultimately resulting in a lower ratio of **3ab** to **4b**.

This hypothesis also helps inform us as to why DM-PEG-500 is observed to perform better than its higher molecular weight analogue when utilised at solvent scale – directly contradicting the findings of experiments utilising DM-PEG at additive scale (see Table 5.5, entries 1-3). Even after drying, DM-PEG-1000 is observed to contain almost six times the quantity of water compared to DM-PEG-500, determined *via* Karl Fischer titration (see Table 5.4). Whilst at additive scale the concentration of water introduced to the reaction mixture in both cases would be low relative to the concentration of other reaction components, at solvent scale this is not the case. The higher water content of DM-PEG-1000 is therefore expressed in the poorer ratio of **3ab** to **4b** observed when utilising it at solvent scale compared to its lower molecular weight, drier analogue DM-PEG-500.

#### 5.4. Reaction Optimisation for Substrate with Lower Degrees of Fluorination

As Table 5.5 clearly shows, DMSO is an excellent solvent for the copper/palladium bimetallic DCC reaction between benzoate substrate **1a** and coupling partner **2bI**. However, **1a** represents an idealised substrate owing to the five electron-withdrawing fluoro- groups weakening the aryl-carboxylate C-C bond and therefore resulting in easier to induce decarboxylation. As previous work has elucidated (see Table 4.1), bringing about DCC couplings when utilising substrate with differing

functionalisation is more challenging, be it fluoroaryl compounds with lower degrees of fluorination or starting materials with entirely different electron-withdrawing functionality such as nitro- groups. Armed with the findings of Table 5.5, it was decided to investigate the scope of using DM-PEG spiked DMSO solvent systems with these more challenging couplings. Potassium 2,6-difluorobenzoate (**1b**) was chosen as benzoate substrate for these initial investigations, utilising both neat and spiked DMSO in an otherwise standard DCC protocol (see Scheme 5.5). Temperature was varied between 100-130 °C as prior work suggested DCC coupling of **1b** under low-temperature DCC conditions was an ambitious prospect.



*Scheme 5.5: DCC reaction of **1b** and **2bI**, showing expected DCC product **3bb** and potential side product **4b**.*

Although the molecular weight screening experiments in DMA (see Table 5.5, entries 1-3) would seem to suggest that higher average molecular weight DM-PEG performs better in the role of additive, the higher observed water content of DM-PEG-1000 (see Table 5.4) coupled with its dramatically poorer performance when utilised at a higher loading (see Table 5.6) caused some reservations at its continued use, especially as investigation into the role of PEG loading (see Table 5.5, entries 7-9) present a strong case for utilising DM-PEG in larger quantities. Alongside this, its nature as a waxy semi-solid at room temperature results in a relatively cumbersome user experience for both drying and utilisation in DCC compared to its lower average molecular weight, liquid analogue. With these considerations, DM-PEG-500 was selected as additive, at a loading of 150 mg. The resulting experiments were followed *via*  $^1\text{H}$  NMR to determine the yields of DCC product **3bb** and side product **4b**, the results of which are displayed in Figure 5.7 and Figure 5.8, respectively.

In both the presence and absence of DM-PEG-500, a linear correlation between reaction temperatures and yields of DCC product **3bb** was observed (see Figure 5.7). At every temperature placed under investigation, the addition of DM-PEG-500 was observed to improve yields.

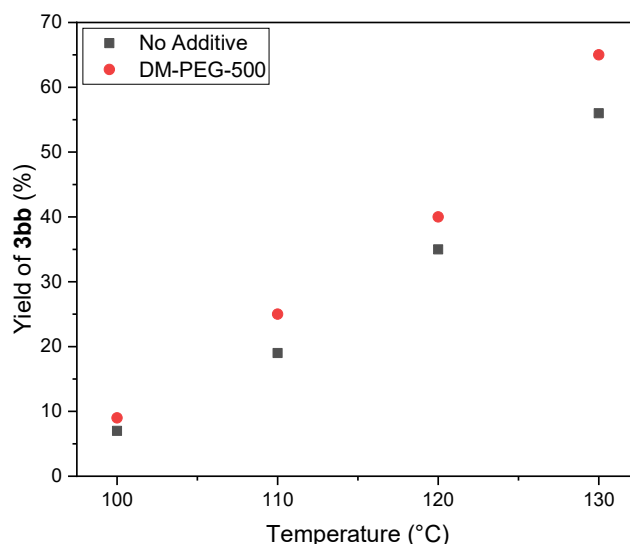


Figure 5.7: Plot depicting the relationship between observed yields of DCC product **3bb** and reaction temperature, both in the presence and absence of additive DM-PEG-500. Yields determined via  $^1\text{H}$  NMR.

When looking at side product yield, a different picture is painted (see Figure 5.8). Without DM-PEG-500 as an additive, a positive correlation between reaction temperature and the yield of **4b** is observed – an intuitive finding. However, when DM-PEG-500 is introduced to the reaction a completely different behaviour is observed. As with the yields of **3bb** (see Figure 5.7), at 100 °C the addition of DM-PEG results in a minor increase in the yield of **4b**. Increasing reaction temperatures by merely 10 °C, however, elicits a 100 % increase in the yield of **4b** compared to the equivalent reaction utilising neat DMSO. At 130 °C however, the addition of DM-PEG results in a reduction of **4b** yield.

Comparing the ratios of **3bb** yield to **4b** yield reveals that below 130 °C the addition of 150 mg DM-PEG-500 results in a greater promotion of the Ullmann homocoupling side reaction compared to the desired DCC reaction, resulting in a poorer ratio (see Table 5.7, entries 2 and 3). However at 130 °C the addition of DM-PEG-500 yields a greater ratio of **3bb** to **4b**, suggesting at higher temperatures the

addition of DM-PEG favours the promotion of DCC reactivity over that of the Ullmann side reaction of **2bI** (see Table 5.7, entry 4).

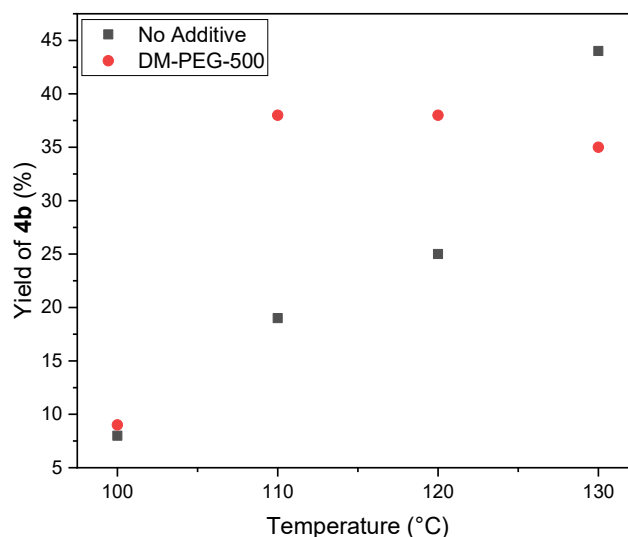


Figure 5.8: Plot depicting the relationship between observed yields of undesirable side product **4b** and reaction temperature, both in the presence and absence of additive DM-PEG-500. Yields determined via  $^1\text{H}$  NMR.

Table 5.7: Table displaying the ratios of yields of DCC product **3bb** and side product **4b** at various temperatures under the conditions displayed in Scheme 5.5. Values calculated from yields determined via  $^1\text{H}$  NMR.

Entry	Temperature (°C)	Ratio 3bb:4b without DM-PEG-500	Ratio 3bb:4b with DM-PEG-500
1	100	0.88	1.00
2	110	1.00	0.66
3	120	1.40	1.05
4	130	1.27	1.86

#### 5.4.1. Design of Experiments

Up to this point, a conventional approach to the optimisation of the DMSO-solvated reaction between **1b** and **2bI** had been followed, wherein variables were varied one at a time. Following this approach, the best conditions identified (130 °C, 150 mg loading of DM-PEG additive) resulted in a 65 % yield of DCC product **3bb**. Prior optimisation, however, identified that when using DMA as solvent, yields as high as 93 % were achievable (see Table 4.4). Scheme 5.6 provides a brief summary of these experiments. The DMSO/DM-PEG system enjoys the benefit of being much



palladium catalyst. For the catalyst factor, a ratio was chosen as DCC is known to be rate limited with respect to decarboxylation, therefore the loading of copper catalyst is held constant at 10 mol% and the loading of palladium catalyst is varied relative to this. In keeping with previous experimentation, the ratio of potassium benzoate substrate loading to aryl halide substrate loading was held constant at a value of 1.5:1.

*Table 5.8: The values of the three levels for each identified input factor.*

<b>Level</b>	<b>2bI (mmol)</b>	<b>Temperature (°C)</b>	<b>DM-PEG (mg)</b>	<b>CuI/Pd(OAc)<sub>2</sub></b>
<b>Low</b>	0.25	110	50	0.5
<b>Middle</b>	0.50	125	100	1
<b>High</b>	0.75	140	150	2

To ensure the DoE contains a degree of rigor, each factor was varied between three levels (see Table 5.8). A truly comprehensive study looking at every possible combination of factors and levels would total  $x^y$  experiments where  $x$  is equal to the number of levels and  $y$  is equal to the number of input factors. This is known as a full factorial design and is useful in that every possible interaction between factors can be considered. However, as the number of factors and/or levels increase, such an experimental design quickly becomes a monumental undertaking. For example, applying a full factorial design to the 4 factor, 3 level system under consideration a total of  $3^4 = 81$  experiments would be generated. Although such a model would generate a wealth of information, the number of combinations was deemed to be too large to be feasible.

Instead MODDE Design of Experiment software was utilised to design a list of experiments that explored the importance of both single factors and factor interactions whilst reducing the overall number of combinations placed under investigation. This is known as a reduced combinatorial design, and the result was a 21-experiment design including three replicate points to provide a measure of error. A tabulated list of these experiments, including the randomised run order so as to minimise the effect extraneous factors might have upon the results, is displayed in Table 5.9.

Table 5.9: Reduced combinatorial experimental design for the investigation of the DM-PEG promoted DCC coupling of **1a** and **2bI**. Design generated using Umetrics MODDE Pro 12.1. <sup>a</sup> The ratio of CuI loading to Pd(OAc)<sub>2</sub> loading.

Run Order	2bI (mmol)	Temperature (°C)	DM-PEG (mg)	CuI/Pd(OAc) <sub>2</sub> <sup>a</sup>
5	0.25	110	100	0.5
6	0.25	110	150	0.5
18	0.75	110	50	1
8	0.75	110	100	1
2	0.5	110	50	2
14	0.5	110	150	2
17	0.5	125	100	0.5
20	0.75	125	150	0.5
7	0.5	125	150	1
1	0.25	125	50	1
21	0.25	125	50	2
4	0.75	125	100	2
16	0.5	140	50	0.5
13	0.75	140	50	0.5
9	0.5	140	100	1
10	0.25	140	150	1
12	0.25	140	100	2
15	0.75	140	150	2
19	0.25	140	150	1
11	0.75	140	150	2
3	0.25	140	100	2

With experimental design in hand, two responses were identified to study: the yield of **3bb** and the yield of **4b**. Each experiment of the design was then completed according to the run order displayed in Table 5.9 and the results analysed *via* <sup>1</sup>H NMR to determine the values of these response factors. The results were then compiled into the MODDE software which utilises response surface methodology to generate a computational model that weighs the importance of various factors and interactions (expressed by coefficients) in determining the value of the responses. The summary of this model with respect to both response factors is displayed in Figure 5.9.

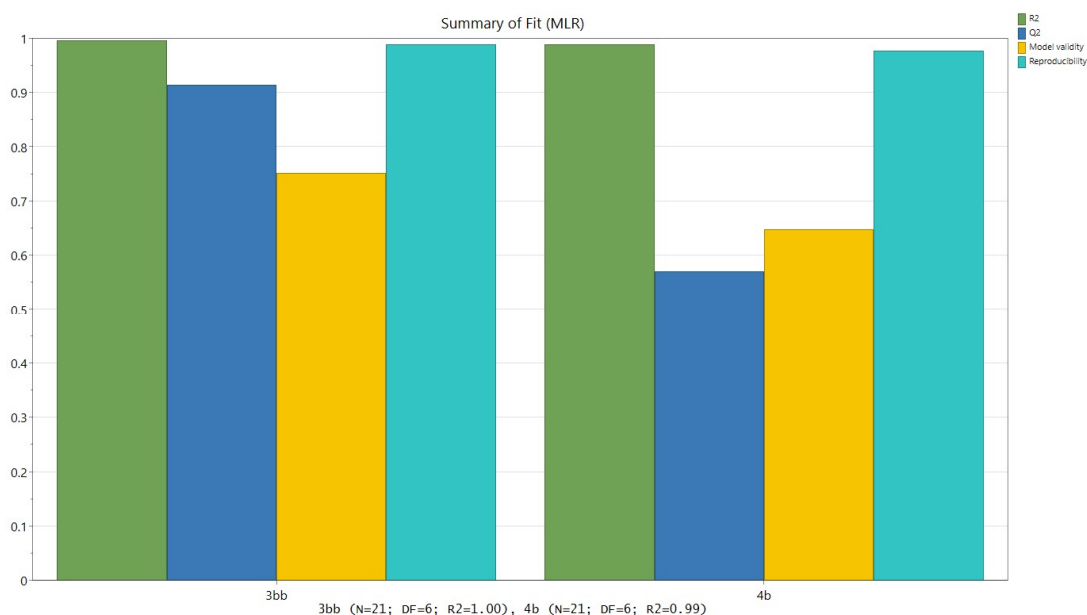


*Figure 5.9: Summary of the overall quality of the model both in terms of determining yields of DCC product **3bb** and homocoupling side product **4b**.*

Quality of a model can be expressed by four parameters:  $R^2$ ;  $Q^2$ ; model validity and reproducibility.  $R^2$  is a measure of how well the model fits the experimental data used to generate it. As this value approaches 1 the better the variation in the observed values for a response factor is accounted for by the model.  $Q^2$  is a measure of how well the model is expected to be able to predict the value of a response factor when given values for the input factors. As this value approaches 1 the more accurate the model will be in its predictions. Model validity is a test performed by the MODDE software to assess various potential problems such as missing model terms or high degrees of outliers. As this value approaches 1 the more trustworthy the model is assumed to be. Finally, reproducibility is a measure of variation of a response factor under the same conditions. It is a representation of error and as the value approaches 1 the lower the observed error.

At a glance, the model parameters displayed in Figure 5.9 for the two response factors **3bb** and **4b** yield reveal that whilst  $R^2$  and reproducibility are high in both cases,  $Q^2$  and overall model validity with respect to **4b** yield are relatively low. This implies that the experimental design did not produce enough information to build a model of how the four input factors relate to **4b** yield that is as coherent as the model for **3bb** yield.

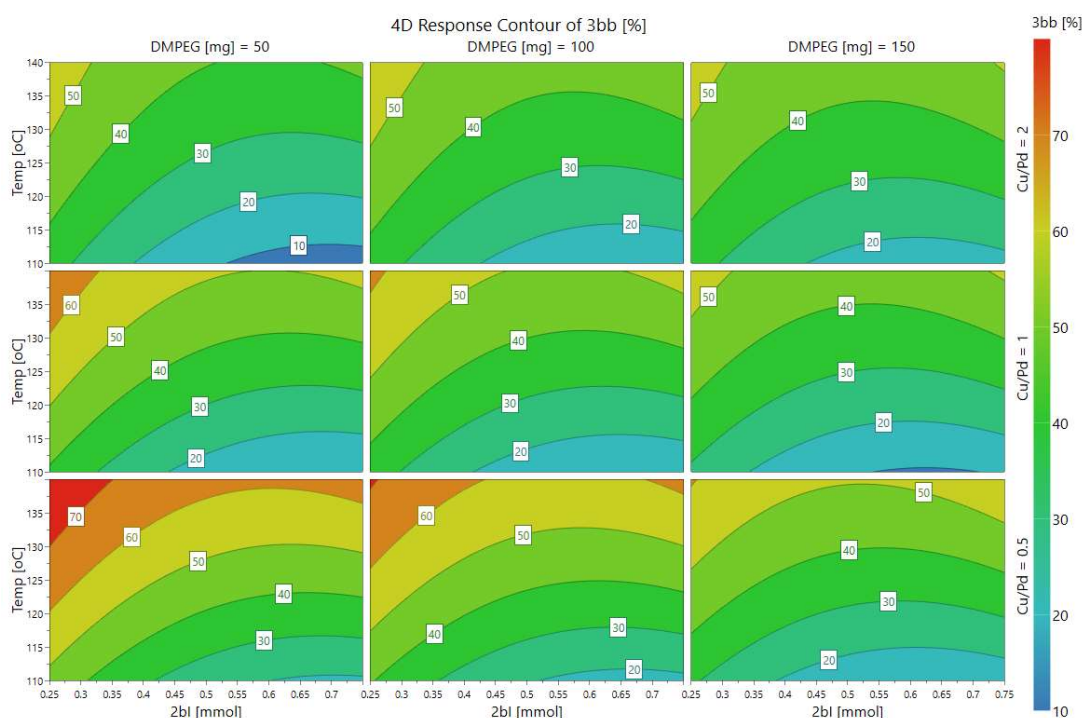


Figure 5.10: 4D contour plot describing the predicted relationships of various input factors and how they affect the yield of DCC product **3bb**.

In simplified terms, the model produced considers a response factor such as **3bb** yield as being a function comprised of several smaller terms and associated coefficients that weights each term based on its importance to the model. These terms fall into one of three categories: input factor terms; square terms and interaction terms. Input factor terms are concerned with how a change made to a particular input factor affects the response factor. Square terms model curvature within the model. Finally, interaction terms describe how changes in two or more input factors simultaneously affect the response factor. Figure 5.10 and Figure 5.11 help to visualise the response surface that results from these terms in the form of contour plots, for the response of **3bb** and **4b** respectively. With a predictive model of the DCC reaction between **1b** and **2bI** in hand, it is then possible to use this model to optimise the reaction conditions with respect to a desired parameter such as highest possible **3bb** yield or lowest possible **4b** yield.

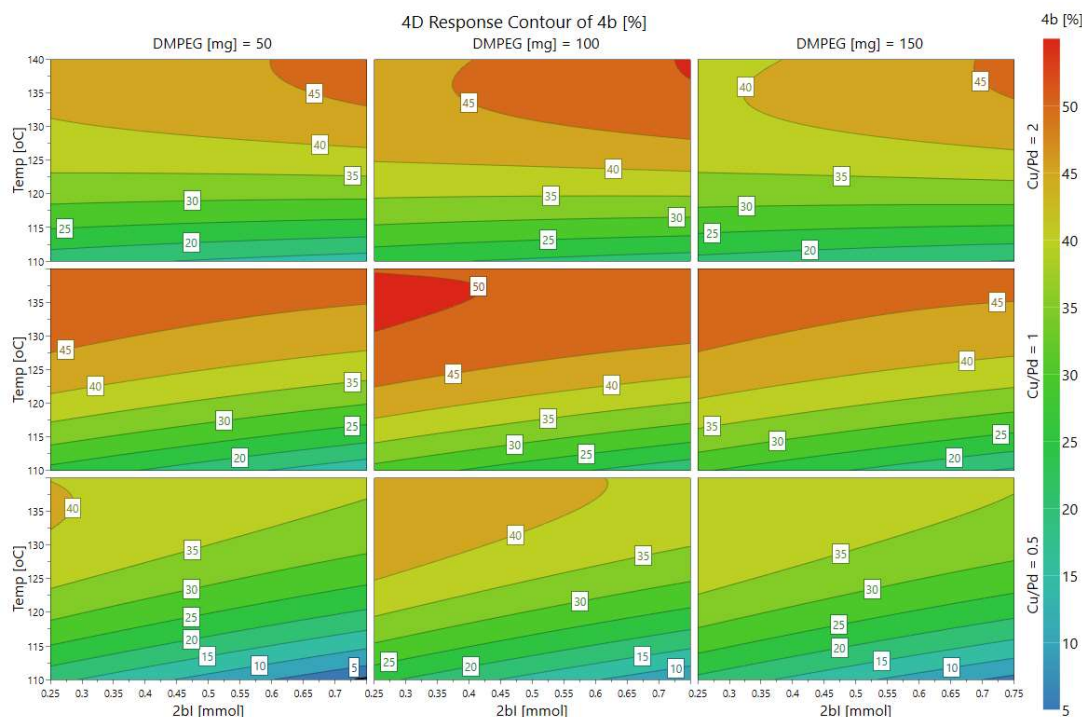


Figure 5.11: 4D contour plot describing the predicted relationships of various input factors and how they affect the yield of homocoupling side product **4b**.

Knowing that the model was stronger with respect to predicting the yield of **3bb**, optimisation with respect to **3bb** yield was chosen for this exercise. The results of this optimisation are displayed in Table 5.10 and reveal the sweet spot to lie at the very edge of the response surface, with input factor values lying close to either their highest or lowest values. This illustrated well by the contour plot displayed in Figure 5.10. These conditions were then applied to three replicate DCC couplings of **1b** and **2bI**, the results of which were determined *via*  $^1\text{H}$  NMR and displayed in Table 5.11. The observed values for both **3bb** yield and **4b** yield differ from their predicted values, however they fall within a 99 % confidence interval of the predictions.

Table 5.10: Predicted experimental conditions for optimisation with respect to largest **3bb** yield, alongside predicted values for the response factors **3bb** yield and **4b** yield under those conditions. Error in predicted response values reported as the 99 % confidence interval.

<b>2bI</b> (mmol)	<b>Temp.</b> (°C)	<b>DM-PEG</b> (mg)	<b>CuI/Pd(OAc)<sub>2</sub></b>	<b>3bb Yield</b> (%)	<b>4b Yield</b> (%)
0.25	139.40	50.37	0.50	78 ± 15	40 ± 18

Table 5.11: Experimental conditions derived from the optimised conditions displayed in Table 5.10, alongside the observed yields of **3bb** and **4b** resulting from those experimental conditions. Yields were determined via  $^1\text{H}$  NMR and represent mean values of 3 replicate experiments. Error reported as standard deviation.

2bI (mmol)	Temp. (°C)	DM-PEG (mg)	CuI/Pd(OAc) <sub>2</sub>	3bb Yield (%)	4b Yield (%)
0.25	139	50.4	0.50	64 ± 1	36 ± 1

The disparity between observed and predicted responses implies poor modelling of the reaction. Looking at the model in greater detail reveals that, for many of the terms produced, confidence intervals are observed to be large with respect to the values of the coefficients themselves. As the confidence interval describes a range of statistically probable values for the coefficient in question, a relatively large confidence interval implies a relatively large degree of uncertainty in that coefficient and therefore a greater degree of inaccuracy in the predictions of the model. An overview of the terms and corresponding coefficients for the response of **3bb** and **4b** is displayed in Figure 5.12 and Figure 5.13, respectively.

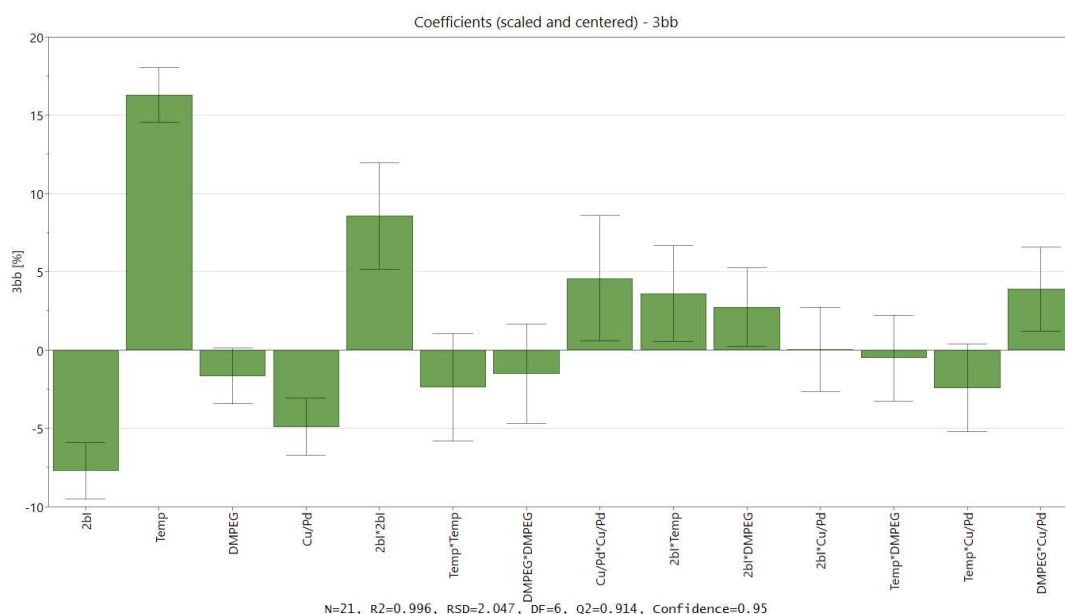
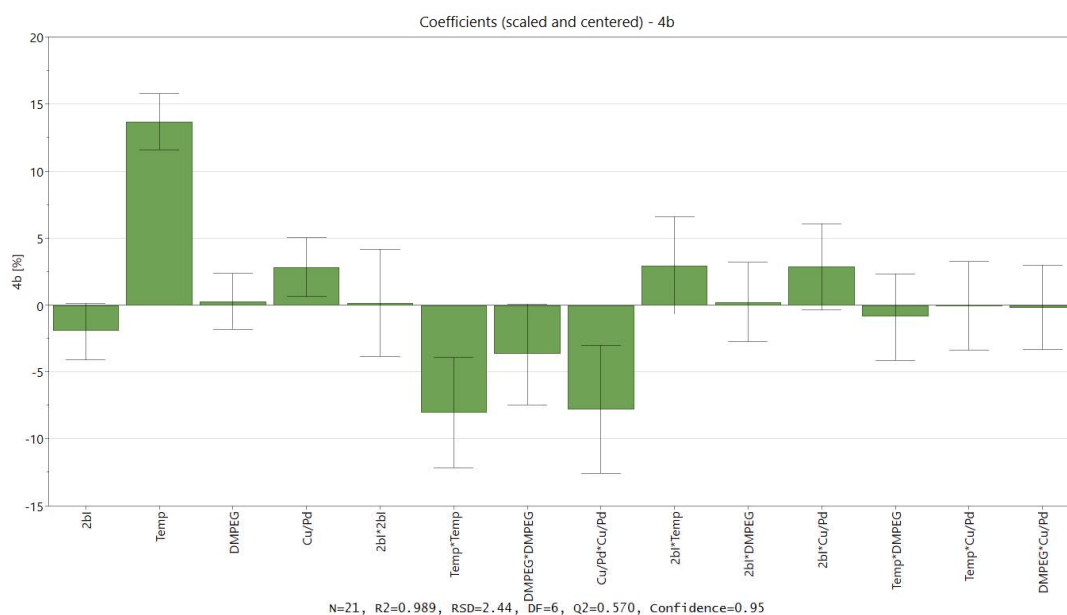


Figure 5.12: Plot describing the coefficients attributed to the various input factors and factor interactions by the model describing the yield of DCC product **3bb**.

A term can be said to be significant to the model if its confidence interval does not cross zero. This is because if the confidence interval contained zero it would be

possible that the true value of that coefficient *is* zero and therefore the associated term would not contribute to the function. With this in mind, it can be observed that, due to the proportionally large confidence intervals, many of the terms displayed in both Figure 5.12 and Figure 5.13 are not statistically significant to the model.



*Figure 5.13: Plot describing the coefficients attributed to the various input factors and factor interactions by the model describing the yield of homocoupling side product **4b**.*

Some elements of the predictive model are in agreement with experimentally observed data. For example, Figure 5.12 reveals that the input factor term for reaction temperature is statistically significant, with a positive coefficient. Its square term, however, is not statistically significant. This suggests a positive, linear correlation between temperature and the yield of DCC product **3bb**. As Figure 5.7 shows, this is exactly what was observed experimentally. Despite this, the input factor term for the loading of additive DM-PEG-500 was found to be insignificant to the yields of both **3bb** and **4b**, despite much experimentally derived evidence to the contrary.

As  $R^2$  and reproducibility were found to be excellent for both response factors (see Figure 5.9), it is clear that the inaccuracies of the model are not due to experimental error. The likely explanation, therefore, is that the model does not contain sufficient

information to make accurate predictions either due to insufficient exploration of the design space (owing to the reduced combinatorial design) or due to consideration of too few input factors.

## 5.5. Conclusions and Future Work

The virtues of using DCC to form carbon-carbon bonds and build organic molecules are often stated by researchers working within the field. Compared to competing methods of carbon-carbon bond formation such as the palladium catalysed Suzuki-Miyaura reaction, DCC chemistry utilises starting materials that are widely available (both commercially and in nature) and that are easy to store and handle<sup>17</sup>. However, even cutting-edge research into the field fundamentally fails from a green chemistry perspective. Anastas and Warner outlined twelve key principles they believed chemical processes should be designed around so as to make them as green a process as reasonably possible<sup>173</sup>. Of particular applicability to DCC research are the first, third, fourth and fifth principles:

- 1) It is better to prevent waste than to treat or clean up waste after it has been created.
- 3) Wherever practicable, synthetic methods should be designed to use and generate substances that possess little or no toxicity to human health and the environment.
- 4) Chemical products should be designed to preserve efficacy of function while reducing toxicity.
- 5) The use of auxiliary substances (for example, solvents) should be made unnecessary wherever possible and innocuous when used.

Ensuring that a chemical process is compliant with these principles without compromising the efficacy or real-world application of the process is not an easy task by any stretch of the imagination. However, with DCC research and application still in its infancy relative to its competition, researchers are in a unique position to develop green DCC protocols before the use of harmful and hazardous solvents becomes commonplace in DCC applications.

To this end, the work presented within this chapter has explored the scope for replacing hazardous solvents with proven DCC reactivity such as diglyme and DMA, two solvents with substantial literature presence. Although a nearest neighbour analysis of PCA data building upon the works of Murray<sup>111</sup> was able to identify several possible candidates for replacement, they were all found to dramatically underperform compared to tried and tested solvents diglyme and DMA. A possible explanation for this is that, whilst Murray's PCA included a number of solvent parameters, none of them accounted for the observed activity of glyme-like solvents in DCC in a meaningful way. It is known from prior work outlined within this thesis that the activity diglyme displays towards promoting DCC coupling is not merely linked to improved solubility (see Table 2.9). From experimentation comparing the effects of introducing small quantities of diglyme and the crown ether 18-crown-6 it was concluded that diglymes efficacy is the result of its ability to chelate potassium ions, promoting the successful copper-catalysed decarboxylation of the carboxylate substrate (see Table 2.8).

However, in theory a PCA approach is still an intelligent approach to identifying potential replacement solvents. When considering the four PC's described by the PCA model as coordinates in a four-dimensional solvent space, nearest neighbour analysis should allow for the identification of solvents with similar properties. The weakness of this methodology lies in the fact that it weighs the effect of each PC equally. Another approach would be to utilise design of experiment methodology, designating each PC as an input factor. As with a nearest neighbour approach, the closest approximation to the starting solvent within the database would be selected as a starting point, and the levels for the PC input factors could be selected based upon the PC coordinates of nearest neighbour solvents. This would allow the model to explore an area of solvent space centred upon the starting solvent. Whilst such an approach would involve a great deal more work than the relatively simplistic nearest neighbour approach to selecting suitable replacement solvents, the resulting model would be able to weigh the importance of each PC as well as identify potential interactions.

Given the fact that PEG and its dimethylated analogue DM-PEG were found to promote successful DCC couplings in all instances of their application, it is clear

that it is indeed possible to replicate the activity of diglyme with greener, innocuous alternatives. Whilst able to serve the role of solvent in model DCC reactions, such reaction conditions were found to under-perform in terms of the yield of DCC product when compared to the hazardous and widely employed alternatives diglyme and DMA. Where PEG derivatives were found to shine, however, is in applications where they are introduced to DCC protocols as an additive. DMSO, a relatively harmless solvent compared to competing DCC solvents, had been identified as a potential replacement solvent but was held back due to the prevalence of copper-catalysed side reactions when using this solvent. With the use of DM-PEG, however, side reactions are suppressed in favour of DCC reactivity, improving the observed ratios of DCC product to undesired side product.

A design of experiments study into a model DM-PEG promoted DCC reaction between substrates **2b** and **4bI** was performed. Although revealing useful information about DCC coupling under these conditions and how DM-PEG interacts with the various reagents and catalysts, there is room for significant improvement. Confidence intervals throughout the model are significant in size with respect to their corresponding parameters. As such, it is difficult to apply it to real world applications, clearly evidenced when utilising the model to predict conditions for optimal **3bb** yield (see Table 5.10 and Table 5.11). Although the observed yield of **3bb** under the predicted conditions fell within a 99 % confidence interval of the predicted yield, the difference between observed and predicted yield was 14 %, a substantial deficit.

Future work would be centred upon expanding on and improving the experimental design. This could be achieved by increasing the number of input factors considered, for example: the loading of potassium carboxylate starting material; the loading of copper catalyst irrespective of palladium loading; reaction time or DM-PEG molecular weight. A key observation of the model presented in this work is that the optimal conditions for **3bb** yield lied at the very edge of the design space considered. Because of this it is uncertain whether the optimal conditions predicted by the model for maximising **3bb** yield is indeed the true optimum. Therefore, another improvement to the model could be to consider adding additional levels to the input factors so as to broaden the response curves. Finally, another improvement

that could be made would be to utilise a different experimental design entirely. Reduced combinatorial was chosen as it represents an excellent compromise between information gained and time required. It uses an algorithm to design a list of experiments with a balanced distribution of factors and levels. However, its reduced design means that not all combinations of levels and factors are experimentally considered. This is likely a key source of the proportionally large confidence intervals when considering the models interaction terms as the reproducibility of the experimentally observed data was found to be excellent (see Figure 5.9). A comprehensive design such as a full factorial approach would explore the design space with a greater degree of rigor and as such be able to give a more accurate description of any interaction terms present within the system.

## 6. Experimental

### 6.1. Methods and Instrumentation

300 MHz  $^1\text{H}$  NMR spectra were recorded on a Bruker AVANCE III 300 spectrometer. 400 MHz  $^1\text{H}$  NMR, 100 MHz  $^{13}\text{C}$  NMR and 376 MHz  $^{19}\text{F}$  NMR spectra were recorded on a Bruker AVANCE III HD-400 spectrometer. Data for NMR experiments is reported as follows: chemical shift ( $\delta$  ppm), multiplicity, coupling constant(s) (J Hz), integration, assignment.  $^{13}\text{C}$  NMR were assigned with the assistance of DEPT-90 or DEPT-135 analysis (See 6.3 Nuclear Magnetic Resonance Spectroscopy for relevant spectra). Fourier-transform infra-red spectroscopy was performed on a Bruker Alpha Platinum-ATR spectrometer. Data for FTIR experiments is reported as follows: significant band  $\nu_{\text{max}}$  ( $\text{cm}^{-1}$ ), assignment. High resolution mass spectrometry was performed on a Bruker maXis II mass spectrometer. High pressure liquid chromatographic analysis was performed on an Agilent/Hewlett Packard 1100 Series HPLC system equipped with a multiple wavelength detector using a standard method (See 6.6 High Pressure Liquid Chromatography Yield Derivation Methodology). Atomic Absorption Spectroscopic measurements were performed with the assistance of Dr. Alexander Kulak of the University of Leeds. Transition Electron Microscopy (TEM) and Energy-dispersive X-ray (EDX) Spectroscopy were performed by Dr. Rebecca Stones of the University of Leeds. TEM data is reported as follows: average long diameter, average short diameter, average aspect ratio (see 6.11 Transition Electron Microscopy Data for histograms). EDX data is reported as follows: emission (keV), assignment. Magnetochemical analysis was performed on a Sherwood Scientific Mk 1 Magnetic Susceptibility Balance.

### 6.2. Experimental Details

#### 6.2.1. Synthesis of Nanoparticles and Catalytic Material

##### *Synthesis of Palladium/Copper 2:1 Bimetallic Nanoparticles Pd<sub>2</sub>Cu-PVP*

A 250 mL round bottomed flask was charged with palladium(II) acetate (140 mg, 0.625 mmol), copper(II) sulphate pentahydrate (78 mg, 0.312 mmol), trisodium citrate (275 mg, 0.938 mmol), poly(vinylpyrrolidone) (500 mg) and deionised water (50 mL). The resulting mixture was then heated to 50 °C with stirring for 30 minutes before being allowed to cool to room temperature. A mixture of formaldehyde

aqueous solution (37 % w/v, 0.5 mL) and sodium hydroxide aqueous solution (1 M, 2 mL) was then added dropwise over 10 minutes with vigorous stirring. Black precipitate was observed to form during this addition. The reaction mixture was then left to stir for 30 minutes to ensure complete reduction before the particulate was separated *via* centrifugation (6000 rpm, 15 minutes), washed with 5:1 acetone-methanol solution (3 × 50 mL) and subsequently dried *in vacuo* for 2 hours, yielding a fine black powder (314 mg)

**AAS** (2.5 ppm sample in 8 mM HNO<sub>3</sub>) 25.68 ± 0.04 % Pd, 7.57 ± 0.03 % Cu

**TEM** 4.1 ± 0.5 nm, 3.6 ± 0.5 nm, 1.1 ± 0.1

**EDX** 0.227 (C K<sub>α</sub>), 0.525 (O K<sub>α</sub>), 0.930 (Cu L<sub>α</sub>), 1.104 (Na K<sub>α</sub>), 2.307 (S K<sub>α</sub>), 2.839 (Pd L<sub>α</sub>), 8.048 (Cu K<sub>α</sub>), 8.905 (Cu K<sub>β</sub>)

#### *Synthesis of Palladium/Copper 1:1 Bimetallic Nanoparticles PdCu-PVP*

A 250 mL round bottomed flask was charged with palladium(II) acetate (105 mg, 0.469 mmol), copper(II) sulphate pentahydrate (117 mg, 0.469 mmol), trisodium citrate (275 mg, 0.938 mmol), poly(vinylpyrrolidone) (500 mg) and deionised water (50 mL). The resulting mixture was then heated to 50 °C with stirring for 30 minutes before being allowed to cool to room temperature. A mixture of formaldehyde aqueous solution (37 % w/v, 0.5 mL) and sodium hydroxide aqueous solution (1 M, 2 mL) was then added dropwise over 10 minutes with vigorous stirring. Black precipitate was observed to form during this addition. The reaction mixture was then left to stir for 30 minutes to ensure complete reduction before the particulate was separated *via* centrifugation (6000 rpm, 15 minutes), washed with 5:1 acetone-methanol solution (3 × 50 mL) and subsequently dried *in vacuo* for 2 hours, yielding a fine black powder (309 mg)

**AAS** (2.5 ppm sample in 8 mM HNO<sub>3</sub>) 13.45 ± 0.02 % Pd, 9.33 ± 0.06 % Cu

**TEM** 3.8 ± 0.4 nm, 3.7 ± 0.4 nm, 1.05 ± 0.07

**EDX** 0.227 (C K<sub>α</sub>), 0.525 (O K<sub>α</sub>), 0.930 (Cu L<sub>α</sub>), 1.104 (Na K<sub>α</sub>), 2.307 (S K<sub>α</sub>), 2.839 (Pd L<sub>α</sub>), 8.048 (Cu K<sub>α</sub>), 8.905 (Cu K<sub>β</sub>)

#### *Synthesis of Palladium/Copper 1:2 Bimetallic Nanoparticles PdCu<sub>2</sub>-PVP*

A 250 mL round bottomed flask was charged with palladium(II) acetate (70 mg, 0.3125 mmol), copper(II) sulphate pentahydrate (156 mg, 0.625 mmol), trisodium citrate (275 mg, 0.938 mmol), poly(vinylpyrrolidone) (500 mg) and deionised water

(50 mL). The resulting mixture was then heated to 50 °C with stirring for 30 minutes before being allowed to cool to room temperature. A mixture of formaldehyde aqueous solution (37 % w/v, 0.5 mL) and sodium hydroxide aqueous solution (1 M, 2 mL) was then added dropwise over 10 minutes with vigorous stirring. Black precipitate was observed to form during this addition. The reaction mixture was then left to stir for 30 minutes to ensure complete reduction before the particulate was separated *via* centrifugation (6000 rpm, 15 minutes), washed with 5:1 acetone-methanol solution (3 × 50 mL) and subsequently dried *in vacuo* for 2 hours, yielding a fine black powder (295 mg)

**AAS** (2.5 ppm sample in 8 mM HNO<sub>3</sub>) 9.18 ± 0.02 % Pd, 10.84 ± 0.03 % Cu

**TEM** 4.5 ± 0.7 nm, 4.4 ± 0.7 nm, 1.02 ± 0.05

**EDX** 0.227 (C K<sub>α</sub>), 0.525 (O K<sub>α</sub>), 0.930 (Cu L<sub>α</sub>), 1.104 (Na K<sub>α</sub>), 2.307 (S K<sub>α</sub>), 2.839 (Pd L<sub>α</sub>), 8.048 (Cu K<sub>α</sub>), 8.905 (Cu K<sub>β</sub>)

#### *Synthesis of Palladium Monometallic Nanoparticles Pd-PVP*

A 100ml round bottomed flask was charged with palladium(II) acetate (105 mg, 0.469 mmol), trisodium citrate (138 mg, 0.469 mmol), poly(vinylpyrrolidone) (250 mg) and deionised water (25 mL). The resulting mixture was then heated to 50 °C with stirring for 30 minutes before being allowed to cool to room temperature. A mixture of formaldehyde aqueous solution (37 % w/v, 0.25 mL) and sodium hydroxide aqueous solution (1 M, 1 mL) was then added dropwise over 10 minutes with vigorous stirring. Black precipitate was observed to form during this addition. The reaction mixture was then left to stir for 30 minutes to ensure complete reduction before the particulate was separated *via* centrifugation (6000 rpm, 15 minutes), washed with 5:1 acetone-methanol solution (3 × 50 mL) and subsequently dried *in vacuo* for 2 hours, yielding a fine black powder (174 mg)

**AAS** (2.5 ppm sample in 8 mM HNO<sub>3</sub>) 16.4 ± 0.1 % Pd

**TEM** 3.2 ± 0.5 nm, 2.9 ± 0.4 nm, 1.1 ± 0.1

**EDX** 0.227 (C K<sub>α</sub>), 0.525 (O K<sub>α</sub>), 1.104 (Na K<sub>α</sub>), 2.839 (Pd L<sub>α</sub>)

#### *Synthesis of Copper Monometallic Material Cu-PVP*

A 250 mL round bottomed flask was charged with copper(II) sulphate pentahydrate (234 mg, 0.938 mmol), trisodium citrate (276 mg, 0.938 mmol), poly(vinylpyrrolidone) (500 mg) and deionised water (50 mL). The resulting

mixture was then heated to 50 °C with stirring for 30 minutes before being allowed to cool to room temperature. A mixture of formaldehyde aqueous solution (37 % w/v, 0.5 mL) and sodium hydroxide aqueous solution (1 M, 2 mL) was then added dropwise over 10 minutes with vigorous stirring. Black precipitate was observed to form during this addition. The reaction mixture was then left to stir for 30 minutes to ensure complete reduction before the particulate was separated *via* centrifugation (6000 rpm, 15 minutes), washed with 5:1 acetone-methanol solution (3 × 50 mL) and subsequently dried *in vacuo* for 2 hours, yielding a fine black powder (24 mg)

**AAS** (2.5 ppm sample in 8 mM HNO<sub>3</sub>) 50.21 ± 0.08 % Cu

**TEM** Nanoparticles not observed.

**EDX** 0.227 (C K<sub>α</sub>), 0.525 (O K<sub>α</sub>), 0.930 (Cu L<sub>α</sub>), 1.104 (Na K<sub>α</sub>), 2.307 (S K<sub>α</sub>), 8.048 (Cu K<sub>α</sub>), 8.905 (Cu K<sub>β</sub>)

#### *Synthesis of Palladium/Silver 1:1 Bimetallic Nanoparticles PdAg-PVP*

A 100 mL round bottomed flask, occluded with aluminium foil, was charged with sodium tetrachloropalladate(II) trihydrate (163 mg, 0.469 mmol), silver(I) nitrate (78 mg, 0.469 mmol), trisodium citrate (275 mg, 0.938 mmol), poly(vinylpyrrolidone) (500 mg) and deionised water (50 mL). The resulting mixture was then stirred for 30 minutes. A mixture of formaldehyde aqueous solution (37 % w/v, 0.5 mL) and sodium hydroxide aqueous solution (1 M, 2 mL) was then added dropwise over 10 minutes with vigorous stirring. The reaction mixture was then left to stir for 30 minutes to ensure complete reduction before the particulate was separated *via* centrifugation (6000 rpm, 15 minutes), washed with 5:1 acetone-methanol solution (3 × 50 mL) and subsequently dried *in vacuo* for 2 hours, yielding a fine grey powder (160 mg)

**AAS** (2.5 ppm sample in 8 mM HNO<sub>3</sub>) 30.7 ± 0.4 % Pd, 29.5 ± 0.1 % Ag

**TEM** 11 ± 6 nm, 10 ± 5 nm, 1.1 ± 0.1

**EDX** 0.227 (C K<sub>α</sub>), 0.525 (O K<sub>α</sub>), 1.104 (Na K<sub>α</sub>), 2.307 (S K<sub>α</sub>), 2.622 (Cl K<sub>α</sub>), 2.839 (Pd L<sub>α</sub>), 2.984 (Ag L<sub>α</sub>)

#### *Synthesis of Silver Monometallic Material Ag-PVP*

A 250 mL round bottomed flask was charged with silver(I) nitrate (159 mg, 0.938 mmol), trisodium citrate (276 mg, 0.938 mmol), poly(vinylpyrrolidone) (500 mg) and deionised water (50 mL). The resulting mixture was then stirred for 30 minutes.

A mixture of formaldehyde aqueous solution (37 % w/v, 0.5 mL) and sodium hydroxide aqueous solution (1 M, 2 mL) was then added dropwise over 10 minutes with vigorous stirring. The reaction mixture was then left to stir for 30 minutes to ensure complete reduction before the particulate was separated *via* centrifugation (6000 rpm, 15 minutes), washed with 5:1 acetone-methanol solution (3 × 50 mL) and subsequently dried *in vacuo* for 2 hours, yielding a grey powder (94 mg)

**AAS** (2.5 ppm sample in 8 mM HNO<sub>3</sub>) 89.4 ± 0.4 % Ag

**TEM** Nanoparticles not observed.

**EDX** 2.984 (Ag L<sub>α</sub>)

#### *Synthesis of Palladium/Gold 1:1 Bimetallic Nanoparticles PdAu-PVP*

A 100 mL round bottomed flask, occluded with aluminium foil, was charged with sodium tetrachloropalladate(II) trihydrate (163 mg, 0.469 mmol), hydrogen tetrachloroaurate(III) trihydrate (185 mg, 0.469 mmol), trisodium citrate (275 mg, 0.938 mmol), poly(vinylpyrrolidone) (500 mg) and deionised water (50 mL). The resulting mixture was then stirred for 30 minutes. A mixture of formaldehyde aqueous solution (37 % w/v, 0.5 mL) and sodium hydroxide aqueous solution (1 M, 2 mL) was then added dropwise over 10 minutes with vigorous stirring. The reaction mixture was then left to stir for 30 minutes to ensure complete reduction before the particulate was separated *via* centrifugation (6000 rpm, 15 minutes), washed with 5:1 acetone-methanol solution (3 × 50 mL) and subsequently dried *in vacuo* for 2 hours, yielding a fine deep-purple powder (448 mg)

**AAS** (2.5 ppm sample in 8 mM HNO<sub>3</sub>) 26.1 ± 0.3 % Pd, 17.2 ± 0.3 % Au

**TEM** 7 ± 2 nm, 7 ± 2 nm, 1.03 ± 0.07

**EDX** 0.227 (C K<sub>α</sub>), 0.525 (O K<sub>α</sub>), 1.104 (Na K<sub>α</sub>), 1.739 (Si K<sub>α</sub>), 2.206 (Au M<sub>45</sub>), 2.839 (Pd L<sub>α</sub>), 9.628 (Au L<sub>α</sub>)

#### *Synthesis of Gold Monometallic Nanoparticles Au-PVP*

A 250 mL round bottomed flask, occluded with aluminium foil, was charged with hydrogen tetrachloroaurate(III) trihydrate (369 mg, 0.938 mmol), trisodium citrate (276 mg, 0.938 mmol), poly(vinylpyrrolidone) (500 mg) and deionised water (50 mL). The resulting mixture was then stirred for 30 minutes. A mixture of formaldehyde aqueous solution (37 % w/v, 0.5 mL) and sodium hydroxide aqueous solution (1 M, 2 mL) was then added dropwise over 10 minutes with vigorous

stirring. The reaction mixture was then left to stir for 30 minutes to ensure complete reduction before the particulate was separated *via* centrifugation (6000 rpm, 15 minutes), washed with 5:1 acetone-methanol solution ( $3 \times 50$  mL) and subsequently dried *in vacuo* for 2 hours, yielding a fine wine-red powder (426 mg)

**AAS** (2.5 ppm sample in 8 mM HNO<sub>3</sub>)  $17.5 \pm 0.6$  % Au

**TEM**  $7 \pm 4$  nm,  $7 \pm 4$  nm,  $1.03 \pm 0.06$

**EDX** 0.227 (C K<sub>α</sub>), 0.525 (O K<sub>α</sub>), 1.104 (Na K<sub>α</sub>), 1.739 (Si K<sub>α</sub>), 2.206 (Au M<sub>45</sub>), 2.622 (Cl K<sub>α</sub>), 9.628 (Au L<sub>α</sub>)

#### *Synthesis of Copper Monometallic Material **Cu-EG***

A 25 mL round bottomed flask was charged with copper(II) sulphate pentahydrate (560 mg, 2.25 mmol) and ethylene glycol (10 mL). The resulting mixture was heated to 60 °C with vigorous stirring until complete solvation before hydrazine hydrate (2.79 mL) and an aqueous solution of sodium hydroxide (0.72 mL) was added. A black precipitate was observed to form, as well as effervescence, upon the addition of hydrazine. The resulting mixture was stirred vigorously for 1 hour before being diluted in acetone (40 mL) and the precipitate separated *via* centrifugation (6000 rpm, 2 min), washed with acetone ( $3 \times 50$  mL) and subsequently dried *in vacuo* for 2 hours, yielding a black powder (104 mg).

**AAS** (2.5 ppm sample in 8 mM HNO<sub>3</sub>)  $102.6 \pm 0.2$  % Cu

**TEM**  $68 \pm 45$  nm,  $64 \pm 44$  nm,  $1.1 \pm 0.1$

**EDX** 0.227 (C K<sub>α</sub>), 0.525 (O K<sub>α</sub>), 0.930 (Cu L<sub>α</sub>), 2.307 (S K<sub>α</sub>), 8.048 (Cu K<sub>α</sub>), 8.905 (Cu K<sub>β</sub>)

#### *Synthesis of Palladium/Copper 1:1 Bimetallic Material **PdCu-EG***

A 25 mL round bottomed flask was charged with palladium(II) acetate (252 mg, 1.125 mmol), copper(II) sulphate pentahydrate (280 mg, 1.125 mmol) and ethylene glycol (10 mL). The resulting mixture was heated to 60 °C with vigorous stirring until complete solvation. A black precipitate was observed to form. The resulting mixture was stirred vigorously for 1 hour before being diluted in acetone (40 mL) and the precipitate separated *via* centrifugation (6000 rpm, 2 min), washed with acetone ( $3 \times 50$  mL) and subsequently dried *in vacuo* for 2 hours, yielding a black powder (150 mg).

**AAS** (2.5 ppm sample in 8 mM HNO<sub>3</sub>)  $61.2 \pm 0.3$  % Pd,  $24.05 \pm 0.05$  % Cu

**TEM**  $3 \pm 1$  nm,  $3 \pm 1$  nm,  $1.0 \pm 0.1$

**EDX** 0.227 (C  $K_{\alpha}$ ), 0.525 (O  $K_{\alpha}$ ), 0.930 (Cu  $L_{\alpha}$ ), 2.839 (Pd  $L_{\alpha}$ ), 8.048 (Cu  $K_{\alpha}$ ), 8.905 (Cu  $K_{\beta}$ )

#### *Synthesis of Palladium Bimetallic Material Pd-EG*

A 25 mL round bottomed flask was charged with palladium(II) acetate (505 mg, 2.25 mmol) and ethylene glycol (10 mL). The resulting mixture was heated to 60 °C with vigorous stirring until complete solvation. A black precipitate was observed to form. The resulting mixture was stirred vigorously for 1 hour before being diluted in acetone (40 mL) and the precipitate separated *via* centrifugation (6000 rpm, 2 min), washed with acetone ( $3 \times 50$  mL) and subsequently dried *in vacuo* for 2 hours, yielding a black powder (143 mg).

**AAS** (2.5 ppm sample in 8 mM HNO<sub>3</sub>)  $90.8 \pm 0.5$  % Pd

**TEM**  $16 \pm 3$  nm,  $14 \pm 2$  nm,  $1.18 \pm 0.07$

**EDX** 0.227 (C  $K_{\alpha}$ ), 0.525 (O  $K_{\alpha}$ ), 2.839 (Pd  $L_{\alpha}$ )

#### *Synthesis of Nickel/Copper 1:1 Bimetallic Material NiCu-EG*

A 25 mL round bottomed flask was charged with nickel(II) chloride hexahydrate (267 mg, 1.125 mmol), copper(II) sulphate pentahydrate (280 mg, 1.125 mmol) and ethylene glycol (10 mL). The resulting mixture was heated to 60 °C with vigorous stirring until complete solvation before hydrazine hydrate (2.79 mL) and an aqueous solution of sodium hydroxide (0.72 mL) was added. A red precipitate was observed to form, as well as effervescence, upon the addition of hydrazine. The resulting mixture was stirred vigorously for 1 hour before being diluted in acetone (40 mL) and the precipitate separated *via* centrifugation (6000 rpm, 2 min), washed with acetone ( $3 \times 50$  mL) and subsequently dried *in vacuo* for 2 hours, yielding a terracotta-red powder (158 mg).

**AAS** (2.5 ppm sample in 8 mM HNO<sub>3</sub>)  $8.8 \pm 0.1$  % Ni,  $41.3 \pm 0.1$  % Cu

#### *Synthesis of Nickel Monometallic Material Ni-EG*

A 25 mL round bottomed flask was charged with nickel(II) chloride hexahydrate (535 mg, 2.25 mmol) and ethylene glycol (10 mL). The resulting mixture was heated to 60 °C with vigorous stirring until complete solvation before hydrazine hydrate (2.79 mL) and an aqueous solution of sodium hydroxide (0.72 mL) was added. A

violet-purple precipitate was observed to form upon the addition of hydrazine, which darkened upon stirring. Effervescence was also observed during this time. The resulting mixture was stirred vigorously for 1 hour before being diluted in acetone (40 mL) and the precipitate separated *via* centrifugation (6000 rpm, 2 min), washed with acetone (3 × 50 mL) and subsequently dried *in vacuo* for 2 hours, yielding a black powder (333 mg).

**AAS** (2.5 ppm sample in 8 mM HNO<sub>3</sub>) 28.1 ± 0.3 % Ni

#### *Synthesis of Copper (0) Monometallic Material **Cu(mono)***

A solution of copper(II) chloride dihydrate (733 mg, 4.30 mmol) in deionised water (100 mL) was added dropwise *via* a pressure equalising funnel to a round bottomed flask containing sodium borohydride (500 mg, 12.00 mmol) with vigorous stirring. Black precipitate and effervescence was immediately observed. The precipitate was separated *via* centrifugation (6000 rpm, 10 mins) before being washed with deionised water (2 × 20 mL) and ethanol (2 × 20 mL). The solvent was then decanted off and the solid dried *in vacuo* for 3 hours, yielding a fine black powder (265 mg, 4.17 mmol, 97 %)

**AAS** (2.5 ppm sample in 8 mM HNO<sub>3</sub>) 92.5 ± 0.2 % Cu

**EDX** 0.227 (C K<sub>α</sub>), 0.525 (O K<sub>α</sub>), 0.930 (Cu L<sub>α</sub>), 8.048 (Cu K<sub>α</sub>), 8.905 (Cu K<sub>β</sub>)

#### *Synthesis of Iron-Copper 2:1 Bimetallic Material **Fe<sub>2</sub>Cu***

A solution of iron(II) chloride (272 mg, 2.15 mmol) and copper(II) chloride dihydrate (183 mg, 1.08 mmol) in deionised water (100 mL) was added dropwise *via* a pressure equalising funnel to a round bottomed flask containing sodium borohydride (250 mg, 6.60 mmol) with vigorous stirring. Black precipitate and effervescence was immediately observed. The precipitate was separated *via* centrifugation (6000 rpm, 10 mins) before being washed with deionised water (2 × 20 mL) and ethanol (2 × 20 mL). The solvent was then decanted off, and the solid dried *in vacuo* for 3 hours, yielding a fine black powder (199 mg)

**AAS** (2.5 ppm sample in 8 mM HNO<sub>3</sub>) 80.8 ± 0.2 % Cu

**EDX** 0.227 (C K<sub>α</sub>), 0.525 (O K<sub>α</sub>), 0.705 (Fe L<sub>α</sub>), 0.930 (Cu L<sub>α</sub>), 6.398 (Fe K<sub>α</sub>), 8.048 (Cu K<sub>α</sub>), 8.905 (Cu K<sub>β</sub>)

**X<sub>g</sub>** (2 % suspended in MgSO<sub>4</sub>): 0.022

### *Synthesis of Iron-Copper 1:2 Bimetallic Material FeCu<sub>2</sub>*

A solution of iron(II) chloride (136 mg, 1.08 mmol) and copper(II) chloride dihydrate (366 mg, 2.15 mmol) in deionised water (100 mL) was added dropwise *via* a pressure equalising funnel to a round bottomed flask containing sodium borohydride (250 mg, 6.60 mmol) with vigorous stirring. Black precipitate and effervescence was immediately observed. The precipitate was separated *via* centrifugation (6000 rpm, 10 mins) before being washed with deionised water (2 × 20 mL) and ethanol (2 × 20 mL). The solvent was then decanted off, and the solid dried *in vacuo* for 3 hours, yielding a fine black powder (170 mg)

AAS (2.5 ppm sample in 8 mM HNO<sub>3</sub>) 79.7 ± 0.5 % Cu

EDX 0.227 (C K<sub>α</sub>), 0.525 (O K<sub>α</sub>), 0.705 (Fe L<sub>α</sub>), 0.930 (Cu L<sub>α</sub>), 2.621 (Cl K<sub>α</sub>), 6.398 (Fe K<sub>α</sub>), 8.048 (Cu K<sub>α</sub>), 8.905 (Cu K<sub>β</sub>)

X<sub>g</sub> (2 % suspended in MgSO<sub>4</sub>): 0.008

### *Synthesis of Iron-Copper 4:1 Bimetallic Material Fe<sub>4</sub>Cu*

A solution of iron(II) chloride (327 mg, 2.58 mmol) and copper(II) chloride dihydrate (101 mg, 0.64 mmol) in deionised water (100 mL) was added dropwise *via* a pressure equalising funnel to a round bottomed flask containing sodium borohydride (250 mg, 6.60 mmol) with vigorous stirring. Black precipitate and effervescence was immediately observed. The precipitate was separated *via* centrifugation (6000 rpm, 10 mins) before being washed with deionised water (2 × 20 mL) and ethanol (2 × 20 mL). The solvent was then decanted off, and the solid dried *in vacuo* for 3 hours, yielding a fine black powder (196 mg)

AAS (2.5 ppm sample in 8 mM HNO<sub>3</sub>) 67.3 ± 0.3 % Cu

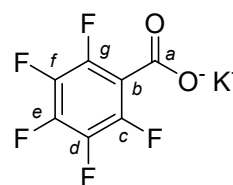
EDX 0.227 (C K<sub>α</sub>), 0.525 (O K<sub>α</sub>), 0.705 (Fe L<sub>α</sub>), 0.930 (Cu L<sub>α</sub>), 6.398 (Fe K<sub>α</sub>), 8.048 (Cu K<sub>α</sub>), 8.905 (Cu K<sub>β</sub>)

X<sub>g</sub> (2 % suspended in MgSO<sub>4</sub>): 0.017

## 6.2.2. Synthesis of Functionalised Potassium Benzoates

### *Synthesis of Potassium Pentafluorobenzoate 1a*

Potassium hydroxide pellets (0.56 g, 10 mmol) were added to a 250 mL round bottomed flask containing a solution of pentafluorobenzoic acid (2.12 g, 10 mmol) in ethanol (25 mL). The resulting mixture was then stirred at room temperature for



1 hour. Evolution of a colourless precipitate was immediately observed upon stirring. A water condenser was then fitted to the flask and the reaction mixture was heated to reflux. Ethanol (150 mL) was then added in 25 mL aliquots until complete solvation of precipitate was observed, at which point the reaction mixture was allowed to cool to room temperature before being placed in a freezer overnight. During this time colourless plate-like crystals were observed to form. These crystals were then collected *via* vacuum filtration and washed with cold ethanol (3 × 5 mL) and diethyl ether (3 × 25 mL) before finally being dried *in vacuo* for 2 hours to remove excess solvent, yielding product **1a** (2.258 g, 9.03 mmol, 90 %).

<sup>19</sup>F NMR (377 MHz, D<sub>2</sub>O) δ -162.0 (td, *J* = 22.0, 8.0 Hz, 2F, F-d/F-f), -155.8 (t, *J* = 20.6 Hz, 1F, F-e), -144.2 (dd, *J* = 23.0, 8.0 Hz, 2F, F-c/F-g).

<sup>13</sup>C NMR (100 MHz, D<sub>2</sub>O) δ 165.4 (s, C-a), 142.8 (d, *J* = 246.1 Hz, C-d/C-f), 141.0 (d, *J* = 249.6 Hz, C-e), 137.4 (dt, *J* = 258.4, 19.1 Hz, C-c/C-g), 114.5 (s, C-b).

FTIR (ATR) 1605 (carboxylate asymmetric stretch), 1365 (carboxylate symmetric stretch).

HRMS (ESI<sup>+</sup>): *m/z* calculated: 288.9088 [M+K], *m/z* found: 288.9083 [M+K]

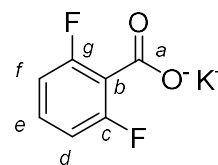
**Literature Data**<sup>33,174</sup>:

<sup>19</sup>F NMR (377 MHz, D<sub>2</sub>O) δ -162.0- -161.9 (m, 2F), -155.8 (t, *J* = 21.0 Hz, 1F), -144.2 (dd, *J* = 7.2, 22.6 Hz, 2F)

FTIR (KBr) 1600 (carboxylate asymmetric stretch)

#### *Synthesis of Potassium 2,6-Difluorobenzoate 1b*

Potassium hydroxide pellets (0.56 g, 10 mmol) were added to a 250 mL round bottomed flask containing a solution of 2,6-difluorobenzoic acid (1.58 g, 10 mmol) in ethanol (25 mL). The resulting mixture was then stirred at room temperature for 1 hour.



Evolution of a colourless precipitate was immediately observed upon stirring. A water condenser was then fitted to the flask and the reaction mixture was heated to reflux. Ethanol (100 mL) was then added in 25 mL aliquots until complete solvation of precipitate was observed, at which point the reaction mixture was allowed to cool to room temperature before being placed in a freezer overnight. During this time colourless needle-like crystals were observed to form. These crystals were then collected *via* vacuum filtration and washed with cold ethanol (3 × 5 mL) and diethyl

ether (3 × 25 mL) before finally being dried *in vacuo* for 2 hours to remove excess solvent, yielding product **1b** (1.61 g, 8.24 mmol, 82 %).

**<sup>1</sup>H NMR** (400 MHz, D<sub>2</sub>O) δ 7.31 (tt, *J* = 8.4, 6.9 Hz, 1H, H-e), 6.98 (t, *J* = 8.4 Hz, 2H, H-d/f)

**<sup>19</sup>F NMR** (377 MHz, D<sub>2</sub>O) δ -116.1 (t, *J* = 6.8 Hz, 2F, F-c/F-g).

**<sup>13</sup>C NMR** (100 MHz, D<sub>2</sub>O) δ 169.3 (s, C-a), 158.5 (dd, *J* = 245.6, 9.5 Hz, C-c/C-g), 130.1 (t, *J* = 9.8 Hz, C-e), 117.1 (t, *J* = 23.8 Hz, C-b), 111.6 (d, *J* = 25.0 Hz, C-d/C-f).

**FTIR** (ATR) 1659 (aromatic C=C bend), 1609 (carboxylate asymmetric stretch), 1376 (carboxylate symmetric stretch).

**HRMS** (ESI+) *m/z* calculated: 234.9370 [M+K], *m/z* found: 234.9369 [M+K]

**Literature Data** <sup>33,166</sup>:

**<sup>1</sup>H NMR** (400 MHz, DMSO) δ 7.13–7.05 (m, 1H), 6.87–6.83 (m, 1H)

**<sup>19</sup>F NMR** (377 MHz, D<sub>2</sub>O) δ -116.0 (s, 2F)

**<sup>13</sup>C NMR** (101 MHz, DMSO) δ 125.7 (t, *J* = 9.4 Hz), 110.8 (dd, *J* = 19.6, 7.3 Hz)

**FTIR** (method not specified) 1610, 1378

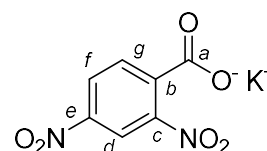
**HRMS** (ESI) *m/z* calculated for C<sub>7</sub>H<sub>3</sub>F<sub>2</sub>O<sub>2</sub>: 157.0107 [M-K]<sup>-</sup>; found: 157.0107 [M-K]<sup>-</sup>.

#### *Synthesis of Potassium 2,4-Dinitrobenzoate 1c*

Potassium hydroxide pellets (0.56 g, 10 mmol) were added to a 500 mL round bottomed flask containing a solution of 2,4-dinitrobenzoic acid (2.12 g, 10 mmol) in ethanol (25 mL).

The resulting mixture was then stirred at room temperature

for 1 hour. Evolution of an off-white precipitate was immediately observed upon stirring. A water condenser was then fitted to the flask and the reaction mixture was heated to reflux. Ethanol (225 mL) was then added in 25 mL aliquots until complete solvation of precipitate was observed, at which point the reaction mixture was allowed to cool to room temperature before being placed in a freezer overnight. During this time off-white crystals were observed to form. These crystals were then collected *via* vacuum filtration and washed with cold ethanol (3 × 5 mL) and diethyl ether (3 × 25 mL) before finally being dried *in vacuo* for 2 hours to remove excess solvent, yielding product **1c** (2.36 g, 9.45 mmol, 94 %).



**<sup>1</sup>H NMR** (400 MHz, D<sub>2</sub>O) δ 8.89 (d, *J* = 2.2 Hz, 1H, H-d), 8.52 (dd, *J* = 8.4, 2.2 Hz, 1H, H-f), 7.68 (d, *J* = 8.4 Hz, 1H, H-g).

**<sup>13</sup>C NMR** (100 MHz, D<sub>2</sub>O) δ 172.4 (s, C-a), 147.0 (s, C-c), 144.5 (s, C-e), 141.2 (s, C-b), 129.3 (s, C-d), 128.9 (s, C-f), 120.2 (s, C-g).

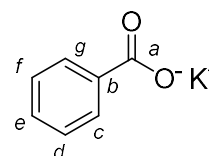
**FTIR** (ATR) 3098 (aromatic C-H stretch), 1613 (carboxylate asymmetric stretch), 1393 (carboxylate symmetric stretch).

**HRMS** (ESI+) *m/z* calculated: 288.9260 [M+K], *m/z* found: 288.9249 [M+K]

*Use of compound 1c has been reported in literature*<sup>175,176</sup>, *but characterisation has not been reported.*

### *Synthesis of Potassium Benzoate 1d*

Potassium hydroxide pellets (0.56 g, 10 mmol) were added to a 250 mL round bottomed flask containing a solution of benzoic acid (1.22 g, 10 mmol) in ethanol (25 mL). The resulting mixture was then stirred at room temperature for 1 hour. Evolution of a



colourless precipitate was immediately observed upon stirring. A water condenser was then fitted to the flask and the reaction mixture was heated to reflux. Ethanol (125 mL) was then added in 25 mL aliquots until complete solvation of precipitate was observed, at which point the reaction mixture was allowed to cool to room temperature before being placed in a freezer overnight. During this time a colourless solid was observed to form. This solid was then collected *via* vacuum filtration and washed with cold ethanol (3 × 5 mL) and diethyl ether (3 × 25 mL) before finally being dried *in vacuo* for 2 hours to remove excess solvent, yielding product **1d** (1.47 g, 9.19 mmol, 92 %).

**<sup>1</sup>H NMR** (400 MHz, D<sub>2</sub>O) δ 7.81 (d, *J* = 7.0 Hz, 2H, H-c/H-g), 7.49 (tt, *J* = 7.3, 1.4 Hz, 1H, H-e), 7.42 (tt, *J* = 7.3, 1.4 Hz, 2H, H-d/H-f).

**<sup>13</sup>C NMR** (100 MHz, D<sub>2</sub>O) δ 175.8 (s, C-a), 136.3 (s, C-b), 131.2 (s, C-c/C-g), 128.8 (s, C-d/C-f), 128.3 (s, C-e).

**FTIR** (ATR) 3066 (aromatic C-H stretch), 1594 (aromatic C=C bend), 1548 (carboxylate asymmetric stretch), 1383 (carboxylate symmetric stretch).

**HRMS** (ESI+) *m/z* calculated: 198.9564 [M+K], *m/z* found: 198.9553 [M+K]

### **Literature Data**<sup>177,178</sup>:

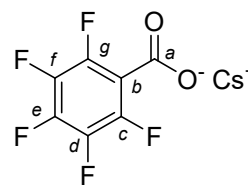
**<sup>1</sup>H NMR** (80 MHz, D<sub>2</sub>O) δ 7.4-8.0 (m, 5H, Ar-H)

**FTIR** (KBr) 3067, 1595, 1553, 1397

### 6.2.3. Synthesis of Functionalised Caesium Benzoates

#### *Synthesis of Caesium Pentafluorobenzoate 6a*

A 50 mL round bottomed flask was charged with pentafluorobenzoic acid (2.12 g, 10.00 mmol), caesium carbonate (1.63 g, 5.00 mmol) and ethanol (20 mL). The resulting mixture was then heated to reflux with stirring for 1



hour. Upon cooling, colourless solid began to precipitate from solution. Two thirds of the solvent was then removed *via* rotary evaporation and diethyl ether (20 mL) was added. The resulting colourless precipitate was collected *via* vacuum filtration and washed with ice cold ethanol (2 × 5 mL) and diethyl ether (2 × 10 mL), before being dried *in vacuo* for 2 hours, yielding a colourless solid (2.67 g, 7.77 mmol, 78 %)

**<sup>19</sup>F NMR** (376 MHz, D<sub>2</sub>O) δ -144.03 (2F, dd, *J* 23.4 and 6.7, F-c/F-g), -155.53 (1F, t, *J* 20.8, F-e), -161.94 (2F, td, *J* 20.7 and 7.0, F-d/F-f).

**<sup>13</sup>C NMR** (100 MHz, D<sub>2</sub>O) δ 165.3 (s, C-a), 142.8 (dddd, *J* 245.8, 16.4, 9.0, and 4.1, C-c/C-g), 141.0 (dt, *J* 251.4, 13.6 and 5.4, C-e), 137.4 (dt, *J* 251.3, 13.0, 4.5, C-d/C-f), 114.5 (t, *J* 21.6, C-b).

**FTIR** (ATR) 2978 (aromatic C-H stretch), 1645 (aromatic C=C bend), 1601 (carboxylate asymmetric stretch), 1362 (carboxylate symmetric stretch).

**HRMS** (ESI+) *m/z* calculated: 234.9789 [M-Cs+H+Na], 256.9608 [M-Cs+2Na], *m/z* found: 234.0805 [M-Cs+H+Na], 256.9669 [M-Cs+2Na].

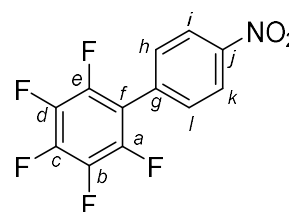
#### **Literature Data**<sup>174</sup>:

**FTIR** (KBr) 1600 (carboxylate asymmetric stretch)

### 6.2.4. Synthesis and Purification of Biphenyl Products

#### *Synthesis of 4'-Nitro-2,3,4,5,6-pentafluorobiphenyl 3aa*

A Schleck tube was charged with potassium pentafluorobenzoate (725 mg, 3 mmol, **1a**), 1-iodo-4-nitrobenzene (500 mg, 2 mmol, **2a**) and copper(I) iodide (38 mg, 0.2 mmol, 10 mol%). The vessel was then placed under vacuum and back filled with nitrogen 3 times, before



diglyme (anhydrous, 2 mL) was added with stirring. This slurry was left to stir for 10 minutes before being heated to 130 °C for 24 hours. The mixture was then left to cool before being diluted in ethyl acetate (50 mL) and filtered over a short silica

column to remove a yellowish solid deposition. The filtrate was washed with water (3 × 40 mL) and brine (40 mL) before being dried over magnesium sulphate and concentrated *via* rotary evaporation to yield a viscous brown oil (880 mg). This was redissolved in a minimum of ethyl acetate and purified *via* flash column chromatography (silica, 40:1 petroleum ether–ethyl acetate) yielding an off-white solid (463 mg). This was then recrystallised from a minimum of boiling ethanol to give colourless needle-like crystals (200 mg, 0.70 mmol, 35 %).

**<sup>1</sup>H NMR** (400 MHz, CDCl<sub>3</sub>) δ 8.37 (d, *J* = 8.8 Hz, 2H, H-i/k), 7.64 (d, *J* = 8.8 Hz, 2H, H-h/l)

**<sup>19</sup>F NMR** (377 MHz, CDCl<sub>3</sub>) δ -160.8 (td, *J* = 21.8, 8.3 Hz, 2F, F-b/F-d), -152.4 (t, *J* = 21.1 Hz, 1F, F-c), -142.5 (dd, *J* = 22.8, 8.0 Hz, 2F, F-a/F-e)

**<sup>13</sup>C NMR** (100 MHz, CDCl<sub>3</sub>) δ 148.3 (s, C-j), 144.0 (d, *J* = 256.6 Hz, C-b/d), 141.3 (dt, *J* = 256.6, 4.5 Hz, C-c), 138.0 (dt, *J* = 254, 16.6 Hz, C-a/e), 132.9 (s, C-g), 131.3 (s, C-i/k), 123.9 (s, C-h/l), 113.8 (td, *J* = 16.5, 4.5 Hz, C-f)

**HRMS** (ESI+): *m/z* calculated: 290.0235 [M+H], *m/z* found: 290.0177 [M+H]

**Literature Data**<sup>33,179</sup>:

**<sup>1</sup>H NMR** (400 MHz, CDCl<sub>3</sub>) δ 7.64-7.66 (m, 2H), 8.35-8.38 (m, 2H)

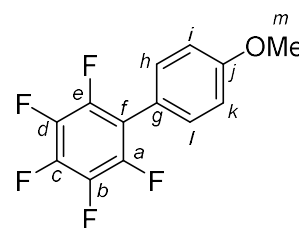
**<sup>19</sup>F NMR** (377 MHz, D<sub>2</sub>O) δ -160.8 (m, 2F), -152.5 (t, *J* = 20.7 Hz, 1F), -142.5 (dd, *J* = 22.6, 8.7 Hz, 2F)

**<sup>13</sup>C NMR** (100 MHz, CDCl<sub>3</sub>) δ 148.2, 144.0(dm, *J* = 259.0 Hz), 141.3(dm, *J* = 254.8 Hz), 138.0 (dm, *J* = 252.4 Hz), 132.9, 131.3, 123.8, 113.8 (td, *J* = 3.4, 17.2 Hz)

**HRMS** (ESI+): *m/z* calculated for C<sub>12</sub>H<sub>4</sub>F<sub>5</sub>NO<sub>2</sub>: 289.0162; found: 289.0163

*Synthesis of 2,3,4,5,6-pentafluoro-4'-methoxybiphenyl 3ab*

A Schleck tube was charged with potassium pentafluorobenzoate (375 mg, 1.5 mmol, **1a**), 4-iodoanisole (234 mg, 1 mmol, **2bI**), copper(I) iodide (19 mg, 0.1 mmol, 10 mol%) and palladium(II) acetate (22 mg, 0.1 mmol, 10 mol%). The vessel was then placed under vacuum and back



filled with nitrogen 3 times, before diglyme (anhydrous, 4 mL) was added with stirring. This slurry was left to stir for 10 minutes before being heated to 130 °C for 24 hours. The mixture was then left to cool before being diluted in ethyl acetate (50 mL) and filtered over a short silica column to remove a yellowish solid deposition.

The filtrate was washed with water (3 × 40 mL) and brine (40 mL) before being dried over magnesium sulphate and concentrated *via* rotary evaporation to yield a brown solid (660 mg). This was redissolved in a minimum of ethyl acetate and purified *via* flash column chromatography (silica, 9:1 petroleum ether–ethyl acetate) yielding a pale yellow solid (257 mg). This was then recrystallised from a minimum of boiling ethanol to give colourless plate-like crystals (113 mg, 0.40 mmol, 40 %).

**<sup>1</sup>H NMR** (400 MHz, CDCl<sub>3</sub>) δ 7.29 (d, *J* = 8.8 Hz, 2H, H-i/k), 6.95 (d, *J* = 8.8 Hz, 2H, H-h/l), 3.80 (s, 3H, H-m)

**<sup>19</sup>F NMR** (377 MHz, CDCl<sub>3</sub>) δ -162.3 (td, *J* = 23.1, 8.0 Hz, 2F, F-b/F-d), -156.5 (t, *J* = 23.1 Hz, 1F, F-c), -143.6 (dd, *J* = 23.1, 8.0 Hz, 2F, F-a/F-e)

**<sup>13</sup>C NMR** (100 MHz, CDCl<sub>3</sub>) δ 160.3 (s, C-j), 144.0 (d, *J* = 249 Hz, C-F's), 140.0 (d, *J* = 254 Hz, C-F's), 137.8 (d, *J* = 253 Hz, C-F's), 131.4 (s, C-i/k), 118.4 (s, C-g), 155.7 (td, *J* = 17.2, 3.4 Hz, C-f), 114.2 (s, C-h/l), 55.3 (s, C-m)

**HRMS** (ESI<sup>+</sup>): *m/z* calculated: 275.0490 [M+H]; *m/z* found: 275.0401 [M+H]

#### Literature Data <sup>33</sup>:

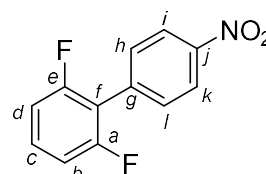
**<sup>1</sup>H NMR** (400 MHz, CDCl<sub>3</sub>) δ 7.36-7.34 (m, 2H), 7.02-6.99 (m, 2H), 3.85 (s, 3H)

**<sup>19</sup>F NMR** (377 MHz, D<sub>2</sub>O) δ -162.6 (m, 2F), -156.5 (t, *J* = 21.5 Hz, 1F), -143.6 (dd, *J* = 23.4, 8.3 Hz, 2F)

**<sup>13</sup>C NMR** (100 MHz, CDCl<sub>3</sub>) δ 160.2, 144.1 (dm, *J* = 249.4 Hz), 140.0 (dm, *J* = 251.5 Hz), 137.8 (dm, *J* = 249.0 Hz), 131.4, 118.4, 115.7 (td, *J* = 17.2, 3.4 Hz), 114.2, 55.3

#### Synthesis of 2,6-difluoro-4'-nitrobiphenyl **3ba**

A Schleck tube was charged with potassium 2,6-difluorobenzoate (392 mg, 2 mmol, **1b**), 1-iodo-4-nitrobenzene (332 mg, 1.33 mmol, **2a**), copper(I) iodide (49



mg, 0.26 mmol, 20 mol%) and 1,10-phenanthroline (47 mg, 0.26 mmol, 20 mol%). The vessel was then placed under vacuum and back filled with nitrogen 3 times, before *N,N*-dimethylacetamide (anhydrous, 2 mL) was added with stirring. This slurry was left to stir for 10 minutes before being heated to 160 °C for 24 hours. The mixture was then left to cool before being diluted in ethyl acetate (50 mL) and filtered over a short silica column to remove a yellowish solid deposition. The filtrate was washed with water (3 × 40 mL) and brine (40 mL) before being dried over magnesium sulphate and concentrated *via* rotary evaporation to yield a brown

solid. This was redissolved in a minimum of dichloromethane, dry loaded onto silica and subsequently purified *via* flash column chromatography (silica, 40:1 petroleum ether–ethyl acetate) yielding colourless needles (60 mg, 0.26 mmol, 20 %)

$^1\text{H NMR}$  (400 MHz,  $\text{CDCl}_3$ )  $\delta$  8.25 (d,  $J = 8.8$  Hz, 2H, H-i/k), 7.60 (d,  $J = 8.8$  Hz, 2H, H-h/l), 7.31 (tt,  $J = 8.3, 6.4$  Hz, 1H, H-c), 6.98 (t,  $J = 8.3$  Hz, 2H, H-b/d)

$^{19}\text{F NMR}$  (377 MHz,  $\text{CDCl}_3$ )  $\delta$  -114.1 (t,  $J = 6.4$  Hz, 2F, F-a/e)

$^{13}\text{C NMR}$  (100 MHz,  $\text{CDCl}_3$ )  $\delta$  159.8 (dd,  $J = 250.6, 6.6$  Hz, C-a/e), 147.6 (s, C-j), 136.0 (s, C-g), 131.4 (s, C-h/l), 130.4 (t,  $J = 9.8$  Hz, C-c), 123.4 (s, C-i/k), 116.4 (t,  $J = 22.0$  Hz, C-f), 112.0 (d,  $J = 25.8$  Hz, C-b/d)

**HRMS** (ESI+):  $m/z$  calculated: 236.0518 [M+H],  $m/z$  found: 236.0512 [M+H]

#### Literature Data<sup>123</sup>:

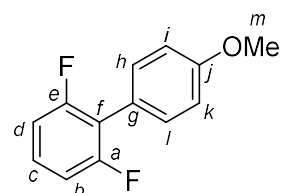
$^1\text{H NMR}$  (400 MHz,  $\text{CDCl}_3$ )  $\delta$  8.22 (d,  $J = 8.4$  Hz, 2H), 7.57 (d,  $J = 8.4$  Hz, 2H), 7.35-7.24 (m, 1H), 6.95 (t,  $J = 8.0$  Hz, 2H)

$^{19}\text{F NMR}$  (377 MHz,  $\text{D}_2\text{O}$ )  $\delta$  -114.1 (s, 2F)

$^{13}\text{C NMR}$  (100 MHz,  $\text{CDCl}_3$ )  $\delta$  159.8 (dd,  $J = 250.4, 6.5$  Hz), 147.6, 136.0, 131.4 (t,  $J = 2.2$  Hz), 130.5 (t,  $J = 10.4$  Hz), 123.5, 116.4 (t,  $J = 18.1$  Hz), 112.0 (dd,  $J = 19.5, 6.6$  Hz)

#### Synthesis of 2,6-difluoro-4'-methoxybiphenyl **3bb**

A Schleck tube was charged with potassium 2,6-difluorobenzoate (296 mg, 1.5 mmol, **1b**), 4-iodoanisole (234 mg, 1 mmol, **2bI**), copper(I) iodide (40 mg, 0.2 mmol,



20 mol%) and 1,10-phenanthroline (36 mg, 0.2 mmol, 20 mol%). The vessel was then placed under vacuum and back filled with nitrogen 3 times, before *N,N*-dimethylacetamide (anhydrous, 2 mL) was added with stirring. This slurry was left to stir for 10 minutes before being heated to 160 °C for 24 hours. The mixture was then left to cool before being diluted in ethyl acetate (50 mL) and filtered over a short silica column to remove a yellowish solid deposition. The filtrate was washed with water (3 × 40 mL) and brine (40 mL) before being dried over magnesium sulphate and concentrated *via* rotary evaporation to yield a brown solid. This was redissolved in a minimum of dichloromethane, dry loaded onto silica and subsequently purified *via* flash column chromatography (silica, 4:1 petroleum ether–ethyl acetate) yielding a pale orange solid (86 mg). This solid was then recrystallised from boiling ethanol, yielding colourless plate-like crystals, which were collected

via vacuum filtration and washed with cold ethanol (3 × 5 mL) before being dried *in vacuo*, yielding product **3bb** (80 mg, 0.36 mmol, 36 %)

**<sup>1</sup>H NMR** (400 MHz, CDCl<sub>3</sub>) δ 7.34 (d, *J* = 8.0 Hz, 2H, H-b/d), 7.17 (td, *J* = 8.0, 6.5 Hz, 1H, H-c), 6.95-6.85 (m, 4H, H-h/l / H-i/k), 3.78 (s, 1H, H-m)

**<sup>19</sup>F NMR** (377 MHz, CDCl<sub>3</sub>) δ -114.8 (t, *J* = 6.2 Hz, 2F, F-a/e)

**<sup>13</sup>C NMR** (100 MHz, CDCl<sub>3</sub>) δ 160.2 (dd, *J* = 247.7, 7.3 Hz, C-a/e), 159.5 (s, C-j), 131.5 (s, C-i/k), 128.3 (t, *J* = 10.3 Hz, C-c), 121.3 (s, C-g), 118.2 (t, *J* = 18.4 Hz, C-f), 113.8 (s, C-h/l), 111.6 (dd, *J* = 19.3, 7.3 Hz, C-b/d), 55.3 (s, C-m)

**HRMS** (ESI+): *m/z* calculated: 221.0772 [M+H]; *m/z* found: 221.0764 [M+H]

#### Literature Data<sup>33</sup>:

**<sup>1</sup>H NMR** (400 MHz, CDCl<sub>3</sub>) δ 7.39-7.36 (m, 2H), 7.24-7.17 (m, 1H), 6.98-6.89 (m, 4H), 3.82 (s, 3H)

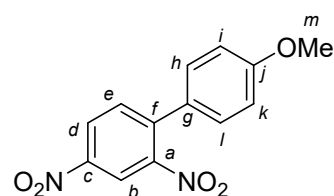
**<sup>19</sup>F NMR** (377 MHz, D<sub>2</sub>O) δ -114.8 (s, 2F)

**<sup>13</sup>C NMR** (100 MHz, CDCl<sub>3</sub>) δ 160.2 (dd, *J* = 246.3, 7.1 Hz), 159.5, 131.5, 128.3 (t, *J* = 10.3 Hz), 121.2, 118.2 (t, *J* = 18.5 Hz), 113.8, 111.5 (dd, *J* = 19.2, 7.3 Hz), 55.2

**HRMS** (ESI+): *m/z* calculated for C<sub>13</sub>H<sub>10</sub>F<sub>2</sub>O (M<sup>+</sup>): 220.0700; found: 220.0706

#### Synthesis of 2,4-dinitro-4'-methoxybiphenyl **3cb**

A Schleck tube was charged with 1-chloro-2,4-dinitrobenzene (415 mg, 2 mmol), 4-methoxyphenylboronic acid (455 mg, 3 mmol), palladium(II) chloride (18 mg, 0.1 mmol, 5 mol%) and



potassium carbonate (829 mg, 6 mmol). The vessel was then placed under vacuum and back filled with nitrogen 3 times, before poly(ethylene glycol)-300 (8 mL) was added with stirring. This viscous slurry was left to stir vigorously for 10 minutes before being heated to 30 °C for 30 minutes. After 10 minutes, the solution had developed an orange colouration. The resulting mixture was diluted in methanol (50 mL) and filtered over celite to remove unreacted base and other solid depositions. The solvent was then removed, yielding a yellow solid. This solid was then recrystallised from boiling ethanol, yielding yellow needle-like crystals, which were collected *via* vacuum filtration and washed with cold ethanol (3 × 5 mL) before being dried *in vacuo*, yielding product **3cb** (521 mg, 1.9 mmol, 95 %)

**<sup>1</sup>H NMR** (400 MHz, CDCl<sub>3</sub>) δ 8.58 (d, *J* = 2.2 Hz, 1H, H-b), 8.36 (dd, *J* = 8.5, 2.2 Hz, 1H, H-d), 7.58 (d, *J* = 8.5 Hz 1H, H-e), 7.21 (d, *J* = 8.9 Hz, 2H, H-i/k), 6.92 (d, *J* = 8.7 Hz, 2H, H-h/l), 3.79 (s, 3H, H-m)

**<sup>13</sup>C NMR** (100 MHz, CDCl<sub>3</sub>) δ 160.8 (s, C-j), 149.0 (s, C-a/C-c), 146.4 (s, C-a/C-c), 141.8 (s, C-f), 133.0 (s, C-b), 129.2 (s, C-d), 127.2 (s, C-g), 126.4 (s, C-e), 119.7 (s, C-k/i), 114.7 (s, C-h/l), 55.4 (s, C-m)

**HRMS** (ESI<sup>+</sup>): *m/z* calculated: 275.0662 [M+H]; *m/z* found: 275.0616 [M+H]

**Literature Data**<sup>180</sup>:

**<sup>1</sup>H NMR** (300 MHz, CDCl<sub>3</sub>) δ 8.66 (s, 1H), 8.44 (d, *J* = 8.4 Hz, 1H), 7.66 (d, *J* = 8.4 Hz, 1H), 7.29 (d, *J* = 7.8 Hz, 2H), 7.00 (d, *J* = 7.8 Hz, 2H), 3.87 (s, 3H)

**<sup>13</sup>C NMR** (75 MHz, CDCl<sub>3</sub>) δ 159.8, 147.9, 145.3, 140.8, 132.0, 128.2, 126.1, 125.3, 118.6, 113.6, 54.4

## 6.2.5. General Experimental Procedures

### Chapter 2

#### *General Copper-catalysed DCC Procedure*

A Schleck tube was charged with potassium pentafluorobenzoate (188 mg, 0.75 mmol, **1a**), 1-iodo-4-nitrobenzene (125 mg, 0.5 mmol, **2a**), the catalyst under investigation (0.05-0.15 mmol Cu) and biphenyl (7.7 mg, 0.05 mmol) as an internal standard. The vessel was then placed under vacuum and backfilled with dry nitrogen 3 times, before diglyme (anhydrous, 2 mL) was added with stirring. This mixture was left to stir for 10 minutes before being heated to between 100-130 °C for 5 hours. Samples of 0.1 mL were drawn off at regular intervals and diluted to 1 mL in acetonitrile. This dilution was performed again before being filtered through celite and analysed *via* HPLC.

#### *Solvent & Additive Screening Experiments*

A Schleck tube was charged with potassium pentafluorobenzoate (188 mg, 0.75 mmol, **1a**), 1-iodo-4-nitrobenzene (125 mg, 0.5 mmol, **2a**), Cu(mono) (0.15 mmol), the additive *if solid* (0.05 mmol) and biphenyl (7.7 mg, 0.05 mmol) as an internal standard. The vessel was then placed under vacuum and backfilled with dry nitrogen 3 times, before solvent (anhydrous, 2 mL) and the additive *if liquid* (0.05 mmol) was added with stirring. This mixture was left to stir for 10 minutes before being heated to between 100 °C for 5 hours. Samples of 0.1 mL were drawn off at regular

intervals and diluted to 1 mL in acetonitrile. This dilution was performed again before being filtered through celite and analysed *via* HPLC.

#### *Caesium Substrate Experiments*

A Schleck tube was charged with caesium pentafluorobenzoate (256 mg, 0.75 mmol, **6a**), 1-iodo-4-nitrobenzene (125 mg, 0.5 mmol, **2a**), Cu(mono) (0.05-0.15 mmol) and biphenyl (7.7 mg, 0.05 mmol) as an internal standard. The vessel was then placed under vacuum and backfilled with dry nitrogen 3 times, before solvent (anhydrous, 2 mL) was added with stirring. This mixture was left to stir for 10 minutes before being heated to between 100-130 °C for 5 hours. Samples of 0.1 mL were drawn off at regular intervals and diluted to 1 mL in acetonitrile. This dilution was performed again before being filtered through celite and analysed *via* HPLC.

#### *Induction Heating Protocol – Induction Reactor 1*

The reaction vessel was charged with potassium pentafluorobenzoate (376 mg, 1.5 mmol, **1a**), 1-iodo-4-nitrobenzene (250 mg, 1 mmol, **2a**), the catalyst under investigation (0.1 mmol Cu) and biphenyl (15.4 mg, 0.1 mmol) as an internal standard. The vessel was then placed under vacuum and backfilled with dry nitrogen 3 times, before diglyme (anhydrous, 4 mL) was added with stirring. This mixture was left to stir for 10 minutes, *via* the use of an overhead stirrer. The vessel was then placed within the induction coils of Induction Reactor 1 and the reactor was powered at 117 W for the allotted reaction time. Samples of 0.1 mL were drawn off at regular intervals and diluted to 1 mL in acetonitrile. This dilution was performed again before being filtered through celite and analysed *via* HPLC.

#### *Induction Heating Protocol – Induction Reactor 2*

The reaction vessel was charged with potassium pentafluorobenzoate (376 mg, 1.5 mmol, **1a**), 1-iodo-4-nitrobenzene (250 mg, 1 mmol, **2a**), Fe<sub>2</sub>Cu bimetallic material (0.1 mmol Cu) and biphenyl (15.4 mg, 0.1 mmol) as an internal standard. The vessel was then placed under vacuum and backfilled with dry nitrogen 3 times, before diglyme (anhydrous, 4 mL) was added with stirring. This mixture was left to stir for 10 minutes, *via* the use of an overhead stirrer. The vessel was then placed over the hob of Induction Reactor 2 and the reactor was powered at 200-600 W for the allotted reaction time. Samples of 0.1 mL were drawn off at regular intervals and

diluted to 1 mL in acetonitrile. This dilution was performed again before being filtered through celite and analysed *via* HPLC.

### Chapter 3

#### *General Bimetallic Nanoparticle-catalysed DCC Procedure*

A Schleck tube was charged with potassium pentafluorobenzoate (188 mg, 0.75 mmol, **1a**), 1-iodo-4-nitrobenzene (125 mg, 0.5 mmol, **2a**), the catalyst under investigation (0.05 mmol) and biphenyl (7.7 mg, 0.05 mmol) as an internal standard. The vessel was then placed under vacuum and backfilled with dry argon 3 times, before diglyme (anhydrous, 2 mL) was added with stirring. This mixture was left to stir for 10 minutes before being heated to 100-130 °C for 5 hours. Samples of 0.1 mL were drawn off at regular intervals and diluted to 1 mL in acetonitrile. This dilution was performed again before being filtered through celite and analysed *via* HPLC.

#### *Mercury Spiking Experiment*

A Schleck tube was charged with potassium pentafluorobenzoate (188 mg, 0.75 mmol, **1a**), 1-iodo-4-nitrobenzene (125 mg, 0.5 mmol, **2a**), Pd<sub>2</sub>Cu-PVP (45.7 mg, 0.05 mmol Cu) and biphenyl (7.7 mg, 0.05 mmol) as an internal standard. The vessel was then placed under vacuum and backfilled with dry argon 3 times, before diglyme (anhydrous, 2 mL) and mercury (0.15 mL, 10 mmol) were added with stirring. This mixture was left to stir for 10 minutes before being heated to 100 °C for 3 hours. Samples of 0.1 mL were drawn off at regular intervals and diluted to 1 mL in acetonitrile. This dilution was performed again before being filtered through celite and analysed *via* HPLC.

### Chapter 4

#### *General DCC Procedure (Substrate Exploration)*

A Schleck tube was charged with the potassium salt under investigation (0.75 mmol), the aryl halide under investigation *if solid* (0.5 mmol), the catalyst under investigation (0.05 mmol Cu) and biphenyl (7.7 mg, 0.05 mmol) as an internal standard. The vessel was then placed under vacuum and backfilled with dry argon 3 times, before either *N,N*-dimethylacetamide or diglyme (anhydrous, 2 mL) and the aryl halide under investigation *if liquid* (0.5 mmol) was added with stirring. This

mixture was left to stir for 10 minutes before being heated to either 160, 130 or 100 °C for the allotted reaction time. A Sample of 0.1 mL was drawn off and diluted to 1 mL in acetonitrile at reaction completion. This dilution was performed again before being filtered through celite and analysed *via* HPLC.

## Chapter 5

### *Solvent Exploration*

A Schleck tube was charged with potassium pentafluorobenzoate (188 mg, 0.75 mmol, **1a**), 4-iodoanisole (117 mg, 0.5 mmol, **2bI**), copper (I) iodide (9.5 mg, 0.05 mmol) and palladium(II) acetate (11.2 mg, 0.05 mmol). The vessel was then placed under vacuum and backfilled with dry argon 3 times, before solvent (anhydrous, 2 mL) was added with stirring. This mixture was left to stir for 10 minutes before being heated to 100 °C for 24 hours. The reaction mixture was then allowed to cool before being diluted in ethyl acetate (20 mL) and filtered over celite to remove solid depositions. The filtrate was then transferred to a separating funnel and washed with deionised water (3 × 50 mL) and brine (50 mL). The organic layer was then dried over magnesium sulfate and the solvent was removed *via* rotary evaporation to yield a brown solid. This solid was then redissolved in deuterated chloroform (3 mL). 0.5 mL of the resulting solution was then drawn off and analysed *via* <sup>1</sup>H NMR.

### *Exploring the Use of PEG to Promote Reactivity*

A Schleck tube was charged with the potassium salt under investigation (0.75 mmol), 4-iodoanisole (117 mg, 0.5 mmol, **2bI**), copper(I) iodide (9.5 mg, 0.05 mmol) and palladium(II) acetate (11.2 mg, 0.05 mmol) and PEG additive *if solid* (15-150 mg). The vessel was then placed under vacuum and backfilled with dry argon 3 times, before dimethyl sulfoxide (anhydrous, 2 mL) and PEG additive *if liquid* (15-150 mg) was added with stirring. This mixture was left to stir for 10 minutes before being heated to 100-140 °C for 24 hours. The reaction mixture was then allowed to cool before being diluted in ethyl acetate (20 mL) and filtered over celite to remove solid depositions. The filtrate was then transferred to a separating funnel and washed with deionised water (3 × 50 mL) and brine (50 mL). The organic layer was then dried over magnesium sulfate and the solvent was removed *via* rotary evaporation to yield a brown solid. This solid was then redissolved in

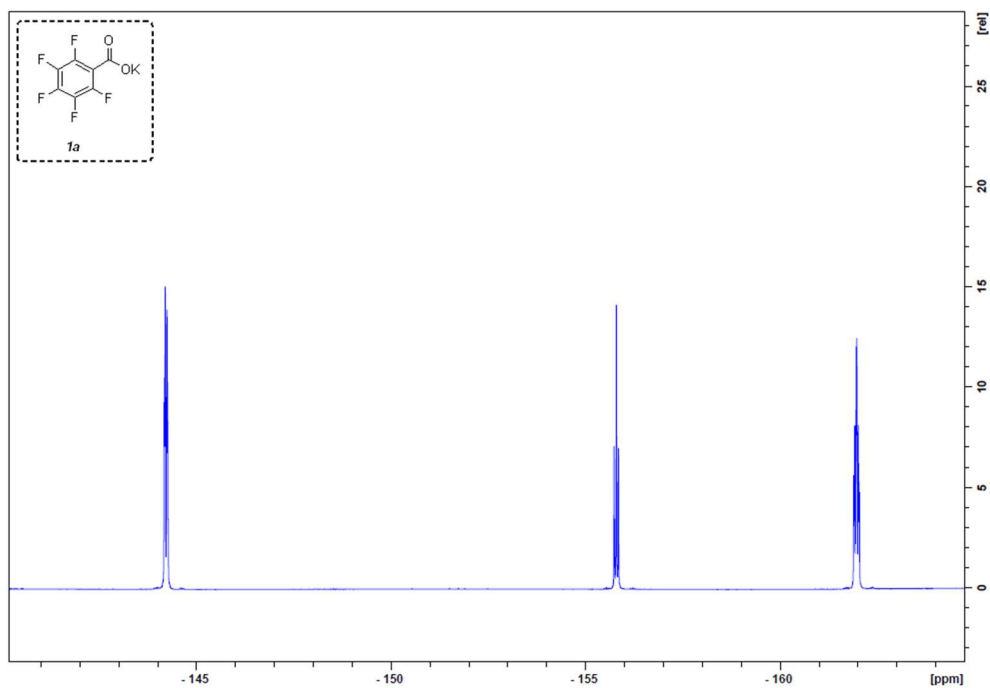
deuterated chloroform (3 mL). 0.5 mL of the resulting solution was then drawn off and analysed *via*  $^1\text{H}$  NMR.

#### *Design of Experiments Investigations*

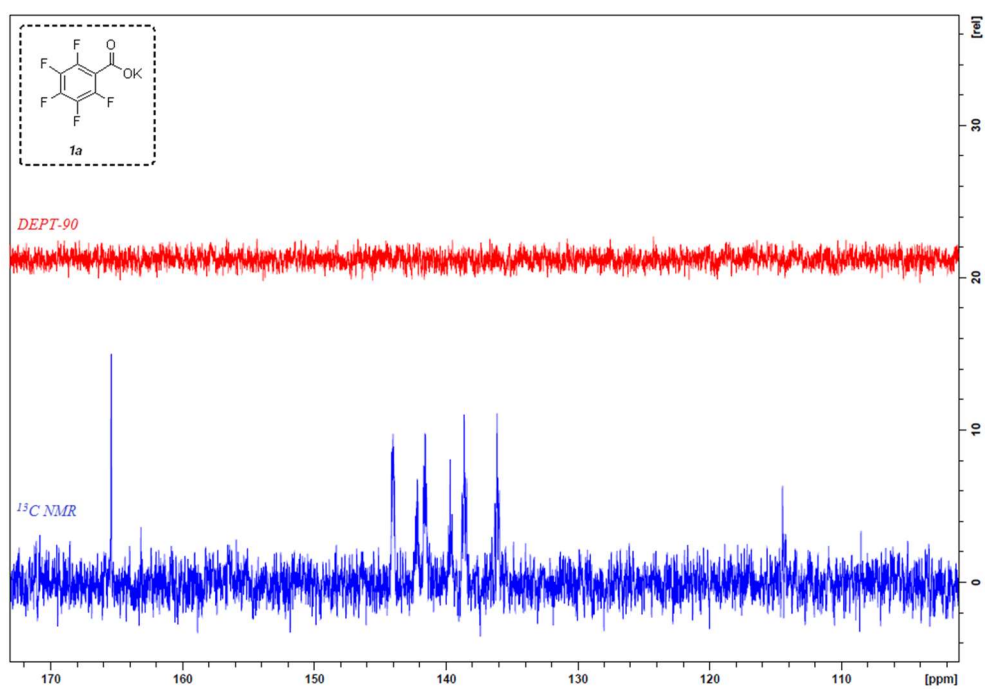
A Schleck tube was charged with potassium 2,6-difluorobenzoate (74-221 mg, 0.375-1.125 mmol, **1b**), 4-iodoanisole (59-176 mg, 0.25-0.75 mmol, **2bI**), copper(I) iodide (9.5 mg, 0.05 mmol) and palladium(II) acetate (6-22 mg, 0.025-0.1 mmol). The vessel was then placed under vacuum and backfilled with dry argon 3 times, before dimethyl sulfoxide (anhydrous, 2 mL) and DM-PEG-500 (50-150 mg) was added with stirring. This mixture was left to stir for 10 minutes before being heated to 110-140 °C for 24 hours. The reaction mixture was then allowed to cool before being diluted in ethyl acetate (20 mL) and filtered over celite to remove solid depositions. The filtrate was then transferred to a separating funnel and washed with deionised water (3 × 50 mL) and brine (50 mL). The organic layer was then dried over magnesium sulfate and the solvent was removed *via* rotary evaporation to yield a brown solid. This solid was then redissolved in deuterated chloroform (3 mL). 0.5 mL of the resulting solution was then drawn off and analysed *via*  $^1\text{H}$  NMR.

### 6.3. Nuclear Magnetic Resonance Spectroscopy of Purified Compounds

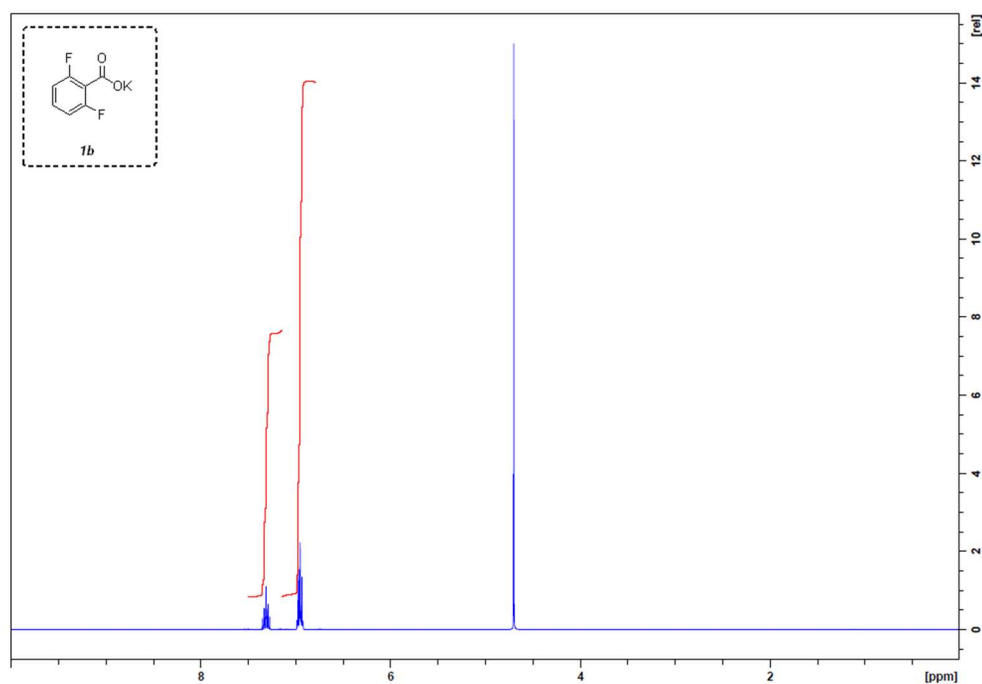
#### **1a** - Potassium Pentafluorobenzoate $^{19}\text{F}$ NMR Spectra, 376 MHz, $\text{D}_2\text{O}$



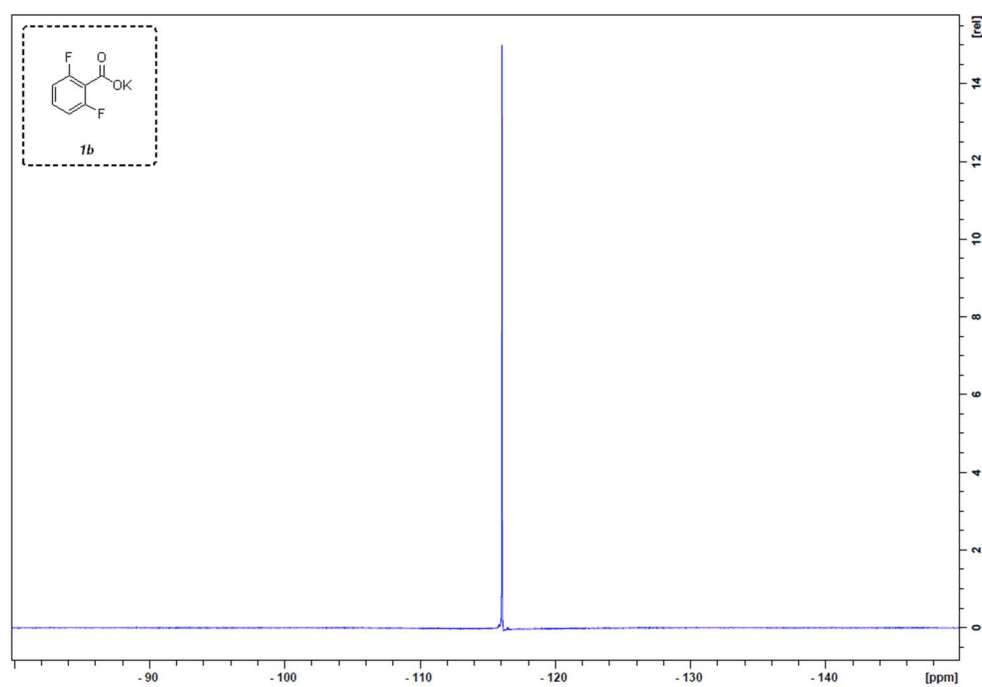
#### **1a** - Potassium Pentafluorobenzoate $^{13}\text{C}$ NMR Spectra, 100 MHz, $\text{D}_2\text{O}$



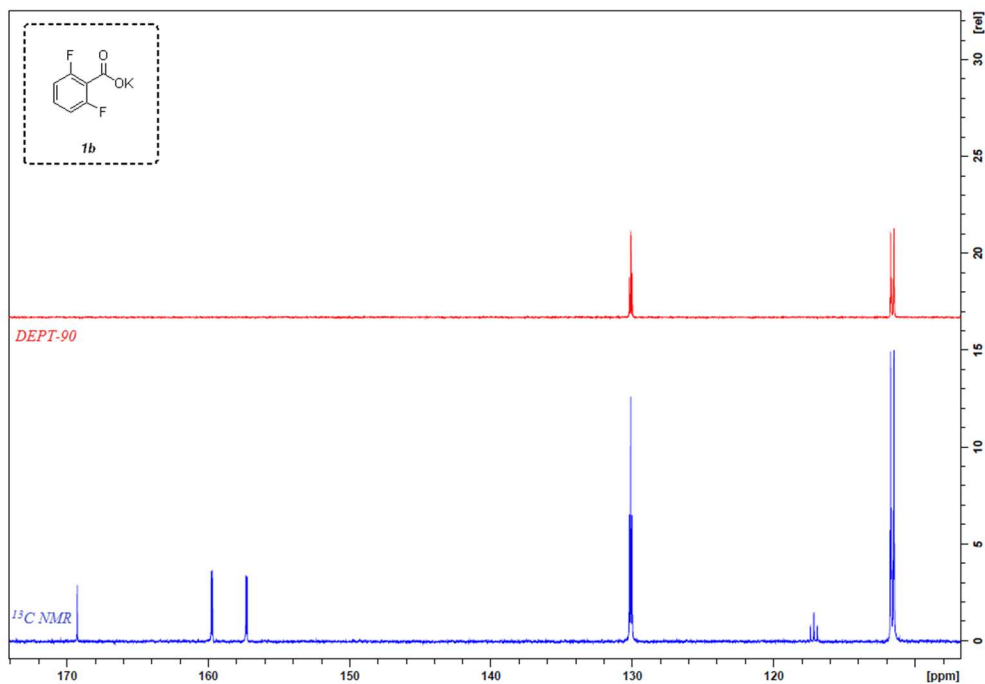
**1b** - Potassium 2,6-Difluorobenzoate  $^1\text{H}$  NMR Spectra, 400 MHz,  $\text{D}_2\text{O}$



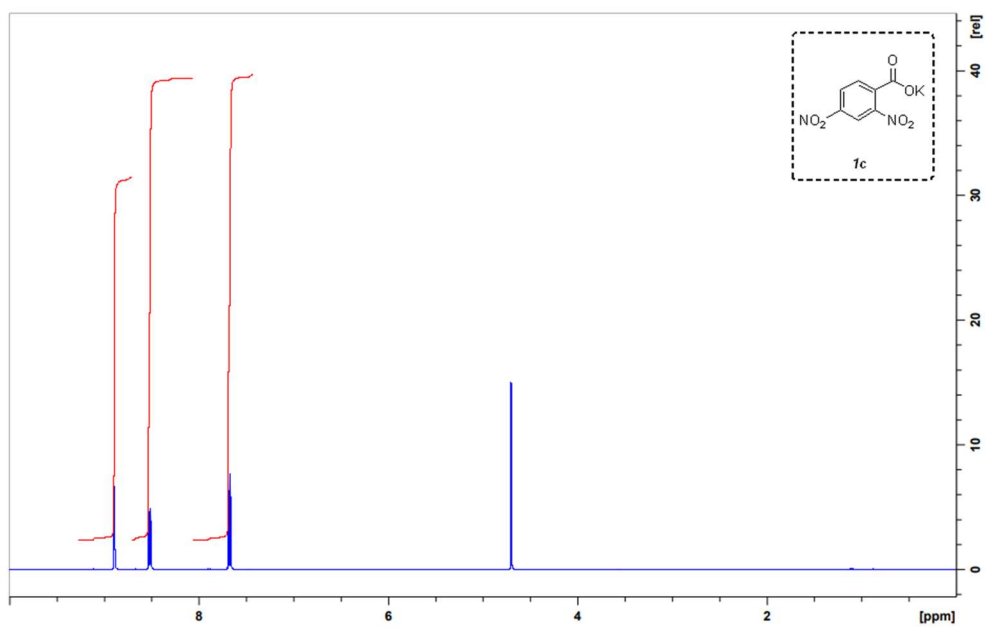
**1b** - Potassium 2,6-Difluorobenzoate  $^{19}\text{F}$  NMR Spectra, 376 MHz,  $\text{D}_2\text{O}$



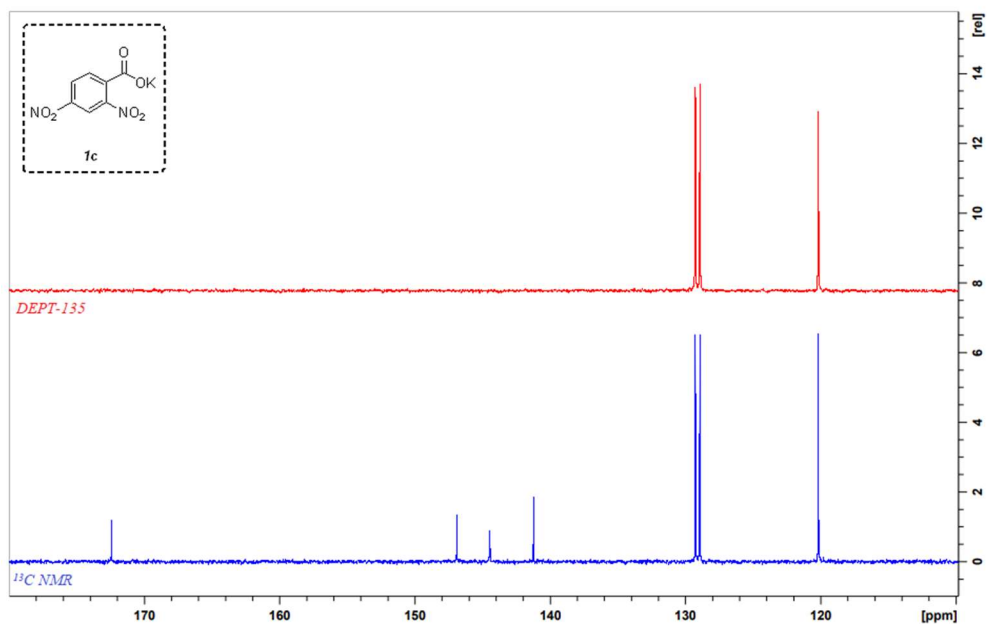
**1b** - Potassium 2,6-Difluorobenzoate  $^{13}\text{C}$  NMR Spectra, 100 MHz,  $\text{D}_2\text{O}$



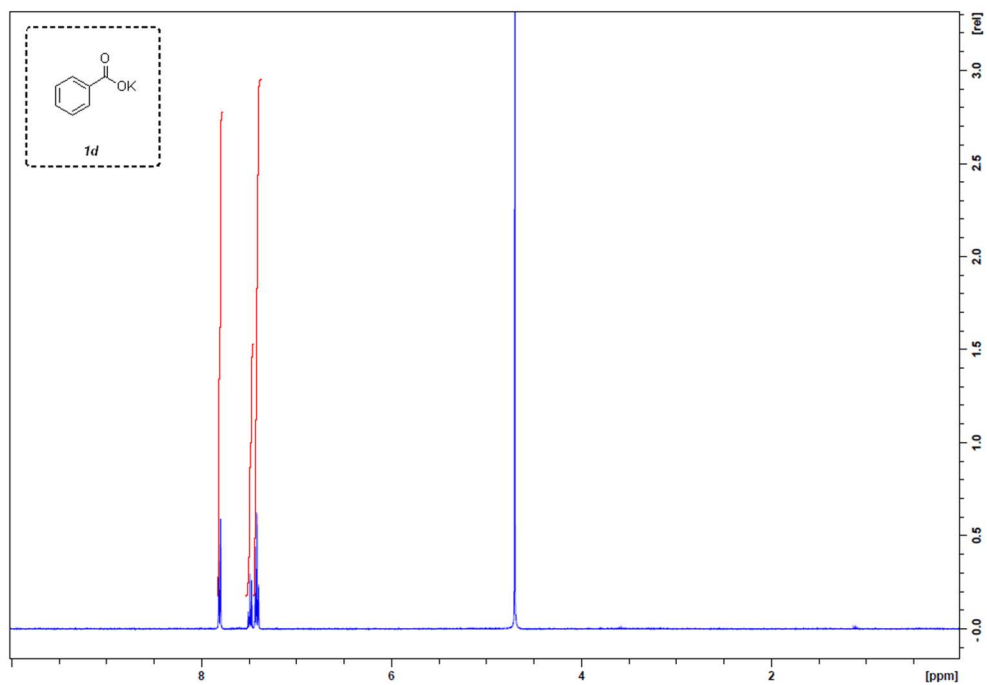
**1c** - Potassium 2,4-Dinitrobenzoate  $^1\text{H}$  NMR Spectra, 400 Hz,  $\text{D}_2\text{O}$



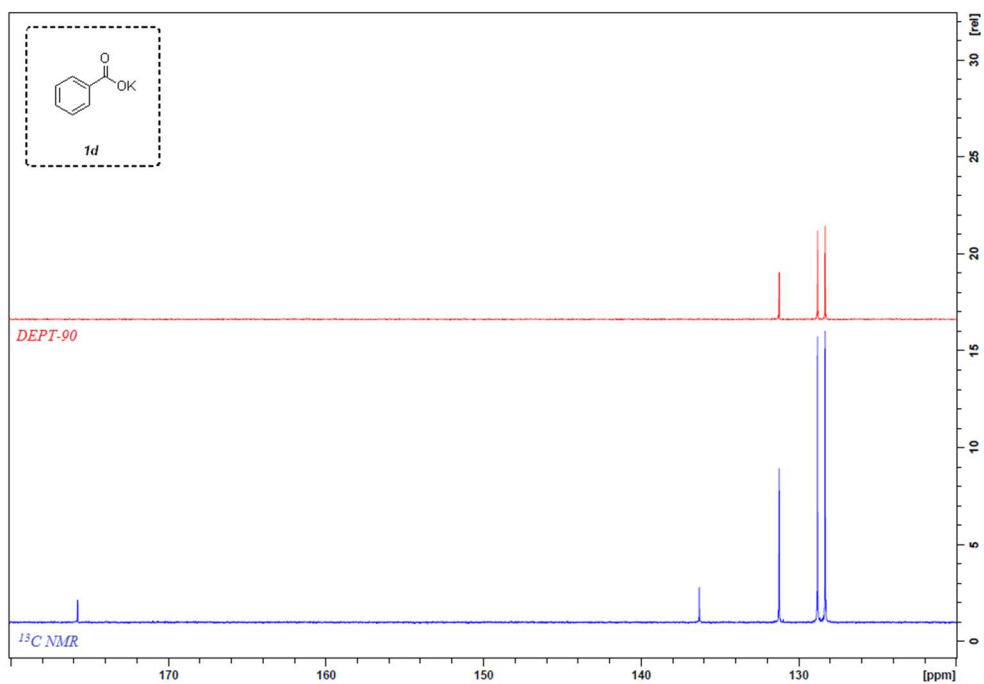
**1c** - Potassium 2,4-Dinitrobenzoate  $^{13}\text{C}$  NMR Spectra, 100 Hz,  $\text{D}_2\text{O}$



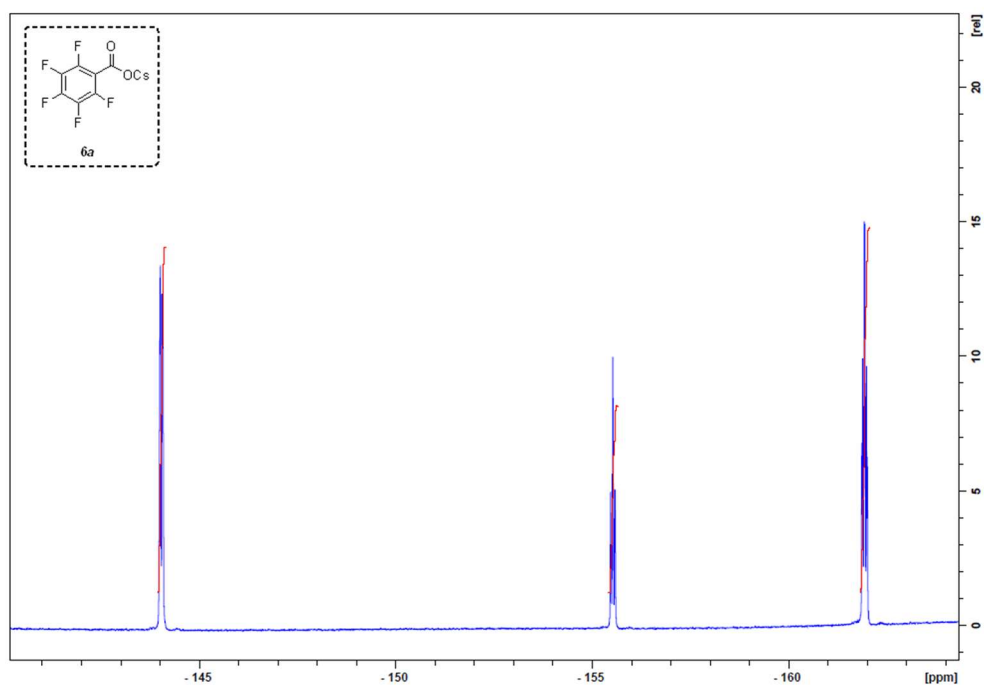
**1d** - Potassium Benzoate  $^1\text{H}$  NMR Spectra, 400 Hz,  $\text{D}_2\text{O}$



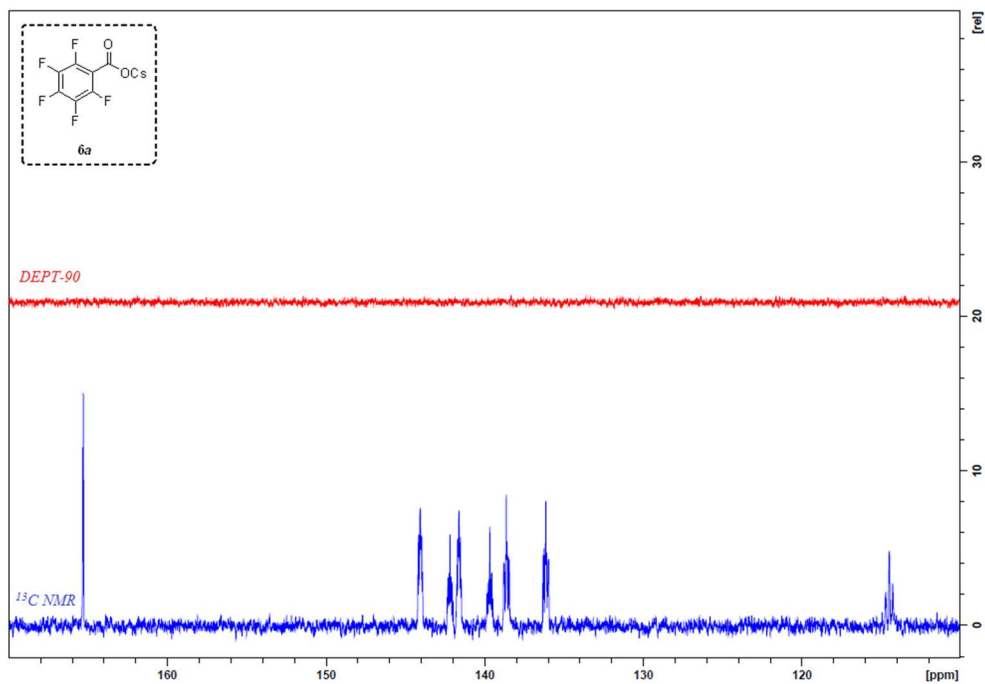
**1d** - Potassium Benzoate  $^{13}\text{C}$  NMR Spectra, 100 Hz,  $\text{D}_2\text{O}$



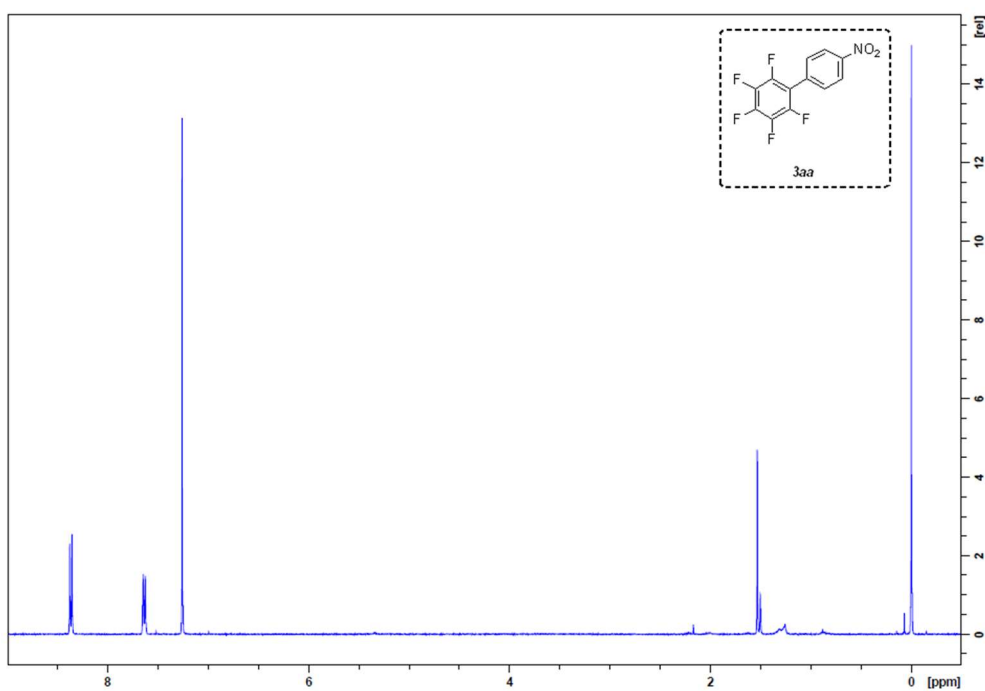
**6a** - Caesium Pentafluorobenzoate  $^{19}\text{F}$  NMR Spectra, 400 MHz,  $\text{D}_2\text{O}$



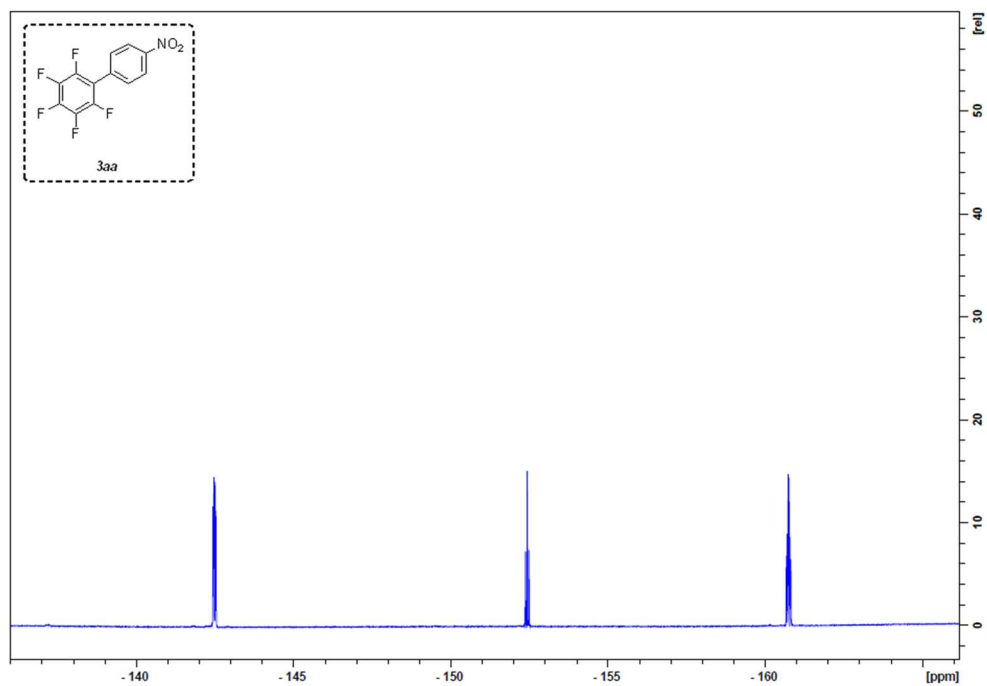
**6a** - Caesium Pentafluorobenzoate  $^{13}\text{C}$  NMR Spectra, 100 MHz,  $\text{D}_2\text{O}$



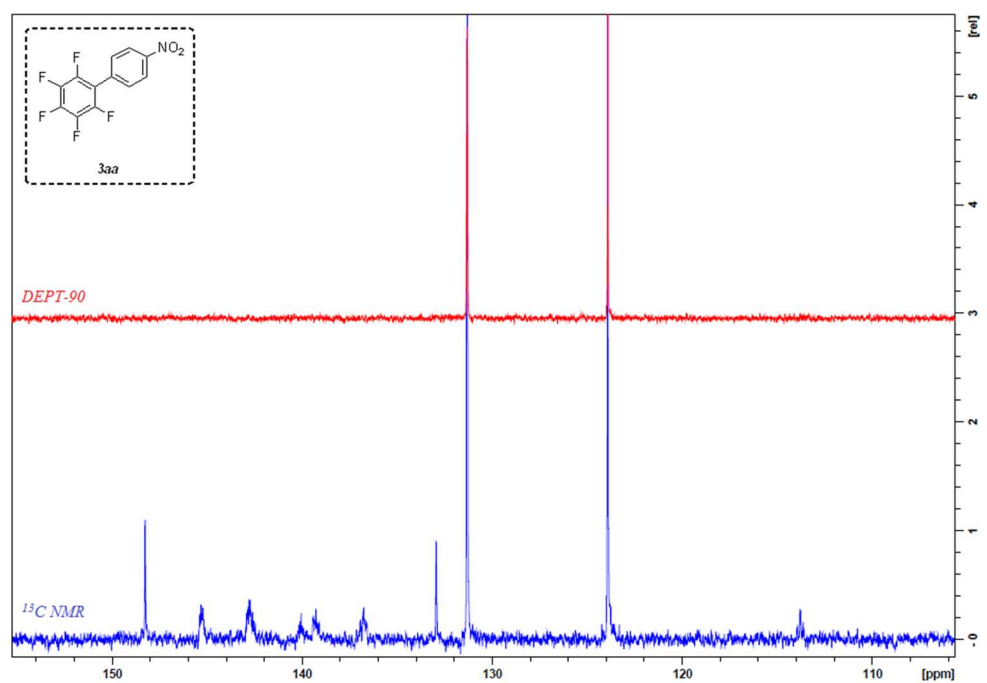
**3aa** - 4'-Nitro-2,3,4,5,6-pentafluorobiphenyl  $^1\text{H}$  NMR Spectra, 400 MHz,  $\text{CDCl}_3$



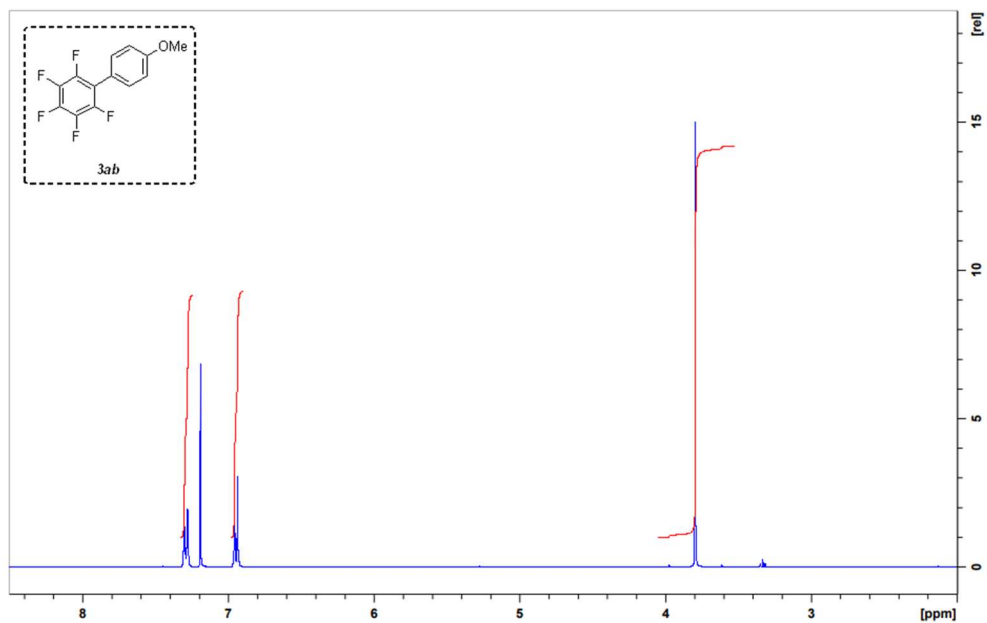
**3aa** - 4'-Nitro-2,3,4,5,6-pentafluorobiphenyl  $^{19}\text{F}$  NMR Spectra, 376 MHz,  $\text{CDCl}_3$



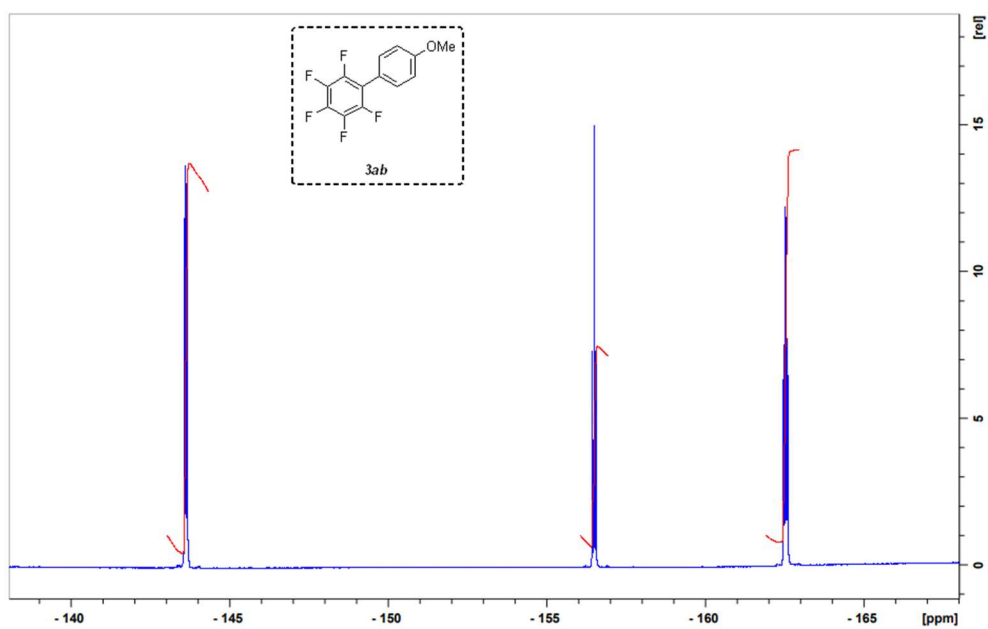
**3aa** - 4'-Nitro-2,3,4,5,6-pentafluorobiphenyl  $^{13}\text{C}$  NMR Spectra, 100 MHz,  $\text{CDCl}_3$



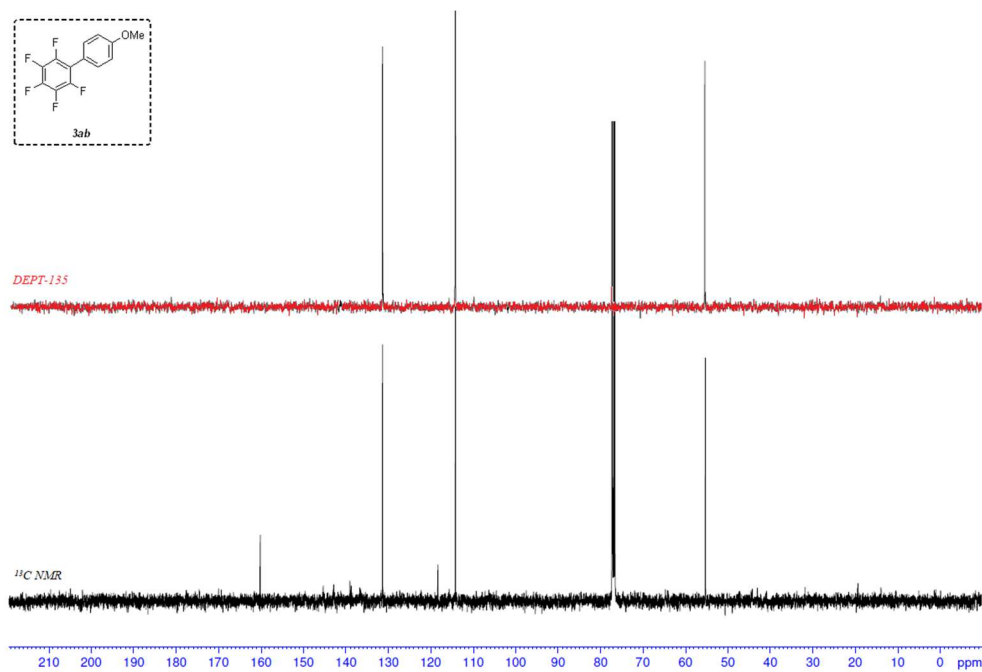
**3ab** - 2,3,4,5,6-pentafluoro-4'-methoxybiphenyl  $^1\text{H}$  NMR Spectra, 400 MHz,  $\text{CDCl}_3$



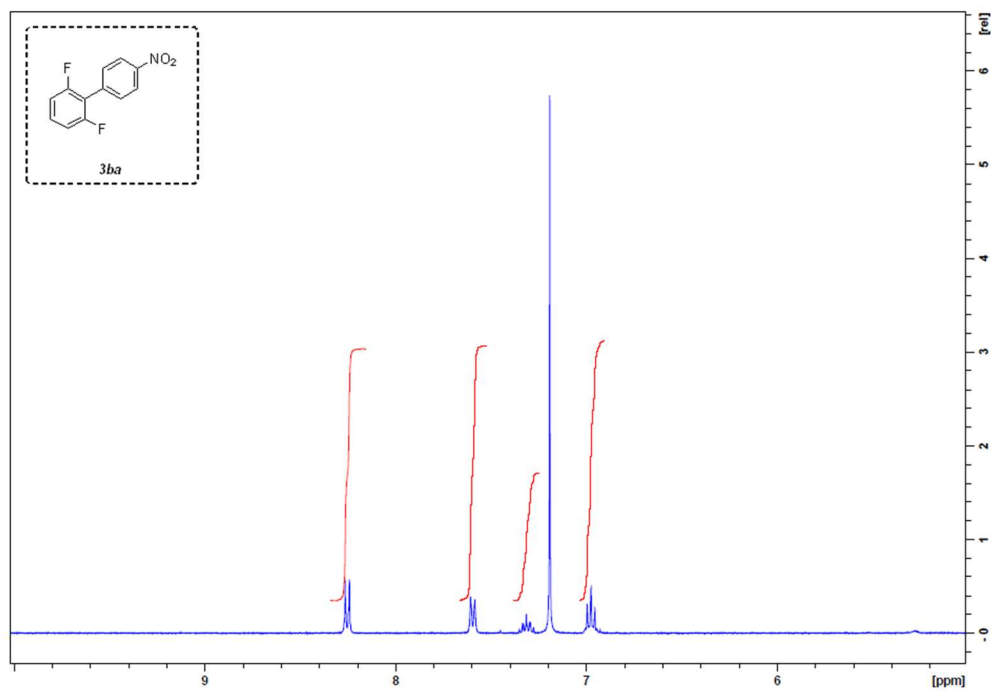
**3ab** - 2,3,4,5,6-pentafluoro-4'-methoxybiphenyl  $^{19}\text{F}$  NMR Spectra, 376 MHz,  $\text{CDCl}_3$



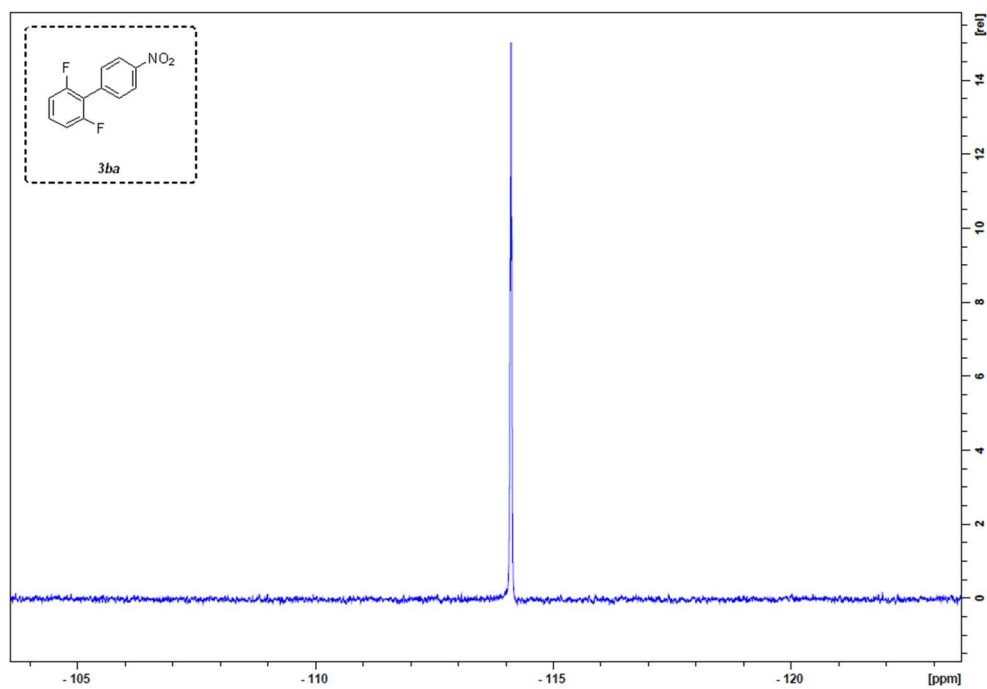
**3ab** - 2,3,4,5,6-pentafluoro-4'-methoxybiphenyl <sup>13</sup>C NMR Spectra, 100 MHz, CDCl<sub>3</sub>



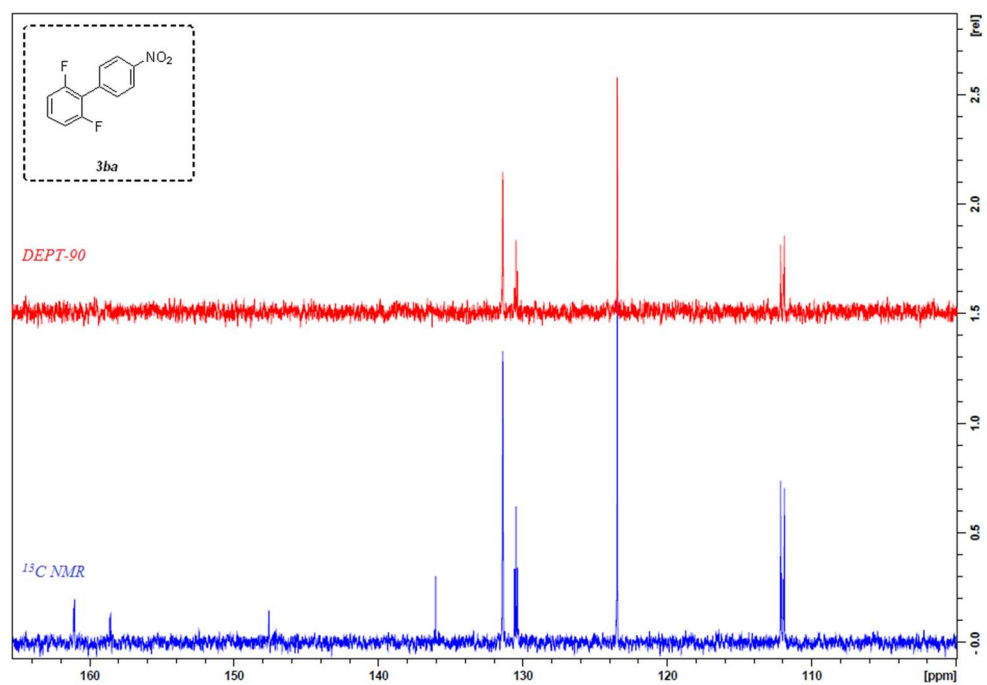
**3ba** - 2,6-difluoro-4'-nitrobiphenyl <sup>1</sup>H NMR Spectra, 400 MHz, CDCl<sub>3</sub>



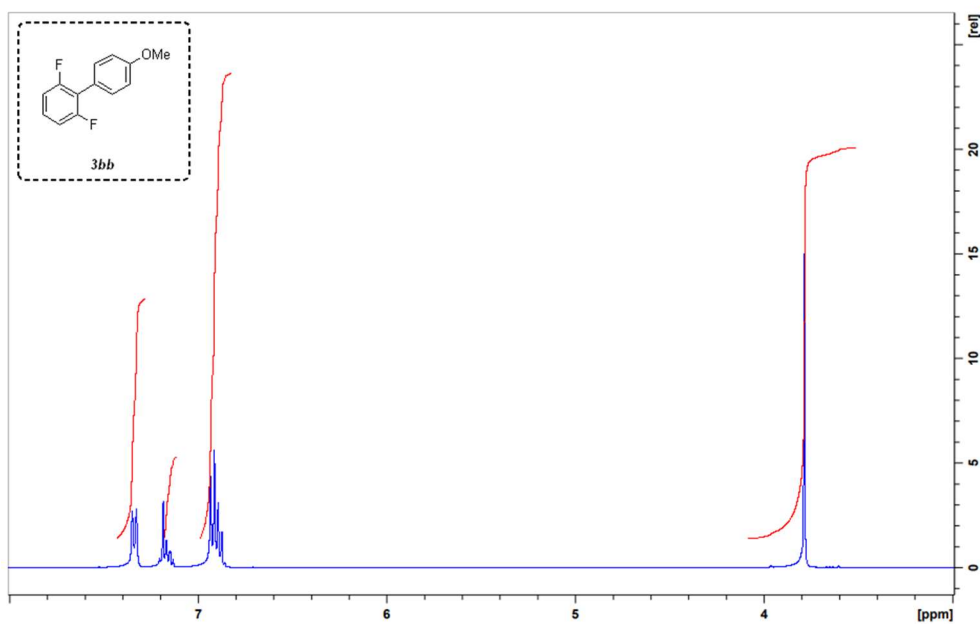
**3ba** - 2,6-difluoro-4'-nitrobiphenyl  $^{19}\text{F}$  NMR Spectra, 376 MHz,  $\text{CDCl}_3$



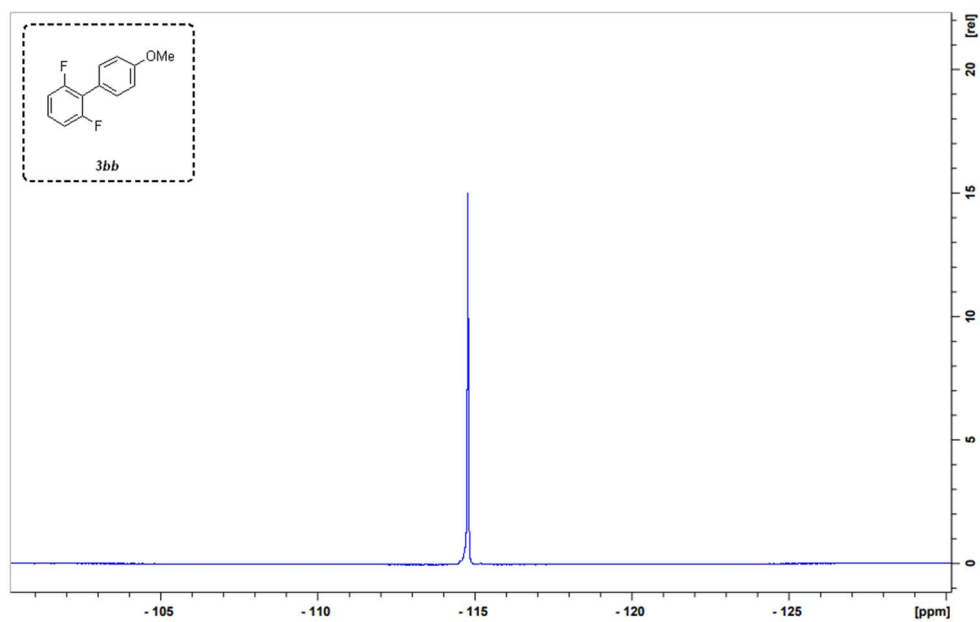
**3ba** - 2,6-difluoro-4'-nitrobiphenyl  $^{13}\text{C}$  NMR Spectra, 100 MHz,  $\text{CDCl}_3$



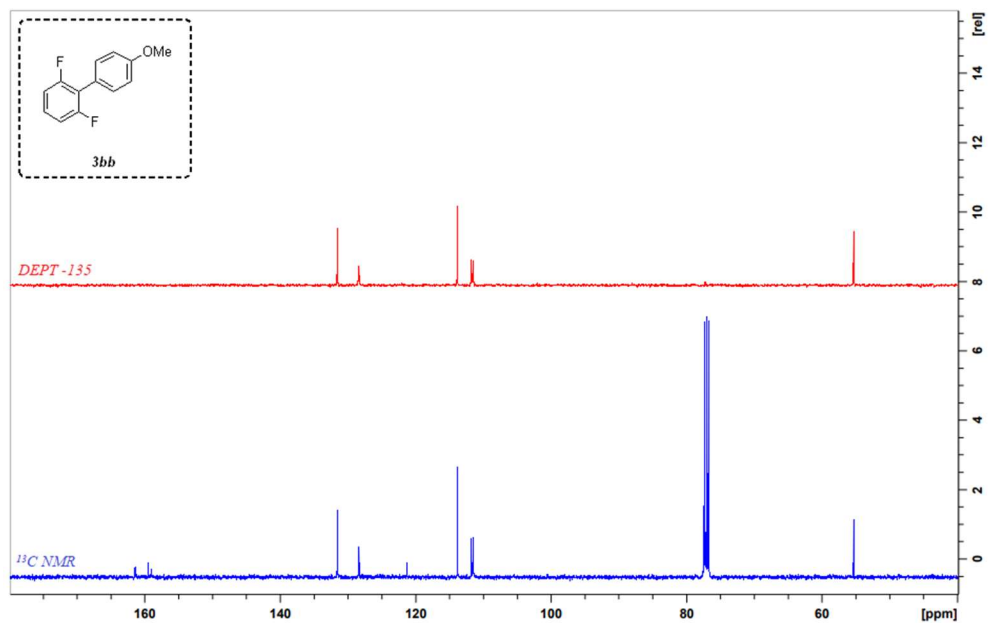
**3bb** - 2,6-difluoro-4'-methoxybiphenyl  $^1\text{H}$  NMR Spectra, 400 MHz,  $\text{CDCl}_3$



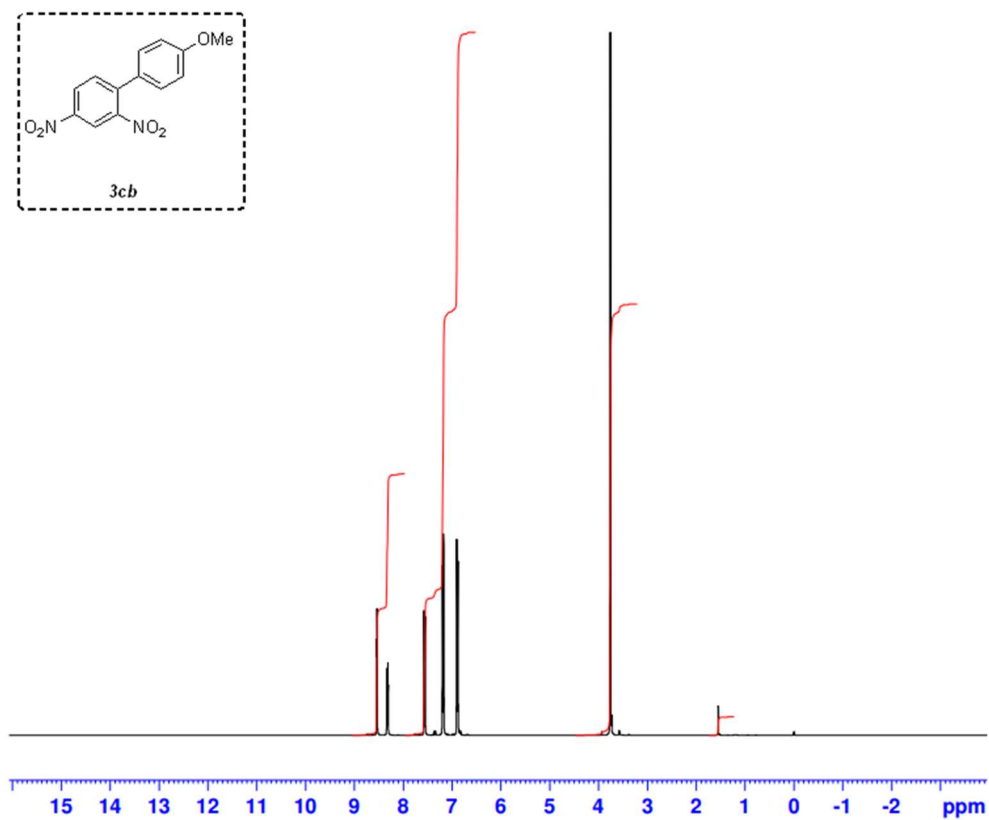
**3bb** - 2,6-difluoro-4'-methoxybiphenyl  $^{19}\text{F}$  NMR Spectra, 376 MHz,  $\text{CDCl}_3$



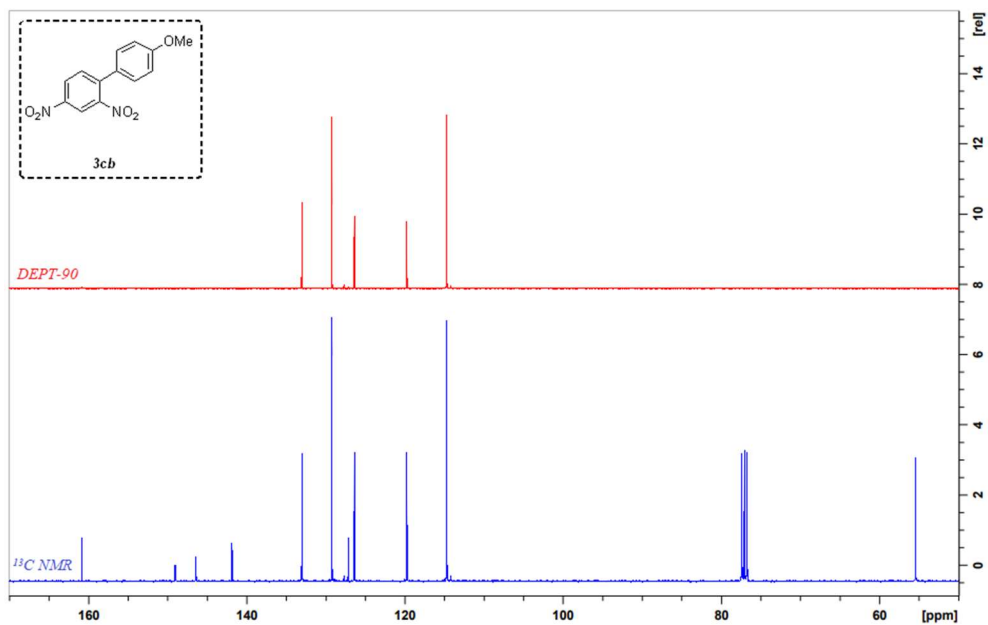
**3bb** - 2,6-difluoro-4'-methoxybiphenyl <sup>13</sup>C NMR Spectra, 100 MHz, CDCl<sub>3</sub>



**3cb** - 2,4-dinitro-4'-methoxybiphenyl <sup>1</sup>H NMR Spectra, 400 MHz, CDCl<sub>3</sub>

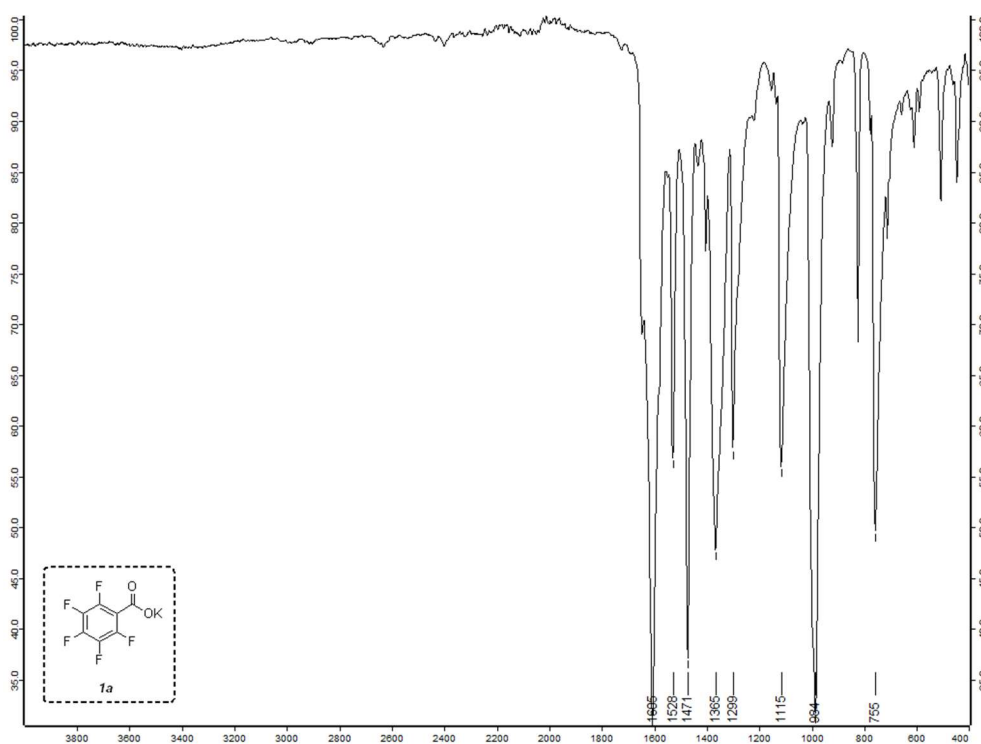


**3cb** - 2,4-dinitro-4'-methoxybiphenyl  $^{13}\text{C}$  NMR Spectra, 100 MHz,  $\text{CDCl}_3$

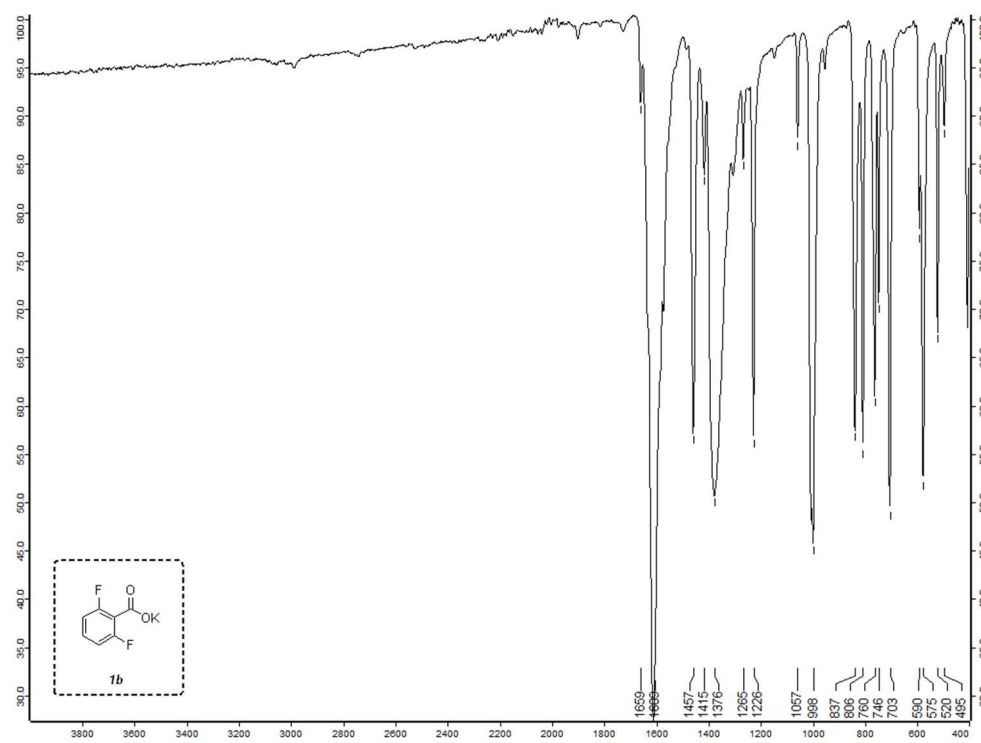


## 6.4. Fourier-transform Infra-red Spectroscopy of Purified Compounds

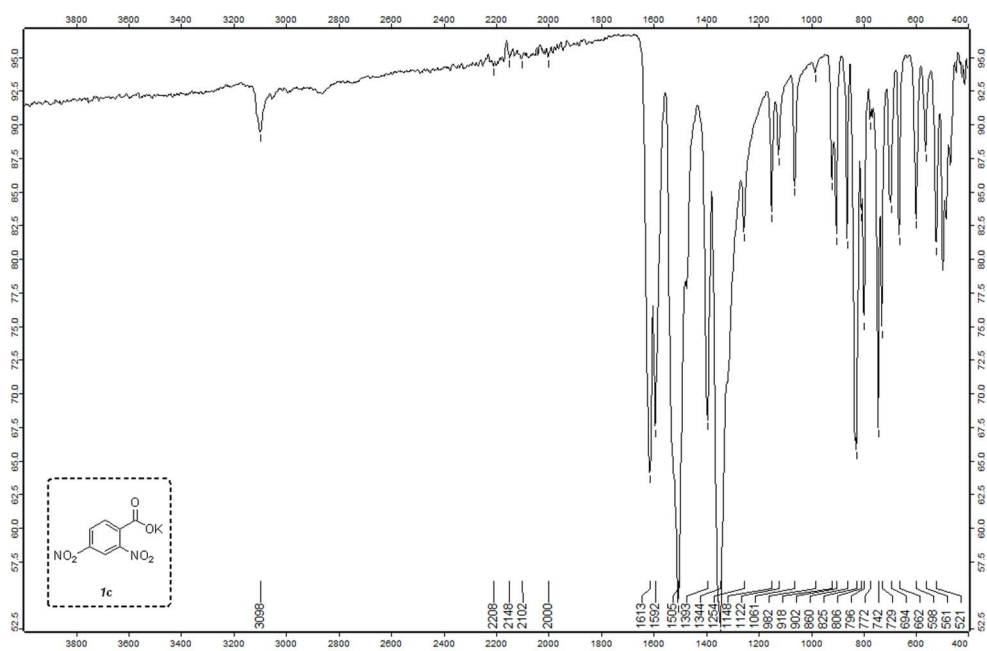
### 1a - Potassium Pentafluorobenzoate FTIR Spectra



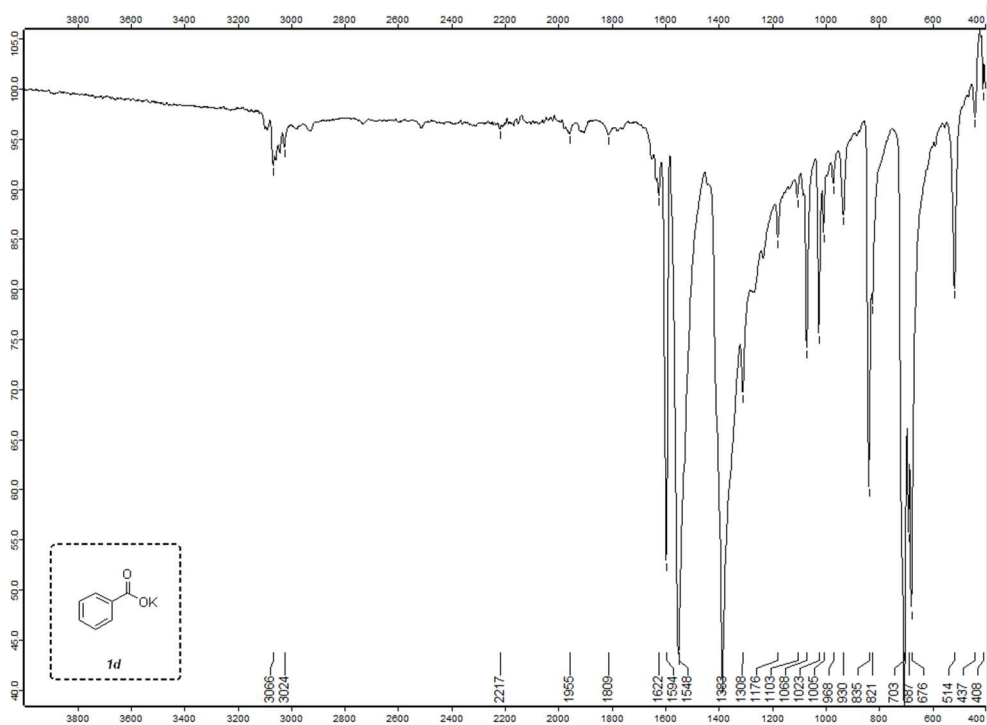
### 1b - Potassium 2,6-Difluorobenzoate FTIR Spectra



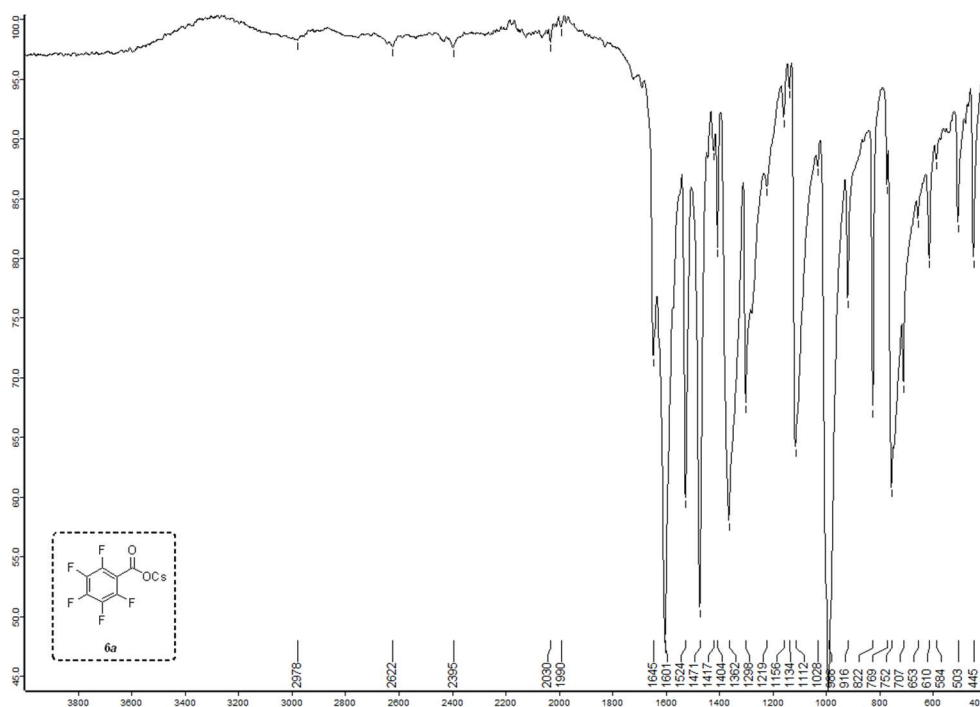
### 1c - Potassium 2,4-Dinitrobenzoate FTIR Spectra



### 1d - Potassium Benzoate FTIR Spectra

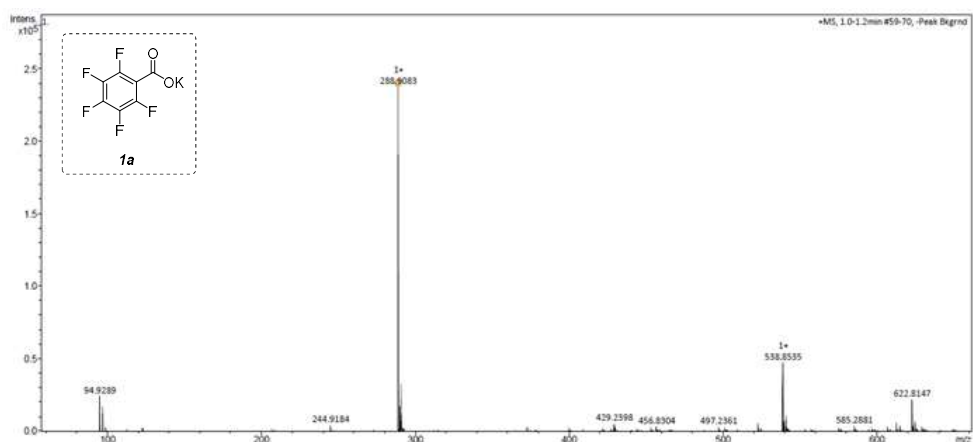


### 6a - Caesium Pentafluorobenzoate FTIR Spectra

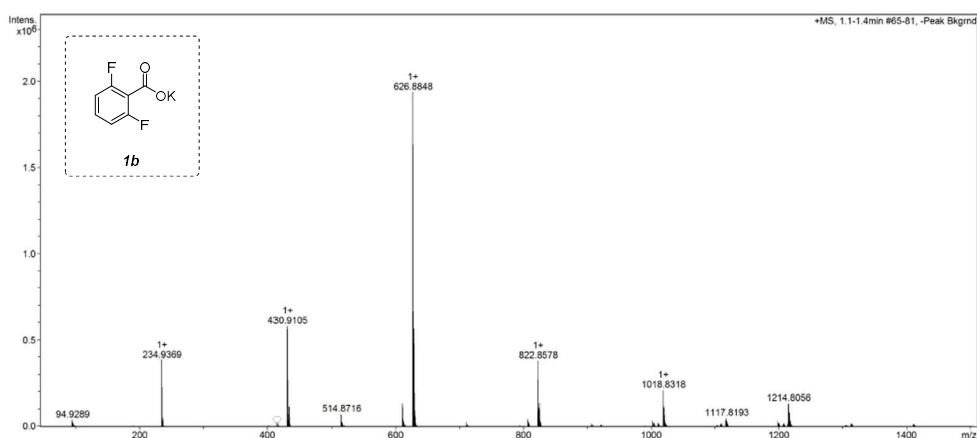


## 6.5. High Resolution Mass Spectrometry of Purified Compounds

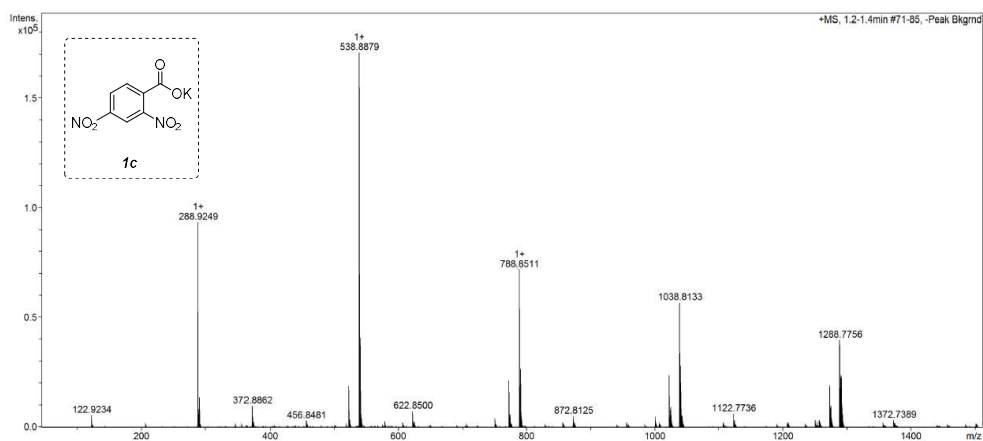
### 1a - Potassium Pentafluorobenzoate HRMS Spectra



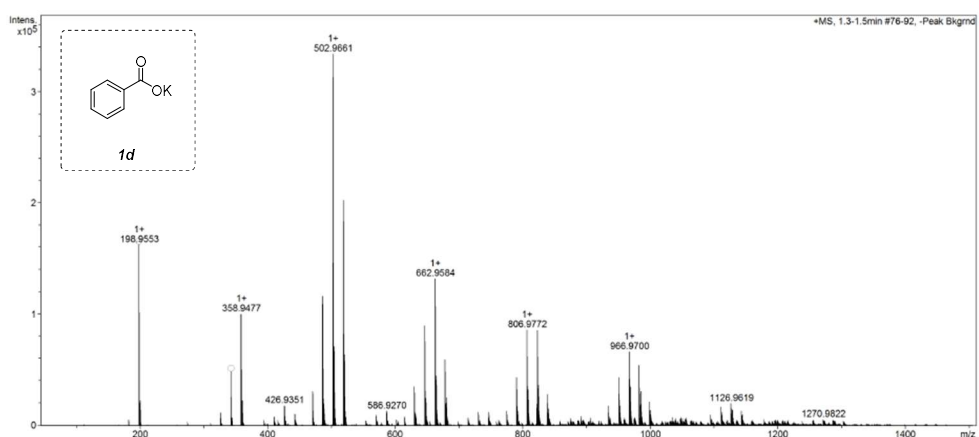
### 1b - Potassium 2,6-Difluorobenzoate HRMS Spectra



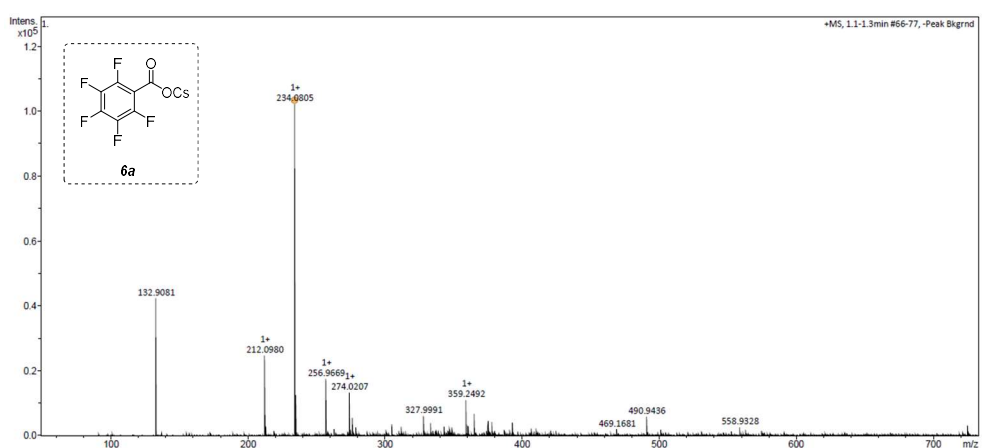
### 1c - Potassium 2,4-dinitrobenzoate HRMS Spectra



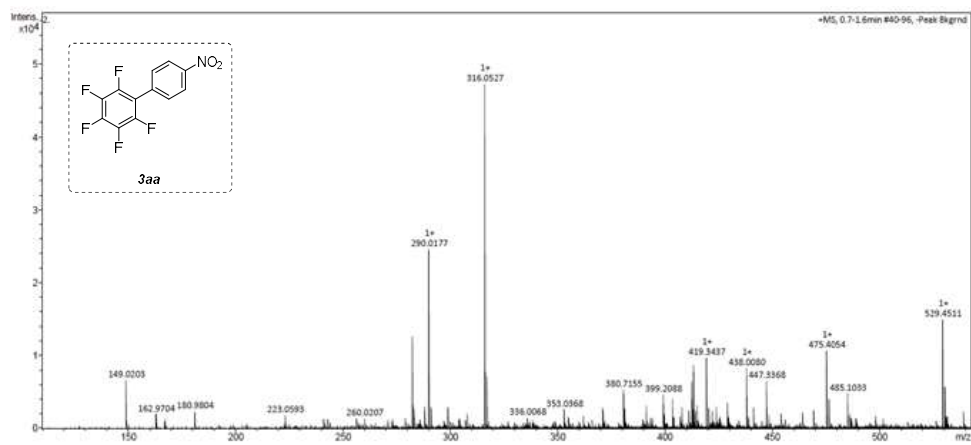
## 1d - Potassium Benzoate HRMS Spectra



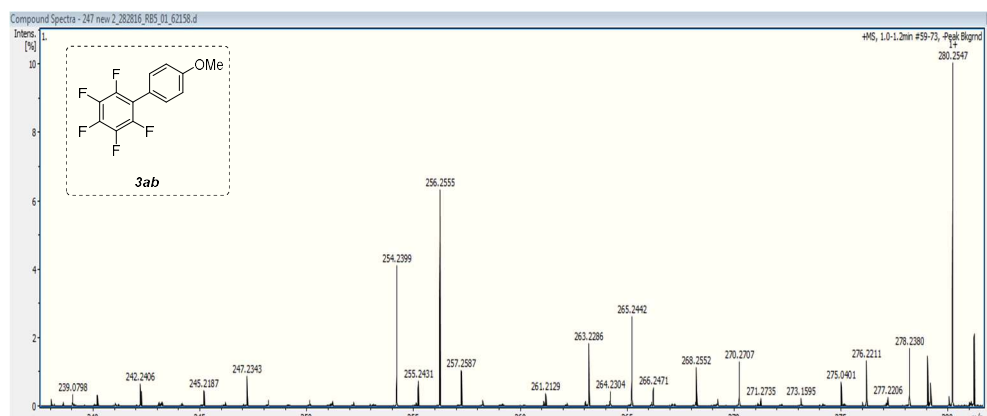
## 6a - Caesium Pentafluorobenzoate HRMS Spectra



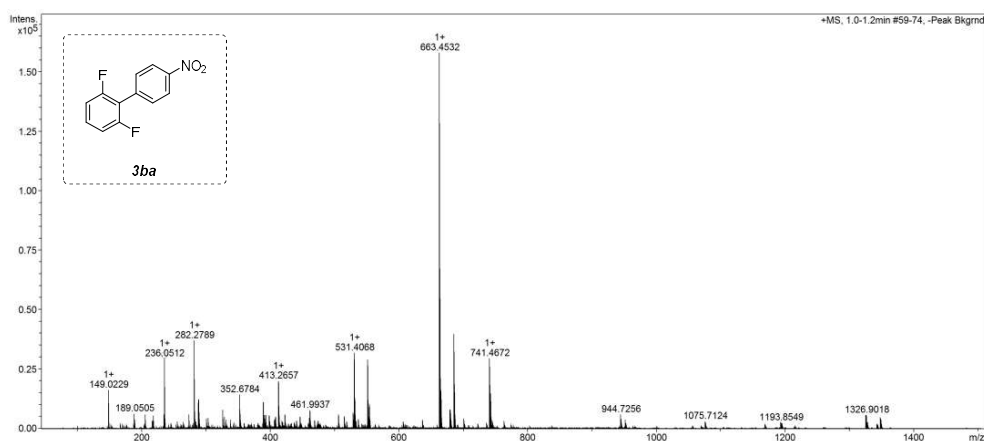
## 3aa - 4'-Nitro-2,3,4,5,6-pentafluorobiphenyl HRMS Spectra



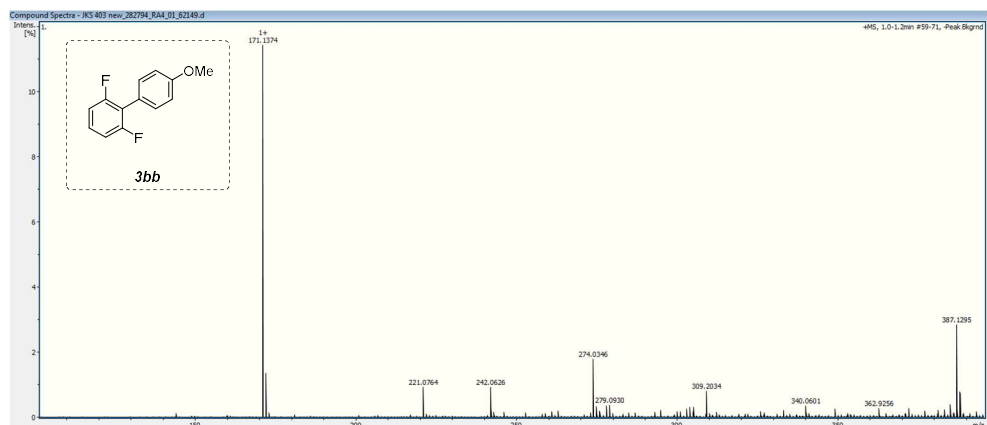
### 3ab - 2,3,4,5,6-pentafluoro-4'-methoxybiphenyl HRMS Spectra



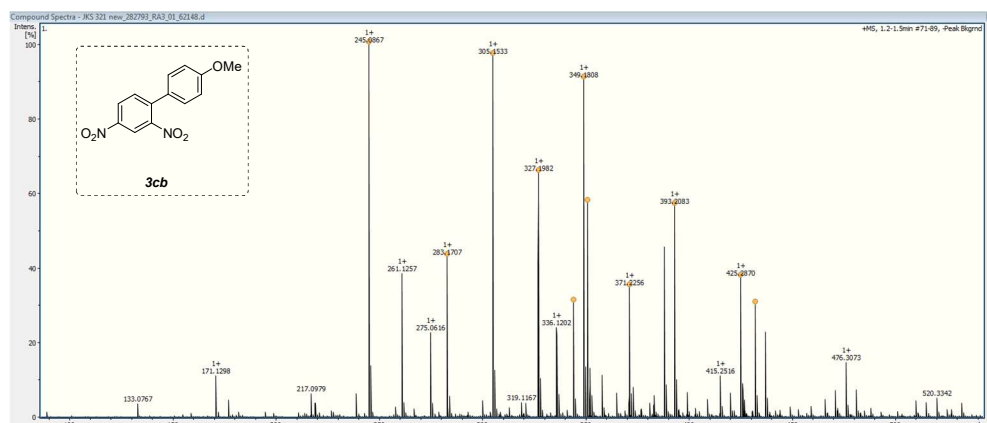
### 3ba - 2,6-difluoro-4'-nitrobiphenyl HRMS Spectra



### 3bb - 2,6-difluoro-4'-methoxybiphenyl <sup>1</sup>H NMR Spectra

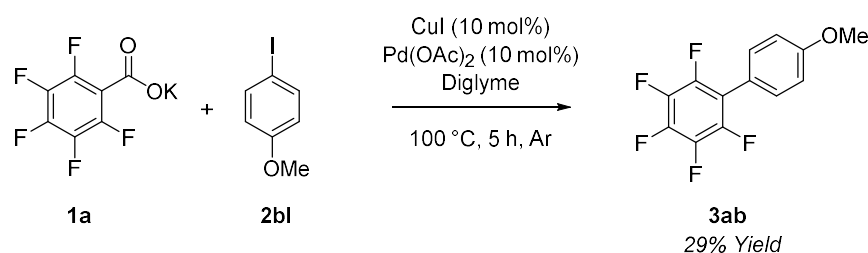


### 3cb - 2,4-dinitro-4'-methoxybiphenyl HRMS Spectra



## 6.6. High Pressure Liquid Chromatography Yield Derivation Methodology

What follows is an in depth look at how HPLC was utilised throughout this thesis to quantify amounts of substance in reaction mixtures, with an accompanying experimental write up as an example.



*Scheme 6.1 An example decarboxylative cross-coupling reaction.*

A Schlenk tube was charged with potassium pentafluorobenzoate (188 mg, 0.75 mmol, **1a**), 4-iodoanisole (117 mg, 0.5 mmol, **2bI**), copper(I) iodide (9.5 mg, 0.05 mmol), palladium(II) acetate (11.2 mg, 0.05 mmol) and biphenyl (7.7mg, 0.05mmol) as an internal standard. The tube was then evacuated and backfilled with dry Argon three times, before anhydrous diglyme (2 mL) was added. The resulting mixture was then stirred at room temperature for 10 minutes to aid in solvation, before being heated to  $100\text{ }^\circ\text{C}$  for 5 hours.

At this point 0.1 mL of reaction mixture was drawn off *via* an argon-flushed syringe and diluted to 1 mL in methanol. From this 1 mL solution a further 0.1 mL was drawn off and diluted to 1 mL in methanol, for a total dilution factor of 100. This ensures the analytes in the sample are of a concentration that falls within the ranges of their respective calibration curves. This 100-times diluted sample was then filtered over celite to remove any solid particulate that would interfere with the HPLC autosampler before finally being analysed using an Agilent/Hewlett Packard 1100 Series HPLC system. The wavelength of light used for analysis was set to 254 nm. See Figure 6.2 for the resulting chromatogram.

All HPLC analysis was performed using the following method on a YMC-Pack ODS-AM 303 C18 reverse phase column, particle size  $5\text{ }\mu\text{m}$ , pore size  $120\text{ \AA}$ ,

internal dimensions 250 × 4.6 mm. Water and acetonitrile, spiked with 0.1 % trifluoroacetic acid (TFA), was used as mobile phase. The ratio of water to acetonitrile was gradated with time, See Figure 6.1 for details. Column temperature was held at 30 °C. Flowrate was 1 mL/min.

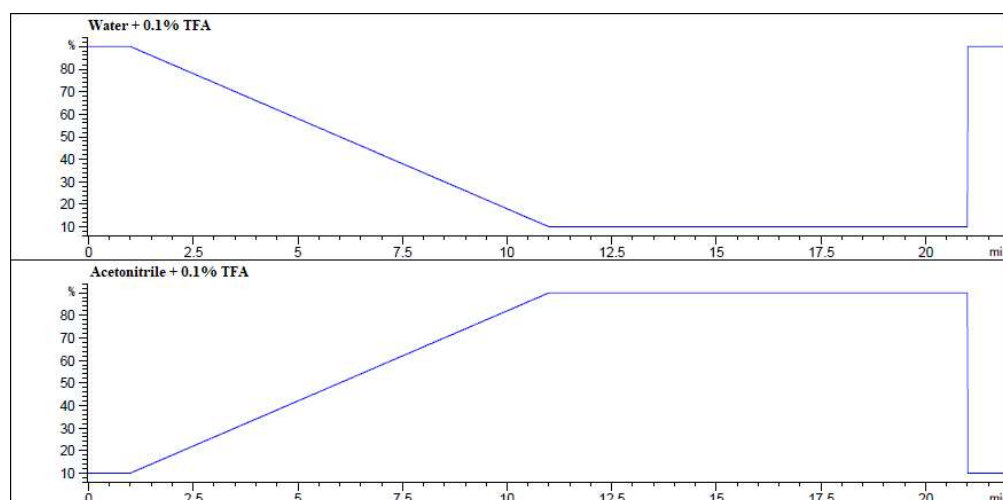


Figure 6.1 Plots to show how the ratios of the chosen mobile phases varies with time.

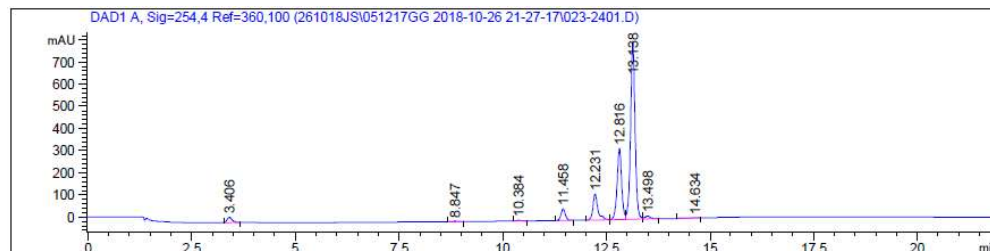


Figure 6.2 The resulting chromatogram from the analysis of the reaction depicted in Scheme 6.1.

Table 6.1 Data gathered from the integration of the chromatogram displayed in Figure 6.2

Peak #	Compound	Retention Time (min)	Peak Width (min)	Peak Height (mAU)	Peak Area (mAU*s)
1	<b>2bI</b>	12.231	0.1217	116.51424	976.17987
2	<b>3ab</b>	12.816	0.1140	321.05997	2422.31982
3	Biphenyl	13.138	0.1116	800.39911	6010.69434

Analysing pure reference samples utilising the same method that was used for the reaction sample, it is known that the peaks observed at 12.231, 12.816 and 13.138 minutes correspond to **2bI**, **3ab** and biphenyl respectively. Biphenyl is unreactive under the reaction and analytical conditions described and therefore the concentration of biphenyl in the sample is known. By looking at the ratios of peaks of unknown concentration to the known biphenyl peak, errors in sample volume are eliminated. However, as the absorption of light (and therefore the size of the resulting peak in the chromatogram) for a compound is dependent on its specific absorption coefficient, these ratios cannot be directly compared. Instead these ratios are compared to calibration curves (see 6.8 Calibration Data for Benzoate/Aryl Halide Coupling Reactions) using Equation 6.1 to yield concentration values which can be directly compared (See Table 6.3). Knowing that the theoretical maximum concentration of both **2bI** and **3ab** in the sample, given the loading of starting material **2bI** and the dilutions performed, is 0.0025 M, a percentile value for amount of substance can then be derived.

*Table 6.2 Information extracted from relevant calibration curves.*

Analyte	Intercept (M)	Gradient (M*mAU <sup>-1</sup> *s <sup>-1</sup> )
<b>2bI</b>	0.00174	223.98918
<b>3ab</b>	0.10055	3303.52012

*Table 6.3 Processing the chromatogram data to determine the concentration of **2bI** and **3ab** in the sample.*

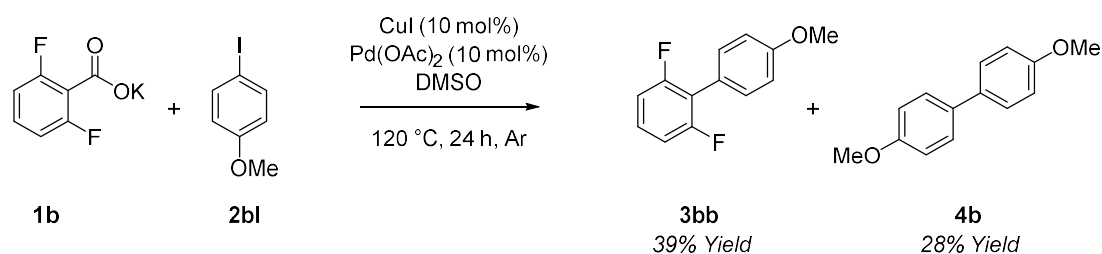
Analyte	Peak Area (mAu*s)	Analyte/Internal Standard (mAU*s)	Concentration (M)	Amount of Substance (%)
<b>2bI</b>	976.17987	0.403	0.0018	71
<b>3ab</b>	2422.31982	2.4814	0.000721	29

$$x = (y - c)/m$$

*Equation 6.1 Equation for deriving concentration from chromatogram peak areas, where  $x$  = concentration (M),  $y$  = analyte peak area/internal standard peak area (mAU\*s),  $c$  = intercept from calibration curve (M),  $m$  = gradient from calibration curve (M\*mAU<sup>-1</sup>\*s<sup>-1</sup>).*

## 6.7. Nuclear Magnetic Resonance Yield Derivation Methodology

What follows is an in depth look at how NMR was utilised throughout this thesis to quantify amounts of substance in reaction mixtures, with an accompanying experimental write up as an example.



*Scheme 6.2 An example decarboxylative cross-coupling reaction*

A Schlenk tube was charged with potassium 2,6-difluorobenzoate (147 mg, 0.75 mmol, **1b**), 4-iodoanisole (117 mg, 0.5 mmol, **2bI**), copper(I) iodide (9.5 mg, 0.05 mmol) and palladium(II) acetate (11.2 mg, 0.05 mmol). The tube was then evacuated and backfilled with dry Argon three times, before anhydrous dimethyl sulfoxide (2 mL) was added. The resulting mixture was then stirred at room temperature for 10 minutes to aid in solvation, before being heated to 120 °C for 24 hours.

The reaction mixture was then allowed to cool before being diluted in ethyl acetate (20 mL) and filtered over celite to remove solid depositions. The filtrate was then transferred to a separating funnel and washed with deionised water (3 × 50 mL) and brine (50 mL). The organic layer was then dried over magnesium sulfate and the solvent was removed *via* rotary evaporation to yield a brown solid. This solid was then redissolved in deuterated chloroform (3 mL). 0.5 mL of the resulting solution was then drawn off and analysed *via* <sup>1</sup>H NMR at 400 MHz on a Bruker AVANCE III HD-400 spectrometer.

Using pure reference compounds and literature values<sup>33,181</sup> the resulting spectrum was then fully assigned (see Figure 6.3 and Figure 6.4). With all peaks accounted for, isolated peaks for each compound under analysis were integrated. The area of a <sup>1</sup>H NMR peak is directly proportional to the number of protons responsible for the

signal, which is also proportional to the amount of the analyte in the sample. The areas of these peaks were therefore divided by the number of protons responsible for the signal, and these values can be directly compared to yield percentile values for amount of substance (see Table 6.4 and Equation 6.2)

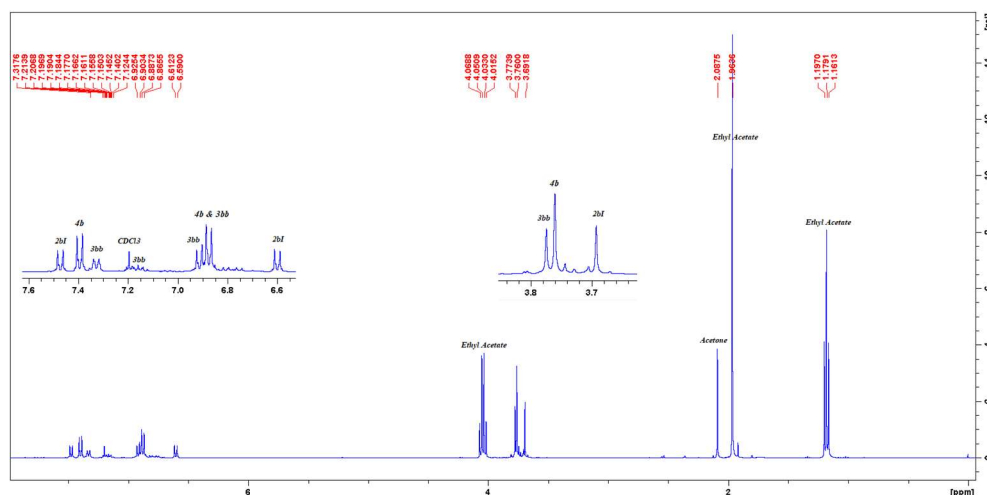


Figure 6.3 The resulting  $^1\text{H}$  NMR spectrum from the analysis of the reaction depicted in Scheme 6.2

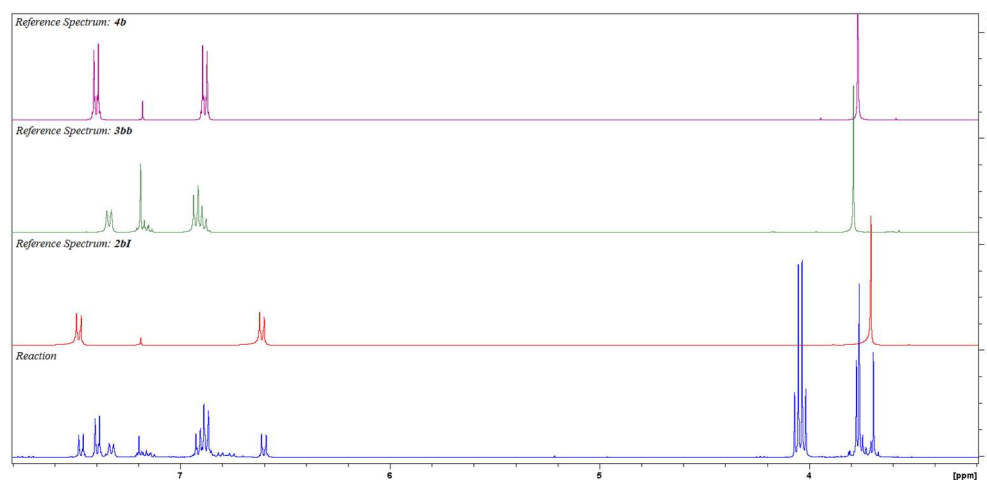


Figure 6.4 Stacked spectrum view comparing the spectrum from Figure 6.3 to pure reference compounds.

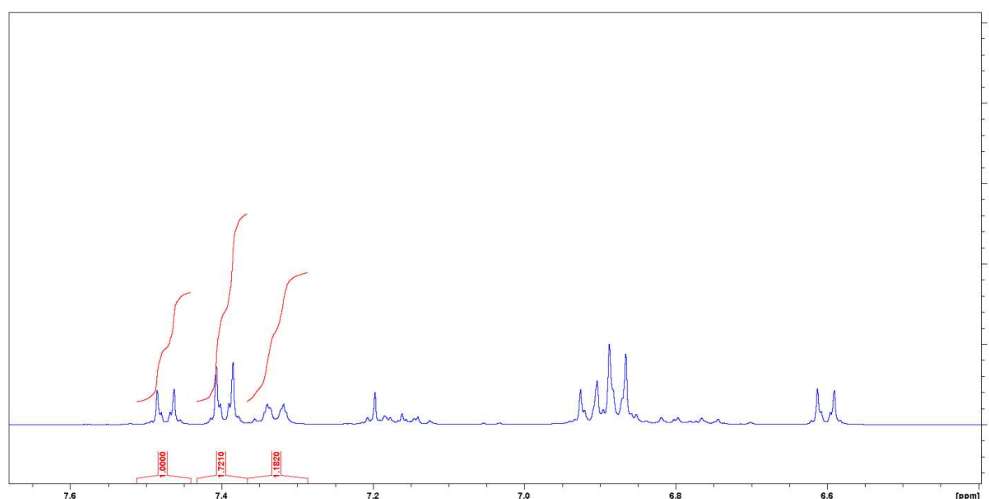


Figure 6.5 Integrating the  $^1\text{H}$  NMR spectrum from Figure 6.3

Table 6.4 Processing the integration data from Figure 6.5 to quantify the amount of analytes **2bI**, **3bb** and **5b** in the sample.

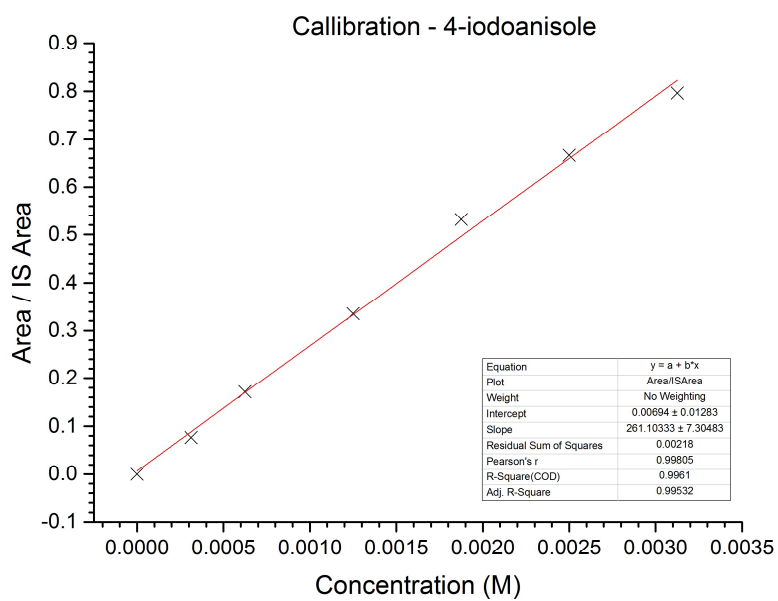
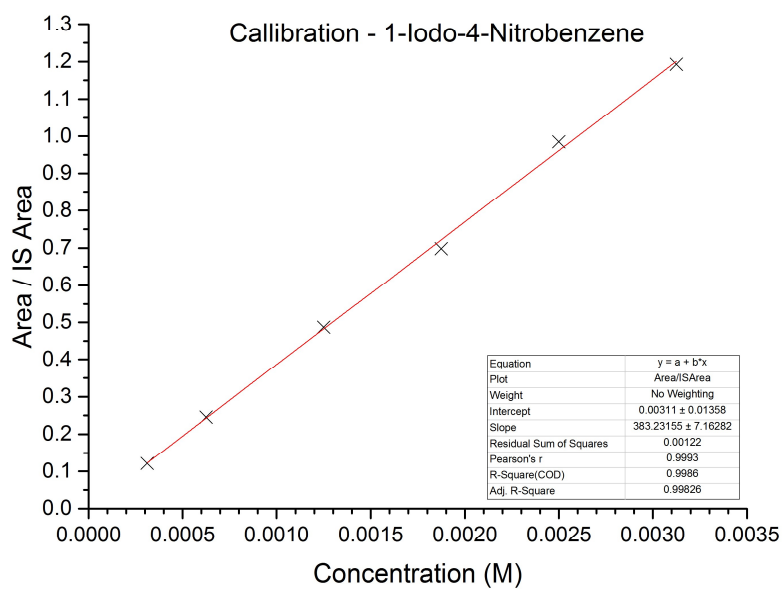
Analyte	Peak (ppm)	Integration	Number of Protons	Integration / # Protons	Amount of Substance (%)
<b>2bI</b>	7.47	1.0000	2	0.5000	33
<b>4b</b>	7.40	1.7210	4	0.4302	28
<b>3bb</b>	7.33	1.1820	2	0.5910	39

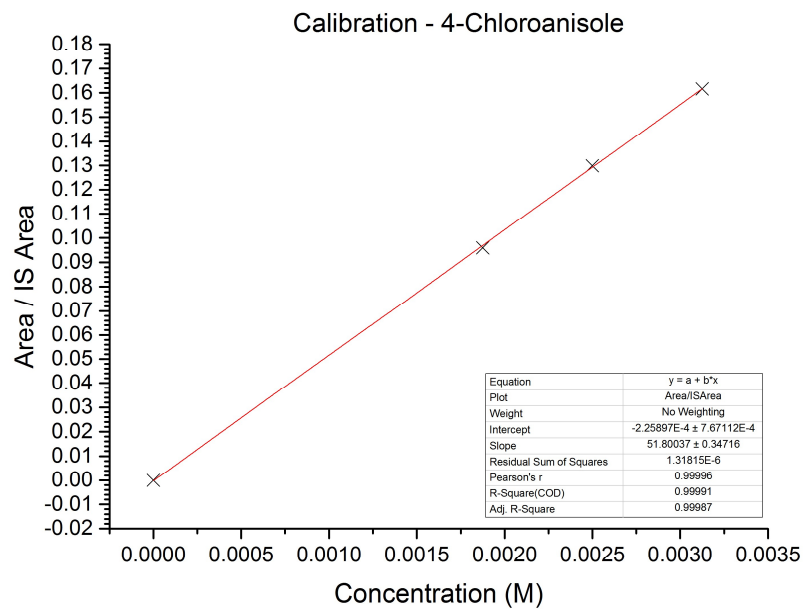
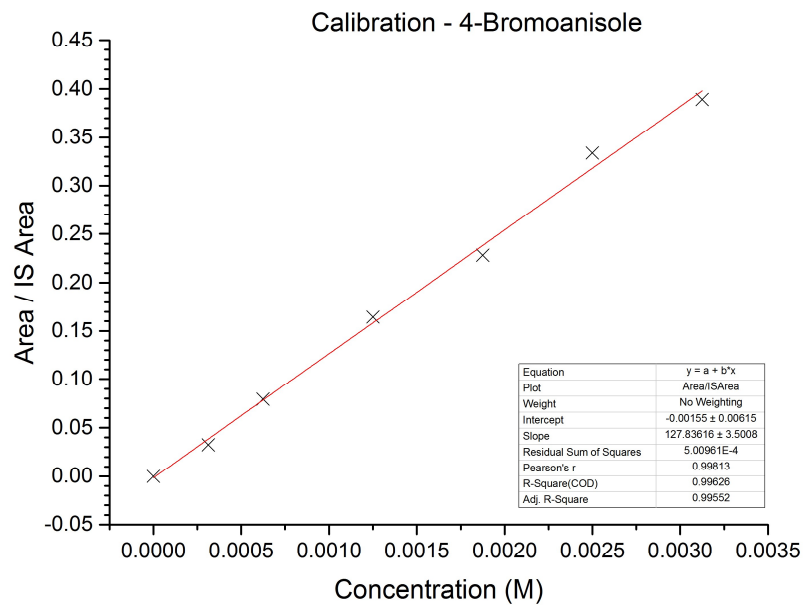
$$Xa = (Xi/Ti) * 100$$

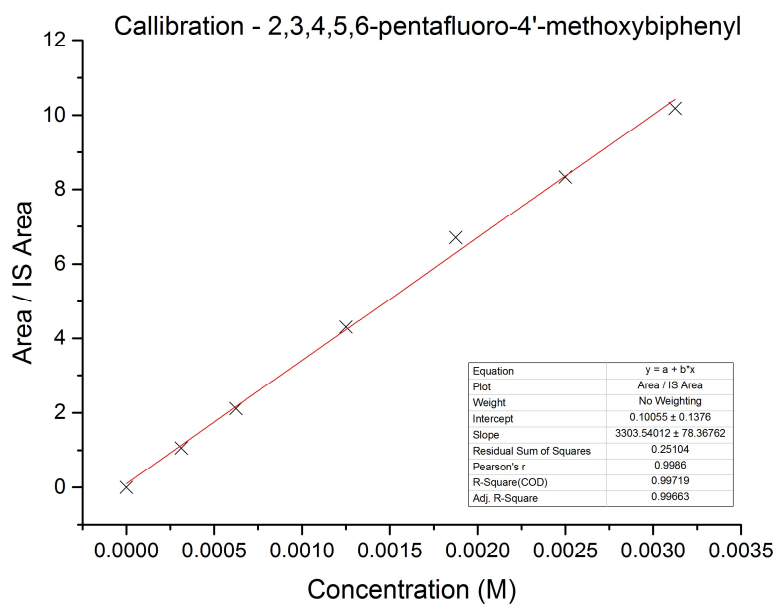
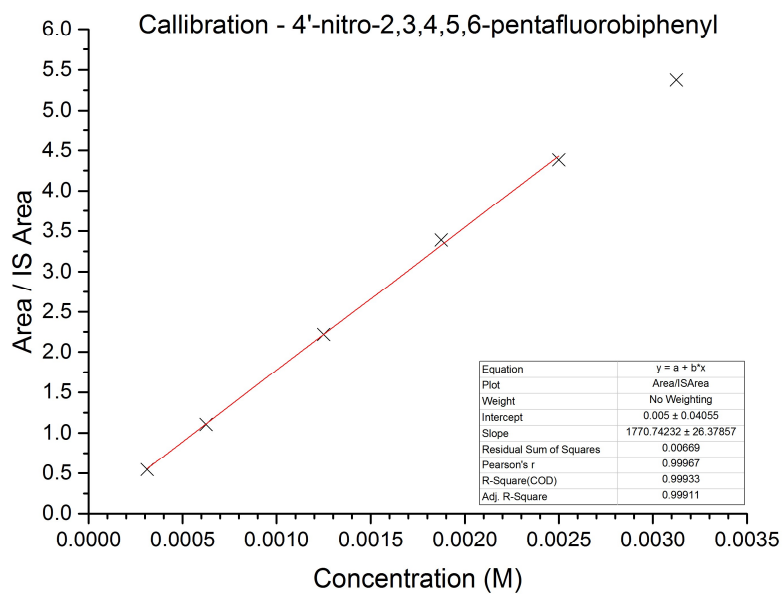
Equation 6.2 Equation for determining percentile amount of substance values from integration data, where  $Xa$  = amount of substance of analyte  $X$ ,  $Xi$  = integration divided by number of protons for analyte  $X$ ,  $Ti$  = sum of integration divided by number of protons for all analytes.

## 6.8. Calibration Data for Benzoate/Aryl Halide Coupling Reactions

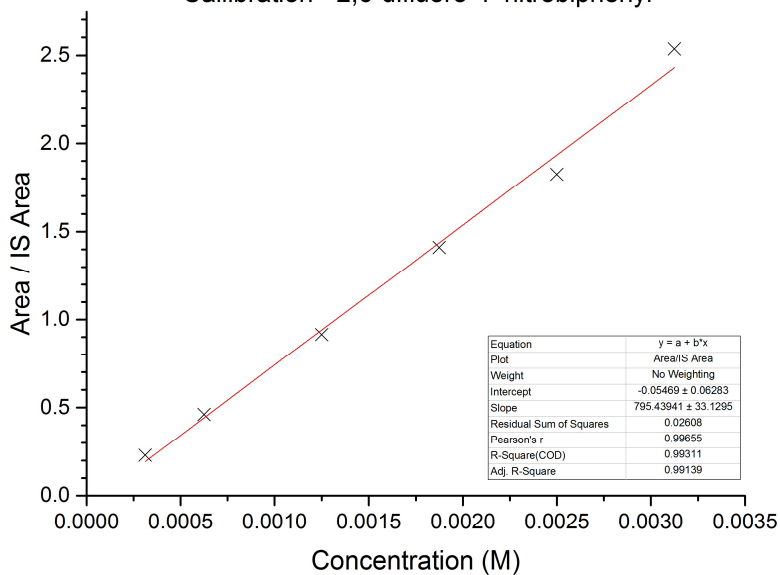
What follows is the calibration graphs used to determine reaction yields and kinetic profiles of the various decarboxylative cross-coupling reactions performed during the course of the work presented. Both starting materials and reaction products have been calibrated for. These graphs are plotted as the response of the relevant compound under the HPLC method (described in 6.6 High Pressure Liquid Chromatography Yield Derivation Methodology) against concentration, standardised using biphenyl as an internal standard. The concentration of biphenyl was 0.25 mM for all data points, as this represents the concentration of biphenyl expected in all of the samples analysed in the work presented, after dilutions. Some data points have been omitted when determining the line of best fit, as they produced a bad plot.



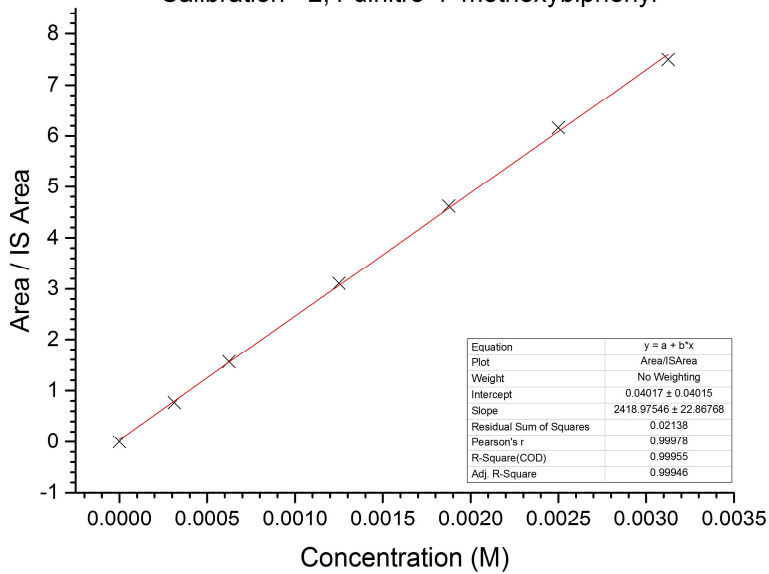




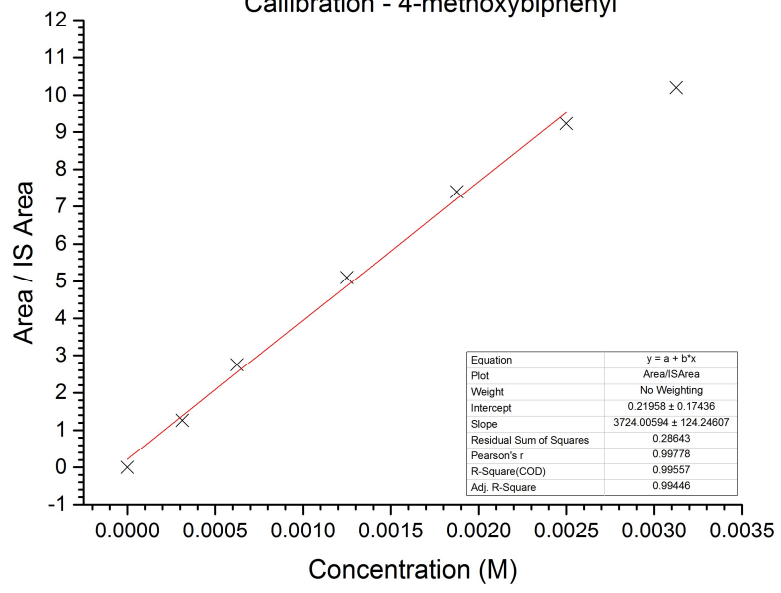
Calibration - 2,6-difluoro-4'-nitrobiphenyl



Calibration - 2,4-dinitro-4'-methoxybiphenyl



Calibration - 4-methoxybiphenyl



## 6.9. Magnetochemical Analysis

What follows is a discussion on the methodology and subsequent data for the derivation of values for the magnetic susceptibility of the various magnetic materials discussed in Chapter 2. Magnetic susceptibility is a parameter that describes the extent to which a material is magnetised by an external magnetic field, where a positive value indicates paramagnetic behaviour (attraction to the external field) and a negative value indicated diamagnetic behaviour (repulsion to the external field). The magnitude of the parameter describes the strength of this behaviour. Magnetic susceptibility is given by Equation 6.3.

$$X_g = \frac{C_{bal} * L * (R - R_0)}{10^9 * m}$$

*Equation 6.3: Formula for the determination of magnetic susceptibility, where:  $C_{bal}$  = a constant relating to the magnetic susceptibility of callibrant  $Hg[C(NCS)_4]$  at a given temperature;  $L$  = the length of the sample in cm;  $m$  = the mass of the sample in g,  $R$  = the response of the balance with respect to the sample and  $R_0$  = the response of the balance with respect to a blank.*

$C_{bal}$ , the balance calibration constant, is given by rearranging the formula, knowing that the magnetic susceptibility of callibrant  $Hg[Co(NCS)_4]$  is equal to  $(4981/273 * T) * 10^{-6} \text{ cm}^3 \text{ g}^{-1}$  (see Equation 6.4).

$$C_{bal} = \frac{\left(\frac{4981}{273 + T}\right) * 10^3 * m}{L * (R_{cal} - R_0)}$$

*Equation 6.4: Formula for the determination of the calibration constant  $C_{bal}$ , where  $T$  = temperature in °C,  $m$  = mass of the calibrant in g,  $L$  = length of the calibrant sample in cm,  $R_{cal}$  = the response of the calibrant and  $R_0$  = the response of a blank sample.*

Values for  $R$ ,  $R_{cal}$  and  $R_0$  were determined *via* the use of a Sherwood Scientific Mk1 Magnetic Susceptibility Balance. The samples were prepared as a 2 wt% suspension in magnesium sulfate, so as to avoid oversaturation of the susceptibility balance. This suspension was then packed into a preweighed glass tube and the response was measured. These values were then used to derive values for  $X_g$  as a 2 wt% suspension. Response values were taken in triplicate and used as an average.

Responses for Fe<sub>3</sub>O<sub>4</sub> and Fe<sub>2</sub>Cu were measured with sample tube A. The response for Fe<sub>2</sub>Cu was measured with sample tube B. The response for Fe<sub>4</sub>Cu was measured with sample tube C. Blank responses for each of these sample tubes were measured separately (see Table 6.6).

Table 6.5: Experimental data for the derivation of the balance calibration constant  $C_{bal}$  using Equation 6.4.

Material	Run 1	Run 2	Run 3	Avg.	Mass (g)	L (cm)	$C_{cal}$ (cm <sup>2</sup> )
Blank	-60	-60	-60	-60			
Hg[Co(NCS) <sub>4</sub> ]	710	713	712	712	0.1118	1.9	2.954

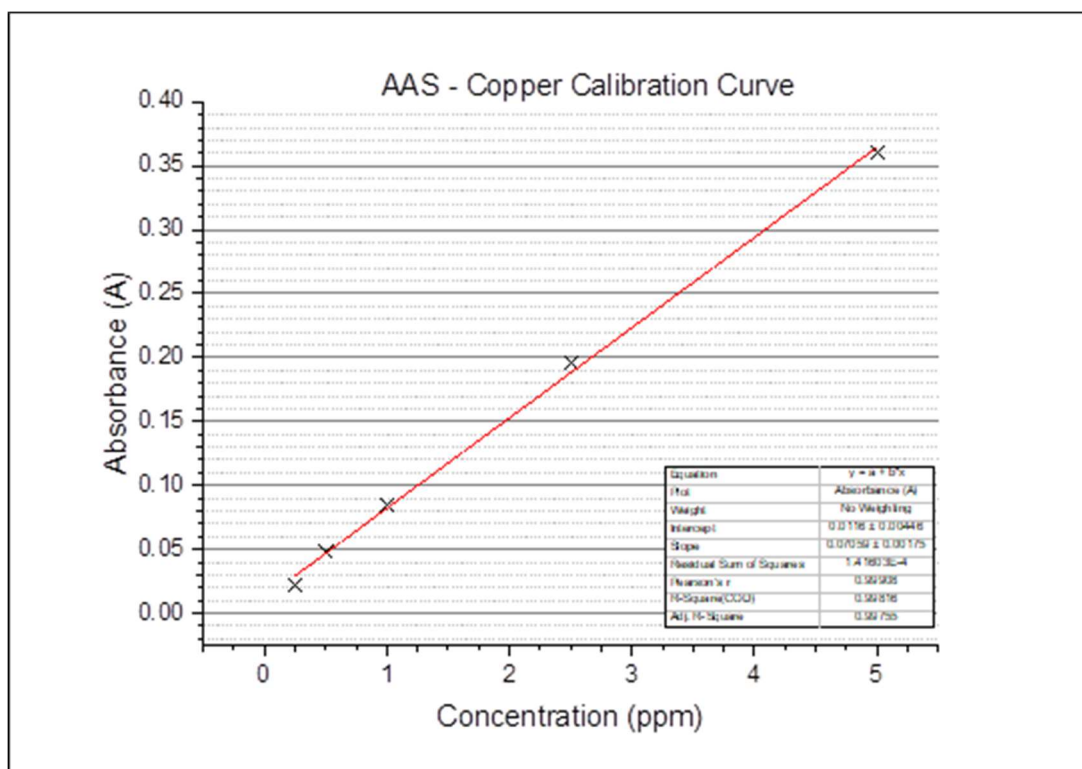
Table 6.6: Experimental data for the derivation of magnetic susceptibility using Equation 6.3.

Material	Run 1	Run 2	Run 3	Avg.	Mass (mg)	L (cm)	$\chi_g$ (cm <sup>3</sup> g <sup>-1</sup> )
MgSO <sub>4</sub>	-70	-71	-70	-70.33			
Blank A							
MgSO <sub>4</sub>	-60	-61	-61	-60.67			
Blank B							
MgSO <sub>4</sub>	-71	-72	-72	-71.67			
Blank C							
Fe <sub>3</sub> O <sub>4</sub>	9200	9170	9180	9183.33	2.5	2	0.0217
Fe <sub>2</sub> Cu	2030	2045	2035	2036.67	0.6	2	0.0215
FeCu <sub>2</sub>	1834	1836	1834	1834.67	1.4	2	0.0077
Fe <sub>4</sub> Cu	1168	1175	1170	1171	0.4	2	0.0169

## 6.10. Atomic Absorption Spectroscopy Data

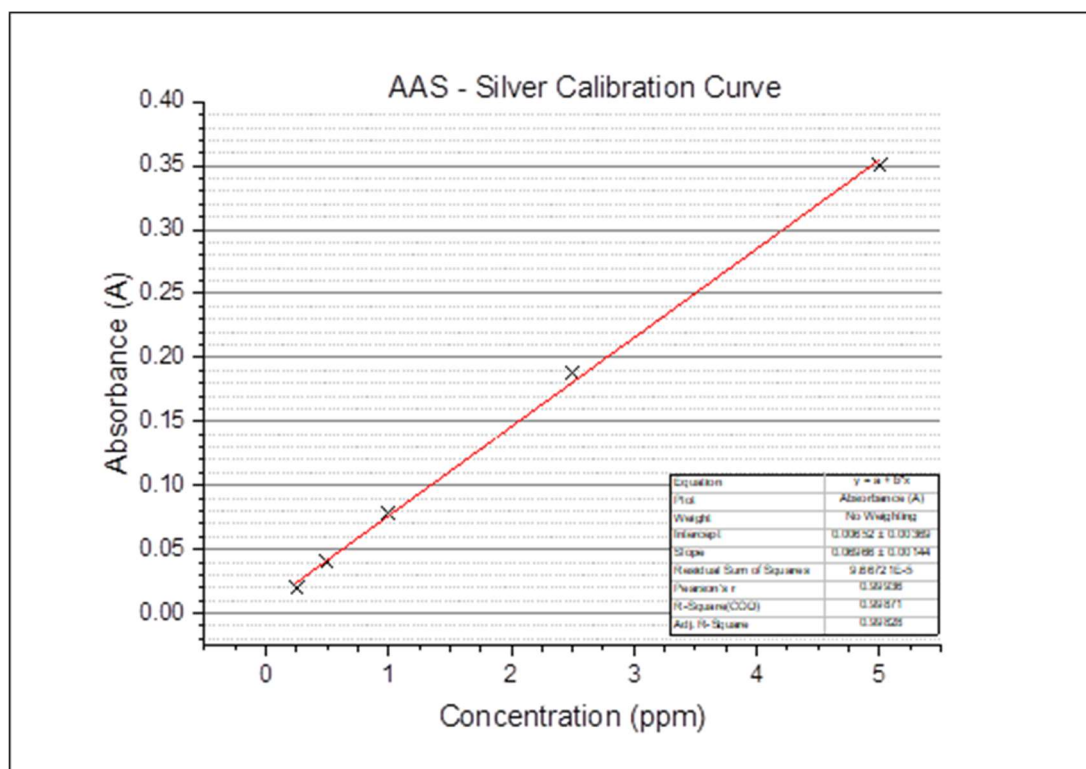
What follows is the calibration data and subsequent sample measurements for all atomic absorption spectroscopy performed. Samples were prepared to a concentration of 1000 ppm of the element under investigation in concentrated nitric acid, and subsequently diluted to 2.5 ppm in deionized water. The standard used to prepare the calibration samples for the copper measurements was purchased as a 1000 ppm solution of copper (metal) in 2 % nitric acid from Sigma Aldrich. The standard used to prepare the calibration samples for the silver measurements was purchased as a 1000 ppm solution of silver (metal) in 2 % nitric acid from Sigma Aldrich. The standard used to prepare the calibration samples for the gold measurements was purchased as a 1000 ppm solution of gold (metal) in 5 % hydrochloric acid (with trace nitric acid) from Sigma Aldrich. The standard used to prepare the calibration samples for the palladium measurements was purchased as a 1000 ppm solution of palladium (metal) in 5 % hydrochloric acid (with trace nitric acid) from Sigma Aldrich. The standard used to prepare the calibration samples for the nickel measurements was purchased as a 1000 ppm solution of nickel (metal) in 2 % nitric acid from Sigma Aldrich. Calibration samples were prepared to concentrations of 0.25, 0.5, 1, 2.5 and 5 ppm with respect to the element under investigation in deionised water. Data was taken in triplicate and represented as an average.

Copper containing samples:



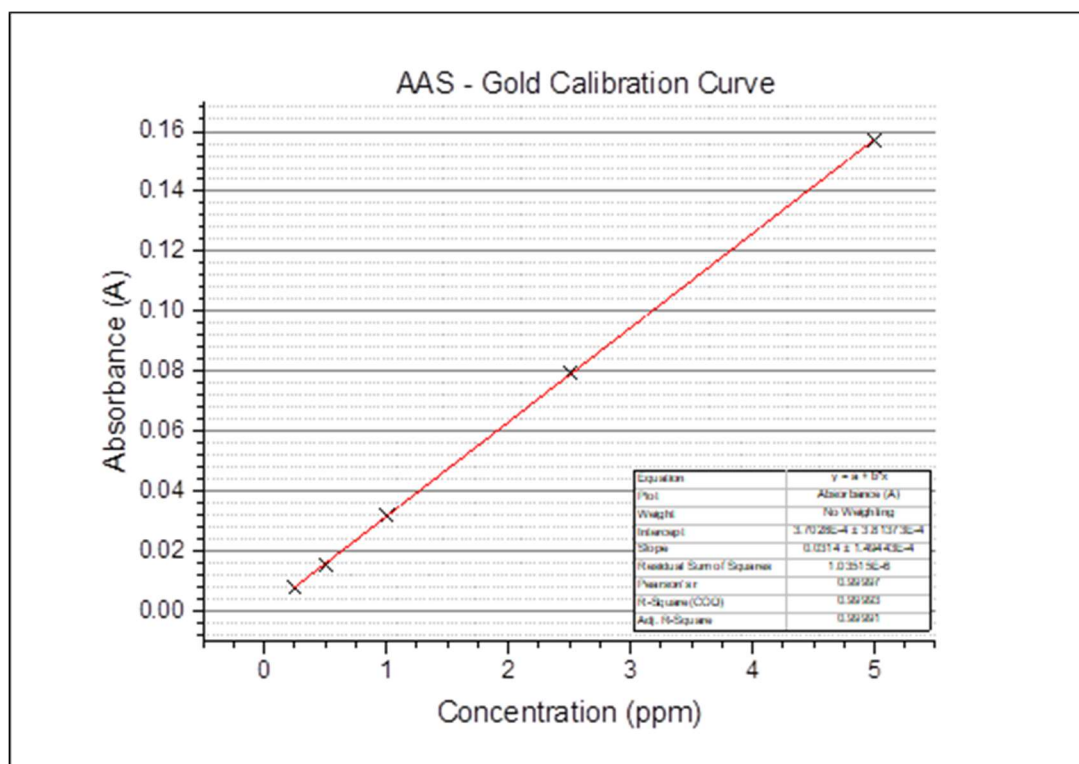
Cu Samples	1	2	3	Average (ppm)	Error (ppm)	Content (%)	Error (%)
<b>Cu-PVP</b>	1.256	1.253	1.257	1.255	0.004	50.21	0.08
<b>Pd2Cu-PVP</b>	0.221	0.219	0.220	0.220	0.008	7.57	0.03
<b>PdCu-PVP</b>	0.246	0.247	0.251	0.248	0.005	9.33	0.06
<b>PdCu2PVP</b>	0.286	0.289	0.290	0.288	0.004	10.84	0.03
<b>Cu-EG</b>	2.559	2.562	2.571	2.564	0.006	102.56	0.25
<b>NiCu2-EG</b>	0.707	0.710	0.709	0.709	0.002	28.35	0.06
<b>NiCu-EG</b>	1.030	1.036	1.035	1.034	0.003	41.35	0.13
<b>NiCu2-EG</b>	0.829	0.816	0.830	0.825	0.008	33.00	0.31
<b>PdCu-EG</b>	0.600	0.602	0.602	0.601	0.001	24.05	0.05
<b>Cu(mono)</b>	2.308	2.314	2.317	2.313	0.005	92.51	0.19
<b>Fe2Cu</b>	2.017	2.019	2.028	2.021	0.006	80.85	0.23
<b>FeCu2</b>	1.998	2.003	1.980	1.994	0.012	79.74	0.48
<b>Fe4Cu</b>	1.674	1.685	1.687	1.682	0.007	67.27	0.28

Silver containing samples:



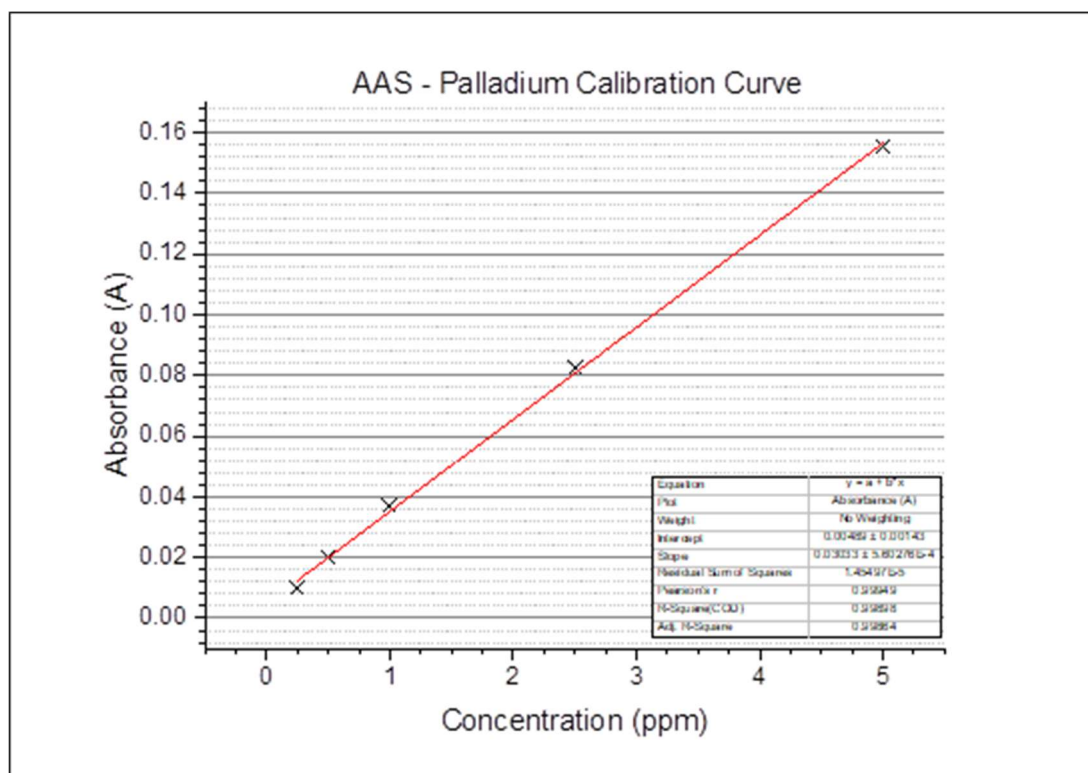
Ag Samples	1	2	3	Average (ppm)	Error (ppm)	Content (%)	Error (%)
<b>Ag-PVP</b>	2.222	2.236	2.244	2.234	0.011	89.36	0.45
<b>PdAg-PVP</b>	0.739	0.740	0.736	0.738	0.002	29.53	0.08

Gold containing samples:



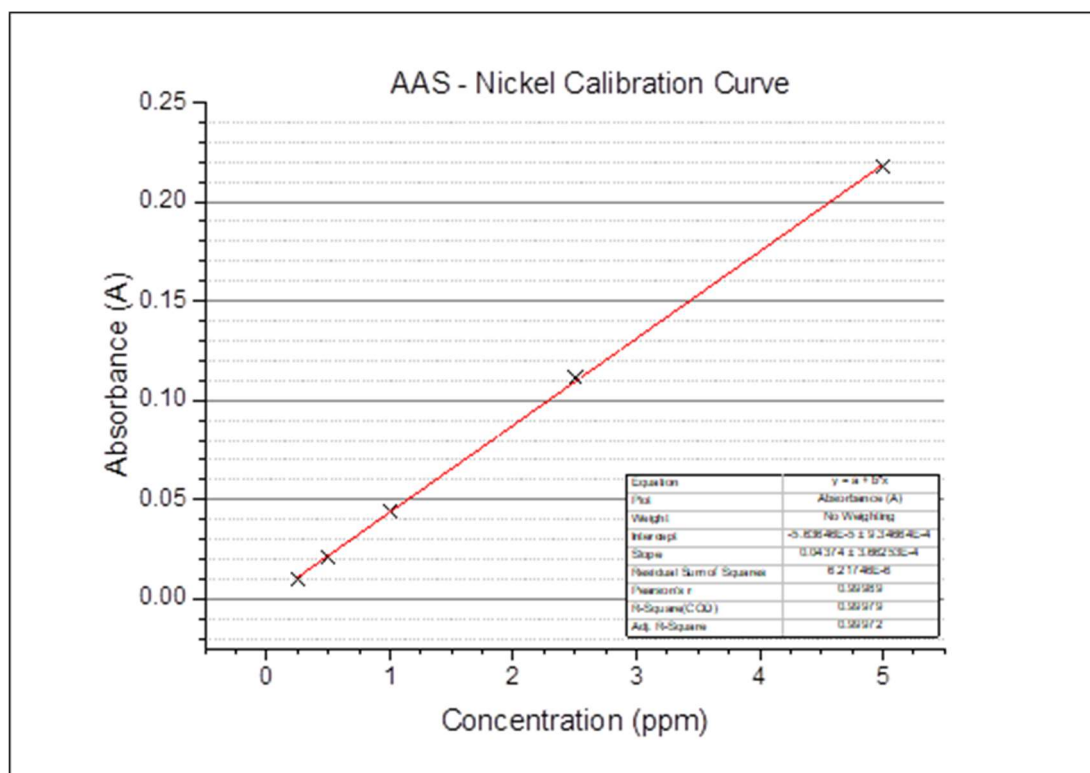
Au Samples	1	2	3	Average (ppm)	Error (ppm)	Content (%)	Error (%)
<b>Au-PVP</b>	0.428	0.431	0.456	0.438	0.015	17.53	0.61
<b>PdAu-PVP</b>	0.421	0.435	0.435	0.430	0.008	17.21	0.32

Palladium containing samples:



Pd Samples	1	2	3	Average (ppm)	Error (ppm)	Content (%)	Error (%)
<b>Pd-PVP</b>	0.408	0.407	0.413	0.409	0.006	16.37	0.13
<b>Pd2Cu-PVP</b>	0.685	0.689	0.681	0.685	0.008	25.68	0.04
<b>PdCu-PVP</b>	0.346	0.347	0.350	0.348	0.001	13.45	0.02
<b>PdCu2PVP</b>	0.240	0.236	0.236	0.237	0.001	9.18	0.02
<b>PdAg-PVP</b>	0.779	0.767	0.760	0.769	0.010	30.75	0.38
<b>PdAu-PVP</b>	0.659	0.646	0.654	0.653	0.007	26.12	0.26
<b>Pd-EG</b>	2.273	2.281	2.255	2.270	0.013	90.79	0.53
<b>PdCu-EG</b>	1.533	1.536	1.522	1.530	0.007	61.21	0.29

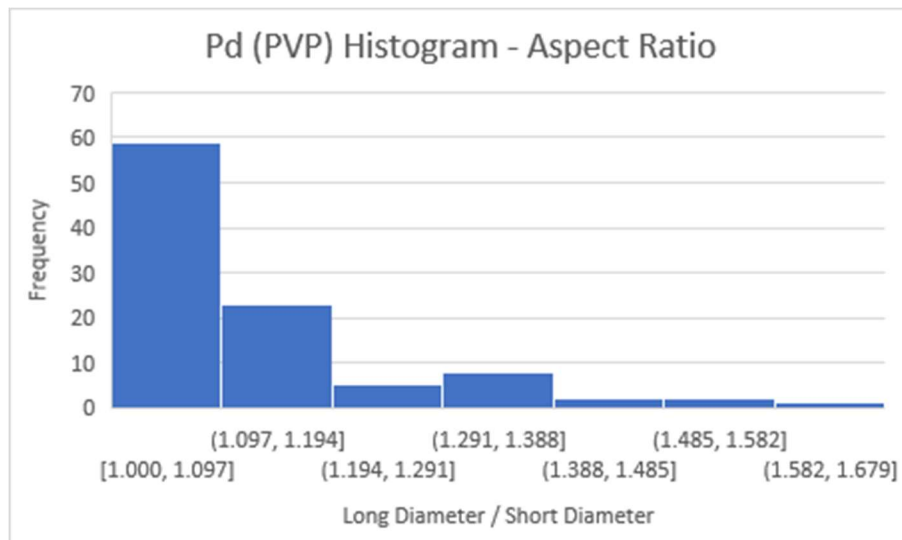
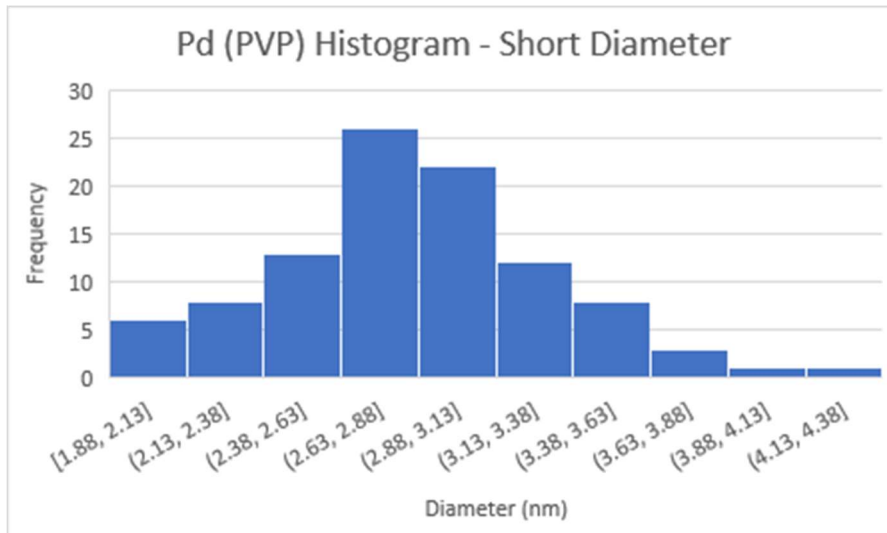
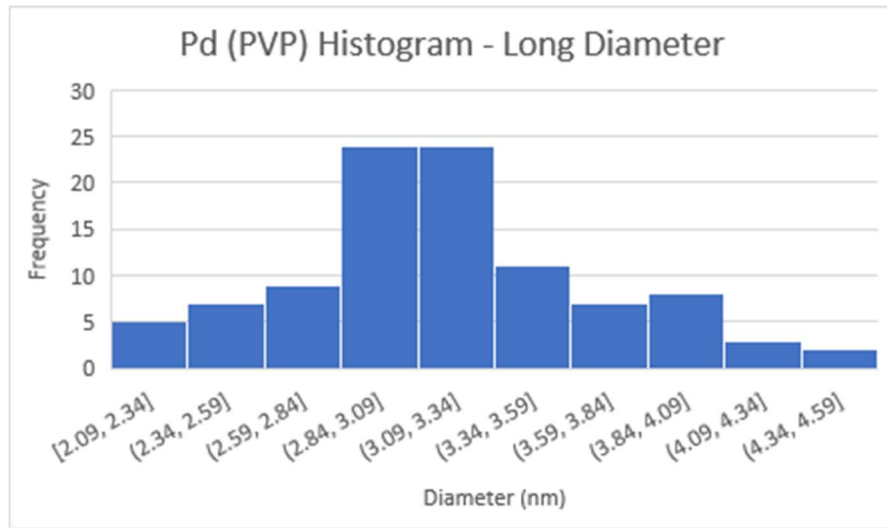
Nickel containing samples:

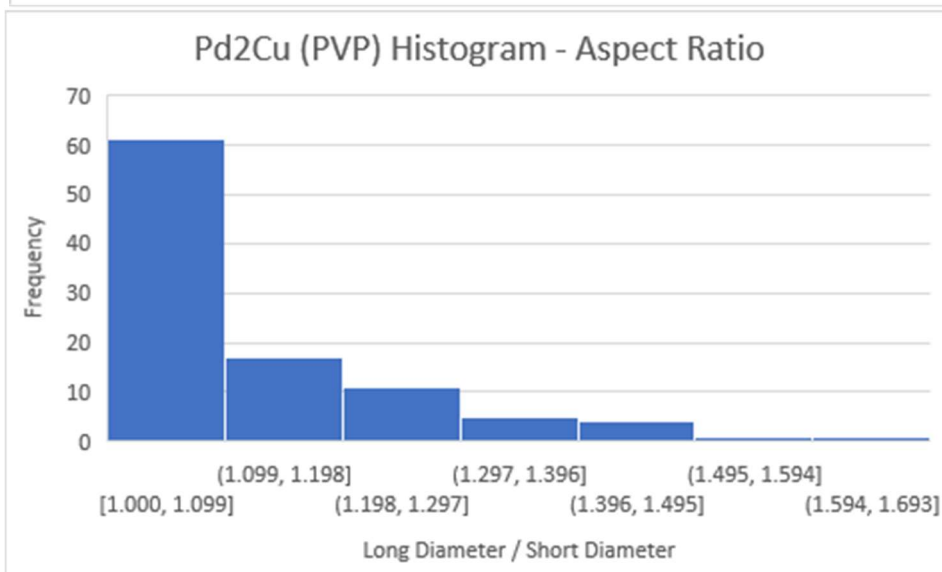
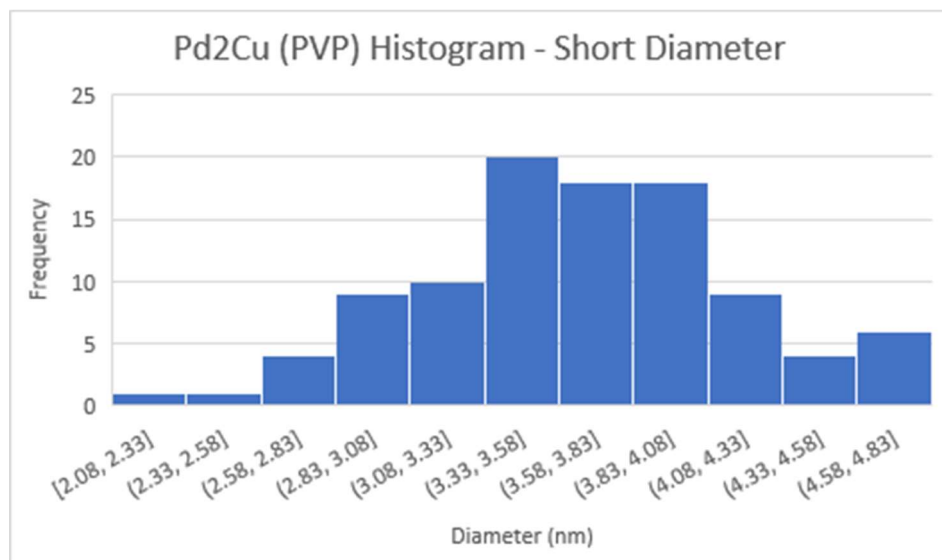
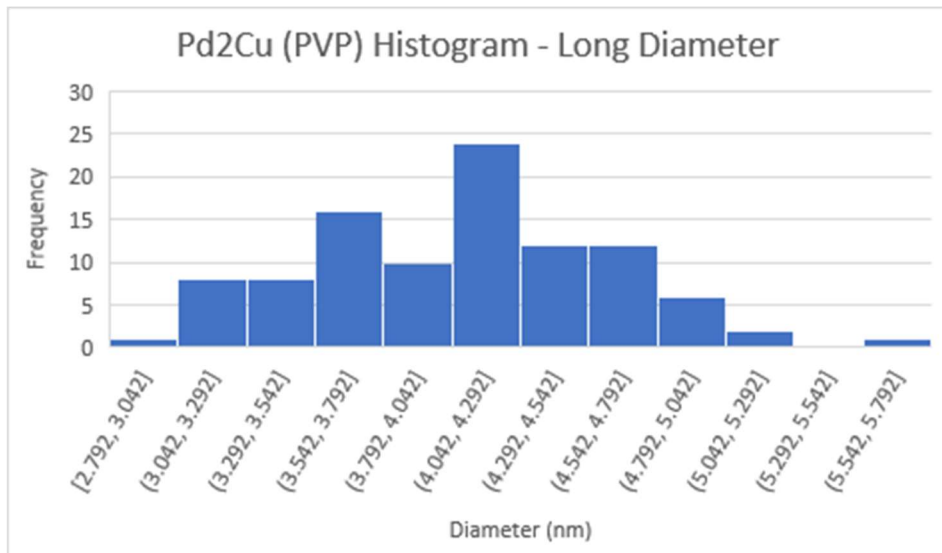


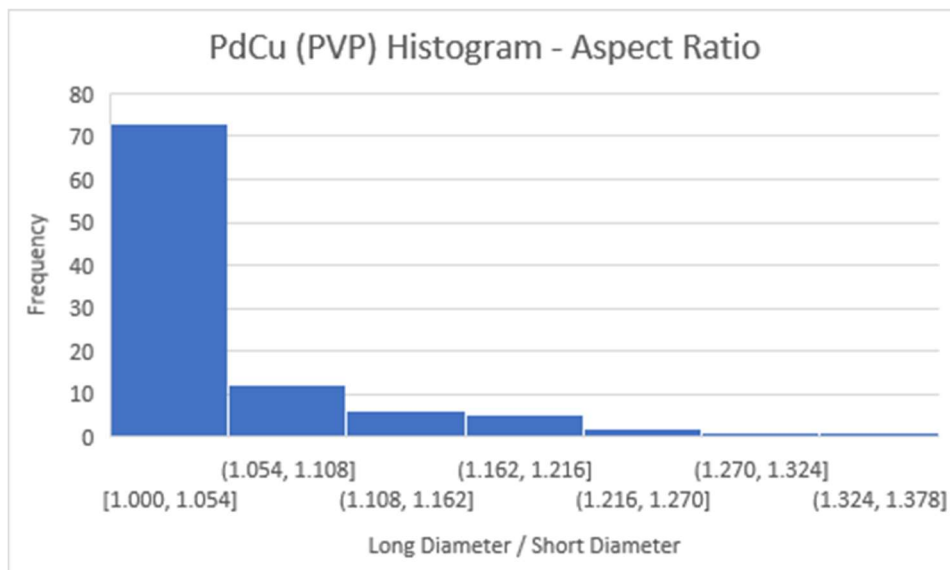
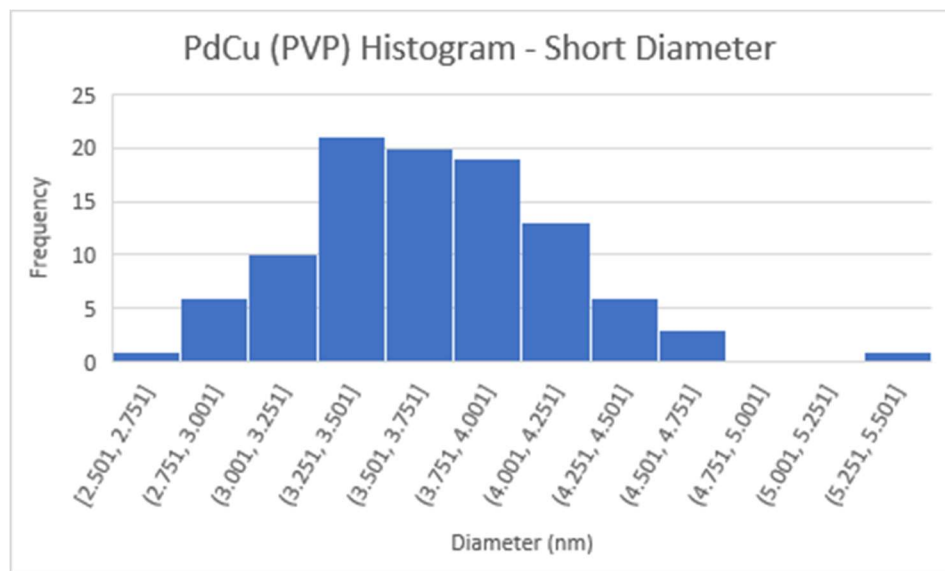
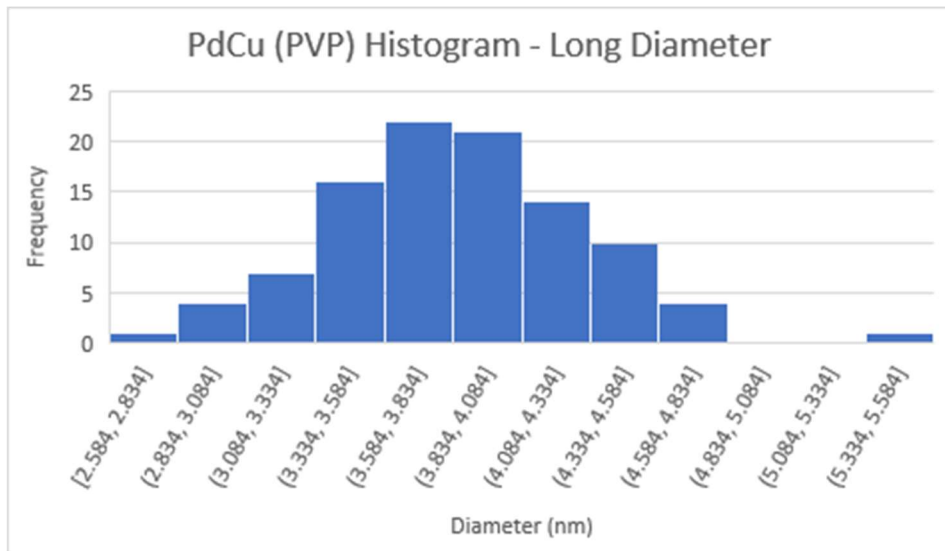
Ni Samples	1	2	3	Average (ppm)	Error (ppm)	Content (%)	Error (%)
<b>Ni-EG</b>	0.696	0.709	0.699	0.701	0.007	28.05	0.27
<b>NiCu2-EG</b>	0.377	0.382	0.381	0.380	0.003	15.20	0.11
<b>NiCu-EG</b>	0.223	0.216	0.221	0.220	0.004	8.80	0.14
<b>NiCu2-EG</b>	0.225	0.222	0.220	0.222	0.003	8.89	0.10

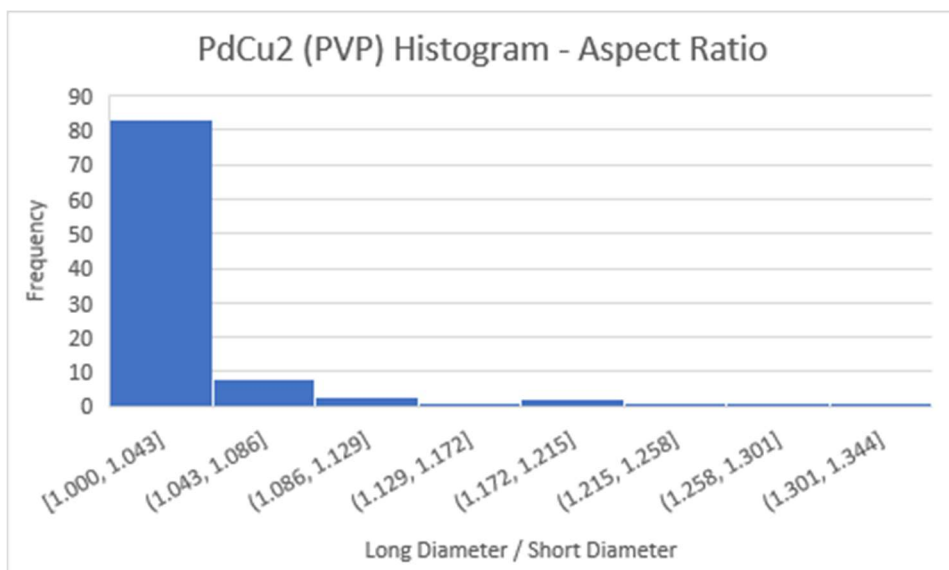
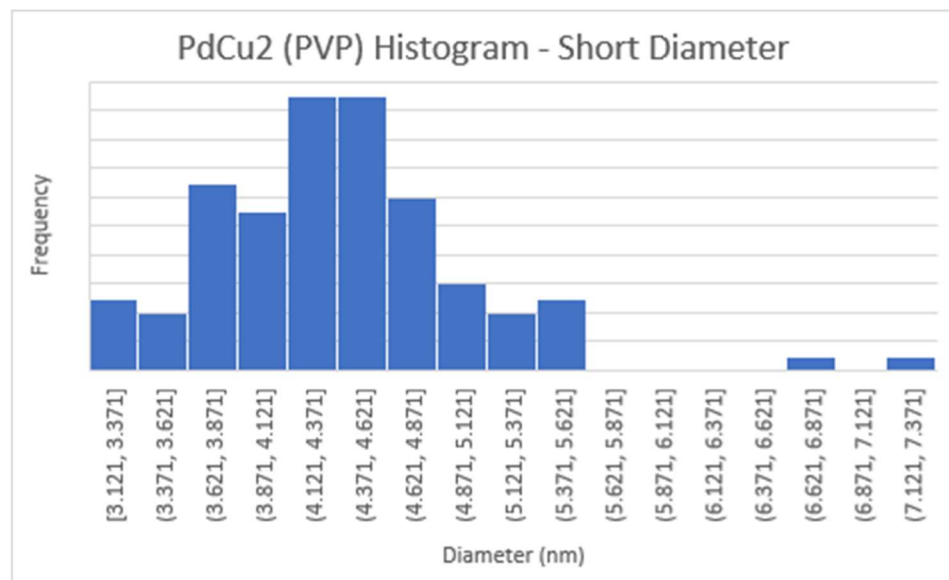
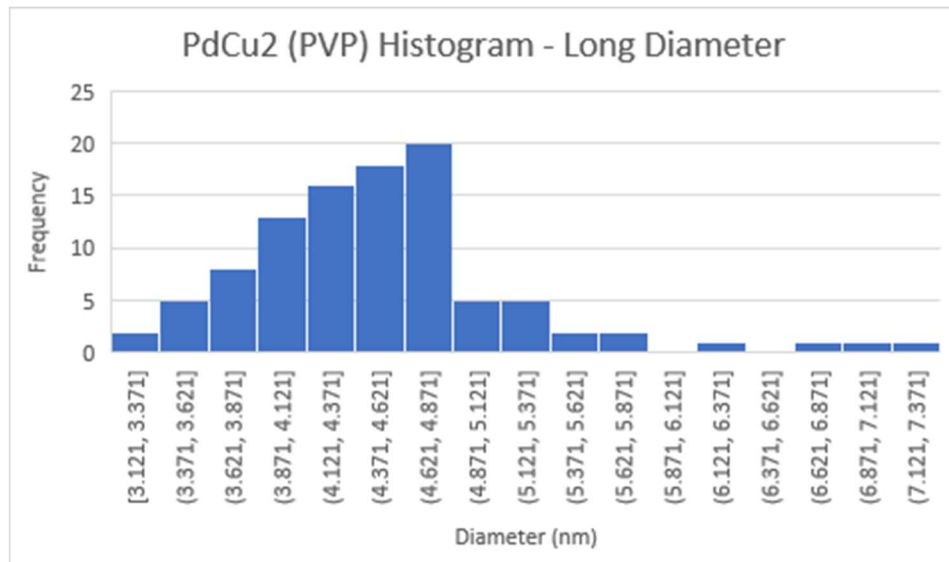
### 6.11. Transition Electron Microscopy Data

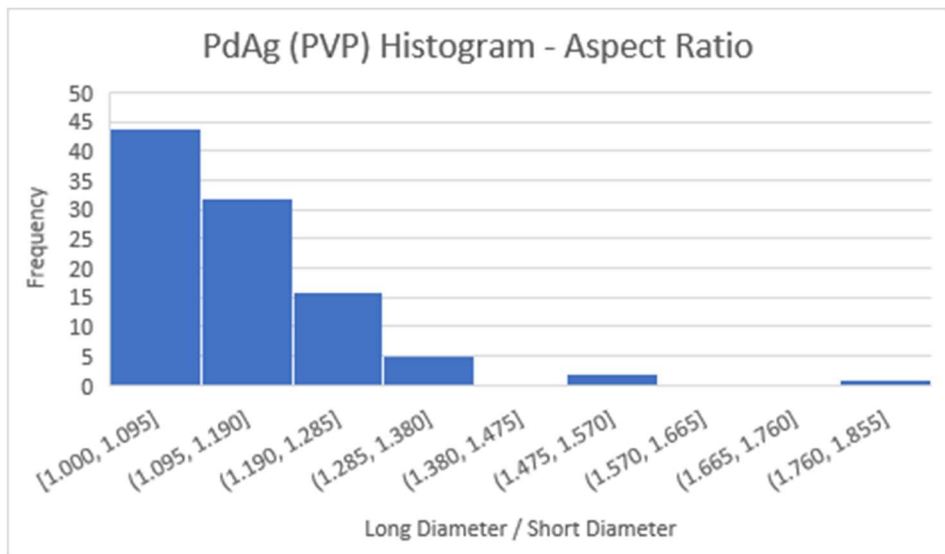
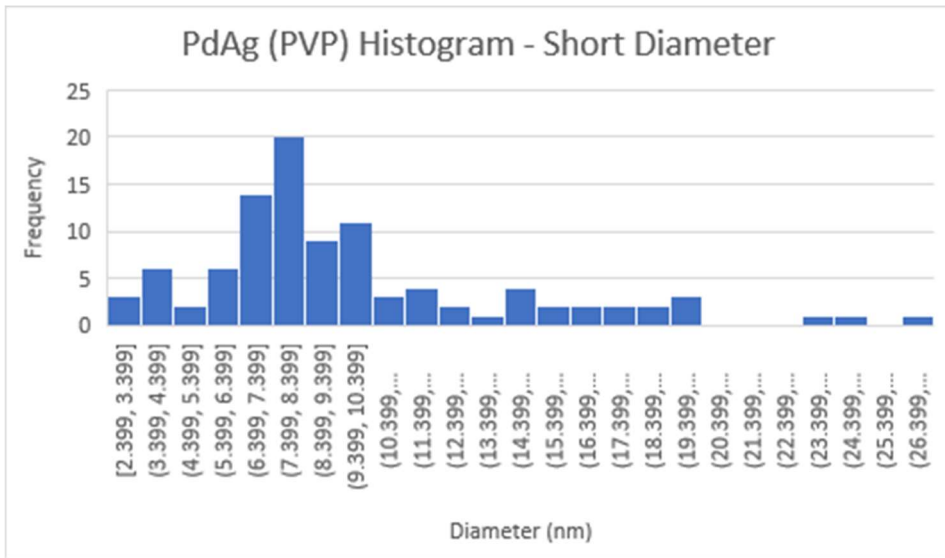
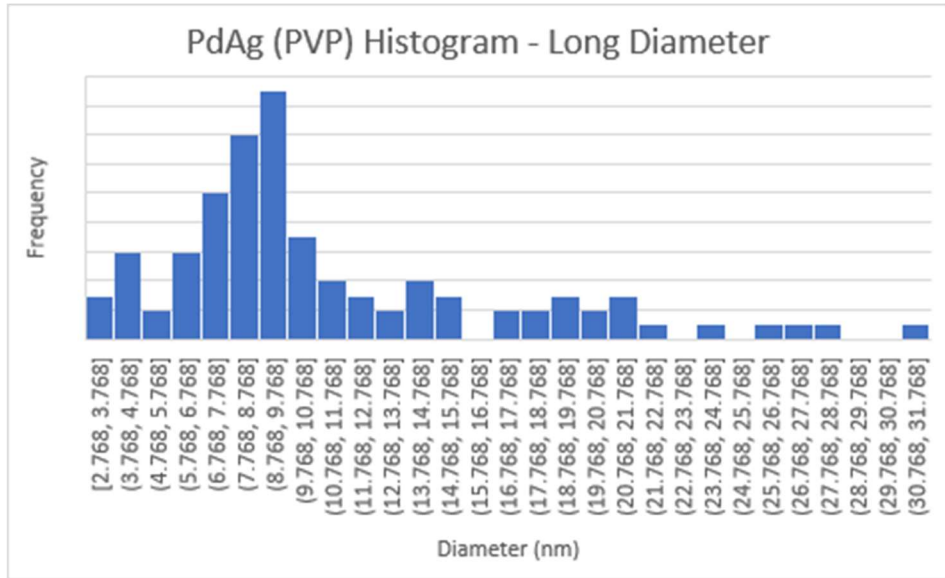
What follows is histograms for all samples analysed *via* transition electron microscopy. All histograms represent 100 data points collected over 5 distinct sample regions captured *via* transition electron microscopy. Long diameter refers to the longest diameter of the nanoparticle measured. Short diameter refers to the diameter perpendicular to the long diameter. Aspect ratio is a derived value calculated by dividing the long diameter by the short diameter. For spherical nanoparticles a value of 1 implies true spherical shape and values greater than 1 imply an ellipsoid shape.

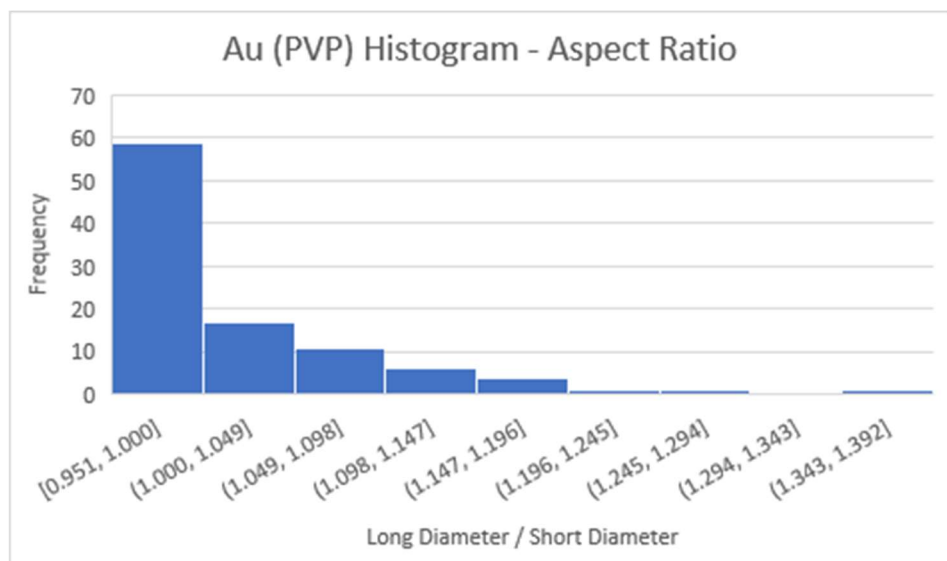
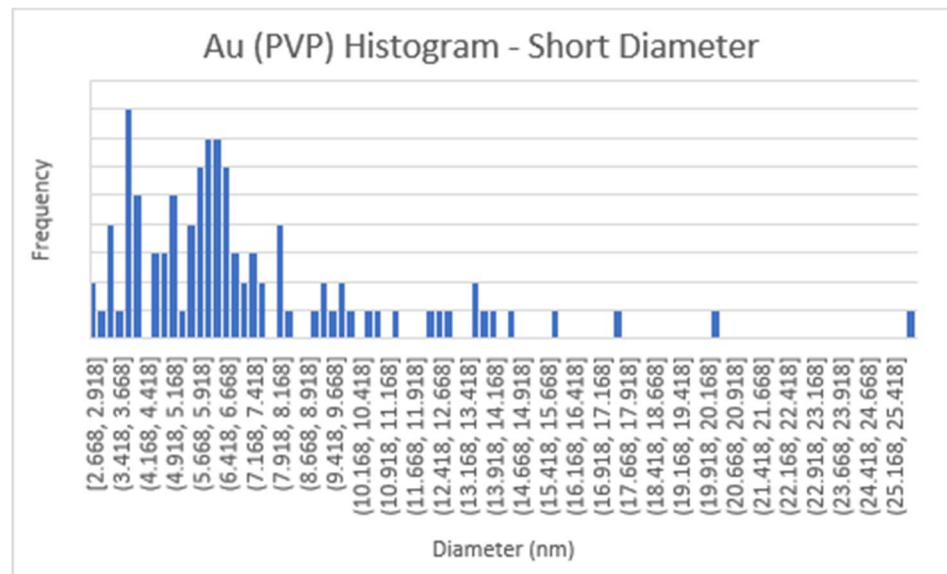
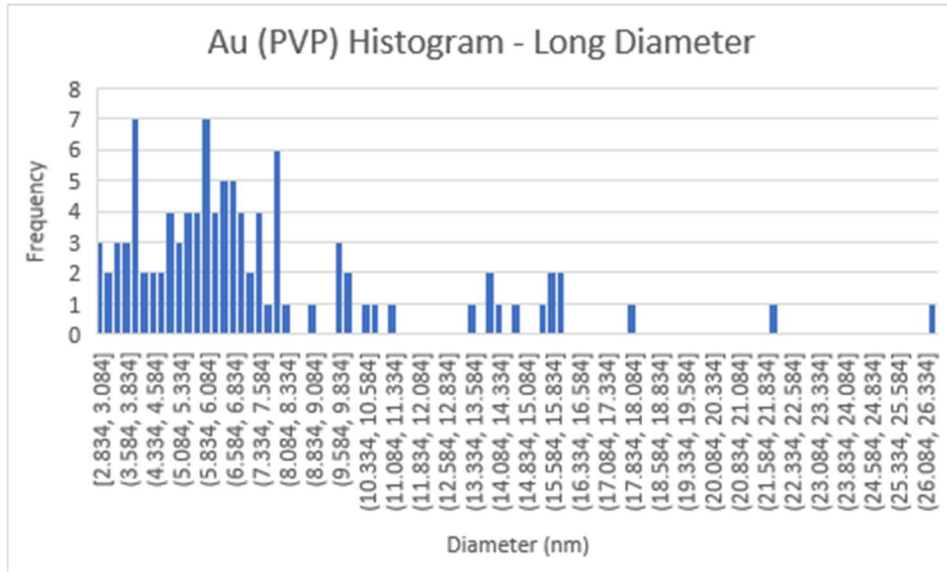


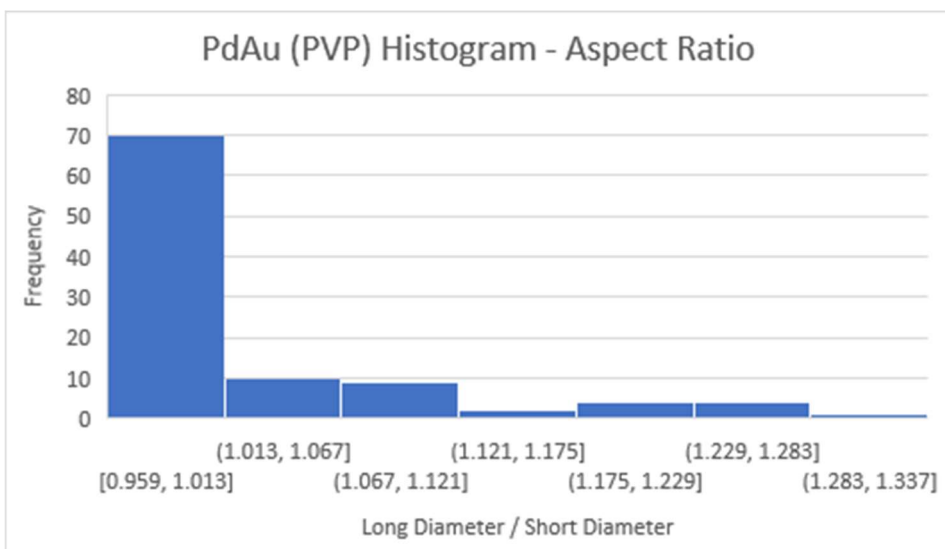
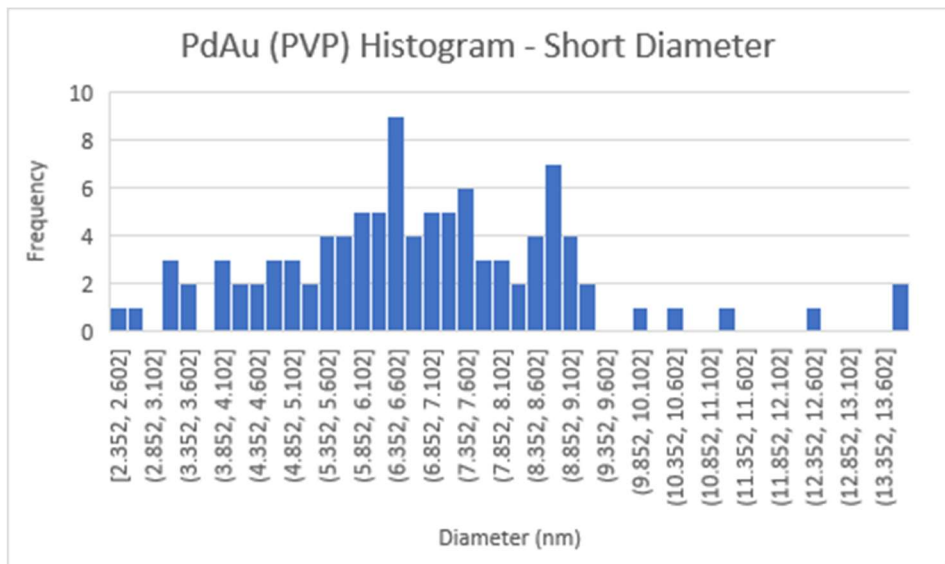
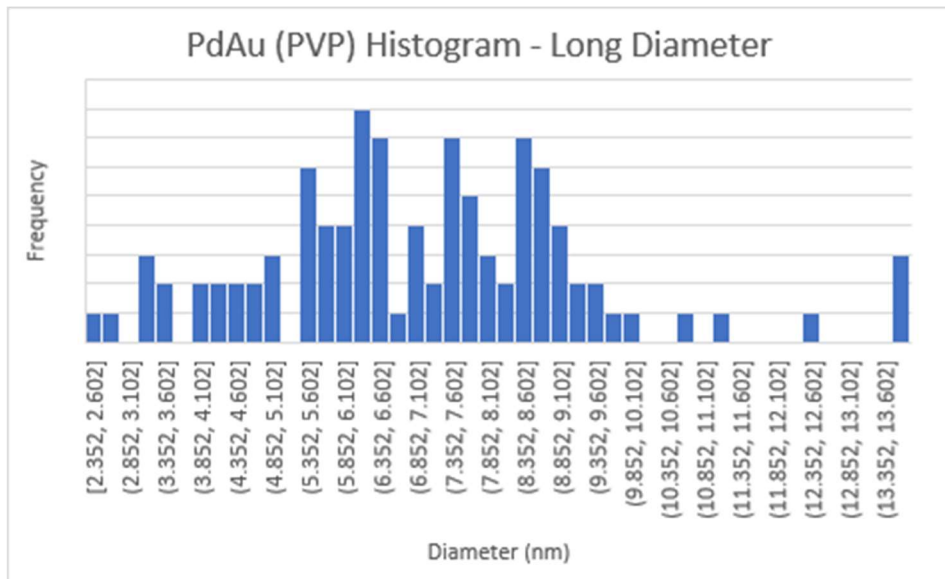


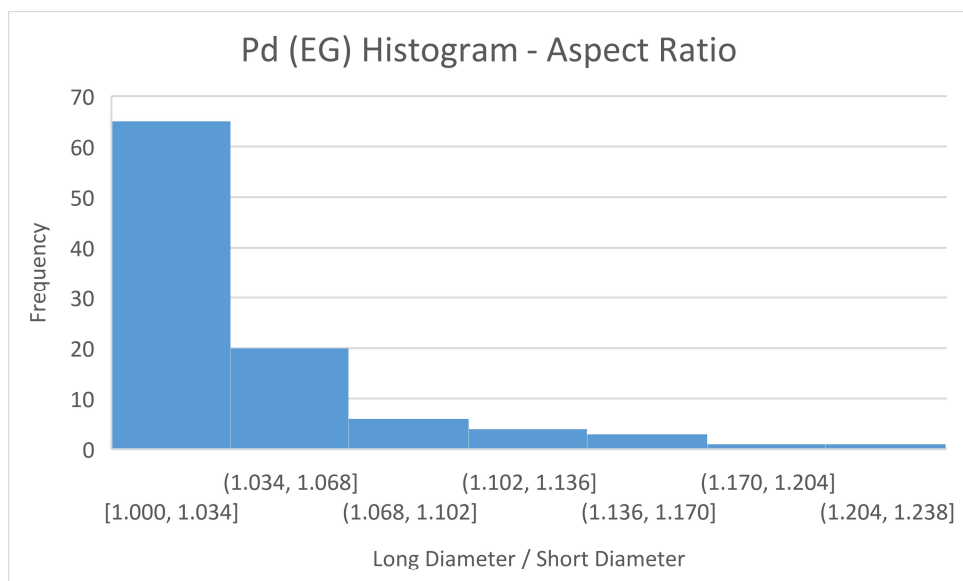
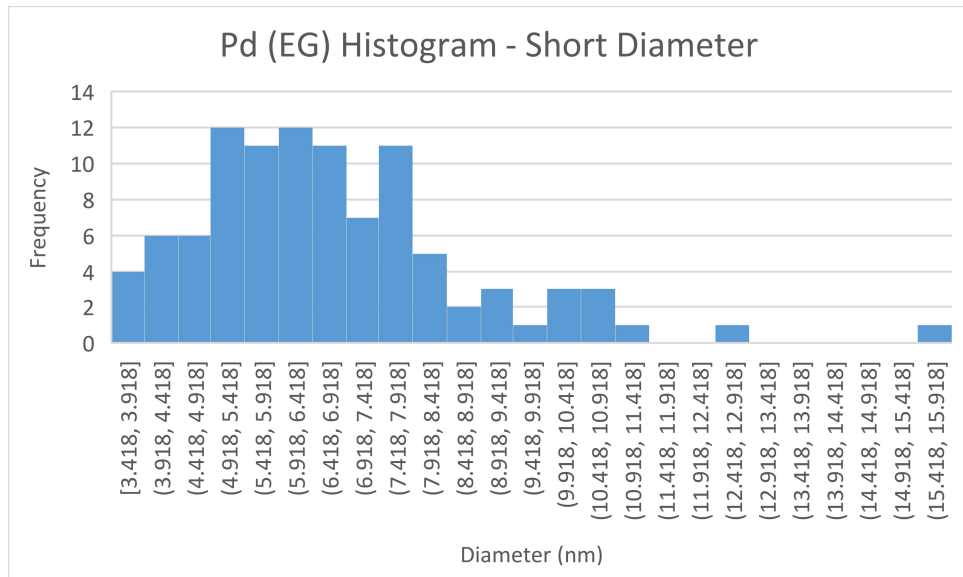
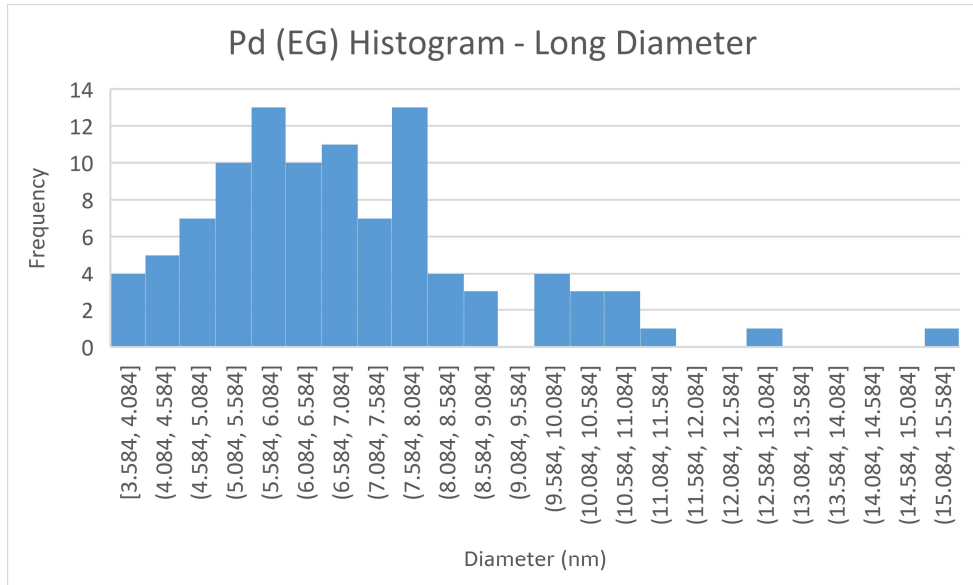


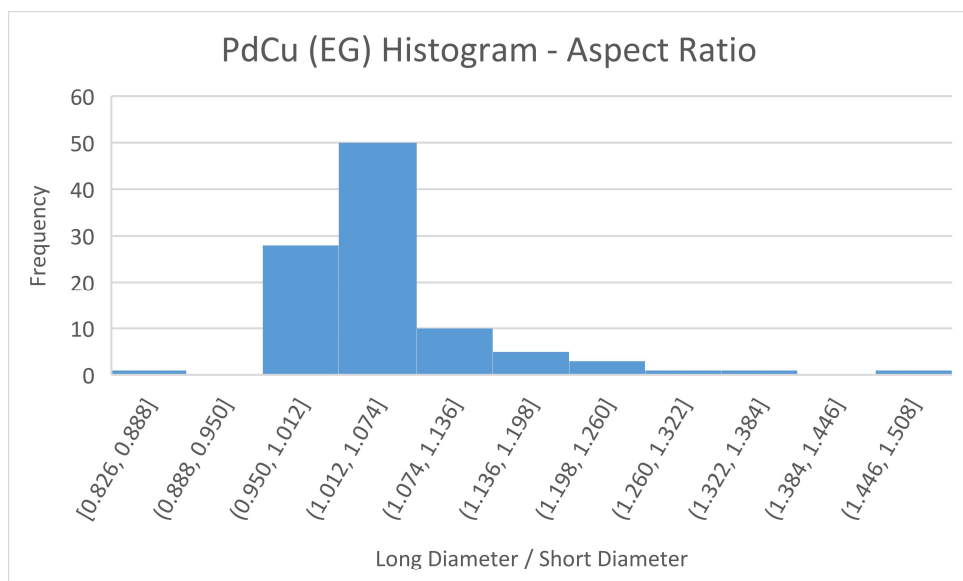
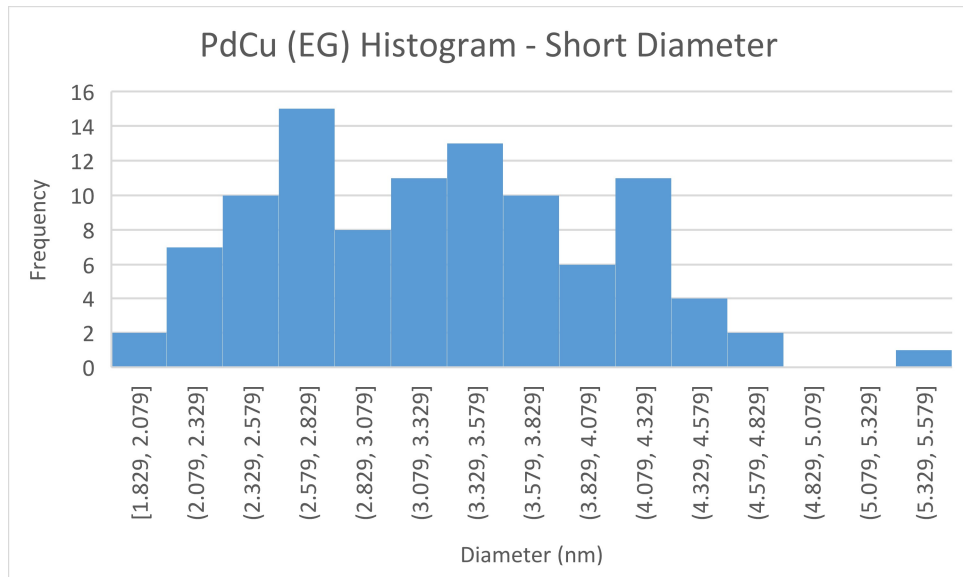
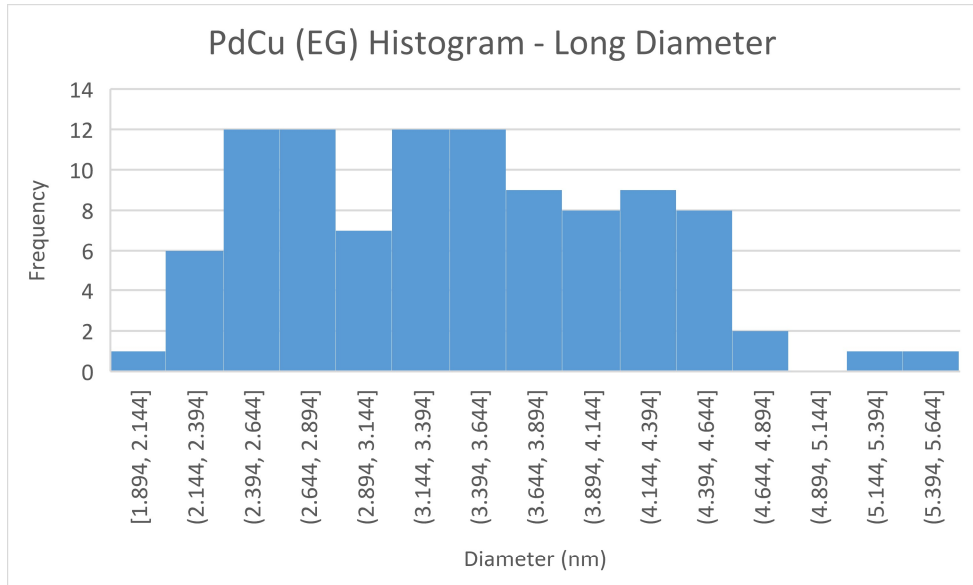


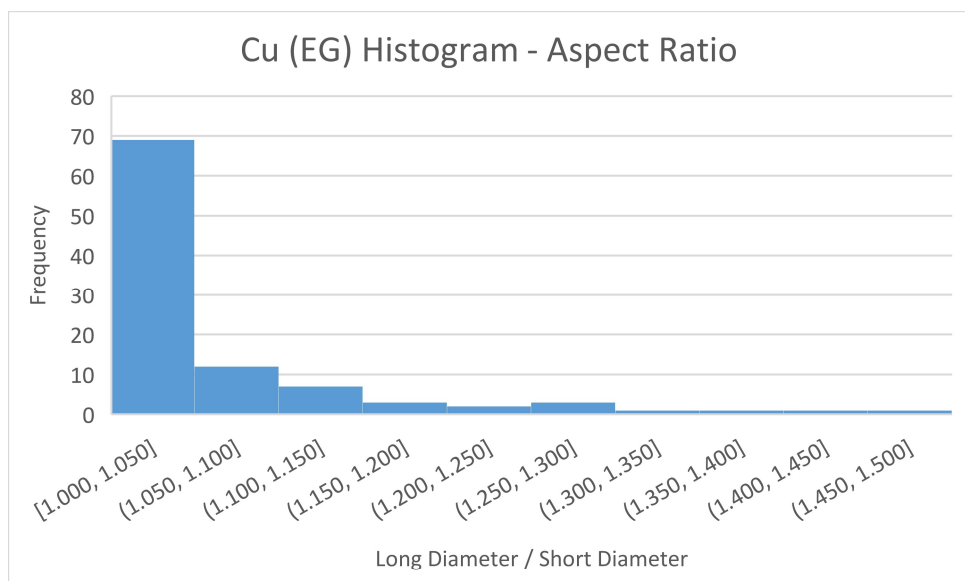
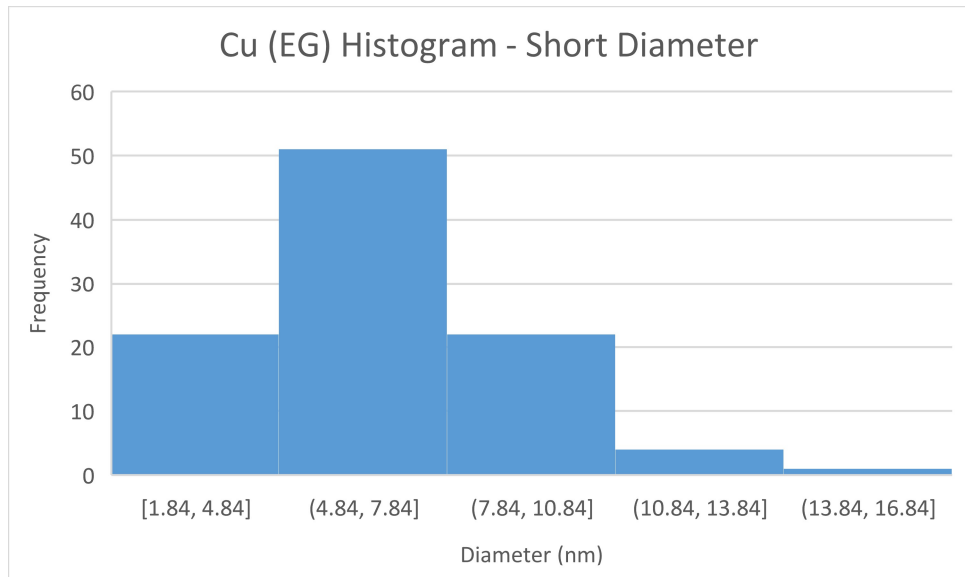
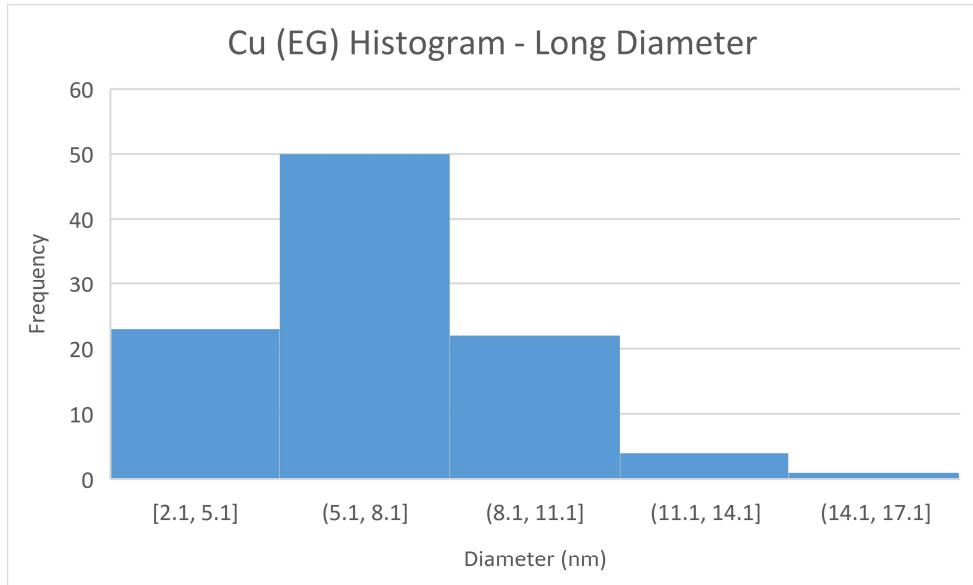


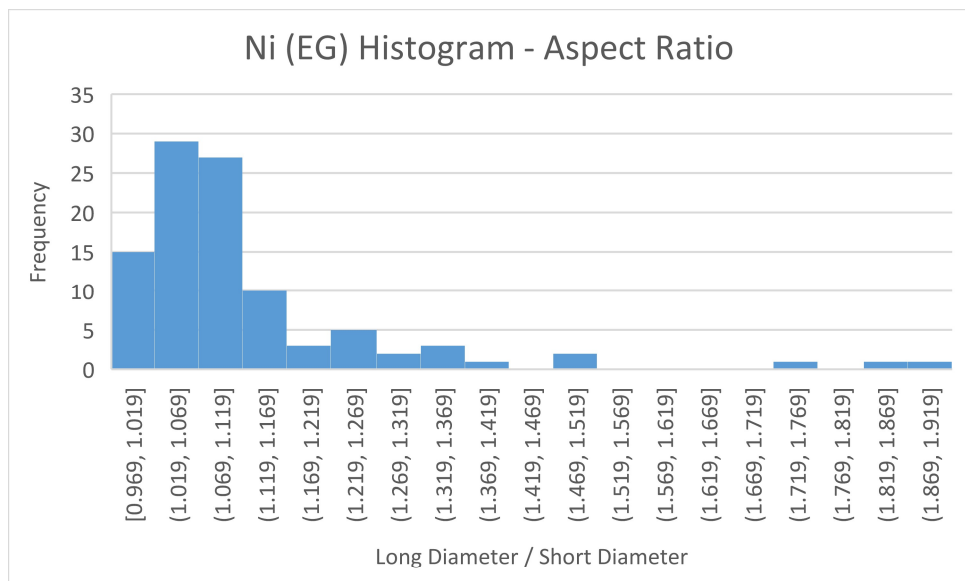
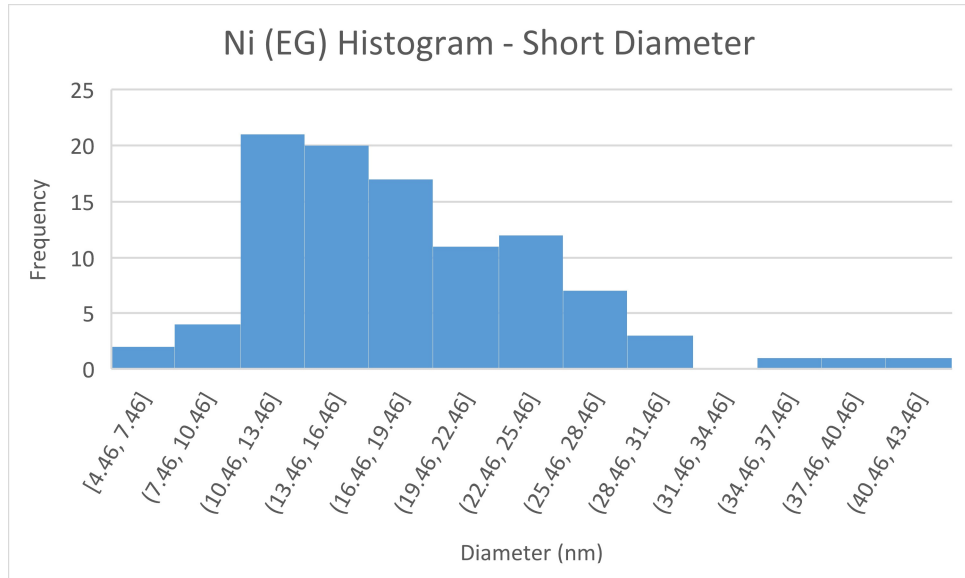
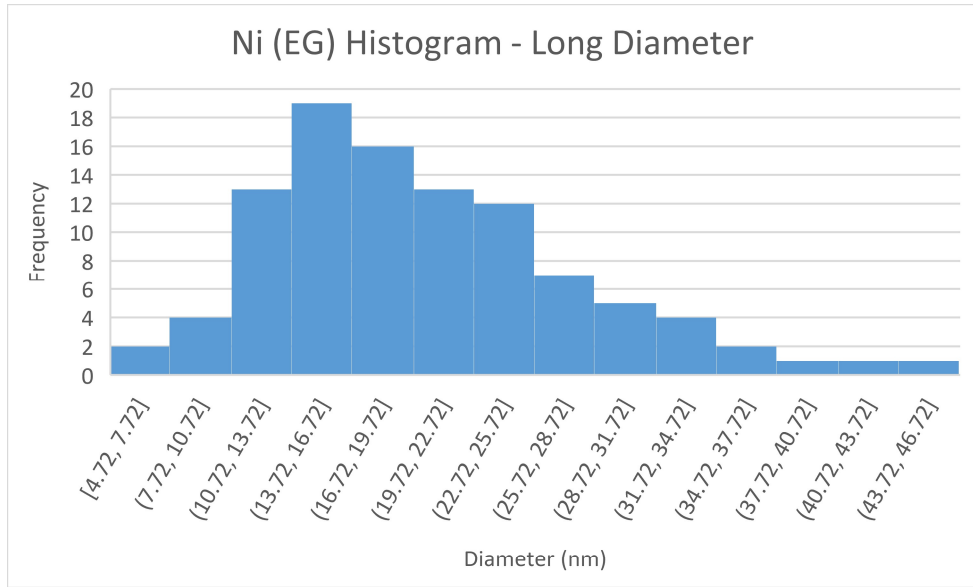


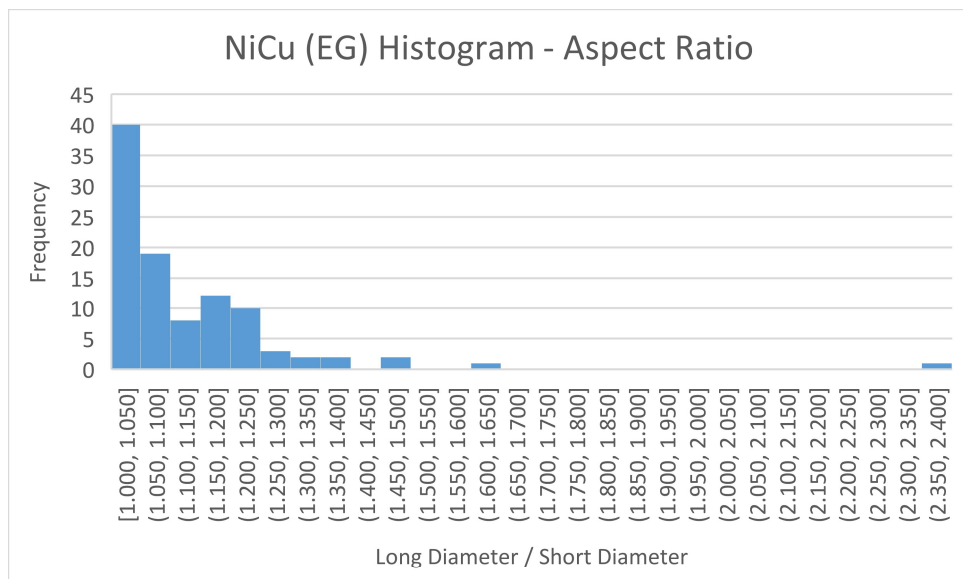
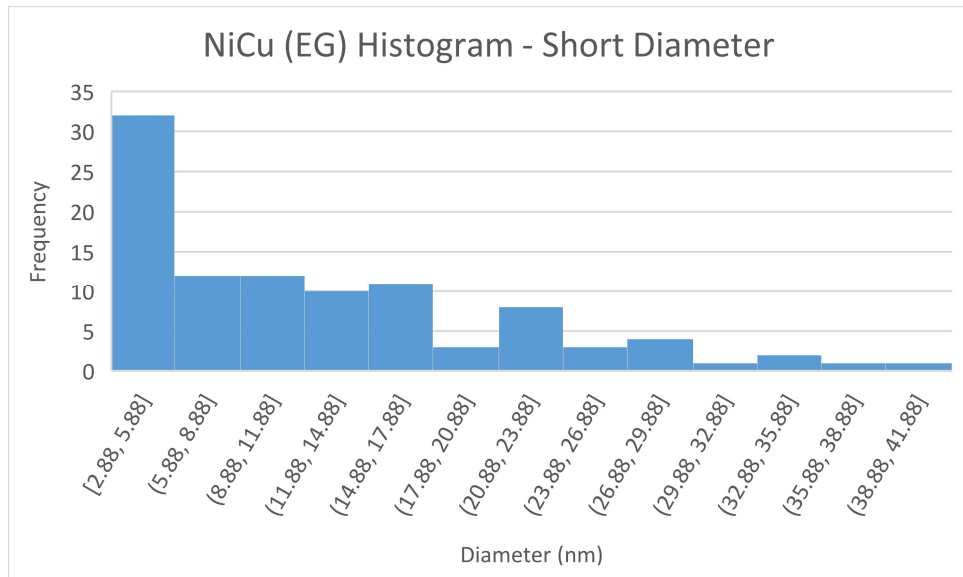
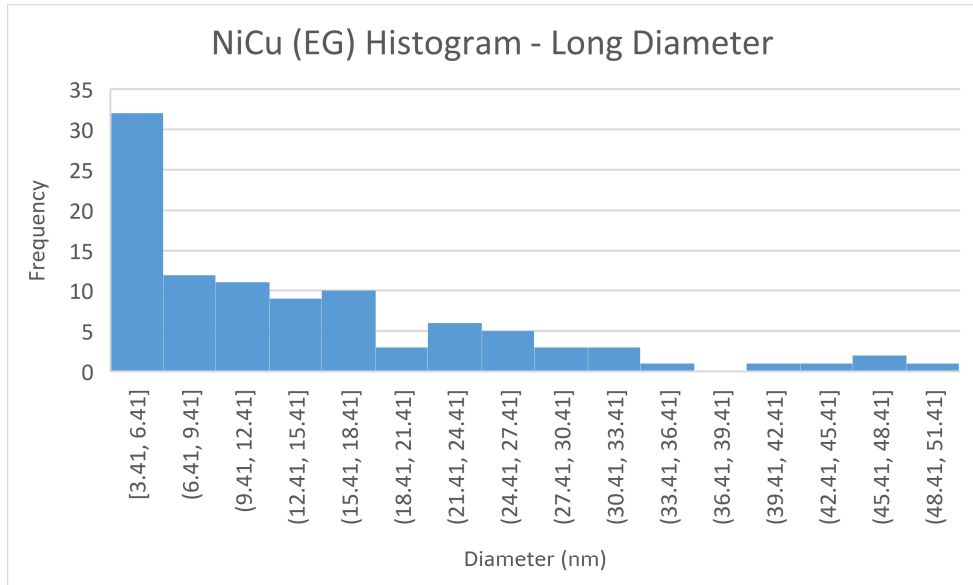






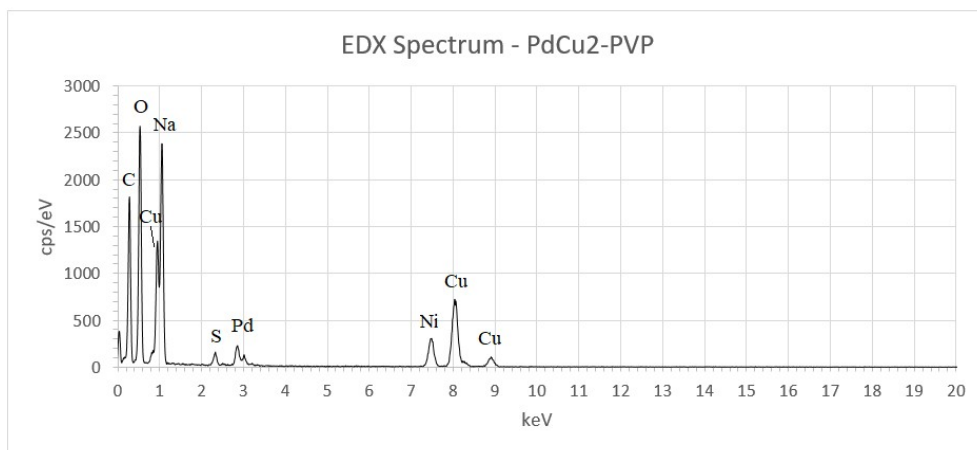
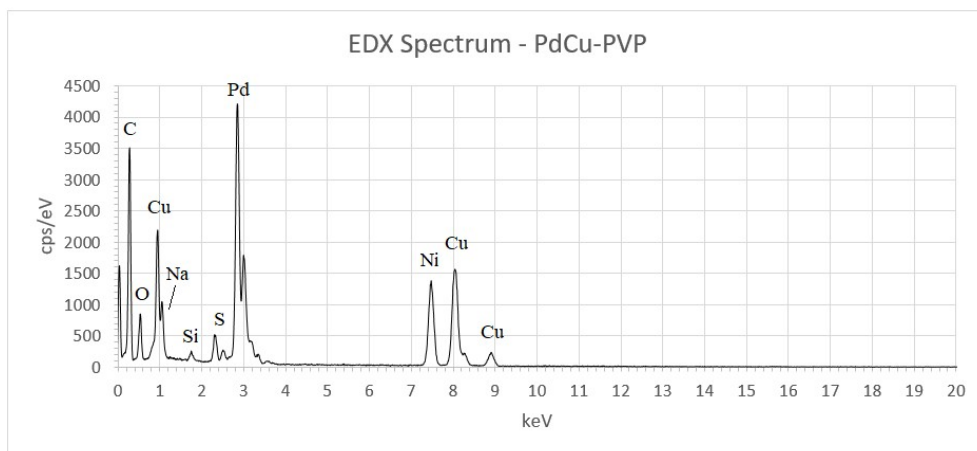
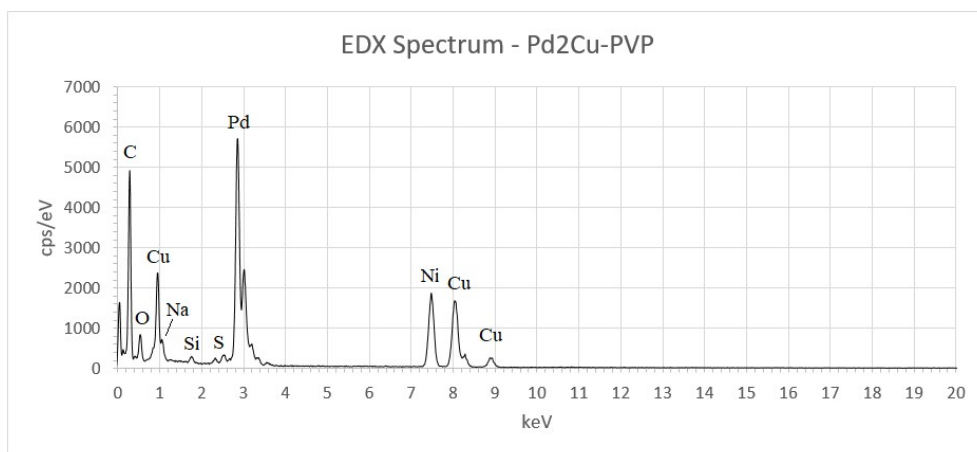


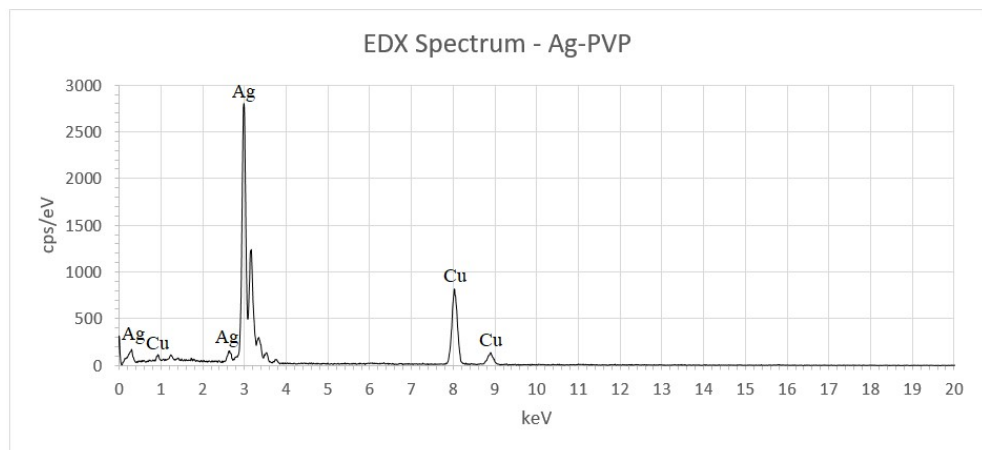
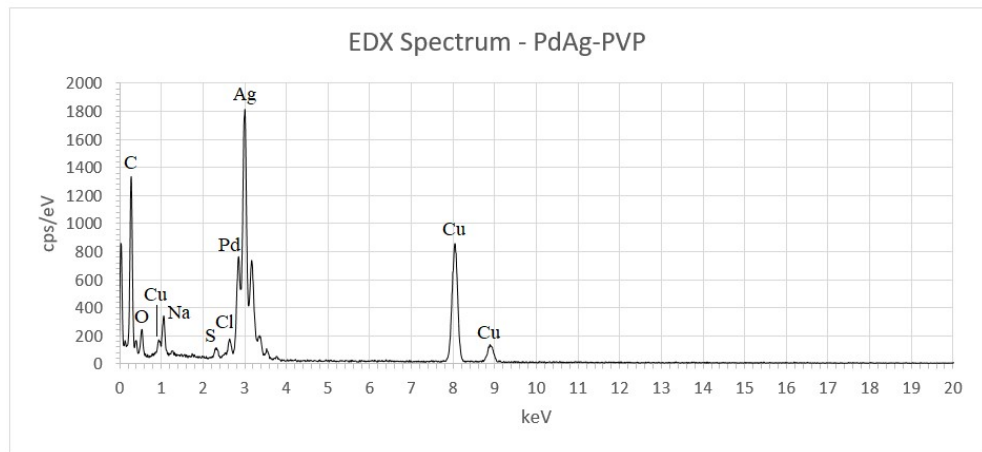
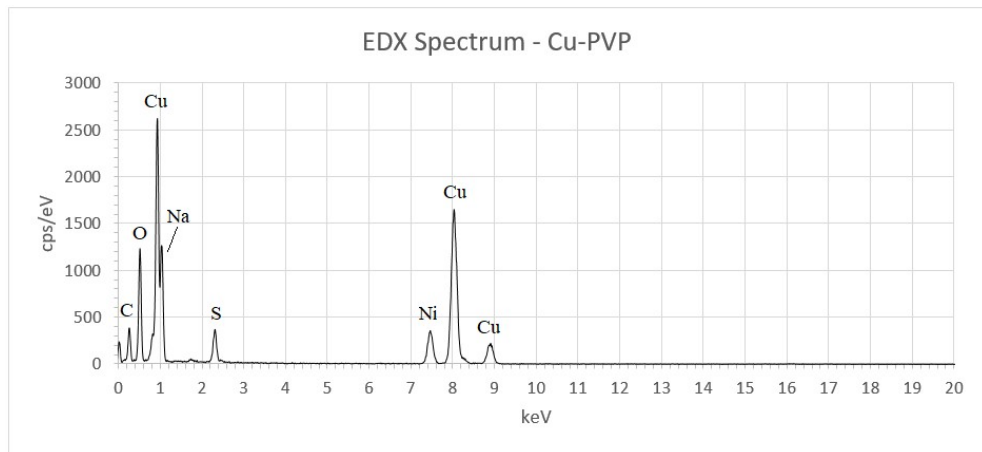
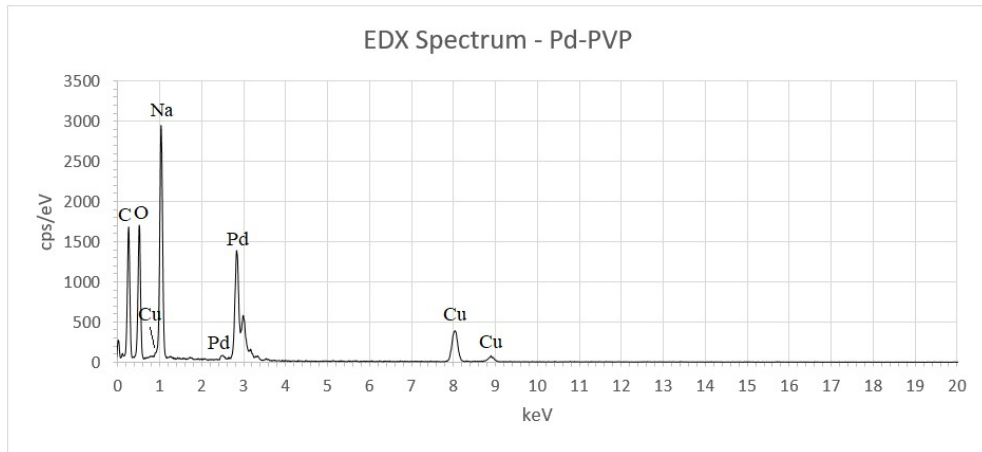


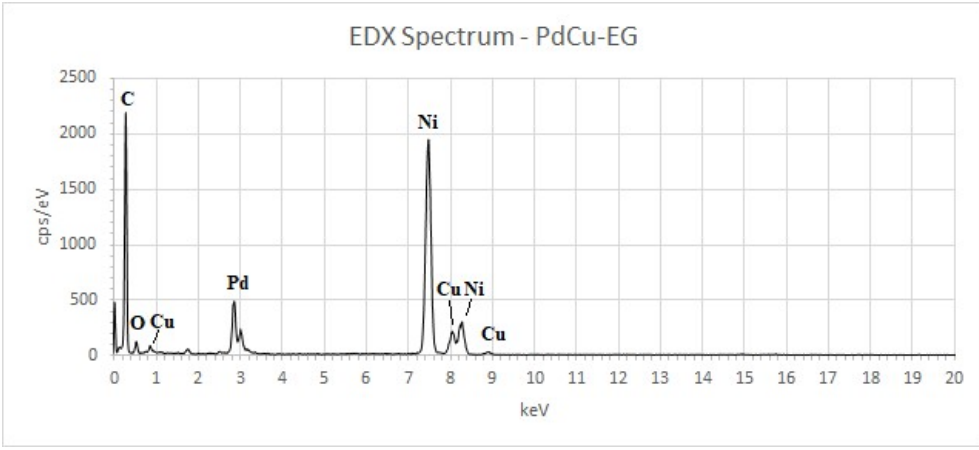
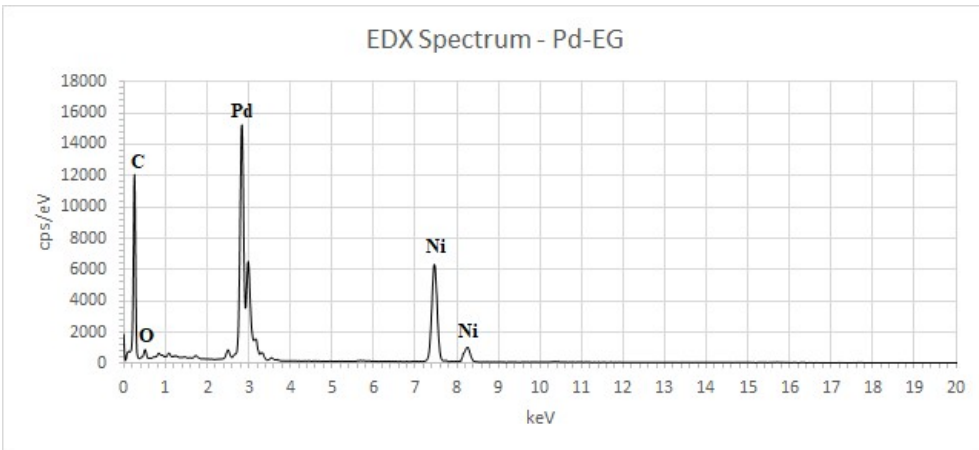
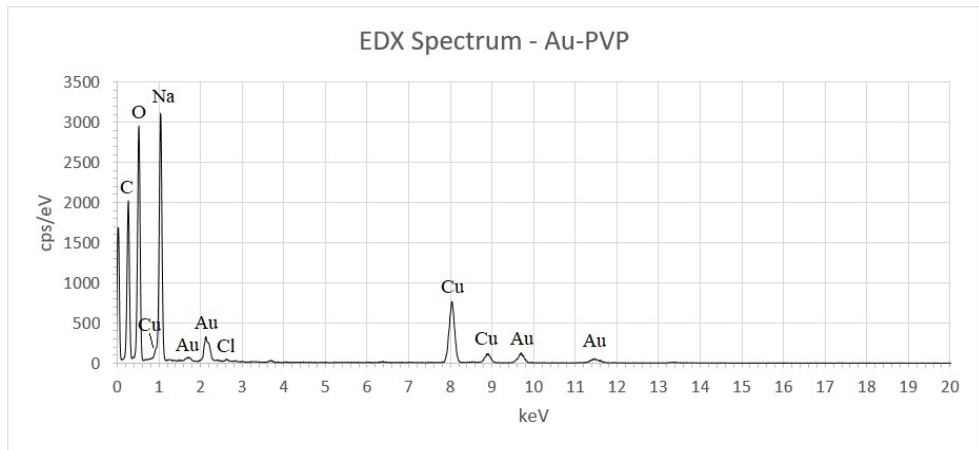
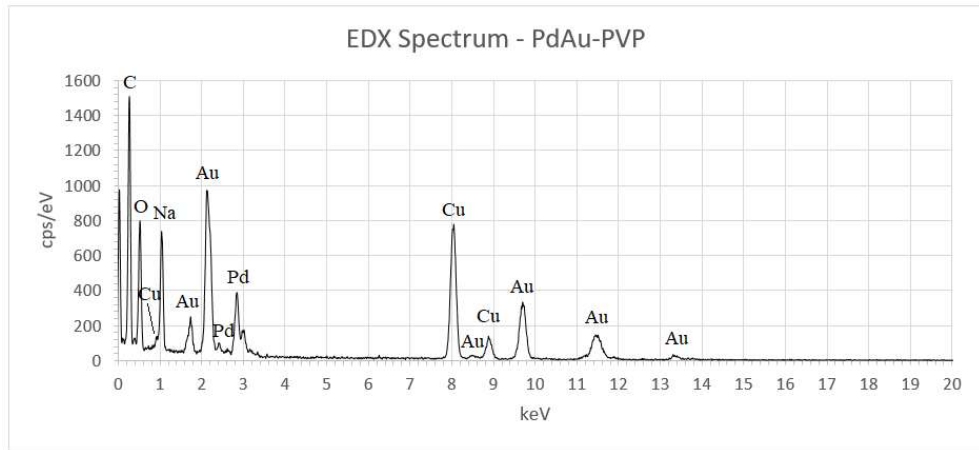


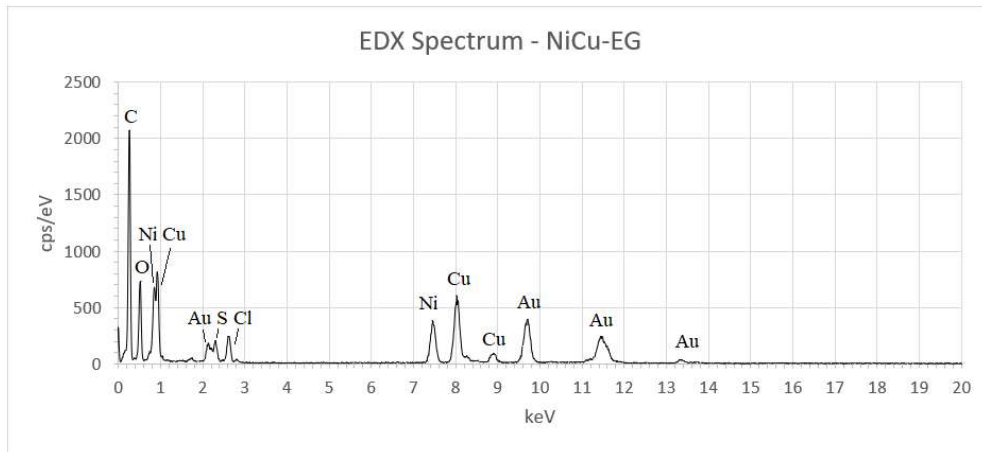
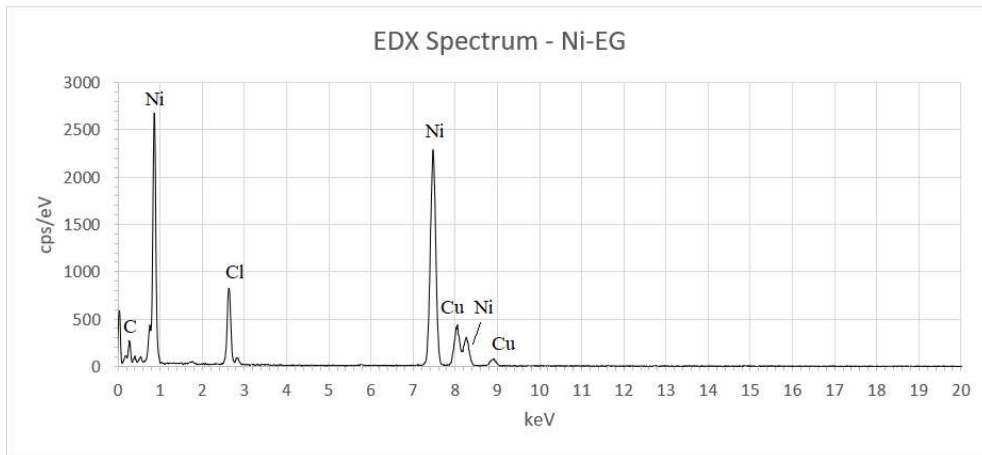
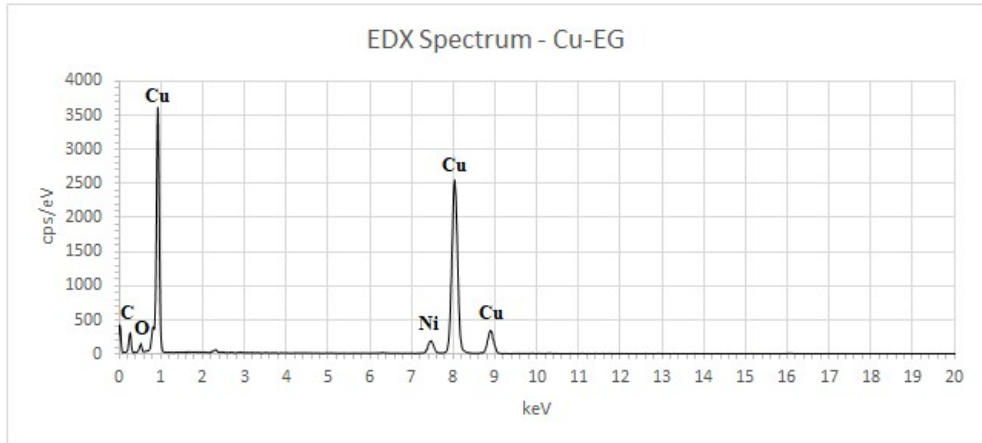
## 6.12. Energy-dispersive X-ray Spectroscopy Data

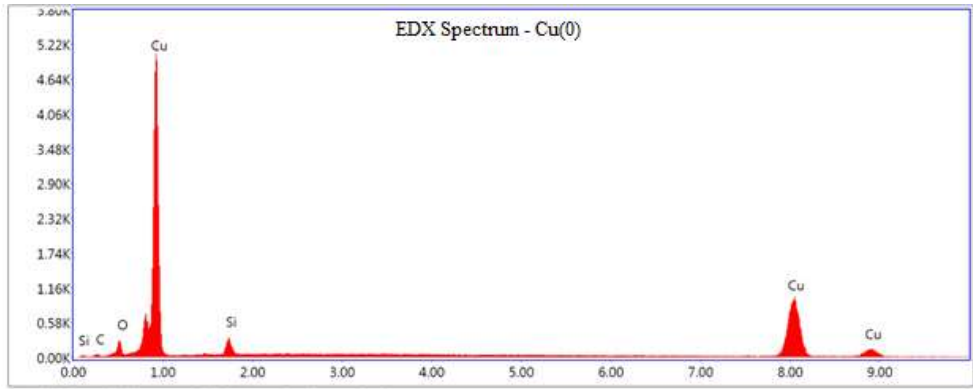
The presence of nickel, copper or silicon peaks in samples that do not contain these elements is due to the choice of media used to mount the samples for analysis.



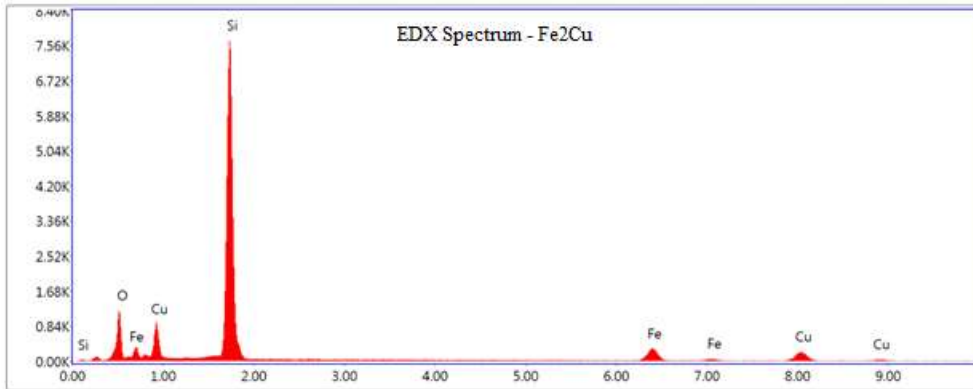




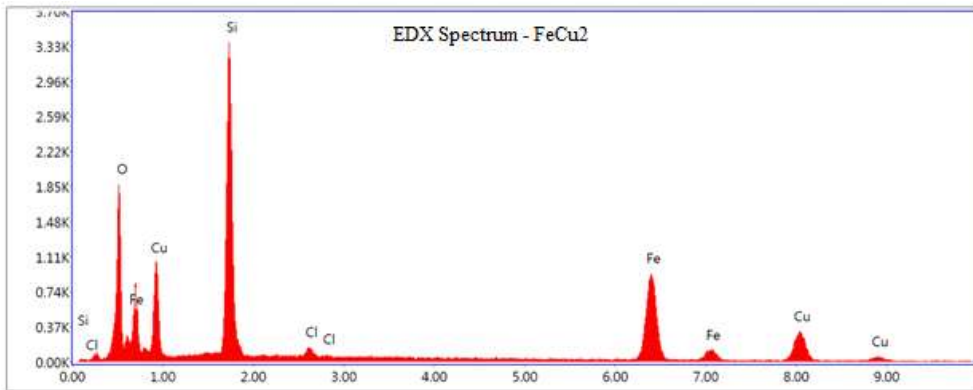




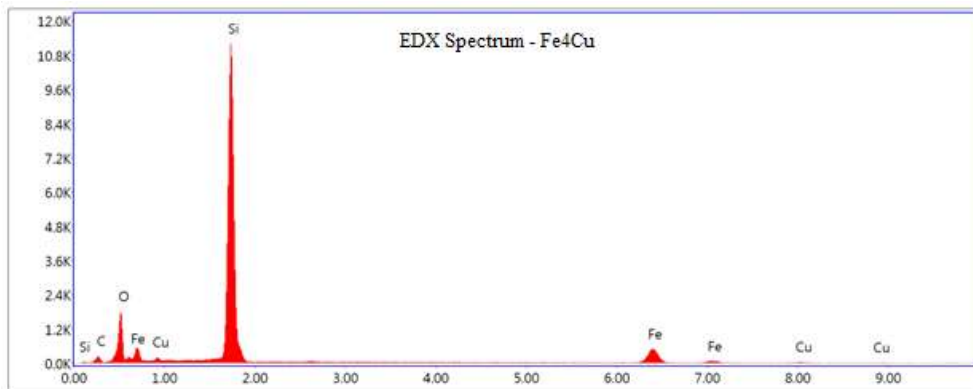
Lsec: 27.5 732 Cnts 0.820 keV Det: Octane Pro Det



Lsec: 26.9 163 Cnts 0.820 keV Det: Octane Pro Det



Lsec: 27.1 70 Cnts 1.990 keV Det: Octane Pro Det



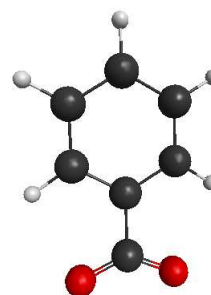
Lsec: 26.2 46 Cnts 2.200 keV Det: Octane Pro Det

### 6.13. Computational Chemistry Data

What follows is the cartesian coordinates for all optimised geometries calculated in the work presented. The software used to perform these geometry optimisations was the Windows 64-bit distribution of GAMESS-US Version 2018-R1-pgi-mk1<sup>182</sup>, using a Restricted Hartree-Fock (RHF) method and a 3.21g basis set. This level of theory was chosen due to computational time considerations as the calculations were performed on an Intel Core i5-2400 processor, clocked to 3.10 GHz, with 8.00 GB of available RAM. All geometries were calculated in their ground state in the gas phase. Initial coordinate guesses for the geometry optimisation calculations were generated using Avogadro Version 1.1.1.<sup>183</sup> Subsequent processing of data and extraction of cartesian coordinates was performed with the aid of wxMacMolPlt Version 7.7<sup>184</sup>. For compounds lacking a plane of symmetry through the aryl-carboxylate carbon-carbon bond (2,4- and 2- substituted compounds), both the ‘cis’ and ‘trans’ versions of these molecules were calculated, with the reported bond length represented as the average value of both ‘isomers’.

#### Benzoate

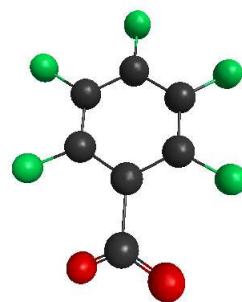
H	1.0	-3.19195986	1.97394145	-2.94601464
C	6.0	-2.72159863	2.25160789	-2.02546215
C	6.0	-2.97919154	3.45311642	-1.38787627
H	1.0	-3.67477131	4.15344000	-1.81233227
C	6.0	-2.33715129	3.75515747	-0.19609013
H	1.0	-2.53464317	4.68669367	0.30146682
C	6.0	-1.43935144	2.85054445	0.35110071
H	1.0	-0.94170195	3.08387804	1.27437592
C	6.0	-1.18813956	1.65159369	-0.29371884
H	1.0	-0.50435233	0.92226708	0.08875766
C	6.0	-1.82730412	1.34978306	-1.48104942
C	6.0	-1.54308319	0.01132696	-2.19621444
O	8.0	-2.17287350	-0.15972762	-3.26158547
O	8.0	-0.71940833	-0.72898233	-1.61789763



#### Pentafluorobenzoate

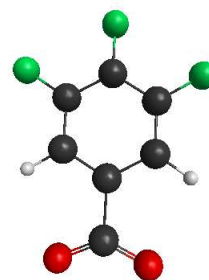
F	9.0	-4.09748173	1.83508360	0.89288354
---	-----	-------------	------------	------------

C	6.0	-3.06457686	2.14658237	0.08485484
C	6.0	-2.92939615	3.47661090	-0.23279414
F	9.0	-3.81107283	4.39449739	0.23620318
C	6.0	-1.89748681	3.88958836	-1.02847672
F	9.0	-1.76706791	5.19836426	-1.35099018
C	6.0	-0.99812979	2.97278428	-1.49651861
F	9.0	0.01658972	3.38953352	-2.29431462
C	6.0	-1.12768614	1.64688659	-1.15977144
F	9.0	-0.20899379	0.81228828	-1.68542767
C	6.0	-2.16457224	1.20999634	-0.36829451
C	6.0	-2.31750965	-0.32557657	0.01021450
O	8.0	-3.48987341	-0.68238634	0.17010225
O	8.0	-1.24056244	-0.92686307	0.08672947



### 3,4,5-Trifluorobenzoate

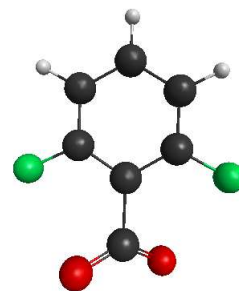
H	1.0	-2.52692175	1.24302685	0.11593559
C	6.0	-2.45524526	1.72495091	-0.83436710
C	6.0	-2.43400049	3.08752060	-0.96654510
F	9.0	-2.50425053	3.90091467	0.12333130
C	6.0	-2.34105468	3.67389083	-2.20540738
F	9.0	-2.32088399	5.02918530	-2.32480168
C	6.0	-2.26872301	2.87747598	-3.32244158
F	9.0	-2.17732882	3.48534846	-4.53755999
C	6.0	-2.28824043	1.51277339	-3.21434212
H	1.0	-2.23343706	0.87020111	-4.06553030
C	6.0	-2.38194156	0.93668848	-1.96425080
C	6.0	-2.40521240	-0.60506952	-1.82853913
O	8.0	-2.49221444	-1.01585472	-0.65555781
O	8.0	-2.33382559	-1.21673250	-2.91157413



### 2,6-Difluorobenzoate

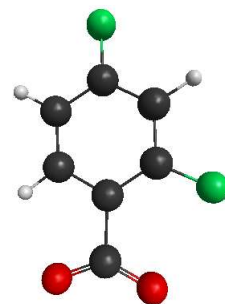
F	9.0	-4.03554344	1.93028808	0.39691019
C	6.0	-2.90572524	2.41442657	-0.17394055
C	6.0	-2.85788178	3.78146958	-0.35090601

H	1.0	-3.68396592	4.37452936	-0.01837497
C	6.0	-1.75226724	4.34944439	-0.94925439
H	1.0	-1.69819820	5.41102791	-1.08771169
C	6.0	-0.71691543	3.53959560	-1.36802983
H	1.0	0.16002819	3.94223642	-1.83011472
C	6.0	-0.80858815	2.17506385	-1.18902779
F	9.0	0.25946742	1.45032656	-1.60227358
C	6.0	-1.89400041	1.57344186	-0.58751070
C	6.0	-1.97362697	0.01662900	-0.38457209
O	8.0	-2.58647728	-0.33451444	0.63519037
O	8.0	-1.41263616	-0.64339465	-1.27250433



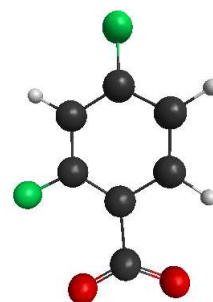
#### 2,4-Difluorobenzoate (*cis*)

H	1.0	-1.52357984	1.39282787	1.09631169
C	6.0	-1.23981917	1.90671515	0.20285711
C	6.0	-1.72796261	3.15574670	-0.12608524
H	1.0	-2.42549586	3.67467165	0.49774799
C	6.0	-1.29389155	3.73368979	-1.29478920
F	9.0	-1.75680268	4.96875048	-1.65127826
C	6.0	-0.40086809	3.09848595	-2.11624527
H	1.0	-0.06684043	3.56022072	-3.01950598
C	6.0	0.06546587	1.84644651	-1.76316047
F	9.0	0.94830203	1.28717959	-2.62353826
C	6.0	-0.34422117	1.22618914	-0.60481477
C	6.0	0.10479784	-0.18668309	-0.12766120
O	8.0	0.83667177	-0.82361674	-0.89831603
O	8.0	-0.35709617	-0.49369362	0.99428779



#### 2,4-Difluorobenzoate (*trans*)

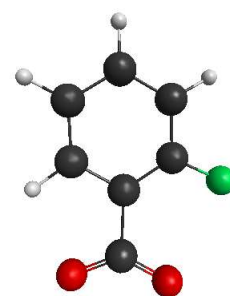
F	9.0	-3.27419782	1.48466182	1.18274271
C	6.0	-2.35335875	1.85533333	0.26234955
C	6.0	-2.08347607	3.20918059	0.19919315
H	1.0	-2.58557272	3.88737893	0.85386819



C	6.0	-1.16631353	3.66466498	-0.71030587
F	9.0	-0.89700460	5.00310040	-0.76365328
C	6.0	-0.51859051	2.80580997	-1.56535971
H	1.0	0.19286558	3.18863034	-2.26697135
C	6.0	-0.81515813	1.45969296	-1.48403776
H	1.0	-0.36071271	0.72898722	-2.11840224
C	6.0	-1.72601318	0.95678520	-0.57030725
C	6.0	-1.94192779	-0.58555406	-0.56395185
O	8.0	-2.67717028	-1.03695858	0.32536545
O	8.0	-1.31595969	-1.17081332	-1.47606981

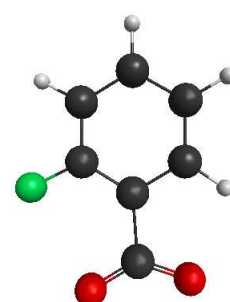
### 2-Fluorobenzoate (*cis*)

H	1.0	-3.37230396	1.48477936	0.03033905
C	6.0	-2.52895379	1.93288255	-0.45076048
C	6.0	-2.51364636	3.25164127	-0.86132640
H	1.0	-3.36585760	3.88265800	-0.69578999
C	6.0	-1.38543868	3.75332355	-1.49042428
H	1.0	-1.35032701	4.77518511	-1.81684625
C	6.0	-0.29962206	2.92673993	-1.69841206
H	1.0	0.58346134	3.28041673	-2.19045067
C	6.0	-0.33549488	1.61393809	-1.26871336
F	9.0	0.77617151	0.87692493	-1.52384126
C	6.0	-1.44192636	1.09397411	-0.63569766
C	6.0	-1.56843638	-0.36059120	-0.09200522
O	8.0	-2.71589088	-0.63109070	0.32909563
O	8.0	-0.54228491	-1.05563176	-0.12481710



### 2-Fluorobenzoate (*trans*)

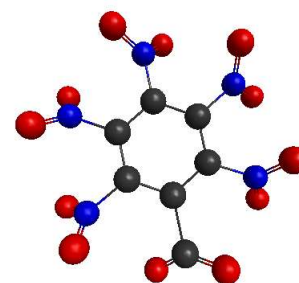
F	9.0	-2.64292026	1.90905190	0.69624650
C	6.0	-1.56676853	2.26067924	-0.05362698
C	6.0	-1.51216936	3.58512545	-0.44413874
H	1.0	-2.30030680	4.24212885	-0.13717066
C	6.0	-0.45874488	4.03768873	-1.21281719
H	1.0	-0.41609904	5.06857920	-1.50848460



C	6.0	0.53494078	3.15153694	-1.59703517
H	1.0	1.35859776	3.48954177	-2.19635010
C	6.0	0.45307940	1.83076751	-1.20133996
H	1.0	1.18277311	1.09750259	-1.47209859
C	6.0	-0.58995652	1.36192155	-0.41907221
C	6.0	-0.55164546	-0.14254978	-0.01507452
O	8.0	0.38691729	-0.77305198	-0.55253649
O	8.0	-1.42369747	-0.52625185	0.77823853

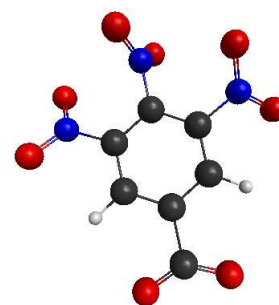
### Pentanitrobenzoate

N	7.0	-4.30031872	1.14960611	-0.21543753
C	6.0	-3.19046736	2.08158374	-0.36400476
C	6.0	-3.47853899	3.41747475	-0.49009809
N	7.0	-4.85489178	3.88036728	-0.49375990
C	6.0	-2.45966721	4.32828426	-0.63698345
N	7.0	-2.75522637	5.73977804	-0.76364505
C	6.0	-1.15784693	3.88790321	-0.66246879
N	7.0	-0.08065069	4.85370779	-0.78719765
C	6.0	-0.88562083	2.54765749	-0.54797983
N	7.0	0.50804329	2.12404180	-0.57467759
C	6.0	-1.89368296	1.62519538	-0.39395183
C	6.0	-1.55636382	0.01524264	-0.24883519
O	8.0	-2.37592220	-0.66041142	-0.85402787
O	8.0	-0.55778319	-0.16324174	0.43337405
O	8.0	-2.21271110	6.33328438	-1.70355856
O	8.0	-3.52236557	6.21906805	0.08000012
O	8.0	0.73245615	4.65381289	-1.69378352
O	8.0	-0.08307315	5.78135681	0.03200369
O	8.0	-5.19267559	4.57754612	-1.45891547
O	8.0	-5.55325365	3.53132153	0.46200505
O	8.0	1.23452413	2.63306928	0.29728889
O	8.0	0.84026307	1.36982155	-1.48133731
O	8.0	-5.13754702	1.17011034	-1.13513446
O	8.0	-4.33723974	0.49256021	0.81805503



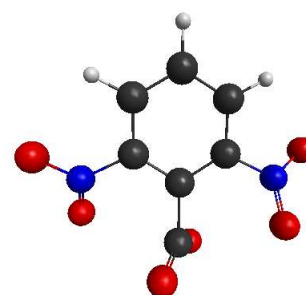
### 3,4,5-Trinitrobenzoate

C	6.0	-3.19630527	2.05315018	-0.45485389
C	6.0	-3.47553825	3.39590144	-0.59365696
N	7.0	-4.86138058	3.77728057	-0.75625396
C	6.0	-2.46049333	4.33234501	-0.63730687
N	7.0	-2.75736976	5.75103188	-0.76513034
C	6.0	-1.15580237	3.88486481	-0.55641037
N	7.0	-0.04337420	4.80837059	-0.51110429
C	6.0	-0.87211806	2.53984523	-0.45346215
C	6.0	-1.89335954	1.62360370	-0.39359102
C	6.0	-1.57638621	0.11034813	-0.25753874
O	8.0	-2.58932257	-0.60764658	-0.22498874
O	8.0	-0.36084735	-0.13881460	-0.20339356
O	8.0	-2.40553999	6.29312849	-1.81775820
O	8.0	-3.33324218	6.28050613	0.19066620
O	8.0	1.06141400	4.37937307	-0.88164055
O	8.0	-0.25892785	5.95005989	-0.06941052
O	8.0	-5.10274220	4.81725168	-1.39291203
O	8.0	-5.71650314	3.01344228	-0.27960733
H	1.0	0.13281381	2.18357921	-0.40038031
H	1.0	-3.97376466	1.32288909	-0.41027641



### 2,6-Dinitrobenzoate

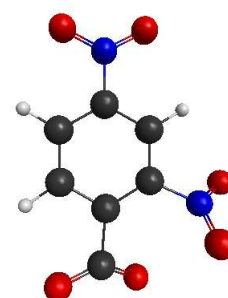
N	7.0	-4.11847258	1.18130004	0.00210044
C	6.0	-2.99448276	2.08307195	-0.18653761
C	6.0	-3.29313827	3.42564702	-0.07572009
H	1.0	-4.28722477	3.70487261	0.19295473
C	6.0	-2.31845546	4.36857367	-0.32045212
H	1.0	-2.54160118	5.41299248	-0.25317755
C	6.0	-1.05109870	3.94206095	-0.65298462
H	1.0	-0.26392019	4.63235617	-0.85817283
C	6.0	-0.77410638	2.59160161	-0.71638149
N	7.0	0.61458814	2.25618649	-0.98331749
C	6.0	-1.72948706	1.61205244	-0.49884608



C	6.0	-1.38955796	0.01190985	-0.60163265
O	8.0	-1.54605126	-0.55873096	0.47335756
O	8.0	-1.04391491	-0.31170505	-1.73348200
O	8.0	1.28780043	3.11198401	-1.62281513
O	8.0	1.07336855	1.21218836	-0.52881122
O	8.0	-5.05824137	1.59877241	0.73492622
O	8.0	-4.13051414	0.11060645	-0.59853804

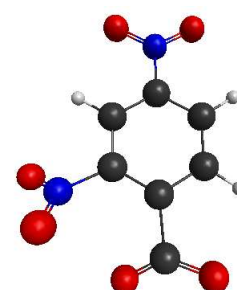
#### 2,4-Dinitrobenzoate (*cis*)

H	1.0	-3.38127303	1.21807766	-0.09804592
C	6.0	-2.65807629	1.98250759	-0.28235593
C	6.0	-2.95563293	3.31997633	-0.21014571
H	1.0	-3.93193674	3.67111731	0.04058325
C	6.0	-1.95843518	4.24096107	-0.48358947
N	7.0	-2.25334477	5.64765882	-0.43226504
C	6.0	-0.68450111	3.83608580	-0.79975754
H	1.0	0.07428205	4.55265141	-1.01176679
C	6.0	-0.40536705	2.48821115	-0.83319753
N	7.0	0.99453580	2.16545725	-1.04831672
C	6.0	-1.38352334	1.53967035	-0.61454529
C	6.0	-1.22419274	-0.01210943	-0.85715353
O	8.0	-2.15131783	-0.67268521	-0.35778150
O	8.0	-0.25911921	-0.32027733	-1.56224310
O	8.0	1.58629525	2.83711171	-1.93180621
O	8.0	-3.41999388	5.98755074	-0.14607045
O	8.0	-1.32951260	6.45069408	-0.67372221
O	8.0	1.53268385	1.36592114	-0.28910029



#### 2,4-Dinitrobenzoate (*trans*)

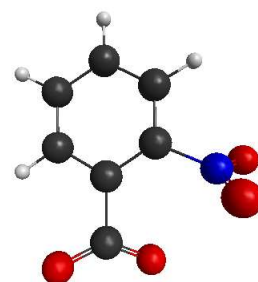
C	6.0	-2.97547126	-0.76621228	-0.01812511
C	6.0	-2.86497283	0.61750901	-0.08164736
C	6.0	-1.59921217	1.16704810	-0.06502173
C	6.0	-0.46912318	0.38053879	-0.06056876
C	6.0	-0.61266810	-0.98473781	-0.01431640



C	6.0	-1.86596298	-1.57255626	0.01926568
H	1.0	-1.93927097	-2.63644791	0.06403199
H	1.0	-3.97158599	-1.15219247	-0.00881608
H	1.0	0.49936363	0.82246679	-0.08885799
C	6.0	-4.20631742	1.41495502	-0.32106659
O	8.0	-4.05069304	2.53453708	-0.81672770
O	8.0	-5.21685266	0.74729145	-0.04126240
N	7.0	-1.34346974	2.59465265	0.01616365
N	7.0	0.56359482	-1.81198478	0.00512753
O	8.0	-0.40656671	3.02936935	-0.70159405
O	8.0	-1.95751452	3.25114799	0.85120261
O	8.0	1.67735755	-1.24991524	-0.01249446
O	8.0	0.40413523	-3.04965949	0.04080717

#### 2-Nitrobenzoate (*cis*)

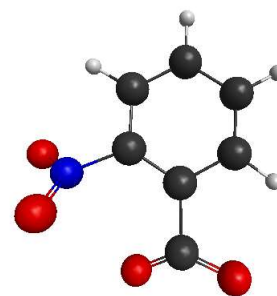
H	1.0	-3.43466187	1.23532450	-0.16550991
C	6.0	-2.67733335	1.97624528	-0.33423385
C	6.0	-2.96235681	3.32715154	-0.25712511
H	1.0	-3.96225190	3.65279937	-0.02492100
C	6.0	-1.96588469	4.26487112	-0.48631993
C	6.0	-0.68736541	3.83381653	-0.78353548
H	1.0	0.10628434	4.53449154	-0.96530163
C	6.0	-0.42994830	2.47486472	-0.84009081
N	7.0	0.97601146	2.12729669	-1.06929111
C	6.0	-1.40100658	1.50956595	-0.63727099
C	6.0	-1.17549574	-0.01606295	-0.84841800
O	8.0	-2.00473356	-0.72942197	-0.29304960
O	8.0	-0.22868294	-0.28081968	-1.57918119
O	8.0	1.47691846	2.51992536	-2.08361530
O	8.0	1.56067514	1.58390152	-0.18837756
H	1.0	-2.17879868	5.31832075	-0.43321839



#### 2-Nitrobenzoate (*trans*)

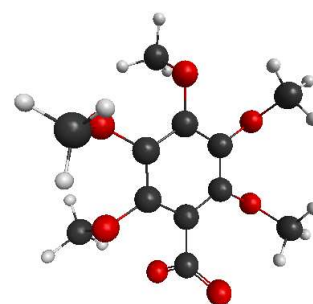
C	6.0	-2.98478961	-0.75958610	-0.03305342
---	-----	-------------	-------------	-------------

C	6.0	-2.87972856	0.62251812	-0.08883740
C	6.0	-1.61595047	1.16713727	-0.08403105
C	6.0	-0.48068762	0.37505817	-0.09112488
C	6.0	-0.60243529	-0.99628091	-0.04828043
C	6.0	-1.86760271	-1.56591833	-0.00619761
H	1.0	-1.97293758	-2.63307428	0.03548004
H	1.0	-3.98199272	-1.14485681	-0.02296245
H	1.0	0.47680280	0.84822762	-0.12676157
C	6.0	-4.20824337	1.42621028	-0.29720342
O	8.0	-4.05765009	2.57691836	-0.72804236
O	8.0	-5.23200274	0.75560057	-0.06082026
N	7.0	-1.35484684	2.59660029	0.00039620
O	8.0	-0.47615013	3.04781628	-0.77871692
O	8.0	-1.89074469	3.24094200	0.89868945
H	1.0	0.27611941	-1.61090291	-0.04510391



#### Pentamethoxybenzoate

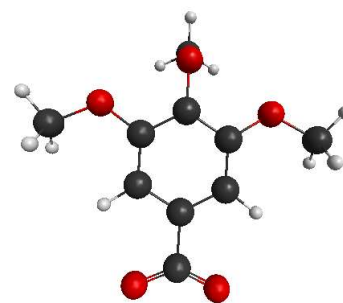
C	6.0	-3.11058879	2.53709507	-0.35386837
C	6.0	-3.14366555	3.90293503	-0.14381514
O	8.0	-4.26094246	4.52433491	0.40158406
C	6.0	-2.06488490	4.68124008	-0.49913079
O	8.0	-2.06587958	6.04968500	-0.25461951
C	6.0	-0.96496338	4.10234499	-1.09844232
O	8.0	0.09692725	4.89551449	-1.50833714
C	6.0	-0.93156999	2.73118567	-1.30822790
C	6.0	-2.00757051	1.93746674	-0.93576765
C	6.0	-1.99731565	0.40240374	-1.17715645
O	8.0	-2.93621087	-0.03665626	-1.87138450
O	8.0	-1.05836511	-0.22596496	-0.64684671
O	8.0	-4.20228291	1.80992091	0.09755968
C	6.0	-2.92896438	6.82326078	-1.12752485
O	8.0	0.17352223	2.21099687	-1.95360327
C	6.0	0.88858300	5.49321795	-0.45377845
C	6.0	-4.50343847	4.24345207	1.80502474



H	1.0	1.67849147	6.03727818	-0.94992709
H	1.0	1.32064295	4.73230982	0.18417150
H	1.0	0.28228152	6.16280270	0.13415022
H	1.0	-2.61965680	6.71242857	-2.15895057
H	1.0	-2.82096910	7.85329819	-0.82044971
H	1.0	-3.95105815	6.50098515	-1.00698340
H	1.0	-5.40494299	4.77911234	2.06490803
H	1.0	-4.63740873	3.18408918	1.94258702
H	1.0	-3.67917299	4.60030270	2.41034818
C	6.0	-5.20845079	1.48995590	-0.91669267
C	6.0	1.17430568	1.55805337	-1.11330891
H	1.0	0.69759852	0.73506856	-0.61077237
H	1.0	1.60311663	2.27015615	-0.41549155
H	1.0	1.93934298	1.21723545	-1.79555535
H	1.0	-4.72228479	0.91171372	-1.68161643
H	1.0	-5.64662600	2.40430856	-1.29851782
H	1.0	-5.96018982	0.90806901	-0.40316457

### 3,4,5-Trimethoxybenzoate

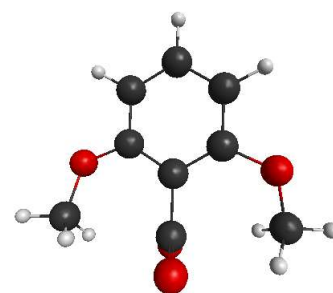
C	6.0	-3.82147264	1.95560777	-0.81206203
C	6.0	-3.64227700	3.25103617	-0.37152597
O	8.0	-4.57202864	3.94484615	0.37839285
C	6.0	-2.49055386	3.94824624	-0.70151490
O	8.0	-2.31011558	5.25207806	-0.25659889
C	6.0	-1.53644562	3.34657621	-1.50790656
O	8.0	-0.43727174	4.12189722	-1.81925809
C	6.0	-1.71280789	2.04938006	-1.94431067
C	6.0	-2.85481882	1.36301112	-1.59437108
C	6.0	-3.06639600	-0.07751864	-2.10831952
O	8.0	-4.13966560	-0.60804236	-1.75208616
O	8.0	-2.13925219	-0.52195299	-2.81763315
H	1.0	-4.69325590	1.37480688	-0.60588974
C	6.0	-2.83234024	6.25567913	-1.15735400
H	1.0	-1.01318336	1.53203464	-2.56259441



C	6.0	0.66469872	3.51602077	-2.50423384
C	6.0	-5.70896721	3.24102950	0.89122385
H	1.0	0.38581210	3.19996119	-3.50169373
H	1.0	1.04798758	2.66466737	-1.95597672
H	1.0	1.42397285	4.28166819	-2.56826711
H	1.0	-2.62798619	7.21153021	-0.69463724
H	1.0	-3.89921975	6.12726450	-1.27987051
H	1.0	-2.32993674	6.19601107	-2.11331797
H	1.0	-6.23552227	3.95160198	1.51143301
H	1.0	-5.41147995	2.38627744	1.48536766
H	1.0	-6.35865402	2.90862226	0.09106518

### 2,6-Dimethoxybenzoate

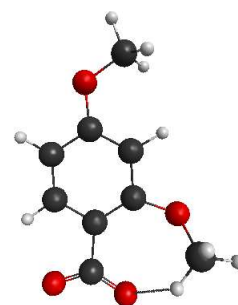
O	8.0	-4.19520092	2.35720682	-0.19011323
C	6.0	-2.95412421	2.81048369	-0.57801706
C	6.0	-2.87245035	4.19521189	-0.64440620
H	1.0	-3.74919701	4.75939083	-0.40514261
C	6.0	-1.68850780	4.79969978	-1.00364661
H	1.0	-1.62595809	5.86995173	-1.05681181
C	6.0	-0.58514994	4.02887154	-1.29458416
H	1.0	0.34987506	4.46074724	-1.58349228
C	6.0	-0.66561610	2.64439154	-1.22324944
O	8.0	0.51160711	2.01342654	-1.55770147
C	6.0	-1.85185027	2.01069140	-0.86487514
C	6.0	-1.94180810	0.46086755	-0.78733921
O	8.0	-2.54635692	-0.09010135	-1.73190522
O	8.0	-1.39883709	-0.05904416	0.21054466
C	6.0	-4.43988800	1.01428747	0.29226163
C	6.0	0.59525329	0.61027753	-1.90472090
H	1.0	-4.48338032	0.32754502	-0.53406966
H	1.0	-5.38482380	1.07104790	0.81412739
H	1.0	-3.65164566	0.69813973	0.95925361
H	1.0	0.56626081	0.00819017	-1.01439857
H	1.0	1.53582549	0.50544947	-2.42711329



H	1.0	-0.23012705	0.32357749	-2.53920054
---	-----	-------------	------------	-------------

**2,4-Dimethoxybenzoate (*cis*)**

C	6.0	-2.78767729	1.91665459	-0.39854208
C	6.0	-3.24736118	3.21048045	-0.39203373
H	1.0	-4.21165848	3.47148228	-0.00768804
C	6.0	-2.43834519	4.21030474	-0.90967798
O	8.0	-2.94670224	5.49778938	-0.88578165
C	6.0	-1.19774568	3.88596749	-1.40217757
H	1.0	-0.53751308	4.62025976	-1.80899620
C	6.0	-0.73831707	2.56696677	-1.40351176
O	8.0	0.51923496	2.43572378	-1.95806599
C	6.0	-1.53983605	1.55343699	-0.89819443
C	6.0	-1.23975992	0.02991509	-0.85871708
O	8.0	-0.13557549	-0.36261147	-1.30089891
O	8.0	-2.16184402	-0.65795785	-0.37377888
C	6.0	-2.18047285	6.57334900	-1.43181062
H	1.0	-3.37682605	1.10657108	-0.02559425
C	6.0	1.58521962	1.85312021	-1.15533316
H	1.0	1.30482793	0.84568828	-0.90884936
H	1.0	2.46099091	1.87745571	-1.78888464
H	1.0	1.76187897	2.46176529	-0.27266806
H	1.0	-1.96718132	6.41871643	-2.48308158
H	1.0	-1.24408102	6.70669317	-0.90247595
H	1.0	-2.78780580	7.45828819	-1.31447816



**2,4-Dimethoxybenzoate (*trans*)**

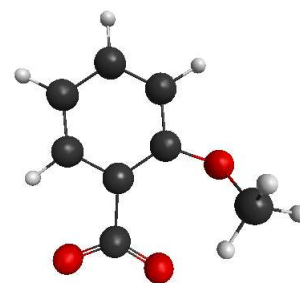
C	6.0	-2.94386578	2.68028545	0.28517652
C	6.0	-2.74176240	4.04694796	0.16097835
H	1.0	-3.45257211	4.71703339	0.59317237
C	6.0	-1.64177024	4.55846024	-0.49436891
O	8.0	-1.54601812	5.93933916	-0.55078930
C	6.0	-0.72178471	3.69271445	-1.05332029
H	1.0	0.14341673	4.05138254	-1.57131922



C	6.0	-0.93158919	2.33281016	-0.92522991
H	1.0	-0.24336475	1.61937821	-1.32565713
C	6.0	-2.02093744	1.78981888	-0.26839370
C	6.0	-2.03684640	0.23666066	-0.20358269
O	8.0	-1.05359173	-0.30495647	-0.75088841
O	8.0	-3.00312567	-0.31674245	0.36818898
O	8.0	-4.07977200	2.34888792	0.99481726
C	6.0	-5.10725975	1.55325532	0.33799213
C	6.0	-0.43313617	6.54441738	-1.21093917
H	1.0	-4.68014956	0.60177946	0.08102128
H	1.0	-5.49208975	2.08340573	-0.52853346
H	1.0	-5.89377308	1.44690466	1.07173216
H	1.0	-0.57857507	7.61028337	-1.11850893
H	1.0	0.50678682	6.26824284	-0.74700189
H	1.0	-0.39533973	6.27661133	-2.26072598

### 2-Methoxybenzoate (*cis*)

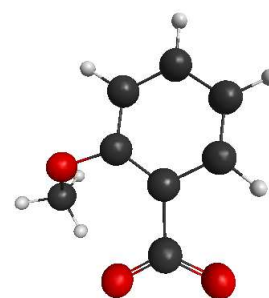
C	6.0	-2.63029575	2.25628948	-0.44471166
C	6.0	-3.09792376	3.55054688	-0.36207131
H	1.0	-3.99998999	3.76975346	0.17700955
C	6.0	-2.39078426	4.56167555	-0.99174374
C	6.0	-1.23479378	4.25256348	-1.67425525
H	1.0	-0.66669297	5.01101494	-2.17363071
C	6.0	-0.76284409	2.94494390	-1.75493431
O	8.0	0.39452901	2.81228828	-2.50170302
C	6.0	-1.46988130	1.92067432	-1.13093328
C	6.0	-1.13269424	0.39907405	-1.13814199
O	8.0	-1.97055733	-0.30968839	-0.54361379
O	8.0	-0.08347897	0.03609814	-1.71521676
H	1.0	-3.14257407	1.43457329	0.00803565
C	6.0	1.58728683	2.29872274	-1.84619355
H	1.0	1.38425577	1.29605758	-1.51932681
H	1.0	2.35805798	2.31553483	-2.60438824
H	1.0	1.87506425	2.95147467	-1.02635694



H	1.0	-2.73344350	5.57862282	-0.94839418
---	-----	-------------	------------	-------------

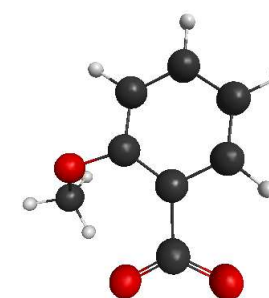
**2-Methoxybenzoate (*trans*)**

C	6.0	-2.95440793	2.68117929	0.26205316
C	6.0	-2.78498936	4.05273390	0.09148864
H	1.0	-3.52183962	4.69631720	0.52764678
C	6.0	-1.70916820	4.56658077	-0.59872085
C	6.0	-0.77672344	3.69978428	-1.14471042
H	1.0	0.06793915	4.07899332	-1.68805349
C	6.0	-0.94502866	2.34227324	-0.97298175
H	1.0	-0.24966867	1.62778866	-1.35846484
C	6.0	-2.01947570	1.80197120	-0.27748367
C	6.0	-2.00872397	0.24779665	-0.16359846
O	8.0	-1.01641297	-0.29326376	-0.69295526
O	8.0	-2.96738100	-0.30147955	0.42355153
O	8.0	-4.07273483	2.34231782	1.00322592
C	6.0	-5.10330582	1.53369641	0.37059373
H	1.0	-4.67458248	0.58162743	0.11961002
H	1.0	-5.50320721	2.04900289	-0.49862042
H	1.0	-5.88102436	1.43056524	1.11471784
H	1.0	-1.60163510	5.62911558	-0.71235847
C	6.0	1.58728683	2.29872274	-1.84619355
H	1.0	1.38425577	1.29605758	-1.51932681
H	1.0	2.35805798	2.31553483	-2.60438824
H	1.0	1.87506425	2.95147467	-1.02635694
H	1.0	-2.73344350	5.57862282	-0.94839418



**2-Methoxybenzoate (*trans*)**

C	6.0	-2.95440793	2.68117929	0.26205316
C	6.0	-2.78498936	4.05273390	0.09148864
H	1.0	-3.52183962	4.69631720	0.52764678
C	6.0	-1.70916820	4.56658077	-0.59872085
C	6.0	-0.77672344	3.69978428	-1.14471042
H	1.0	0.06793915	4.07899332	-1.68805349



C	6.0	-0.94502866	2.34227324	-0.97298175
H	1.0	-0.24966867	1.62778866	-1.35846484
C	6.0	-2.01947570	1.80197120	-0.27748367
C	6.0	-2.00872397	0.24779665	-0.16359846
O	8.0	-1.01641297	-0.29326376	-0.69295526
O	8.0	-2.96738100	-0.30147955	0.42355153
O	8.0	-4.07273483	2.34231782	1.00322592
C	6.0	-5.10330582	1.53369641	0.37059373
H	1.0	-4.67458248	0.58162743	0.11961002
H	1.0	-5.50320721	2.04900289	-0.49862042
H	1.0	-5.88102436	1.43056524	1.11471784
H	1.0	-1.60163510	5.62911558	-0.71235847

## References

1. F. Ullmann and J. Bielecki, *Chem. Ber.*, 1901, **34**, 2174–2185.
2. F. Ullmann, *Chem. Ber.*, 1903, **36**, 2389.
3. W. R. H. Hurtley, *J. Chem. Soc.*, 1929, 1870–1873.
4. R. Q. Brewster and T. Groening, *Org. Synth.*, 1934, **14**, 66.
5. R. G. R. Bacon, *Q. Rev. Chem. Soc.*, 1965, **19**, 19–125.
6. P. Kovacic and M. Jones, *Chem. Rev.*, 1987, **87**, 357–379.
7. M. Gomberg and W. E. Bachmann, *J. Am. Chem. Soc.*, 1924, **46**, 2339–2343.
8. L. J. Goossen, N. Rodríguez, B. Melzer, C. Linder, G. Deng and L. M. Levy, *J. Am. Chem. Soc.*, 2007, **129**, 4824–4833.
9. W. I. Dzik, P. P. Lange and L. J. Goossen, *Chem. Sci.*, 2012, **3**, 2671–2678.
10. R. F. Heck and J. P. Nolley Jr, *J. Org. Chem.*, 1972, **37**, 2320–2322.
11. N. Miyaura and A. Suzuki, *Chem. Rev.*, 1995, **95**, 2457–2483.
12. A. O. King, N. Okukado and E. Negishi, *J. Chem. Soc., Chem. Commun.*, 1977, 683–684.
13. L. J. Goossen, G. Deng and L. M. Levy, *Science*, 2006, **313**, 662–664.
14. D. G. Hall, *Boronic Acids: Preparation and Applications in Organic Synthesis and Medicine*, Wiley-VCH Verlag GmbH & Co., 2005.
15. K. C. Lam, T. B. Marder and Z. Lin, *Organometallics*, 2010, **29**, 1849–1857.
16. M. Nilsson, E. Kulonen, S. Sunner, V. Frank, J. Brunvoll, E. Bunnenberg, C. Djerassi and R. Records, *Acta Chem. Scand.*, 1966, **20**, 423–426.
17. N. Rodríguez and L. J. Goossen, *Chem. Soc. Rev.*, 2011, **40**, 5030–5048.
18. J. Lindley, *Tetrahedron*, 1984, **40**, 1433–1456.
19. C. Björklund, M. Nilsson, C. Pedersen and T. Norin, *Acta Chem. Scand.*, 1968, **22**, 2585–2588.
20. A. Cairncross, J. R. Roland, R. M. Henderson and W. A. Sheppard, *J. Am. Chem. Soc.*, 1970, **92**, 3187–3189.
21. T. Cohen, R. W. Berninger and J. T. Wood, *J. Org. Chem.*, 1978, **43**, 837–848.
22. T. Cohen and R. A. Schambach, *J. Am. Chem. Soc.*, 1970, **92**, 3189–3190.
23. C. Maaliki, E. Thiery and J. Thibonnet, *Eur. J. Org. Chem.*, 2017, **2017**, 209–228.
24. L. J. Goossen, N. Rodríguez and C. Linder, *J. Am. Chem. Soc.*, 2008, **130**, 15248–15249.
25. L. J. Goossen, N. Rodríguez, P. P. Lange and C. Linder, *Angew. Chem., Int. Ed.*, 2010, **49**, 1111–1114.
26. S. Dupuy, L. Crawford, M. Bühl and S. P. Nolan, *Chem. Eur. J.*, 2015, **21**, 3399–3408.
27. L. J. Goossen, W. R. Thiel, N. Rodríguez, C. Linder and B. Melzer, *Adv. Synth. Catal.*, 2007, **349**, 2241–2246.
28. J. M. Becht, C. Catala, C. Le Drian and A. Wagner, *Org. Lett.*, 2007, **9**, 1781–1783.
29. Z. Wang, Q. Ding, X. He and J. Wu, *Tetrahedron*, 2009, **65**, 4635–4638.
30. Z. Wang, Q. Ding, X. He and J. Wu, *Org. Biomol. Chem.*, 2009, **7**, 863.
31. R. Shang and Lei. Liu, *Sci. China: Chem.*, 2011, **54**, 1670–1687.
32. L. J. Goossen, P. P. Lange, N. Rodríguez and C. Linder, *Chem. Eur. J.*, 2010, **16**, 3906–3909.
33. R. Shang, Y. Fu, Y. Wang, Q. Xu, H.-Z. Yu and L. Liu, *Angew. Chem., Int. Ed.*, 2009, **48**, 9350–9354.

34. H.-Y. Xiong, Z.-Y. Yang, Z. Chen, J.-L. Zeng, J. Nie and J.-A. Ma, *Chem. Eur. J.*, 2014, **20**, 8325–8329.
35. P. Forgione, M.-C. Brochu, M. St-Onge, K. H. Thesen, M. D. Bailey and F. Bilodeau, *J. Am. Chem. Soc.*, 2006, **128**, 11350–11351.
36. R. Shang, Q. Xu, Y.-Y. Jiang, Y. Wang and L. Liu, *Org. Lett.*, 2010, **12**, 1000–1003.
37. L. Xue, W. Su and Z. Lin, *Dalton Trans.*, 2010, **39**, 9815.
38. L. J. Goossen, C. Linder, N. Rodríguez, P. P. Lange and A. Fromm, *Chem. Commun.*, 2009, 7173.
39. C. Arroniz, A. Ironmonger, G. Rassias and I. Larrosa, *Org. Lett.*, 2013, **15**, 910–913.
40. S. Dupuy and S. P. Nolan, *Chem. Eur. J.*, 2013, **19**, 14034–14038.
41. J. Cornella, C. Sanchez, D. Banawa and I. Larrosa, *Chem. Commun.*, 2009, 7176.
42. P. Lu, C. Sanchez, J. Cornella and I. Larrosa, *Org. Lett.*, 2009, **11**, 5710–5713.
43. S. Dupuy, F. Lazreg, A. M. Z. Slawin, C. S. J. Cazin and S. P. Nolan, *Chem. Commun.*, 2011, **47**, 5455.
44. G. J. P. Perry and I. Larrosa, *Eur. J. Org. Chem.*, 2017, **2017**, 3517–3527.
45. L. J. Goossen, F. Manjolinho, B. A. Khan and N. Rodríguez, *J. Org. Chem.*, 2009, **74**, 2620–2623.
46. R. Grainger, J. Cornella, D. C. Blakemore, I. Larrosa and J. M. Campanera, *Chem. Eur. J.*, 2014, **20**, 16680–16687.
47. L. Xue, W. Su and Z. Lin, *Dalton Trans.*, 2011, **40**, 11926–11936.
48. G. Schmid, *Nanoparticles - From Theory to Application*, Wiley-VCH, 2004.
49. W. R. Algar, A. J. Tavares and U. J. Krull, *Anal. Chim. Acta*, 2010, **673**, 1–25.
50. N. Lane, *J. Nanopart. Res.*, 2001, **3**, 95–103.
51. W. R. Browne and B. L. Feringa, *Nat. Nanotechnol.*, 2006, **1**, 25–35.
52. R. Ghosh, L. Pradhan, Y. P. Devi, S. S. Meena, R. Tewari, A. Kumar, S. Sharma, N. S. Gajbhiye, R. K. Vatsa, B. N. Pandey and R. S. Ningthoujam, *J. Mater. Chem.*, 2011, **21**, 13388.
53. R. Hiergeist, W. Andrä, N. Buske, R. Hergt, I. Hilger, U. Richter and W. Kaiser, *J. Magn. Magn. Mater.*, 1999, **201**, 420–422.
54. J. S. Bradley and G. Schmid, in *Nanoparticles - From Theory to Application*, ed. G. Schmid, Wiley-VCH, 2004.
55. G. Nimtz, P. Marquardt and H. Gleiter, *J. Cryst. Growth*, 1988, **86**, 66–71.
56. R. Rossetti, S. Nakahara and L. E. Brus, *J. Chem. Phys.*, 1983, **79**, 1086–1088.
57. M. G. Bawendi, A. R. Kortan, M. L. Steigerwald and L. E. Brus, *J. Chem. Phys.*, 1989, **91**, 7282–7290.
58. L. Brus, *Appl. Phys. A*, 1991, **53**, 465–474.
59. L. Brus, *J. Phys. Chem.*, 1986, **90**, 2555–2560.
60. U. Simon, in *Nanoparticles - From Theory to Application*, ed. G. Schmid, Wiley-VCH, 2004.
61. C. E. Housecroft and A. G. Sharpe, *Inorganic Chemistry - Fourth Edition*, Pearson, 2012.
62. A. K. Gupta and S. Wells, *IEEE Trans. Nanobioscience*, 2004, **3**, 66–73.
63. A. K. Gupta and M. Gupta, *Biomaterials*, 2005, **26**, 3995–4021.
64. S. Ceylan, C. Friese, C. Lammel, K. Mazac and A. Kirschning, *Angew. Chem., Int. Ed.*, 2008, **47**, 8950–8953.
65. A. H. Lu, E. L. Salabas and F. Schüth, *Angew. Chem., Int. Ed.*, 2007, **46**, 1222–1244.

66. L. Djakovitch, K. Kohler and J. G. de Vries, in *Nanoparticles and Catalysis*, ed. D. Astruc, Wiley-VCH, 2008.
67. R. Ghorbani-Vaghei, S. Hemmati and M. Hekmati, *J. Chem. Sci.*, 2016, **128**, 1157–1162.
68. M.-J. Jin and D.-H. Lee, *Angew. Chem., Int. Ed.*, **49**, 1119–1122.
69. J. Liu, X. Peng, W. Sun, Y. Zhao and C. Xia, *Org. Lett.*, 2008, **10**, 3933–3936.
70. A. Corma and H. Garcia, in *Nanoparticles and Catalysis*, ed. D. Astruc, Wiley-VCH, 2008.
71. M. Haruta and M. Daté, *Appl. Catal. A-Gen.*, 2001, **222**, 427–437.
72. M. Haruta, N. Yamada, T. Kobayashi and S. Iijima, *J. Catal.*, 1989, **115**, 301–309.
73. S. Biella, G. L. Castiglioni, C. Fumagalli, L. Prati and M. Rossi, *Catal. Today*, 2002, **72**, 43–49.
74. U. Gulati, U. C. Rajesh and D. S. Rawat, *Tetrahedron Lett.*, 2016, **57**, 4468–4472.
75. E. Rafiee, M. Joshaghani and A. Ataei, *Lett. Org. Chem.*, 2014, **11**, 707–712.
76. M. Sheykhani, M. Mohammadquli and A. Heydari, *J. Mol. Struct.*, 2012, **1027**, 156–161.
77. F. Epron, C. Especel, G. Lafaye and P. Marécot, in *Nanoparticles and Catalysis*, ed. D. Astruc, Wiley-VCH, 2008.
78. M. Brust, M. Walker, D. Bethell, D. J. Schiffrin and R. Whyman, *J. Chem. Soc., Chem. Commun.*, 1994, 801–802.
79. Z.-H. Lu, J. Li, A. Zhu, Q. Yao, W. Huang, R. Zhou, R. Zhou and X. Chen, *Int. J. Hydrog. Energy*, 2013, **38**, 5330–5337.
80. H. Hirai, Y. Nakao, N. Toshima and K. Adachi, *Chem. Lett.*, 1976, **5**, 905–910.
81. H. Hirai, Y. Nakao and N. Toshima, *J. Macromol. Sci. A*, 1978, **12**, 1117–1141.
82. N. Toshima and K. Hiraoka, *Polym. J.*, 1999, **31**, 1127–1132.
83. P. Lu, T. Teranishi, K. Asakura, M. Miyake and N. Toshima, *J. Phys. Chem. B*, 1999, **103**, 9673–9682.
84. M. T. Reetz and W. Helbig, *J. Am. Chem. Soc.*, 1994, **116**, 7401–7402.
85. M. T. Reetz, W. Helbig and S. A. Quaiser, *Chem. Mater.*, 1995, **7**, 2227–2228.
86. H. Bönemann and R. M. Richards, *Eur. J. Inorg. Chem.*, 2001, **2001**, 2455–2480.
87. J. S. Bradley, E. W. Hill, C. Klein, B. Chaudret and A. Duteil, *Chem. Mater.*, 1993, **5**, 254–256.
88. W. Yu, W. Tu and H. Liu, *Langmuir*, 1999, **15**, 6–9.
89. N. A. Dhas and A. Gedanken, *J. Mater. Chem.*, 1998, **8**, 445–450.
90. K. S. Suslick, *Ultrasound: Its Chemical, Physical and Biological Effects*, VCH Publishers, New York, 1988.
91. Y. Koltypin, A. Fernandez, T. C. Rojas, J. Campora, P. Palma, R. Prozorov and A. Gedanken, *Chem. Mater.*, 1999, **11**, 1331–1335.
92. R. A. Salkar, P. Jeevanandam, S. T. Aruna, Y. Koltypin and A. Gedanken, *J. Mater. Chem.*, 1999, **9**, 1333–1335.
93. D. Cantillo and C. O. Kappe, *ChemCatChem*, 2014, **6**, 3286–3305.
94. P. Devendar, R.-Y. Qu, W.-M. Kang, B. He and G.-Fu. Yang, *J. Agric. Food Chem.*, 2018, **66**, 8914–8934.
95. M. T. Reetz and G. Lohmer, *Chem. Commun.*, 1996, **0**, 1921–1922.
96. M. T. Reetz, G. Lohmer and R. Schwickardi, *Angew. Chem., Int. Ed.*, 1998, **37**, 481–483.
97. J. Le Bars, U. Specht, J. S. Bradley and D. G. Blackmond, *Langmuir*, 1999, **15**, 7621–7625.

98. Y. Li, X. M. Hong, D. M. Collard and M. A. El-Sayed, *Org. Lett.*, 2000, **2**, 2385–2388.
99. M. B. Thathagar, P. J. Kooyman, R. Boerleider, E. Jansen, C. J. Elsevier and G. Rothenberg, *Adv. Synth. Catal.*, 2005, **347**, 1965–1968.
100. S. Reimann, J. Stötzel, R. Frahm, W. Kleist, J.-D. Grunwaldt and A. Baiker, *J. Am. Chem. Soc.*, 2011, **133**, 3921–3930.
101. A. Kumar, R. Parella and S. A. Babu, *Synlett*, 2014, **25**, 835–842.
102. V. S. Rawat and B. Sreedhar, *Synlett*, 2014, **25**, 1132–1136.
103. R. Dey, N. Mukherjee, S. Ahammed and B. C. Ranu, *Chem. Commun.*, 2012, **48**, 7982–7984.
104. H. Yang, H. Yan, P. Sun, Y. Zhu, L. Lu, D. Liu, G. Rong and J. Mao, *Green Chem.*, 2013, **15**, 976.
105. I. Favier, D. Pla and M. Gómez, *Chem. Rev.*, 2020, **120**, 1146–1183.
106. M. T. Reetz, R. Breinbauer and K. Wanninger, *Tetrahedron Lett.*, 1996, **37**, 4499–4502.
107. D. Kundu, T. Chatterjee and B. C. Ranu, *Adv. Synth. Catal.*, 2013, **355**, 2285–2296.
108. J. F. Hartwig, *Angew. Chem.*, 1999, **110**, 2154–2177.
109. A. R. Muci and S. L. Buchwald, *Practical Palladium Catalysts for C-N and C-O Bond Formation*, Springer-Verlag, 2001.
110. S. Handa, Y. Wang, F. Gallou and B. H. Lipshutz, *Science*, 2015, **349**, 1087–1091.
111. P. M. Murray, F. Bellany, L. Benhamou, D.-K. Bučar, A. B. Tabor and T. D. Sheppard, *Org. Biomol. Chem.*, 2016, **14**, 2373–2384.
112. F. Kloss, T. Neuwirth, V. G. Haensch and C. Hertweck, *Angew. Chem. Int. Ed. Engl.*, 2018, **57**, 14476–14481.
113. I. Cepanec, *Synthesis of Biaryls*, Elsevier, 2010.
114. M. Simonetti, D. M. Cannas and I. Larrosa, in *Advances in Organometallic Chemistry*, ed. P. J. Pérez, Academic Press, 2017, vol. 67, pp. 299–399.
115. K. Durairaj, *Curr. Sci.*, 1994, **66**, 833–838.
116. S.-T. Yang, H. Huang, A. Tay, W. Qin, L. De Guzman and E. C. S. Nicolas, in *Bioprocessing for Value-Added Products from Renewable Resources*, ed. S.-T. Yang, Elsevier, Amsterdam, 2007, pp. 421–446.
117. K. C. Nicolaou, P. G. Bulger and D. Sarlah, *Angew. Chem., Int. Ed.*, 2005, **44**, 4442–4489.
118. F. Monnier, F. Turtaut, L. Duroure and M. Taillefer, *Org. Lett.*, 2008, **10**, 3203–3206.
119. National Research Council (US) Chemical Sciences Roundtable, *Replacing Critical Materials with Abundant Materials*, National Academies Press (US), 2012.
120. S. Z. Tasker, E. A. Standley and T. F. Jamison, *Nature*, 2014, **509**, 299–309.
121. J. Miller, Masters Final Report, University of Leeds, 2016.
122. L. Duran Pachon and G. Rothenberg, *Appl. Organomet. Chem.*, 2008, **22**, 288–299.
123. Y. Lin, M. Cai, Z. Fang and H. Zhao, *RSC Adv.*, 2017, **7**, 34722–34729.
124. A. A. Cant, R. Bhalla, S. L. Pimlott and A. Sutherland, *Chem. Commun.*, 2012, **48**, 3993–3995.
125. R. Afshari, S. Emad Hooshmand, M. Atharnezhad and A. Shaabani, *Polyhedron*, 2020, **175**, 114238.
126. M. Edgar, F. Zeinali, M. Mojally, C. Hughes, S. Riaz and G. W. Weaver, *J. Fluor. Chem.*, 2019, **224**, 35–44.

127. Q. Wu and L. Wang, *Synthesis*, 2008, **2008**, 2007–2012.
128. S. Tang and H. Zhao, *RSC Adv.*, 2014, **4**, 11251.
129. I. Mangelsdorf, A. Boehncke and G. Könnecker, *Diethylene glycol dimethyl ether*, World Health Organization, Geneva, 2002.
130. G. Bagchi and D. J. Waxman, *Int. J. Androl.*, 2008, **31**, 269–274.
131. J. Kay, It's Glymes Time, <https://www.scientificamerican.com/article/its-glymes-time-epa-takes/>, (accessed 9 April 2020).
132. J. Pliego, *Org. Biomol. Chem.*, 2018, **16**, 3127–3137.
133. V. I. Yakerson, *Russ. Chem. Bull.*, 1963, **12**, 914–921.
134. Tris[Bis(2-Methoxyethyl)Ether]Potassium and Tetraphenylarsonium Hexacarbonylmetallates(1–) of Niobium and Tantalum - Ellis - 1976 - Inorganic Syntheses - Wiley Online Library, <https://onlinelibrary.wiley.com/doi/abs/10.1002/9780470132470.ch21>, (accessed 3 April 2020).
135. Y. Favennec, V. Labbé and F. Bay, *J. Comput. Phys.*, 2003, **187**, 68–94.
136. A. H. Morrish, *The Physical Principles of Magnetism*, Wiley-IEEE Press, 2001.
137. M. Getzlaff, *Fundamentals of Magnetism*, Springer, 2008.
138. A. Jordan, P. Wust, H. Fähhlin, W. John, A. Hinz and R. Felix, *Int. J. Hyperther.*, 1993, **9**, 51–68.
139. H. Parmar, I. S. Smolkova, N. E. Kazantseva, V. Babayan, P. Smolka, R. Moučka, J. Vilcakova and P. Saha, *Procedia Eng.*, 2015, **102**, 527–533.
140. P. C. Fannin, *J. Phys. D Appl. Phys.*, 1991, **24**, 76.
141. L. J. Goossen and K. Goossen, *Top. Organomet. Chem.*, 2013, **44**, 121–142.
142. S. Ceylan, L. Coutable, J. Wegner and A. Kirschning, *Chem. Eur. J.*, 2011, **17**, 1884–1893.
143. A. Zdražil and F. Štěpánek, *Chem. Eng. Sci.*, 2015, **134**, 721–726.
144. D. Astruc, in *Nanoparticles and Catalysis*, ed. D. Astruc, Wiley-VCH, 2008.
145. J. Sherwood, J. H. Clark, I. J. S. Fairlamb and J. M. Slattery, *Green Chem.*, 2019, **21**, 2164–2213.
146. G. Cahiez, A. Moyeux, O. Gager and M. Poizat, *Adv. Synth. Catal.*, 2013, **355**, 790–796.
147. Favier Isabelle, Gómez Montserrat, Muller Guillermo, Picurelli David, Nowicki Audrey, Roucoux Alain and Bou Jordi, *Journal of Applied Polymer Science*, 2007, **105**, 2772–2782.
148. M. Aygün, C. T. Stoppiello, M. A. Lebedeva, E. F. Smith, M. del C. Gimenez-Lopez, A. N. Khlobystov and T. W. Chamberlain, *J. Mater. Chem. A*, 2017, **5**, 21467–21477.
149. G. Sharma, A. Kumar, S. Sharma, M. Naushad, R. Prakash Dwivedi, Z. A. Alothman and G. T. Mola, *J. King Saud Univ. Sci.*, 2019, **31**, 257–269.
150. H. Dong, Y.-C. Chen and C. Feldmann, *Green Chem.*, 2015, **17**, 4107–4132.
151. S. H. Y. Lo, Y.-Y. Wang and C.-C. Wan, *J. Colloid Interface Sci.*, 2007, **310**, 190–195.
152. H. Grennberg, in *Encyclopedia of Reagents for Organic Synthesis*, American Cancer Society, 2001.
153. P. Boon-Kin, E. Hendry I., C. Jian-Xiong, J. Wei, T. Bernhardt L. and L. Jim-Yang, *J. Phys. Chem. C.*, 2007, **111**, 6281–6287.
154. L. Prati and A. Villa, *Gold Catalysis - Preparation, Characterization, and Applications*, Taylor & Francis, 2016.
155. D. Marie-Christine and A. Didier, *Chem. Rev.*, 2004, **104**, 293–346.
156. S.-H. Wu and D.-H. Chen, *J. Colloid Interface Sci.*, 2003, **259**, 282–286.

157. Y. Holade, N. E. Sahin, K. Servat, T. W. Napporn and K. B. Kokoh, *Catalysts*, 2015, **5**, 310–348.
158. R. K. Rai, K. Gupta, D. Tyagi, A. Mahata, S. Behrens, X. Yang, Q. Xu, B. Pathak and S. K. Singh, *Catal. Sci. Technol.*, 2016, **6**, 5567–5579.
159. D.-B. Trung, D. Pla, I. Favier and M. G. Gomez, *Catalysts*, 2017, **7**, 207/1-207/33.
160. J. Sappl, R. Freund and C. Hoch, *Crystals*, 2017, **7**, 352.
161. A. Zaleska-Medynska, M. Marchelek, M. Diak and Ewelina. Grabowska, *Adv. Colloid Interface Sci.*, 2016, **229**, 80–107.
162. D. V. Talapin and E. V. Shevchenko, *Chem. Rev.*, 2016, **116**, 10343–10345.
163. A. Fromm, C. van Wüllen, D. Hackenberger and L. J. Goossen, *J. Am. Chem. Soc.*, 2014, **136**, 10007–10023.
164. F. Heshmatpour, R. Abazari and S. Balalaie, *Tetrahedron*, 2012, **68**, 3001–3011.
165. J. Clayden, N. Greeves and S. Warren, *Organic Chemistry - Second Edition*, Oxford University Press, New York, 2012.
166. J. Cornella, M. Rosillo-Lopez and I. Larrosa, *Adv. Synth. Catal.*, **353**, 1359–1366.
167. N,N-dimethylacetamide - Substance Information - ECHA, <https://echa.europa.eu/substance-information/-/substanceinfo/100.004.389>, (accessed 3 July 2020).
168. Bis(2-methoxyethyl) ether - Substance Information - ECHA, <https://echa.europa.eu/substance-information/-/substanceinfo/100.003.568>, (accessed 3 July 2020).
169. Quinoline - Substance Information - ECHA, <https://echa.europa.eu/substance-information/-/substanceinfo/100.001.865>, (accessed 3 July 2020).
170. M. A. Newton, J. B. Brazier, E. M. Barreiro, S. Parry, H. Emmerich, L. A. Adrio, C. J. Mulligan, K. Hellgardt and K. K. (Mimi) Hii, *Green Chem.*, 2016, **18**, 406–411.
171. R. A. Sheldon, *Pure Appl. Chem.*, 2000, **72**, 1233–1246.
172. I. T. Jolliffe and J. Cadima, *Philos. Trans. R. Soc. A*, 2016, **374**, 20150202.
173. P. Anastas and J. Warner, *Green Chemistry - Theory and Practice*, Oxford University Press, New York, 1998.
174. P. Sartori and M. Weidenbruch, *Chem. Ber.*, 1967, **100**, 3016–3023.
175. D. Katayev, B. Exner and L. J. Goossen, *Chem. Cat. Chem.*, 2015, **7**, 2028–2032.
176. L. Hu, D. Wang, X. Chen, L. Yu, Y. Yu, Z. Tan and G. Zhu, *Org. Biomol. Chem.*, 2017, **15**, 5674–5679.
177. Q. Gao, S. Liu, X. Wu, J. Zhang and A. Wu, *Org. Lett.*, 2015, **17**, 2960–2963.
178. US Patent and Trademark Office, US4723016, .
179. A. Yu. Shabalin, N. Yu. Adonin, V. V. Bardin and V. N. Parmon, *Tetrahedron*, 2014, **70**, 3720–3725.
180. L. Yin, Z. Zhang and Y. Wang, *Tetrahedron*, 2006, **62**, 9359–9364.
181. S.-L. Mao, Y. Sun, G.-A. Yu, C. Zhao, Z.-J. Han, J. Yuan, X. Zhu, Q. Yang and S.-H. Liu, *Org. Biomol. Chem.*, 2012, **10**, 9410–9417.
182. GAMESS-US, <https://www.msg.chem.iastate.edu/gamess/>, (accessed 31 August 2019).
183. Avogadro - Free cross-platform molecular editor, <https://avogadro.cc/>, (accessed 31 August 2019).
184. wxMacMolPlt, <https://brettbode.github.io/wxmacmolplt/>, (accessed 31 August 2019).

